DETERMINING THE ROLE OF PROTOCADHERIN-1 IN ANGIOGENESIS

by

WERTHER VECCHIATO

A thesis submitted to the University of Birmingham for the degree of

DOCTOR OF PHILOSOPHY

Institute of Cardiovascular Sciences

College of Medical and Dental Sciences

The University of Birmingham

July 2021

Abstract

Protocadherin-1 (PCDH1) is a single-pass transmembrane protein belonging to the Cadherin superfamily of adhesion molecules. Protocadherins are involved in neuronal guidance, however a biological role for PCDH1 has not been established. Many neuronal guidance cues are co-opted as angiogenic cues, and PCDH1 is expressed in both neural tissue and the endothelium. The hypothesis explored in this thesis is that PCDH1 participates in angiogenesis. Different siRNA duplexes reduced PCDH1 expression in human umbilical vein endothelial cells (HUVEC), thereby impairing chemotaxis and connectivity on Matrigel. However, these phenotypes were abolished when all duplexes were delivered as part of a siRNA-mixture. Transcriptomic analysis of siRNA-mixture-treated cells suggested that endogenous PCDH1 has a modestly anti-angiogenic role, but identified no clear candidate to mediate the phenotypes observed initially. Mass spectrometric analysis of the PCDH1 intracellular interactome detected Desmoplakin, a cytosolic scaffold protein. Proximity-sensitive immunofluorescence experiments corroborated these findings, and biochemical analysis revealed that the first four Spectrin repeats of Desmoplakin co-purify with PCDH1. The truncated, soluble PCDH1 ectodomain did not alter HUVEC connectivity on Matrigel, and Pcdh1-knockout embryos displayed no vascular abnormalities at E13.5. Overall, these findings indicate that PCDH1 does not play a critical role in angiogenesis but they do identify a novel intracellular interacting partner for PCDH1.

To Adelina

and Maria.

Thank you.

Acknowledgements

First and foremost, my most sincere thanks to my primary supervisor, Dr Victoria Heath, for always being there over the past (nearly) 4 years. I was lucky to be able to count on her scientific knowledge and integrity from day one to the very last and, without her support, I simply could not have managed to tackle this project. Thank you.

I would also like to thank my secondary supervisor, Prof Roy Bicknell, not only because his help was also extremely beneficial throughout my project, but also because his patenting- and spinout-related woes helped inspire the next step in my career.

The generosity of the British Heart Foundation, who funded my project through the expected years, and then some unexpected months, is also gratefully acknowledged.

Two other people were pivotal in fitting together the PCDH1 puzzle: one is Dr Debbie Cunningham, who kindly gathered and organised the mass spectrometry data, and taught me how to analyse it. The other is Dr Martyn Chidgey, who gracefully helped me over two years in pursuing the Desmoplakin connection (pun intended), and was an extremely generous source of ideas, advice, and reagents.

The extended molecular angiogenesis group, and in particular Dr Pete Hewett, were also helpful throughout all stages of the project, and I am very thankful to them all for our productive discussions every Monday. Equally, Dr Zsuzsanna Nagy spent a lot of her time getting my microarray data ready for in depth pathway analysis, and had the patience to explain to me (a complete microarray novice, *ça va sans dire*) how to analyse the HUVEC transcriptome in a meaningful way, which would not have happened without her expert advice.

The past and current members of the angiogenesis group, and of ICVS at large, were often a source of ideas, and even more often managed to accommodate my last-second antibody requests late in the evening. Thank you to all, there are (and have been) too many of you to

name. I will miss hearing the updates to everyone's story every few months at seminars.

I am grateful to Dr Martijn Nawijn and Prof Gerard Koppelman (and their labs) at the University of Groningen, for agreeing to collaborate on the PCDH1 project and for providing the Pcdh1 Flox mice. Similarly, I am very grateful to the BMSU staff for their efforts in rederiving and breeding them, and for sparing me the rather grim affair of extracting the uteruses. An even larger thank you to Dr Deirdre Kavanagh for the long time she spent acquiring light-sheet images of these embryos in lieu of me, and for four years of relentless microscopy advice.

I am also very grateful to Dr Neena Kalia, and the PGR student admin team, for giving me the chance to learn so much more than I imagined about University – and myself – from the inside.

Thank you to Julian and the volunteers at Harborne's Oxfam bookshop, who allowed me to spend my weekends in a very different way to my weekdays. I will really miss our chats.

Thank you to Aman, Jack, and Lily, whom I met without expectations, in whose company hours pass by easily just talking away, and whose friendship I am lucky to cherish.

Thank you Dr Rebecca Saleeb for being one of the few who will sit through long sessions of me talking about science, and still agree to playing board games and be my friend afterwards.

Thank you to Anna, Beatrice, Federico, Nicola, Valentina, and the rest of the Aye-talians, for the time we spent and spend together every time I go Home.

Thank you to my family, especially my parents and sister, for their trust, and for their unfaltering and unquestioning support over the years. I am very lucky, and forever grateful.

"Thank you" to little Socks for waking me up at 4, 5, *and* 6 am. Every day.

Finally, with the dubious honour of being mentioned twice on different merits, thank you to Dee for being kind, happy, supportive, funny, motivating, honest, patient, inspiring, and a better person than me. Thank you for choosing to share your life with me for the past few years and, hopefully, for the many to come.

Table of contents

Chapter 4: Determining the cytosolic interacting partners of PCDH1……………………132

List of illustrations

List of tables

List of abbreviations

ACN: acetonitrile
Amp: ampicillin
APS: ammonium persulfate
AJ: adherens junction
bp: basepair
BCA assay: bicinchoninic acid assay
BLAST: basic local alignment search tool
bM199: basal M199
BSA: bovine serum albumin
BSL-2: biosafety level 2
Cam: chloramphenicol
CDH: cadherin
cM199: complete M199
Cre: causes recombination of the bacteriophage P1 genome
Cyclic AMP: cyclic adenosine monophosphate
DAPI: 4′,6-diamidino-2-phenylindole
DCM: dichloromethane
DMEM: Dulbecco's modified Eagle medium
DMSO: dimethyl sulfoxide
DP: Desmoplakin
DSP: the gene of Desmoplakin (DP)
DTT: dithiothreitol
EC repeat: extracellular cadherin repeat (can be followed by an identifying number, e.g. “EC2”)
EC: endothelial cell
ECD: extracellular domain
EDTA: ethylenediaminetetraacetic acid
EGFP: enhanced green fluorescent protein
FACS: fluorescence-activated cell sorting
FBS: foetal bovine serum
FGF: fibroblast growth factor
FLAG: protein tag for affinity purification (residues: DYKDDDDK)
Flox: flanked by *loxP*
GSH: glutathione (reduced)
GST: glutathione *S*-transferase; protein tag for purification
GJ: gap junction
HEK: human embryonic kidney cell line
HEK 293T: HEK cell line derivative, transduced with the SV40 T antigen
hFc: Fc (fragment, crystallisable) portion of human IgG protein
HaCaT: keratinocyte cell line (origin of acronym is unknown)
HMVEC: human microvascular endothelial cells
HRP: horseradish peroxidase
HSP: heat-shock protein
HUAEC: human umbilical artery endothelial cells
HUVEC: human umbilical vein endothelial cells
ICD: intracellular domain
iDISCO: immunolabeling-enabled three-dimensional imaging of solvent-cleared organs

IF: immunofluorescence
Ig: immunoglobulin
IPTG: isopropyl β-D-1-thiogalactopyranoside
JUP: the gene of Junction Plakoglobin (PG)
kDa: kilo-Dalton i.e. 1,000 Da
KO: knockout
LB medium: Luria Bertani medium
loxP: *locus* of X-over P1
LSFM: light-sheet fluorescence microscopy
mAb: monoclonal antibody
MCS: multiple cloning site
MIP: maximum intensity projection
MMRN2: multimerin-2
MWCO: molecular weight cut-off
Myc: Myelocytomatosis virus; protein tag for affinity purification (residues: EQKLISEEDL)
NA: numerical aperture
NCBI: National Center for Biotechnology Information
NCD: negative-control duplex
pAb: polyclonal antibody
PBS: phosphate-buffered saline
PCDH: protocadherin
PCM199: Promocell-supplemented M199
PEI: polyethylenimine
PFA: paraformaldehyde
PG: Plakoglobin
PKP: Plakophilin
PLA: proximity ligation assay
Plan Apo: Flat-Field and Apochromatic corrections
PMSF: phenylmethylsulfonyl fluoride
PTwH: PBS, Tween-20, heparin buffer
rM199: reduced-serum-content M199
RNA-ISH: ribonucleic acid *in situ* hybridisation
ROI: region of interest
Rpm: rotations per minute
RT enzyme: reverse transcriptase
sCMOS: scientific complementary metal-oxide-semiconductor
SDS-PAGE: sodium dodecyl sulphate-polyacrylamide gel electrophoresis
s.e.m.: standard error of the mean, i.e. standard deviation ÷ $\sqrt{(n)}$, (where n = number of repeats)
siRNA: short interfering RNA
SOC medium: super optimal broth with catabolite repression
TAE buffer: Tris base, acetic acid, EDTA
TBS-T: tris-buffered saline with Tween-20
TEMED: *N,N,N,N*-tetramethylethylenediamine
Tris: tris(hydroxymethyl)aminomethane
TJ: tight junction
vSMC: vascular smooth muscle cell
WB: western blot i.e. immunoblot
WT: wild-type

CHAPTER 1: GENERAL INTRODUCTION

1.1. Angiogenesis

1.1.1. Blood vessel morphogenesis

Multicellular organisms face the challenges of delivering nutrients and disposing of waste across all their cells. Indeed, it is estimated that nearly all cells reside within 100 μm of their nearest capillary (Alberts et al., 2015), and that for a neoplastic mass to proliferate beyond 1 mm^3 it needs to establish its own blood supply (Gimbrone et al., 1972). As a consequence of these limitations, a widely reaching circulatory system that accomplishes these vital functions forms early on in embryogenesis: 19 dpc in humans (Sadler, 2012), E8.0 in mice (Drake & Fleming, 2000), 24 hpf in zebrafish (Kimmel et al., 1995). The first blood vessels arise during embryogenesis via the process of vasculogenesis, whereby mesodermal precursors (haemangioblasts) migrate as single cells in a process dependent on Apelin receptors (Helker et al., 2015), and then differentiate to form a plexus – a primitive capillary network of endothelial cells (ECs). The main vessels, such as dorsal aortae and then cardinal veins, form by this process. A subset of these haemangioblasts also start to give rise to the haematopoietic lineage, but such *de novo* formation of vessels only takes place in the first stages of development. To achieve a fully formed vascular system, in fact, the immature plexus grows more intricate and is extensively remodelled through a different mechanism, involving successive iterations of network enlargements and pruning, in what is referred to as angiogenesis: the establishment of new blood vessels from pre-existing ones. Much of the process is regulated by dynamic gradients of secreted vascular endothelial growth factor A (VEGFA). Concurrently, arteriogenesis takes place: the newly formed endothelium recruits and is surrounded by pericytes and vascular smooth muscle cells (vSMCs), and the network thus assembled starts to resemble the adult vascular system. The balanced growth of this network occurs through at least two different mechanisms, one being sprouting angiogenesis, whereby one EC emerges laterally from a vessel and spearheads a trail of ECs towards another single cell undergoing the same process. The fusion of these two cells leads to the establishment of a new patent vessel. The other mechanism of physiological vessel formation is non-sprouting (intussusceptive) angiogenesis, where two vessels arise from the physical splitting of a pre-existing one; the two angiogenic processes can in fact take place concurrently (Carmeliet & Jain, 2011). Angiogenesis then occurs in adult physiology as part of wound healing and during the menstrual cycle, and notably in the pathogenesis of tumours, psoriasis, and age-related macular degeneration (Carmeliet & Jain, 2011).

1.1.2. Stages of sprouting angiogenesis

Healthy endothelia are quiescent (**Figure 1.1A**): monolayers of ECs lining adult vessels adopt a phalanx phenotype, and are characterised by long lifespan, a mostly glycolytic metabolism (Potente & Carmeliet, 2017), and well-established connections between themselves, principally mediated by VE-cadherin (Lagendijk & Hogan, 2015). Importantly, ECs are interconnected through the pericytes that cover them abluminally, which facilitate cellular crosstalk (Armulik et al., 2005) and produce angiopoietin 1 (ANG1), maintaining an endothelial quiescent phenotype (Suri et al., 1996). A key regulating factor of sprouting angiogenesis is local oxygen deficiency: under normoxic circumstances, Hypoxia Inducible Factor α (HIFα) subunits are multi-hydroxylated by Prolyl Hydroxylase Domain-containing (PHD) enzymes, which ensures rapid, targeted HIFα proteolysis through the ubiquitin system (Majmundar et al., 2010). During episodes of tissue hypoxia, on the other hand, HIFα subunits fail to be hydroxylated, which allows them to heterodimerise with the cognate HIF1β subunit, stimulating expression of a plethora of hypoxia-responsive genetic elements, including the VEGF and ANG2 genes (**Figure 1.1B**). These elicit extracellular matrix degradation, detachment of ECs from pericytes, and loosening of cell-cell junctions, ultimately allowing for cell migration, which is specifically

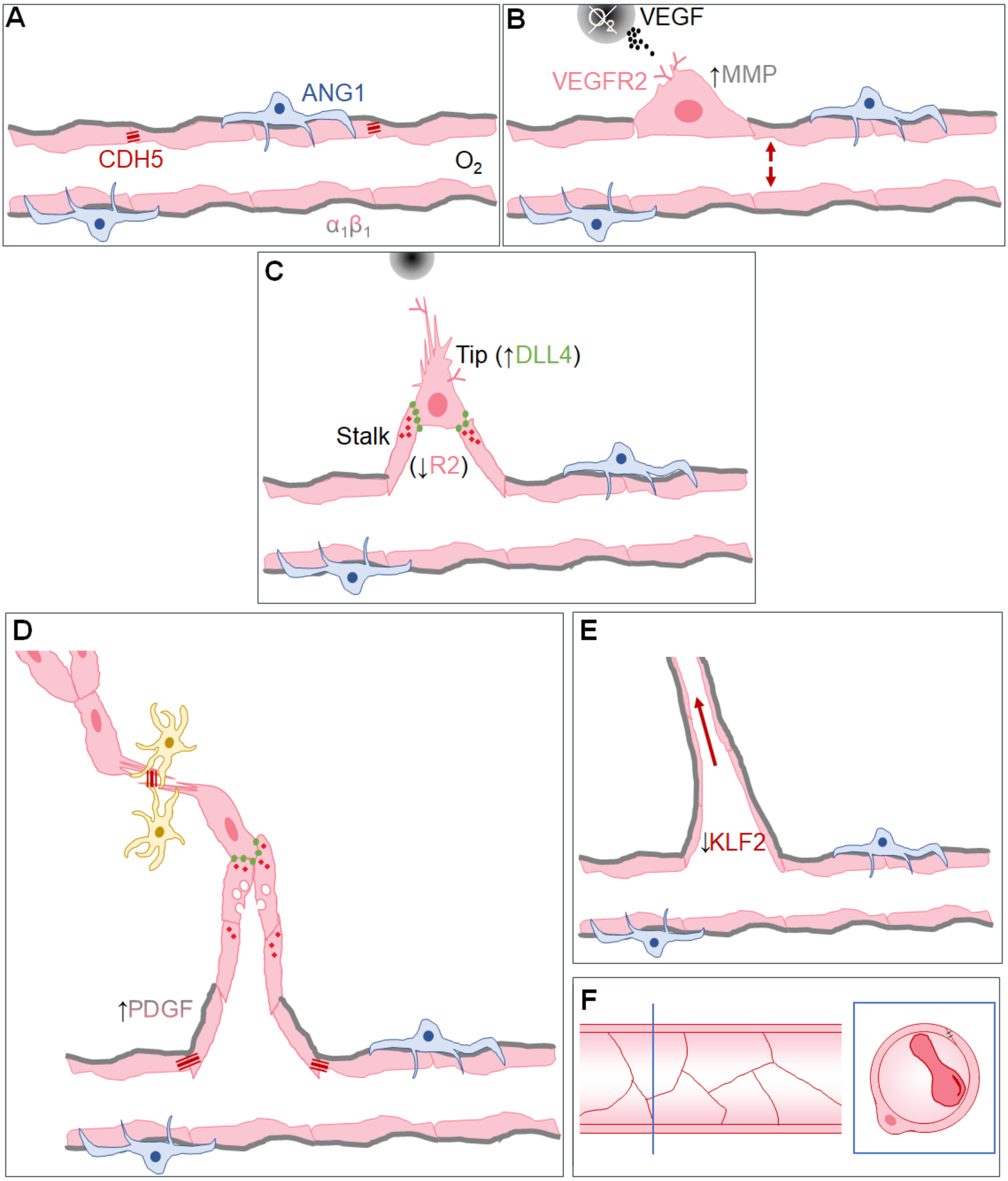

Figure 1.1. Main stages of sprouting angiogenesis in the microvasculature.
A. Blood vessels deliver solutes (e.g. O_2) to extravascular tissues, and scavenge metabolic waste. Endothelial cells (ECs, pink) are joined through extensive adhesion sites, which express VE-cadherin (CDH5, burgundy) at adherens junctions, and claudins at tight junctions (not shown). Specific integrin pairings, such as $\alpha_1\beta_1$, are only found between the endothelium and the surrounding basement membrane (BM, grey) in the abluminal space, imparting directionality for solute transfer. ECs are maintained quiescent by their interactions with mural cells (e.g. pericytes, blue), which present membrane-bound ligands such as ANG1 to endothelial TIE2 receptors.
B. Oxygen-starved tissues secrete pro-angiogenic factors, including VEGFA (black), initiating chemotactic gradients that stimulate filopodial protrusions on ECs in capillaries. In response to VEGF binding, VEGFR2 (pink) is upregulated, VE-cadherin is downregulated and intercellular junctions loosen, resulting in vessel volume enlargement (arrows) and intracellular protein extravasation. Pericytes detach, and the basement membrane is degraded by matrix metalloproteinase proteins (MMP, grey), allowing EC migration.

(Continued from previous page)

C. VEGFR2-expressing filopodia enable chemotaxis by generating motile force *via* cytoskeletal rearrangement. Many other guidance cues (**Table 1.1**), not depicted, are involved in establishing the precise migratory trajectory. Only one cell per sprout leads the migration, because VEGFR2-VEGF interactions increase DLL4 (green) expression on the tip cell, resulting in NOTCH processing (red) among trailing (stalk) cells, which downregulates VEGFR2 expression.

D. Stalk cells proliferate, and secrete factors (e.g. PDGF) that stimulate BM deposition and establishment of intercellular junctions. The abluminal space is augmented by vacuole exocytosis from ECs. Tip cell fusion between filopodia can be facilitated by the recruitment of macrophages (yellow) to the site of anastomosis, with CDH5 strengthening the nascent interfaces.

E. A patent vessel is established once two tip cells fuse. Vessel hollowing is encouraged by blood flow (arrow), which also suppresses the KLF2 transcription factor by mechanotransduction, thereby reinstating a quiescent EC phenotype.

F. ECs in mature vessels adopt a stereotypically flat shape (left, longitudinal section), to maximise free surface area and cell-cell contact spaces. The smallest capillaries can consist of one EC wrapped around itself (right, transverse section through the blue plane), resulting in a typical microvascular cell body thickness below 0.3 μm (Wallez & Huber, 2008), allowing the flow of one red blood cell at a time. *In vivo*, arterial ECs align with blood flow, whereas venous ECs are less elongated (Lampugnani, 2012).

stimulated by the developing ANG2-TIE2 interactions. The next phase involves the selection of a tip cell, a single EC that explores its surroundings via its numerous, long filopodial extensions (**Figure 1.1C**). Tip cells are selected by their expression of VEGF Receptor 2 (VEGFR2), and respond to a gradient of extracellular VEGFA (and other extracellular cues) by increasing their motility and migrating towards the VEGF source. As a result of VEGF binding, they upregulate Delta-like 4 (DLL4), a membrane-bound ligand. NOTCH receptors on neighbouring cells bind DLL4, and thus activate the WNT signalling cascade (Phng et al., 2009), suppressing tip cell identity in favour of a more proliferatory and less motile phenotype, characteristic of the stalk cells; these cells proliferate and form a trail behind the tip cell, establishing the newly growing vessel. At the same time, they propagate the same signal to other neighbouring cells; as a result, only one tip cell per sprout is ever selected to lead. In this way, physiological angiogenesis is a dynamic and very tightly regulated process. Two tip cells that migrate towards each other can coalesce (anastomosis, **Figure 1.1D**), through bridging interactions that can be mediated by specially recruited myeloid cells (Nucera et al., 2011). A patent vessel then finally forms by EC hollowing, once apicobasal identity has been established; key in deciding such polarity are β_1 integrin-matrix interactions, which are only present on the abluminal side of ECs (Zovein et al., 2010). Mural cells recruitment, stimulated by Platelet-Derived Growth Factor (PDGF) B, ANG1, NOTCH, Transforming Growth Factor (TFG) β, and other molecules, re-establishes the endothelial quiescent phenotype and appearance (**Figure 1.1E**,**F**).

1.1.3. Prototypical angiogenic factors: the VEGF family

Vegfr2$^{-/-}$ and *Vegfr1*$^{-/-}$ mice display embryonic lethality at day E8.5-9.5 (Miquerol et al., 1995; Shalaby et al., 1995), as do *Vegfa*$^{+/-}$ mice (Carmeliet et al., 1996; Ferrara et al., 1996), showing acute cardiac and vascular defects; interestingly, overexpression of Vegfa is also embryonic lethal, although at later stages (Miquerol et al., 1995). These observations underscore the importance of VEGF signalling in angiogenesis, considered a master-switch of the whole process (Herbert & Stainier, 2011).

The vertebrate VEGF(R) family comprises five soluble ligands, VEGFA-D and Placental Growth Factor (PlGF), and three plasma membrane receptors, VEGFR1-3. All VEGFRs are structurally related receptor tyrosine kinases with 7 Ig-like domains, which dimerise and then activate by auto-phosphorylation. The ligands bind these receptors with differing selectivity, and the most potently pro-angiogenic stimulation arises in response to VEGFA-VEGFR2 binding, which stimulates a variety of pro-proliferative and cell-migratory targets. As a result of this interaction, ECs increase permeability, vessels enlarge, and the angiogenic programme is started. VEGFA displays higher binding affinity for VEGFR1 than for VEGFR2 (Blanco & Gerhardt, 2013), yet the latter elicits the aforementioned responses much more dramatically. In fact, VEGFR1 has only weak kinase activity, and is presumed to mostly act as a decoy receptor of VEGFA, to downmodulate its activity. sVEGFR1 is an extracellular truncation of the VEGFR1 ectodomain, and itself acts as a decoy for VEGFA molecules, dampening their effects. While VEGFR1/2 are mostly expressed in the cardiovascular endothelium, VEGFR3 is found predominantly on lymphatic ECs, and blood vessels undergoing apoptosis (Blanco & Gerhardt, 2013); VEGFC has highest affinity for VEGFR3, in mediating lymphangiogenesis, but can also bind VEGFR2 to stimulate cardiovascular permeability and growth (Tammela et al., 2008). Further complicating the picture, differential splicing of the 8-exon *VEGFA* gene results in at least four main isoforms – of 121, 165, 189, and 206 residues (Ferrara et al., 2003). $VEGF_{165}$ is the prevalent isoform, and although it is secreted, it is also partly stored in the extracellular matrix (ECM) space, and released by *C*-terminal proteolysis when needed. Importantly, while the soluble portion of VEGFA induces vasodilation, the heparin-bound counterpart in the ECM stimulates vascular branching instead (Ruhrberg et al., 2002). VEGF$_{165}$b, a more recently identified splice variant, can bind VEGRF2 with the same affinity of the main ligand, but inhibits angiogenesis in vertebrates (Woolard et al., 2004). In another fine-tuning mechanism of the signalling cascade, upon VEGFA binding of VEGFR2, the complex is internalised and maintained in its active state inside endosomal vesicles (Alghanem et al., 2017; Lampugnani et al., 2006). These can be recycled in a RAB4A-dependent manner, further enhancing the half-life of the proangiogenic signal (Reynolds et al., 2009).

1.1.4. Molecular processes similar to angiogenesis

Neurogenesis is the process by which the diverse neural cell population of an organism and its complex arrangement are established (Götz & Huttner, 2005). It involves stem cell-like progenitors that, upon cell division, can give rise to distinct populations, including neurons (Götz & Huttner, 2005). Neurons are highly specialised cells responsible for the conduction of nerve signals between sensory zones and the central nervous system, with some neurons growing to lengths of even metres; typically, a single protrusion (axon) in these cells migrates towards its destined environment to establish connections between a variety of other cells, including other neurons. Even at a superficial level, the process is very reminiscent of angiogenesis, as they both largely take place during embryonic development, and establish intricate networks of interconnected cells. The environment-sensing unit of neurogenesis is the axonal growth cone, the distal end of an axon, which consists of a large lamellipodial structure out of which numerous filopodia protrude to bind extracellular cues, directing the cell accordingly. While neurons, unlike ECs, do not physically fuse to other cells once they reach their destination, the structure of an axonal cone is nonetheless very similar to that of an endothelial tip cell (Wälchli et al., 2015). Neurons form stable, lifelong connections whose precise positioning is at the core of their functioning, underscoring the importance of a precise response to sensory cues in this context too. In the case of neurogenesis, navigating axons can respond to both mechanical stimuli (Franze & Guck, 2010) and, largely, to a variety of biochemical signals, that are both attractive and repulsive. Importantly, neurons must be able to avoid making connections to themselves, a process mediated by the Protocadherin family in vertebrates (**Section 1.3**). Some tissues show remarkable superimposition of nerve and endothelial trees (Larrivée et al., 2009) and indeed, both axons and ECs appear to be attracted and repelled by many molecules in the same classes, including ephrins, semaphorins, netrins, and slits (**Table 1.1**). Therefore, it seems likely that endothelial cells co-opted many of the proteins involved in axon guidance when the evolutionary need for a vascular system arose (De Smet et al., 2009).

Another embryonic process that is remarkably similar to angiogenesis is tracheal branching in invertebrates (Affolter et al., 2009), where tubules that deliver oxygen are established throughout the whole organism, a process intensely studied in *D. melanogaster*. Local demand of oxygen by hypoxic tissues in *Drosophila* results in nuclear accumulation of HIF1α (Grifoni et al., 2015), much like in vertebrate angiogenesis (**Section 1.1.2**). This establishes a gradient of BNL, an invertebrate FGF, which is followed chemotactically by tracheal epithelial cells expressing BTL, the transmembrane receptor for BNL (Best, 2019) – a molecular crosstalk analogous to the VEGF-VEGFR axis that elicits angiogenesis. Filopodia in this “terminal cell” allow migration and establishment of the full tracheal tree, while trailing cells are proliferative and prevented from leading other branches by induced expression of Delta and Notch (Affolter et al., 2009). While BNL is the main ligand to drive cell motility in this context, many other biochemical cues are also involved, notably Slit and Robo molecules, which also regulate kidney branching morphogenesis during mouse development (Affolter et al., 2009).

Table 1.1. Examples of chemotactic cues and receptors shared between angiogenesis and neurogenesis.

Angiogenesis			Neurogenesis		
Ligand	**Receptor**	**Details**	**Ligand**	**Receptor**	**Details**
Ephrin-B2	-	Mouse arterial EC marker (Wang et al., 1998); Ephrin-B2$^+$ angioblasts migrate to form the zebrafish dorsal aorta (Herbert et al., 2009)	Ephrin-B2	EphB1	Binding repels axonal growth in mouse retinal explants (Williams et al., 2003)
-	EphB4	Mouse venous EC marker (Wang et al., 1998); Eph-B4$^+$ angioblasts migrate to form the zebrafish cardinal vein (Herbert et al., 2009)			
Ephrin-B2	EphB4	Ephrin-B2 repels neural crest cells away from rat caudal somites (Wang & Anderson, 1997)			
Ephrin-B1,B2	Eph	Soluble Ephrin-B1/B2 repel axonal growth of rat neural explants (Wang & Anderson, 1997)			
			Ephrin-B3	Not known	Neurons in Ephrin-B3-KO mice ectopically cross the motor cortex midline (Kullander et al., 2001)
Sema-3A	Plexin-D1 (*via* Nrp1)	Ectopic vessel growth in zebrafish upon Sema-3A or Plexin-D1 KD, Sema-3A addition inhibits migration in Plexin-D1-expressing HUVEC (Torres-Vázquez et al., 2004); Sema-3A-KO mouse embryos show decreased vascular branching (Serini et al., 2003)	Sema-3A	Neuropilin-1	Sema-3A repels *ex vivo* rat neurons (Messersmith et al., 1995), which is prevented in Nrp1$^{+/-}$ mice (Kitsukawa et al., 1997) – meaning Nrp1 binding mediates the effect
Sema-3A	Not known	No vascular defects in Sema-3A-KO mice (Vieira et al., 2007); Recombinant Sema-3A does not block HUVEC cell migration or adhesion (Pan et al., 2007)			
Sema-3E	Plexin-D1	Sema-3E overexpression in E3 chicken embryos repels vasculature (Gu et al., 2005); in Sema-3E-KO E11.5 embryos, intersomitic vessels are ectopically overextended (Gu et al., 2005)	Sema-3E	Plexin-D1+Nrp1	*Ex vivo* mouse neurons that express PlexD1 **and** Nrp1 grow towards recombinant Sema-3E (Chauvet et al., 2007)
			Sema-3E	Plexin-D1	*Ex vivo* mouse neurons that express PlexD1 **but no** Nrp1 grow away from recombinant Sema-3E (Chauvet et al., 2007)
Netrin-1	Unc5B	Unc5B-KO mice show increased vessel branching and tip cell/filopodial numbers, and KD of Net1 or Unc5B increases intersomitic vessel branching in zebrafish (Lu et al., 2004); recombinant Net1 reduces filopodia/tip cell numbers and sprouting into Matrigel implants	Netrin-1	DCC+UNC5C	Motor neurons grow away from Net1-secreting cells *ex vivo* (Colamarino & Tessier-Lavigne, 1995), **but** only if UNC5C is coexpressed (Burgess et al., 2006)

		in mice (Larrivée et al., 2007)			
Netrin-1	Not known	Recombinant Net1 induces vascular invasion in chick Chorioallantoic Membrane Assay (Park et al., 2004)	Netrin-1	DCC	Net1-KO mice show impaired axonisation of the spine (Rajasekharan & Kennedy, 2009; Serafini et al., 1996)
Netrin-1,4	Not known	HMVEC migrate towards recombinant Net1 or Net4, Matrigel connectivity increases; vessel formation is inhibited by Net1 KD in zebrafish; Net1 or Net4 overexpression alleviates hindlimb ischaemia injury in mice (Wilson et al., 2006)			
Netrin-4	Neogenin-Unc5B	Net4 KD increases Matrigel connectivity, cell migration (Lejmi et al., 2008)			
Netrin-4	Integrin	Net4 stimulates lymphatic endothelial cell adhesion, migration, focal adhesion assembly *in vitro*; overexpression in mice induces lymphangiogenesis (Larrieu-Lahargue et al., 2010)	Netrin-4	DCC, UNC5H1, others (unidentified)	Recombinant Net4 attracts rat neuronal explants through collagen (Qin et al., 2007)
Netrin-4	Not known	Net4 KD induces vascular defects in zebrafish; recombinant Net4 increases Matrigel connectivity and spheroid sprouting of HUVEC/HUAEC (Lambert et al., 2012)			
Robo4*	Unc5B	Blocking antibodies dampen VEGF-R signalling in HUAEC, result in hyperpermeability in mice (Koch et al., 2011)			
Slit2	Robo1,2	Recombinant Slit2 repels growth of ventral spinal cord from E11 rat embryo explants (Brose et al., 1999)	Slit	Robo	Motor axons in Slit-KO *Drosophila* do not migrate away from the ventral midline (Kidd et al., 1999)
Slit2	Robo4	Binding inhibits cell migration/tube formation of mouse lung ECs *in vitro* (Jones et al., 2008)			
VEGF	VEGFR2	Bovine brain VEGF is a potent angiogenic factor (Leung et al., 1989); viral overexpression of VEGFB induces vascularisation in chicken embryos (Flamme et al., 1995)	VEGF	VEGFR2	Recombinant VEGF stimulates *ex vivo* mouse axon outgrowth (Sondell et al., 2000)
			VEGFA	Nrp1	Recombinant VEGF promotes and directs neuronal outgrowth in murine retinal explants (Erskine et al., 2011)

Red = repulsive/anti-angiogenic cue; blue = attractive/pro-angiogenic cue; ***** = membrane-bound receptor.

In conclusion, there is extensive co-option of guidance molecules by many cellular processes that give rise to tubular structures in response to chemotactic gradients, and the overlap is especially prominent between neural and angiogenic molecular cues (**Table 1.1**).

1.2. Adhesion complexes and molecules

1.2.1. Cell adhesion

Cell adhesion is the property that allows cells to organise into functionally distinct and mechanically resistant tissues, and is chiefly mediated by non-covalent interactions between glycoproteins, either membrane-anchored or secreted and reabsorbed. Importantly, it allows attachment both of cells to each other, and of cells to the extracellular matrix (ECM), conferring mechanical stability. In general, cell-ECM junctions mainly involve integrin heterodimers directly binding ECM proteins such as collagen or fibronectin (Theocharis et al., 2016). In contrast, in the simplest depiction of cell-cell adhesion (Honig & Shapiro, 2020), a transmembrane protein on the surface of one cell binds the same protein (homotypic binding) on the surface of an adjacent cell (*trans*-adhesion). Often, however, the extracellular domains of given proteins can also bind to those of non-identical proteins (heterotypic binding). In many cases, lateral association between proteins on the surface of a cell (*cis*-adhesion) allows the formation of large adhesive surfaces. Cell adhesion has been extensively investigated in epithelial cells, which allowed different cell adhesion complexes to be distinguished. In particular, three surfaces can be identified in columnar epithelial cells: a basal surface that is connected to the basal membrane, an apical surface directly opposite, which is normally exposed to extracellular fluid, and a lateral surface that connects the two, which is normally connected to other epithelial cells (Alberts et al., 2015). Remarkably, regardless of cell ontology, the same cell-cell adhesion complexes are shared by most tissues (Plopper et al., 2013), their relative expression levels catering to different requirements of intercellular spacing and mechanical robustness: tight junctions, gap junctions, desmosomes, and adherens junctions (**Figure 1.2**). In fact, most of these types of complexes could be viewed as a context-specific repurposing of the general paradigm of cell-cell adhesion: in the extracellular space, a transmembrane protein binds to its partner (often, an identical molecule) on a different cell, whereas on the cytosolic side it recruits adaptor proteins that allow linkage to the cytoskeleton (Belardi et al., 2020). Each of these complexes will be described below, delineating the general molecular organisation as discovered in epithelial cells first, followed by any endothelial peculiarities. The focus will be on human and murine studies, and very specialised adhesion complexes, such as those involved in protein-carbohydrate adhesion (Cummings, 2019), or transient binding modalities such as the immunological synapse (Belardi et al., 2020) and leukocyte extravasation (Rutledge & Muller, 2020), will not be addressed.

1.2.2. Tight junctions (*zonulae occludentes*)

The lateral surface of epithelial cells is often encircled, just below the apical surface, by a belt-like series of tight junctions (TJs, **Figure 1.2A**). These transmembrane complexes result in virtually non-existent intercellular distances (Tsukita et al., 2001), so much so that the lipid components of the cell membranes of adjacent cells can appear partly fused around TJs (Zihni et al., 2016). TJs in fact seem to be located within cholesterol-rich lipid raft regions, presumably to prevent TJ disassembly (Nusrat et al., 2000). The main function of TJs is to avoid the diffusion and loss of polar solutes across layers of epithelial cells, by virtue of the negligible extracellular space they allow for. Equally, they can prevent basolateral proteins from diffusing into the apical surface. The main molecular components of TJs at the cell membrane are tetraspan proteins, the most abundant being claudins, with over 20 genes in humans; all these

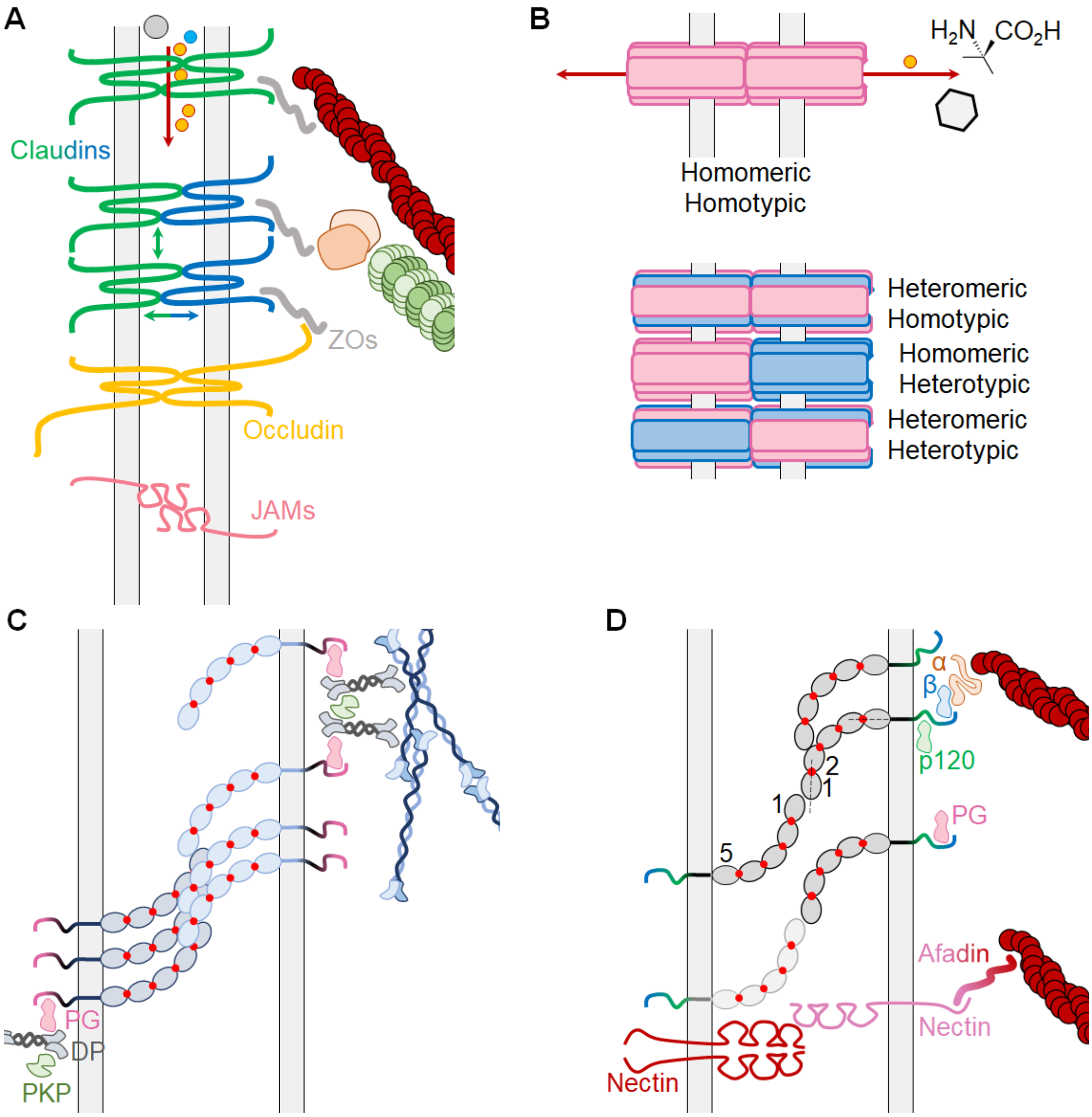

Figure 1.2. Adhesion complexes and molecules (not to scale).
A. Schematic molecular organisation of a tight junction (TJ) at the membrane interface of two adjacent cells (vertical grey lines). Claudins are tetraspan molecules that can either hetero- or homo-dimerise in *trans*, and can associate laterally in *cis* (double-headed arrows). Both extracellular loops mediate adhesion. Their intracellular domains (ICDs) recruit the adaptor ZO proteins (grey), which can interact directly with F-actin (burgundy dots) or recruit cingulin/paracingulin (orange/tan), which in turn interact with microtubules (green dots). Paracellular ion mobility (burgundy arrow) can in fact happen between specific claudin *trans*-homodimers, which allow passage of specific ions (e.g. Na$^+$, yellow dots), but not other charges (anions, blue dots), or bigger ions (grey dots). Occludin is also nearly ubiquitously associated with TJs, and can also recruit ZOs. JAMs can locate at TJs, and dimerise by their membrane-distal Ig domain.
B. Top: schematic molecular organisation of a gap junction (GJ), formed by intercellular adhesion between two connexons, each being a hexamer of connexins (pink). The conduit that forms inside these structures can allow free mobility (double-headed arrow) of small solutes, such as ions (yellow dot), amino acids, and small sugars (hexagon), between adjacent cells. Bottom: connexin proteins can exhibit all combinations of *trans*- and *cis*-interactions.
C. Schematic molecular organisation of a desmosome. Desmogleins (dark blue) and desmocollins (light blue) are single-pass transmembrane cadherins that interact in *trans* hetero-

(Continued from previous page)
typically, and associate in *cis* to create large desmosomes. Their cytosolic tails interact with plakoglobin (pink), which recruits desmoplakin dimers (grey), which in turn interact with the intermediate filaments (blue dimers). Lateral association is augmented by plakophilin (green) recruitment by the cadherins.

D. Schematic molecular organisation of an adherens junction (AJ). Classical cadherins (CDHs, dark grey) readily bind extracellular calcium (red dots) at physiological concentration. They typically adhere homotypically in *trans* by their extracellular cadherin (EC) 1 repeat. The intercellular distance is dictated by the CDH and the bending angle of its ectodomain, which for CDH1 results in EC1 and EC5 being at right angles to each other (dotted lines). CDHs associate laterally owing to EC1-EC2 interactions, and show some promiscuity of interaction in *trans* (paler grey protein). Their cytosolic domains recruit β-catenin (blue), which links to F-actin (burgundy) through α-catenin (orange), which is normally in a closed conformation but, under mechanical stress, can unfold. CDHs can concurrently bind the p120 catenin (green), which regulates CDH half-life. Binding to plakoglobin (PG, pink), a very close relative to β-catenin, has also been reported, but CDH-bound PG cannot interact with α-catenin (Choi et al., 2009). Nectin proteins also co-localise to AJs, and also bind to the actin cytoskeleton, but *via* Afadin adaptors instead; nectins interact both in *trans* (as heterodimers), and in *cis* (as homodimers).

can *trans*-homodimerize, but many were found to also interact in a heterotypic fashion (Furuse et al., 1999). Furthermore, the crystal structure of Claudin-15 showed that the protein is capable of supporting both *trans*-adhesion modes, mediated by five antiparallel β-sheet folds over two extracellular loops, and *cis*-adhesion modes, mediated by interactions between loops of adjacent protomers (Suzuki et al., 2014). The other tetraspan TJ members are occludin, MARVELD3 and, at sites of junction between three cells, tricellulin (Ikenouchi et al., 2005). Interestingly, despite the negligible intercellular distances they create, TJs have been shown to allow at least some degree of paracellular permeability in select tissues: conduits formed between claudins interacting in *trans* can allow ion mobility, as specified by the electrostatic charge of the residues in their extracellular loops, with e.g. Lys65 in Claudin-15 mediating permeability to Na^+ ions (Colegio et al., 2002). Other, single-pass, transmembrane proteins have also been located at TJs, including CRB3, BVES, and the Junctional Adhesion Molecule (JAM) family (Zihni et al., 2016). Interestingly, JAMs adopt a rather different self-adhesion strategy, instead dimerising by their membrane-distal immunoglobulin-like domain (Kostrewa et al., 2001).

On the intracellular side, TJs interact with a variety of cytosolic adaptor proteins, the best characterised of which are the three Zonula Occludens (ZO) proteins, with ZO1 in fact being the first molecular member of TJs to be identified (Stevenson et al., 1986). ZO proteins are very large (> 200 kDa), and consist essentially of a linear arrangement of protein-protein interaction domains: as such, they form essential scaffolds that organise interaction of the cytosolic domains of transmembrane TJ proteins with the cytoskeleton. As an example, claudins, JAMs, and occludin can concurrently bind to different domains of ZO1, separate domains in which are themselves capable of binding to F-actin (Fanning et al., 1998) and, through the adaptors cingulin and paracingulin, the microtubules (Van Itallie et al., 2013; Yano et al., 2013). Interestingly, phase separation of ZO1 is necessary and sufficient to drive TJ assembly (Beutel et al., 2019). Other proteins that locate to the cytosolic region of TJs are MAGI1 and 3, PAR3 and 6, and many actin polymerisers and organisers, such as ARP2/3, CDC42, and Rho GTPases (Van Itallie & Anderson, 2014). Owing to their cytosolic components, TJs can also participate in signalling cascades, for example by suppressing the proliferative effects of the Hippo pathway once stable epithelial sheets with mature TJs are formed (Zihni et al., 2016).

TJs are present in the endothelium but, because ECs lack an extensive lateral surface owing to their thin cross section (**Figure 1.1F**), endothelial TJs are effectively intercalated with gap and adherens junctions (**Sections 1.2.3**, **1.2.5**), rather than forming epithelial-like attachment strands. TJs are very numerous in vessels of neural tissues, where they are critical contributors to establishing the blood-brain barrier (Kniesel et al., 1996), and are less numerous in non-neural endothelia (Bazzoni & Dejana, 2004). The molecular components of endothelial TJs are largely the same as described above, with Claudin-5 being particularly highly expressed in ECs, contributing to the strict absence of paracellular diffusion across neural ECs (Haseloff et al., 2015).

1.2.3. Gap junctions (*maculae communicantes*)

Larger intercellular spaces (~4 nm) form at sites where gap junctions (GJs, **Figure 1.2B**) are present, typically in the lateral regions closest to the basal membrane. These assemblies effectively create channels that allow the free diffusion of solutes up to 1 kDa between neighbouring cells (Kumar & Gilula, 1996). This enables the chemical and electrical coupling of cells in the same tissue, which do not need to invest energy for the export/import of inorganic ions and small organic solutes such as inositol trisphosphate, cyclic AMP, and glucose, while still preventing diffusion of proteins and nucleic acids (Nielsen et al., 2012). The main molecular components of GJs at the cell membrane are tetraspan proteins called connexins, with over 20 genes in humans; these hexamerise in *cis* to assemble a hemichannel with 6-fold symmetry, called connexon, the extracellular portion of which adheres in *trans* to a connexon on another cell, establishing a patent internal conduit. Connexons can either be homomers, when comprised by six identical connexins, or heteromers (**Figure 1.2B**), with up to three different connexin proteins included in a single connexon (Yeh et al., 1998). The connexin makeup of a GJ can subtly vary the internal pore diameter, ~1.4 nm for Cx26 homomers (Maeda et al., 2009), allowing passage of different sizes of solutes; furthermore, different mechanisms allow complete opening or closure of these channels: such gating is sensitive to voltage, pH, [Ca^{2+}], and cytosolic tail phosphorylation, as demonstrated in the most widely expressed member, Cx43 (Nielsen et al., 2012). Only two crystal structures are available, but extracellular adhesion between Cx26 connexons seems to be mediated by hydrophobic interactions involving at least 6 residues distributed across the two extracellular loops (Myers et al., 2018), with only subtle variations observed in the recent structure of Cx46/50 connexon heteromers (Myers et al., 2018). Interestingly, *cis* interactions are also mediated by extracellular residues, resulting in a much larger cytosolic-side channel opening, ~4 nm, thought to work as a “funnel” for incoming solutes (Maeda et al., 2009). Connexins alone are sufficient to constitute functional GJs (Kumar & Gilula, 1996), and there are no other recognised transmembrane members of GJs. Although pannexins share sequence similarity with connexins, they are extensively glycosylated, so it is unlikely that they form functional intercellular channels (Penuela et al., 2007). The intracellular domains of connexins have multiple protein-protein interaction sites (Nielsen et al., 2012), opening up GJs to interaction with a variety of cytosolic adaptor proteins. Some reported interactors are ZO proteins, F-actin, β-catenin, Plakophilin-2, claudins, and tubulin (Giepmans, 2004; Laird, 2010), which suggests extensive crosstalk between GJs, other adhesion complexes, and the cytoskeleton.

Connexin isoforms expressed in the endothelium include Cx32, 37, 40, 43, and 45 (Okamoto et al., 2017; Yeh et al., 1998). GJs, both between ECs, and between ECs and vSMCs, play an important role in mediating longitudinal transfer of action potential, resulting in fast endothelial adaptation to metabolic needs along the length of a blood vessel. For example, second messenger transfer through GJs can mediate quick vasodilation by stimulating NO production along mm-range distances (de Wit & Griffith, 2010). Endothelial GJs were also found to regulate EC stiffness *in vitro*, by increasing focal adhesion numbers in HUVEC (Okamoto et al., 2017). Underscoring the endothelial importance of GJs, $Cx45^{-/-}$ mouse embryos die *in utero* around E9, with severe heart malformations and whole vessels narrowed or even missing (Kruger et al., 2000), and both Cx37 and Cx40 seem to be atheroprotective in mice, by impeding leukocyte trafficking (Chadjichristos et al., 2010; Wong et al., 2006).

1.2.4. Desmosomes (*maculae adherentes*)

Adhesion complexes that result in much larger intercellular spacing on average are desmosomes (**Figure 1.2C**), which enable uniform cell-cell distances of ~30 nm and up to 35 nm (Al-Amoudi et al., 2007). Unlike TJs, they rarely form large lateral assemblies on the cell membrane, instead appearing like small adhesion spots across two cell membranes. The main function of desmosomes is to confer structural stability to tissues by linking together the cytoskeleton – namely, intermediate filaments – of a series of cells through their cell membranes. For this reason, they are found in greater numbers in tissues that are subject to intense mechanical stress, such as skin and myocardium (Al-Amoudi et al., 2007). To provide the required robustness, their extracellular portions adhere very strongly to each other, giving rise to what is termed hyper-adhesion, a type of interaction that resists calcium chelation (Kimura et al., 2007). This is peculiar because the transmembrane components of desmosomes are a family of cadherins, which in general cannot adhere in the absence of Ca^{2+} (**Section 1.2.5**). The desmosomal cadherin genes are all located at one *locus*, Hs Chr 18 (Hunt et al., 1999), whose two clusters code for three desmocollins (DSC1-3) and four desmogleins (DSG1-4). At least one member from each family is generally expressed in the same cell if it forms desmosomes, but only DSC2 and DSG2 are expressed outside of skin tissues (Garrod & Chidgey, 2008). The structures of these seven proteins are very similar: they all have five domains of around 100 residues each (Garrod & Chidgey, 2008), called Extracellular Cadherin (EC) repeats due to their similarities to the EC repeats of classical cadherins, together resulting in similar *trans*-adhesion modalities (**Section 1.2.6**). Surprisingly, however, DSC and DSG extracellular interactions are mainly heterophilic i.e. DSC preferentially binds DSG, with self-affinity in fact being quite low (Harrison et al., 2016). Furthermore, adhesion surfaces are much larger than in classical cadherins, giving rise to more extensive *cis*- and *trans*-interactions (Sikora et al., 2020), at least partly explaining their characteristic hyper-adhesion, with Ca^{2+} buried in stretches inaccessible to chelators. Two other transmembrane proteins, PERP and Corneodesmosin, have been at times associated with desmosomes, but their role and possible importance for adhesion are still unclear (Garrod & Chidgey, 2008).

Desmosomes were first identified by electron microscopy on the basis of the dense proteinaceous plaques they form on the intracellular side, later found to correspond to the extensive repertoire of adaptor proteins that link their cadherins to the intermediate filaments. The linker proteins, in all desmosomes, are Desmoplakin (DP), Plakoglobin (PG, i.e. γ-catenin), and at least one of three plakophilins (PKP). PG and PKP are part of the Armadillo protein family, because they contain multiple ARM repeats, which serve as protein-protein interaction platforms. ARM repeats mediate the interaction of PG with the desmosomal cadherins (Witcher et al., 1996), although they do not for PKP, which has fewer such repeats (Choi & Weis, 2005). Furthermore, only the short "a" isoforms of PKP localise to the desmosomes, whereas the longer “b” isoforms do not (Hatzfeld, 2007). Because of these differences, and based on electro-tomography data (Al-Amoudi et al., 2011), the accepted molecular paradigm is that PG binds desmosomal cadherins and DP, whereas PKPa proteins only bind DP – instead enhancing lateral association and structural integrity of the cytosolic desmosomal plaques. A specialised structure, the hemidesmosome, links epithelial keratin filaments to extracellular collagen in the basement membrane *via* integrin molecules and the two cytosolic adapters plectin and BP230 (Nievers et al., 1999).

DP is the most membrane-distal member of desmosomes: it is a large cytosolic protein with a rigid dumb-bell shape, comprising an *N*-terminal, Armadillo-interacting globular Head domain linked, by a rigid coiled-coil rod domain, to the intermediate filaments-interacting globular Tail domain. The central rod domain contains heptad amino acid repeats, and bears resemblance to the helical domain of intermediate filaments proteins, therefore it is thought to mediate the dimerization of DP molecules (Green et al., 1990). Two isoforms, DPI and DPII, arise from differential splicing of the nascent *DSP* mRNA transcript, resulting in a centrally shortened rod domain in DPII (**Figure 1.3A**); the significance of there being two isoforms is unclear, but it appears that the spliced-out sequence might mediate interaction with microtubules (Sumigray et al., 2011). The Head domain consists of 7 tandem repeats (**Figure 1.3B**), homologous to those of the other three members of the Spectrin family of proteins: spectrin, bullous pemphigoid antigen 1, and plectin (Al-Jassar et al., 2011). This Head domain is necessary and sufficient to form desmosomes *in vitro* (Vasioukhin et al., 2001). On the other hand, the Tail domain is necessary for interaction with intermediate filaments, and because it comprises 3 tandem repeats of a Plakin domain, each DP molecule can in fact interact with at least two intermediate filament strands concurrently (Mohammed et al., 2020). Therefore, DP acts as the pivotal link that interconnects keratin, vimentin, or desmin filaments across neighbouring cells

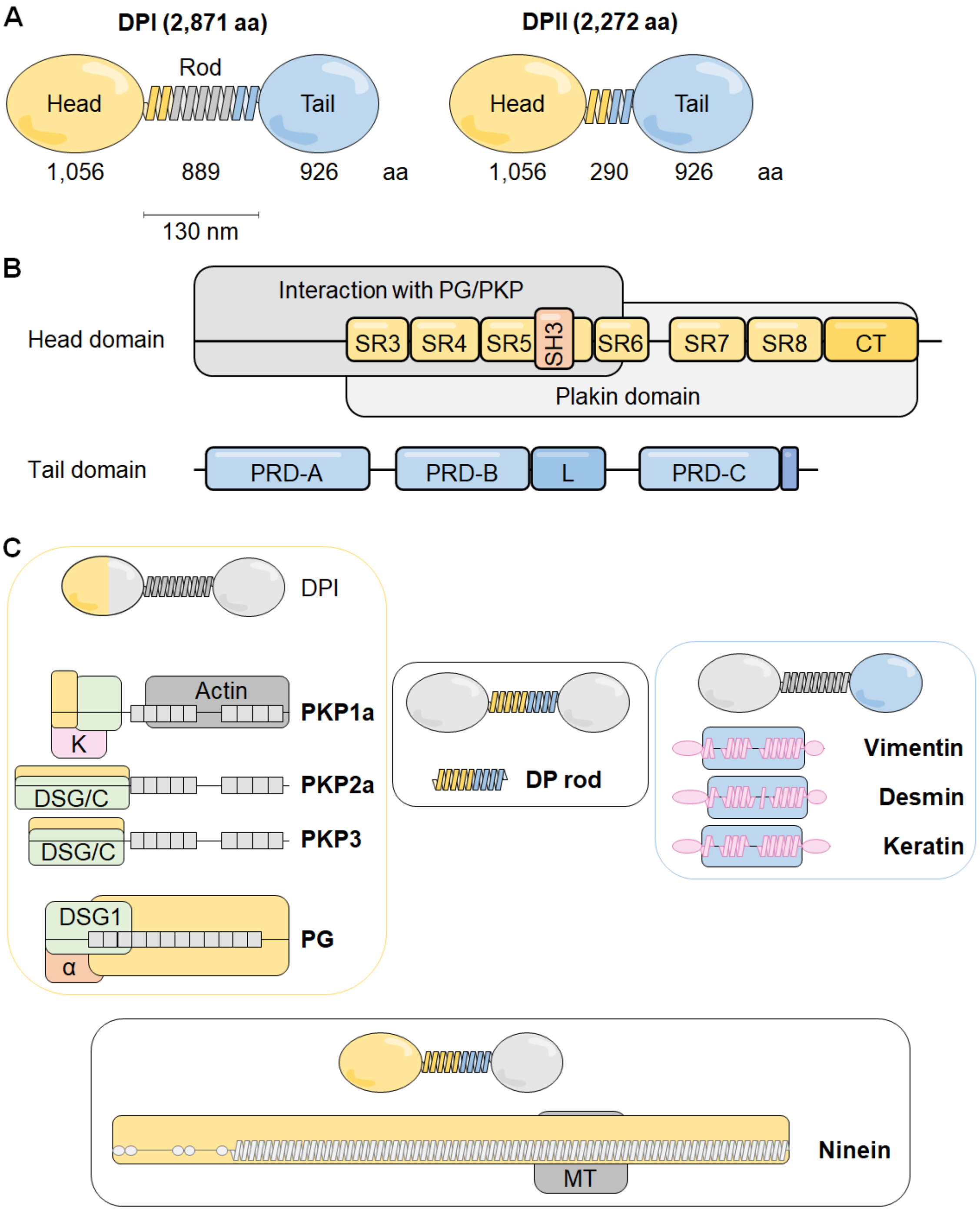

Figure 1.3. Molecular structure and interactors of Desmoplakin.
A. Diagrammatic representation of the two human Desmoplakin isoforms, DPI and DPII, arising from differential splicing of the central rod domain. The amino acid length of each domain is also reported. Physical size of rod domain retrieved from Stokes (2007).
B. A more detailed view of the two globular domains of human Desmoplakin. The colour scheme is consistent with that used in **A**, and features are drawn to scale based on amino acid length. The official numbering of Desmoplakin's Spectrin repeats (SRs), reported in the figure, is based on sequence homology to those of Plectin, including the later renaming of the seventh SR to "CT" on the basis of structural differences (Al-Jassar et al., 2011). Tail domain nomenclature is after Kang et al. (2016). L = linker; PG = Plakoglobin; PKP = Plakophilin; PRD = Plakin repeat domain; SH3 = SRC homology 3.
C. Known interactors of DP are shown, and only the portion of DP that is known to interact with

(Continued from previous page)
them is coloured-in. All proteins and domains are drawn to scale horizontally, except DP and its rod domain. Interaction regions are represented by rounded-corners squares, colour-coded to represent the interacting partner: yellow = DP *N*-terminus; blue = DP *C*-terminus; pink = keratin; green = desmosomal cadherins (desmogleins, desmocollins); orange = α-catenin; MT = microtubules. Grey squares = Armadillo repeats. Interaction domains were mapped *in vitro* by way of truncation experiments, so not all the represented interactions may happen *in vivo* e.g. PKP has not been shown to interact with desmosomal cadherins by experimental methods other than co-purification. Keratin-8 is shown as an example for many keratins. Domain boundaries and interactions were retrieved from both the *UniProt* database and relevant publications, as listed below.
PKP domain boundaries retrieved from *UniProt*.
PKP1a binding to DSG/DP/keratin/actin was shown by Hatzfeld et al. (2000).
PKP2a binding to DSG/DSC/DP was shown by Chen et al. (2002).
PKP3 binding to DSG/DSC/DP was shown by Bonné et al. (2003).
PG domain boundaries retrieved from Witcher et al. (1996), and *UniProt* (#P14923).
PG binding to DSG/α-catenin was shown by Witcher et al. (1996), binding to DP by Kowalczyk et al. (1997).
PG also likely binds to CDH5 (Kowalczyk et al., 1998), through unmapped domains; similarly unmapped are the domain(s) through which it interacts with CDH1 and CDH3 (Lewis et al., 1997).
The DP rod was shown to homodimerise by Green et al. (1992).
DP rod binding to Ninein was shown by Lechler and Fuchs (2007).
The domain of Ninein that binds the microtubules was reported by Stillwell et al. (2004), its domain boundaries were retrieved from *UniProt* (#Q8N4C6).
The DP *C*-terminus can interact with any one of Vimentin, Desmin, and keratin (Mohammed et al., 2020), whose sequences and domain boundaries were retrieved from *UniProt*. Different, although largely overlapping despite not being precisely mapped, regions mediate interaction with Vimentin or keratin (Stappenbeck et al., 1993).
Binding of DP to the Keratin-8/18 heterodimer was shown by Meng et al. (1997).

(**Figure 1.3C**). In fact, while single amino acid mutations of DP have devastating *in vivo* consequences in their own right (see, for example, Whittock et al. (2002)), the DP-Armadillo interaction itself is also of clear clinical importance, with a point mutation in the PG-binding domain of DP resulting in lethal cardiomyopathy (Rampazzo et al., 2002). Interestingly, while DP can directly bind both keratins and vimentin, different sequences in the same domain mediate the interaction of DP with either type of filaments (Stappenbeck et al., 1993). DP was shown to also interact with adherens junctions (Lewis et al., 1997) and microtubules (Lechler & Fuchs, 2007).

The endothelium lacks desmosomes, which means the vimentin intermediate filaments of adjacent ECs are poorly connected (Wallez & Huber, 2008). This would seem at odds with the observations that DP$^{-/-}$ embryos have sparse and easily ruptured capillaries (Gallicano et al., 2001), that both DP isoforms are expressed in ECs (Hermkens et al., 2019; Valiron et al., 1996), and that DP is in fact required for *in vitro* tube formation (Zhou et al., 2004). Indeed, DP assembles related, endothelium-specific adhesive structures called *complexus adhaerentes*, which connect to vimentin filaments and also incorporate PG, as well as proteins more characteristic of other adhesion complexes: p0071, p120, and the transmembrane protein VE-cadherin (Kowalczyk et al., 1998), and Claudin-5 and ZO1 (Hämmerling et al., 2006).

1.2.5. Adherens junctions (*zonulae adherentes*)

The biological role of adherens junctions (AJs, **Figure 1.2D**) is to mediate cell-cell adhesion in a variety of contexts, so as to interconnect the actin cytoskeleton across whole tissues, much like desmosomes do for the intermediate filaments (**Section 1.2.4**). To this end, AJs typically also engage in extensive *cis*-interaction, which allows them to assemble large adhesive surfaces, basolateral to TJs. The intercellular distances yielded by AJ *trans*-interaction vary within the

20-40 nm range, a product of AJs employing cadherins of different extracellular lengths as the main membrane-bound components (**Figure 1.4**). The cadherin superfamily owes its name to the fact that its members require extracellular Ca^{2+} binding to carry out their cell-cell adhesion function (Takeichi, 1977). Subsequently, other roles for this superfamily were identified, now considered key also in mediating embryogenetic cell sorting based on differential cadherin expression, and coordinating neurulation (Halbleib & Nelson, 2006). The first cadherin to be isolated was CDH1, E-cadherin (Yoshida & Takeichi, 1982), which has since been used as a paradigm of cadherin functioning and remains the most studied of the superfamily today.

Cadherins can be grossly divided in 5 families (**Table 1.2**): classical (type I) such as E-cadherin, type II, desmosomal (**Section 1.2.4**), protocadherins, and cadherin-related, classified thus based on their ectodomain sequence, genetic position, and phylogeny (Nollet et al., 2000). Nearly all cadherins are single-pass transmembrane proteins, and are identified as having at least two characteristic extracellular cadherin (EC) repeats; most members have between 5 and 7, tandemly repeated (**Figure 1.4**). These are on average 110 residues long, and fold as two sandwiched β-sheets, resulting in an internal hydrophobic pocket. In between EC repeats are the calcium-binding regions: short aspartate-rich stretches that readily bind 3 Ca^{2+} ions each at physiological extracellular concentrations (1 mM) (Koch et al., 1997), stabilising the whole ectodomain. Cadherins largely mediate homotypic adhesions in *trans*, although heterotypic interactions have been observed between specific family members (Brasch et al., 2018; Shan et al., 2000). The intracellular domain (ICD) of cadherins is generally less conserved across the superfamily, a testament to the variety of their intracellular binding partners, although there are some motifs shared by the members of some subfamilies, like the catenin-binding motif of type I/II cadherins and the CM regions of the δ-PCDH subfamily (**Figure 1.4**). Armadillo proteins (**Section 1.2.4**), of which the catenins are part, form the main adaptors that enable linking to

Table 1.2. Cadherin superfamily phylogeny.

Cadherin family	Members
Type I (classical)	CDH1 (*E-cadherin*)
	CDH2 (*N-cadherin*)
	CDH3 (*P-cadherin*)
	CDH4 (*R-cadherin*)
	CDH15 (*M-cadherin*)
Type II	CDH5 (*VE-cadherin*)
	CDH6 (*K-cadherin*)
	CDH7
	CDH8
	CDH9 (*T1-cadherin*)
	CDH10 (*T2-cadherin*)
	CDH11 (*OB-cadherin*)
	CDH12 (*N-cadherin 2*)
	CDH18
	CDH19
	CDH20
	CDH22
	CDH24
Desmosomal	Desmocollins (DSC1, DSC2, DSC3)
	Desmogleins (DSG1, DSG2, DSG3, DSG4)
Protocadherins	*Table 1.3*
Cadherin-related	Flamingo (CELSR1, CELSR2, CELSR3)
	7D (CDH16, CDH17)
	CDH13 (*T-cadherin*)
	CDH23
	CDH26
	Calsyntenins (CLSTN1, CLSTN2, CLSTN3)
	RET
	FAT (FAT1, FAT2, FAT3, FAT4)
	PCDH15
	Dachsous (DCHS1, DCSH2)
	CDHR1 (*PCDH21*)
	CDHR2 (*PCDH24*)
	CDHR3 (*PCDH28*)
	CDHR4
	CDHR5 (*μ-PCDH*)

Alternative, commonly used names are given between brackets, italicised. Members of a given subfamily are given between brackets, regular typeface. Only human members are tabulated. Assembled from (Hulpiau et al., 2016).

Table 1.3. PCDH family phylogeny.

PCDH subfamily	Members
Non-clustered (δ)	**δ1** (PCDH1, PCDH7, PCDH9, PCDH11X, PCDH11Y, PCDH20)
	δ2 (PCDH8, PCDH10, PCDH12, PDH17, PCDH18, PCDH19)
Clustered	**α** (PCDHA1 to PCDHA13, PCDHAC1, PCDHAC2)
	β (PCDHB1 to PCDHB16)
	γ (PCDHGA1 to PCDHGA12, PCDHGB1 to PCDHGB7, PCDHGC3, PCDHGC4, PCDHGC5)

Members of a given subfamily (bold) are given between brackets. Only human members are tabulated. Assembled from (Hulpiau et al., 2016).

the cytoskeleton, and cadherins engage with different such members based on identity and localisation in the membrane.

Separate components of AJs are the three nectins, also single-pass transmembrane proteins but members of the immunoglobulin superfamily, which do not require Ca^{2+} for adhesion. Nectins co-colocalise with AJs entirely (Takahashi et al., 1999) but in the cytosol, can interact with AJs and TJs alike (McCrea et al., 2009). They bind in *trans* heterotypically and cluster in *cis* (Miyahara et al., 2000) and, similar to CDHs, are also linked to the actin cytoskeleton, but *via* their dedicated cytosolic adaptor Afadin instead (Takahashi et al., 1999).

1.2.6. Classical cadherins: E-cadherin

E-cadherin is the archetypal cadherin, and belongs to the type I family: as such, it is characterised by 5 EC repeats (**Figure 1.4**). In the presence of calcium, the whole ectodomain assumes a pronouncedly curved conformation, with the membrane-distal EC repeat (EC1) nearly at a right angle to EC5, the juxtamembrane EC (Harrison et al., 2011). *Trans*-adhesion between CDH dimers is mediated by a highly conserved tryptophan residue (Trp2) in EC1, which buries itself in the hydrophobic pocket located within another EC1. A very different crystal structure of CDH1 dimers, in which EC1 repeats of *trans*-protomers are arranged in an X-dimer conformation, was shown to be just a transitory arrangement that arises in the first stages of AJs formation (Harrison et al., 2010), which promotes and ultimately resolves into the accepted strand-swapping conformation described above. Surprisingly, however, even “mature” CDH1 adhesive structures result in fairly weak *trans*-adhesion: K_d for dimerisation in solution = 100 μM (Harrison et al., 2010). *Cis*-interaction is even weaker, with K_d > 1 mM, and is also mediated by EC1 on one protomer, which creates a concave surface with a small hydrophobic core into which a convex surface, created by EC2 on an adjacent protomer, can be

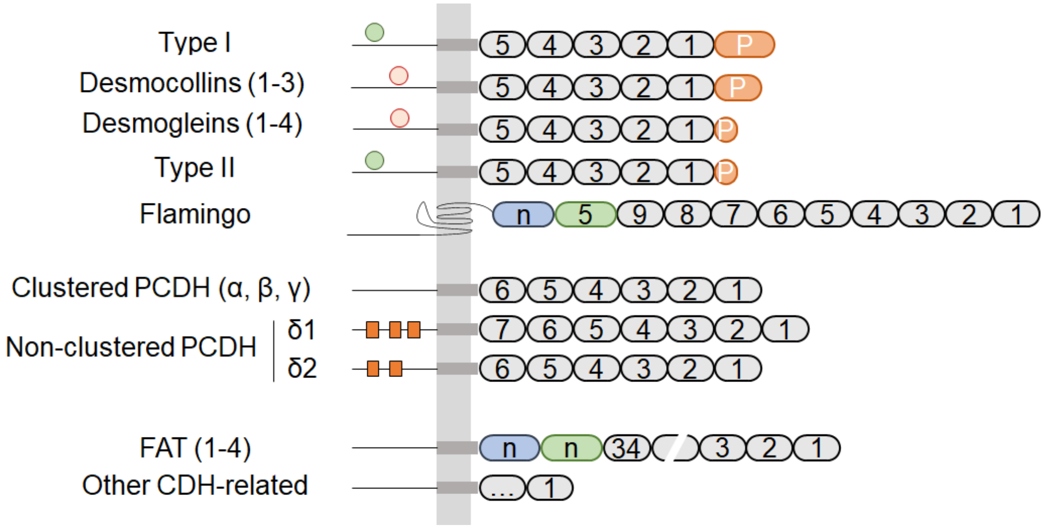

Figure 1.4. The cadherin superfamily.
Molecular organisation of selected members in the cadherin superfamily. The prodomain (P) sequence is related to the EC repeats (grey) but shows no adhesive properties, and needs to be cleaved off for the protein to engage in adhesion altogether (Koch et al., 2004). EGF-like domains (blue) and other extracellular domains (green), present in some subfamilies, are arranged in an alternating pattern. The cytosolic domain is represented as a simplified line, but is in fact different in all cadherins. The conserved motifs (CMs) are represented as orange squares. Cadherins also have a short *N*-terminal signal peptide that targets them to the plasma membrane, not shown here as it is cleaved during peptide maturation. Green ball = interacting β-catenin; orange ball = interacting γ-catenin (Plakoglobin).

inserted. Thus, it is the combination of *cis*- and *trans*-interactions that truly explains adhesion among type-I CDHs: like Velcro® patches, each *trans*-dimer singularly taken is not sufficient to result in strong adhesion, but lateral (albeit weak) association between numerous CDH monomers results in large, regularly arranged arrays of CDH molecules which, as a whole, can easily maintain cell-cell connections. Indeed, different expression levels of CDH1 – and, therefore, different levels of overall cell adhesiveness – on their own result in separate clustering of high- and low-expressing cells, which seems to be an even more important discriminating factor for cell sorting that differential *CDH* gene expression (Duguay et al., 2003).

The ICD of CDHs is unstructured, but binds to a variety of cytosolic adaptors, including Plakoglobin (γ-catenin, **Section 1.2.4**). β-catenin, closely related, is the most well documented interactor: it binds the distal (*C*-terminal) tail of CDH1, and recruits α-catenin, which provides a link to the actin cytoskeleton both directly and by recruiting various F-actin binding partners such as Actinin and ZO1 (Knudsen et al., 1995; Rimm et al., 1995). Some studies, however, challenge the view of cadherins being connected to the actin cytoskeleton through the catenin linkage, since only either α- or β-catenin were isolated in complex with F-actin but not together (Yamada et al., 2005), possibly as a result of the weak interaction between α- and β-catenin. Regardless, the ICD of type I/II CDHs is intrinsically linked to the actin cytoskeleton, which allows for the regulation of cell motility (Scarpa et al., 2015). Importantly, AJs also act as mechanotransducers to regulate the cell cycle: as a result of contractile force, α-catenin switches from its regular folded conformation to a distended, “open” conformation (Yonemura et al., 2010), causing the propagation of tensile strength to other cells. Under such mechanical strain (without being bound by α-catenin), and likely in conjunction to phosphorylation mechanisms (Roura et al., 1999), β-catenin dissociates from CDH1 (Benham-Pyle et al., 2015), and is free to accumulate in the nucleus where, together with YAP1, they stimulate cell-cycle reentry. Underscoring the physiological importance of this mechanism, loss of contact inhibition – both in terms of cell growth and motility – is strongly associated with malignancy (Mendonsa et al., 2018). The membrane-proximal region of the CDH ICD instead interacts with p120, another catenin, but there is no evidence that p120 mediates interaction with the cytoskeleton. Instead, it seems to regulate CDH lateral association, and protein half-life by eliciting CDH recycling, because p120 knockdown results in AJ dismantlement and p120 levels regulate AJs numbers *in vitro* (Davis et al., 2003).

1.2.7. Endothelial AJs: VE-cadherin

The most well studied member of type II CDHs is VE-cadherin (CDH5, CD144), which is expressed in the endothelium and only very few, rare other cell types: circulating endothelial progenitors and renal podocytes (Wallez & Huber, 2008). Therefore, all endothelial AJs have CDH5, as was identified soon after the discovery of the protein (Lampugnani et al., 1992); however, despite CDH5-knockout being embryonic lethal in mouse (Carmeliet et al., 1999), embryos can still form functional AJs in the vasculature before dying (Gory-Faure et al., 1999), highlighting at least some degree of overlap and redundancy across the family. Like CDH1, it has 5 EC repeats and, although there is no complete crystal structure of the CDH5 ectodomain, a partial structure from chicken CDH5 (PDB ID: 3PPE) highlights a similar but different molecular arrangement of *trans*-homotypic binding: the most striking feature is a conserved Trp4, as well as the classical Trp2, resulting in a much bigger contact surface between EC1 repeats across *trans*-protomers. This seemingly small difference has profound effects in the mode of adhesion: the binding K_d is measured at 1 μM (Brasch et al., 2011), orders of magnitude stronger than for CDH1 (**Section 1.2.6**). Furthermore, glycosylation of EC repeats 1-3 plays a pivotal role in dictating the adhesion mode, because it greatly reduces the potential for *cis*-

association (Brasch et al., 2011), although it still allows some degree of structured assembly (Lambert et al., 2005). This suggests a fundamentally different adhesion strategy than that employed by type I CDHs, where a multitude of low-affinity bonds provide overall strongly adhesive patches. CDH5 adhesion seems to instead rely on individual *trans*-dimers, perhaps a product of endothelial cells expressing a smaller repertoire of CDH proteins (Wallez & Huber, 2008) and of the substantial haemodynamic stress that EC withstand (Brasch et al., 2011). It is a drop in local CDH5 concentration due to VEGF-induced cell elongation that stimulates cell migration during the first stages of angiogenesis (Cao et al., 2017).

The ICD of CDH5 is highly homologous to that of classical CDHs and so, like CDH1, it interacts with PG, and β-, α-, and p120 catenins (Brasch et al., 2011; Lampugnani et al., 1995), and can therefore affect the same genes and pathways. An exhaustive list of intracellular interactors can be found in the literature (Giannotta et al., 2013). Importantly for the endothelial context, CDH5 interacts with β-catenin to reduce VEGFR2 phosphorylation levels and, thus, its activation status (Lampugnani et al., 2003). It also reduces the duration of the VEGF proliferative effects by preventing the internalisation of activated VEGFR2 (Lampugnani et al., 2006), further explaining why CDH5 junction disassembly is one of the first steps of the angiogenic programme (**Section 1.1.2**). Similarly, association of CDH5 with TGF-βR also results in inhibition of SMAD signalling (Rudini et al., 2008).

1.2.8. Other vascular adhesion molecules

N-CDH (CDH2) is a type I CDH, and binds homotypically in a virtually identical manner to CDH1 (Harrison et al., 2011). As well as on other tissues, it is expressed abundantly on the endothelium, but it is diffuse on the plasma membrane and does not localise with AJs, suggesting it plays a more important role in mediating adhesion to pericytes instead (Navarro et al., 1998).

T-CDH (CDH13) is a CDH-related gene, and an atypical adhesion protein, in that it is a soluble adhesion molecule that is attached directly to the cell membrane by means of a glycosylphosphatidylinositol tether (Ivanov et al., 2001). Endothelial T-CDH is of interest because it binds adiponectin in the bloodstream (Hug et al., 2004), and acts as a cardioprotective molecule (Denzel et al., 2010), however it also functions as a proangiogenic homotypic binding protein on ECs (Ivanov et al., 2004). Its adhesion modality is different in that it does not involve strand-swapping, but rather an x-shaped interaction surface around the EC1-EC2 calcium-binding domains (Ciatto et al., 2010).

PECAM-1 (CD31) is also a single-pass transmembrane glycoprotein, but belongs to the immunoglobulin superfamily. Through its six extracellular domains, it mediates homo- and heterotypic adhesion among ECs, and is abundantly expressed in mature vascular beds (Privratsky & Newman, 2014). It functions as a mechanosensor, activating ERK in response to shear stress (Osawa et al., 2002). It is implicated in a variety of cell processes including angiogenesis, and it is widely used as an EC marker, but is also expressed as multiple isoforms on platelets and many leukocyte lineages (Privratsky & Newman, 2014). Interestingly, Pecam1 knockout does not result in any overt murine vascular developmental effects (Duncan et al., 1999), and yet when challenged with angiogenesis assays in adulthood, the mice display impaired angiogenic potential (Solowiej et al., 2003) and increased vascular permeability (Graesser et al., 2002).

Endoglin (CD105) is a membrane-bound receptor that exists as a covalently-linked homodimer, and is expressed on a variety of cells, but particularly abundantly at endothelial junctions, although it is not known whether it functions as an adhesion molecule other than transiently, for the recruitment of leukocytes (Schoonderwoerd et al., 2020). It is upregulated by hypoxia, and drives cell proliferation downstream of TGF-β signalling (Schoonderwoerd et al., 2020).

Finally, the ectodomain of CDH5 interacts with that of VE-PTP, an endothelium-specific receptor tyrosine phosphatase. In particular, VE-PTP seems to be preferentially expressed in arterial vessels (Bäumer et al., 2006), where it acts on phospho-CDH5 to reduce permeability and counteract the effects of VEGF signalling (Nawroth et al., 2002). Recently, a phosphatase-independent role was also identified, whereby VE-PTP stabilises endothelial AJs by reducing the internalisation rate of CDH5 in quiescent endothelia *in vitro* (Juettner et al., 2019).

1.3. Protocadherins

Various, diverse members of the cadherin superfamily have been identified so far (**Table 1.2**), totalling more than 110 members across different species, but by far the biggest family is that of the protocadherins (PCDHs), with over 60 members among mammals alone (Hulpiau et al., 2016). These are mostly found in neural tissue, where they contribute to establishing neuronal identity and mediate self-avoidance, but there is evidence of expression in both murine and human endothelia for at least some members (Dilling et al., 2017). Genetic analysis has identified two distinct groups within the family: clustered PCDHs, all residing at *locus* 5q31 in humans (18B3 in mice) and discovered at the same time (Wu & Maniatis, 1999), and non-clustered (or δ) PCDHs, which are scattered elsewhere in the genome. Phylogenetic analysis further classifies both into smaller groupings (**Table 1.3**), based on their degree of sequence similarity and number of EC repeats.

The whole family exhibits great variability of both the cytosolic and extracellular domains, more than other subfamilies of cadherins. Another striking feature of *PCDH* genes that differentiates them from other cadherins is that they contain a relatively large exon, which encodes for most of the ectodomain, the transmembrane region, and part of the cytoplasmic tail without any intervening intronic sequences (Wu & Maniatis, 1999). Furthermore, the ectodomains show low degree of conservation from those of classical CDHs, and in general PCDH EC repeats lack the conserved residues that mediate adhesion in classical cadherins. Instead they are characterised by a much smaller hydrophobic pocket, due to the presence of bulkier amino acids (Morishita et al., 2006).

The ICDs of PCDHs are also quite divergent from those of other cadherins: most PCDHs lack catenin binding domains, or any other cytoskeleton protein-interaction domains found in classical CDHs. All clustered PCDHs share just two, constant ICDs (**Section 1.3.1**), whereas the ICDs of non-clustered PCDHs typically vary extensively by the translation of different splice variants; in an extreme case PCDH11X, due to its large number of exons, can be translated as at least 10 different isoforms (Vanhalst et al., 2005).

1.3.1. Clustered PCDHs

cPCDHs are by far the largest and most studied subfamily of PCDHs; they correspond to three chromosomal groupings, sequentially arranged as three clusters: *PCDHA*, *PCDHB*, and *PCDHG* genes, encoding α-, β-, and γ-PCDHs respectively (Wu & Maniatis, 1999). Each of these clusters comprises a series of ~15 single-exon genes, 3’ to which is a constant region: one exon is chosen randomly among the choice of 15 alternatives, to encode the extracellular-transmembrane region, and is spliced into the constant 3’ exon, which encodes the cytosolic domain – except for β-PCDHs, which lack this constant region and, therefore, the ICD altogether. This means that ICD variation among cPCDHs is minimal. cPCDH expression is predominantly neural (Hirayama & Yagi, 2013), where they have been identified as providing the basis for neuronal "barcoding" during embryogenesis, whereby neurons are imprinted with a unique molecular signature that allows self-avoidance i.e. ensures no connections are established between different regions of the same cell (Lefebvre et al., 2012). In *Drosophila*, this process is mediated by the single *Dscam* gene, stochastic splicing of which on its own can give rise to nearly 40,000 alternative isoforms of the Dscam protein (Schmucker et al., 2000), an immunoglobulin superfamily member; each cell expresses a few thousand Dscam isoforms to be uniquely identifiable (Hattori et al., 2009).

In vertebrates, the cPCDH subfamily satisfies this requirement by combinatorial expression of a small subset of *cPCDH* genes, which results in stochastically different sets of homologous but different extracellular domains in each cell. Even if just one cPCDH *trans*-homodimerizes, this results in repulsive signals and synapse formation is halted (Rubinstein et al., 2015; Thu et al., 2014). Importantly, mouse cerebellar neurons express just 2 *Pcdha* genes on average (Esumi et al., 2005), so expression of cPcdhs from each cluster is necessary to impart a unique molecular repertoire to each neuron; remarkably, however, 4-6 cPcdhs in total per cell seem to be sufficient to allow effective cell discrimination *in vivo* in at least one neuron type (Mountoufaris et al., 2017) – a much more economical approach than in arthropods. To be able to carry out this feat effectively, there can be no tolerance for heterotypic binding, and cPCDH isoforms must be able to infallibly recognise themselves in *trans* (Honig & Shapiro, 2020); indeed, only homotypic binding was detected in aggregation assays (Schreiner & Weiner, 2010; Thu et al., 2014). Likely for this reason, the adhesion interfaces of cPCDHs are very different from those of classical CDHs: cPCDH ectodomains all have 6 EC repeats, quite divergent from classical ones (**Section 1.2.6**). Furthermore, in the presence of calcium, cPCDH ectodomains are much straighter than for type I CDHs, and *trans*-adhesion is mediated by an extensive antiparallel interaction that involves EC repeats 1-4 rather than just EC1 (Rubinstein et al., 2015). Additionally, as seen in the recent crystal structure of PCDHγB4, extensive zipper-like adhesive arrays can assemble because of the lateral association enabled by promiscuous *cis*-interactions that involve EC6 (Brasch et al., 2019). Importantly, while the adhesive interface is much larger, the strength of adhesion it enables is lower than for classical CDHs (Morishita et al., 2006), furthering the hypothesis that cPCDHs expression is required for cell identity rather than strong adhesion.

The cytosolic tails of cPCDHs sequester the PYK2 and FAK kinases to prevent their enzymatic activities (J. Chen et al., 2009). By reducing FAK activity, phospholipase C (PLC) and protein kinase C (PKC) activity is also downregulated, which allows correct neural arborisation of *ex vivo* mouse neurons (Garrett et al., 2012). The ICD can be cleaved by the γ-secretase complex, downstream of ectodomain cleavage by the metalloproteinase ADAM10; the liberated *C*-terminal stretch translocates to the nucleus, where it might affect *cPCDH* gene expression (Reiss et al., 2006). Because this cleavage affects cell adhesion, it might be an important mechanism that regulates axonal self-avoidance. Furthermore, even though they lack the consensus interacting sequences, γ-PCDHs co-purify with α- and β-catenins – as well as tubulin and 14-3-3 proteins (Han et al., 2010). Interestingly, PCDHγA9 overexpression prevents nuclear localisation of β-catenin and SMAD2/3, as well as SMAD2/3 phosphorylation (Weng et al., 2018).

Although cPCDHs are expressed most abundantly in the central nervous system (Kim et al., 2011), some have been detected in the endothelium, and particularly in the cerebral endothelium (Dilling et al., 2017), where their function is not clear. Notably, PCDHγC3 KO results in the upregulation of TJ proteins in a mouse microvascular cerebellar endothelial cell line; however, cellular permeability and motility increase (Gabbert et al., 2020), hinting at a complex involvement of the protein in these processes. Furthermore, various cPCDHs have been associated with various types of cancer, as a result of both somatic abnormalities and promoter epigenetic modifications (Pancho et al., 2020).

1.3.2. Non-clustered PCDHs

Unlike cPCDHs, δ-PCDHs do not cluster at a specific *locus*, but are instead found dotted around the genome, and are therefore also known as non-clustered PCDHs. The subgroupings within δ-PCDHs are two, δ1 and δ2, the former characterised by an additional EC repeat and longer cytosolic domains than the latter (**Figure 1.4**). Like cPCDHs, δ-PCDHs are also widely expressed in the central nervous system during embryogenesis, with lower expression persisting through adulthood, and detectable expression in other tissues, including the endothelium (Colás-Algora & Millán, 2019). Given these similar patterns, it had long been assumed that δ-PCDHs are also implicated in assigning neuronal identity, perhaps to expand the repertoire of possibilities conferred by cPCDHs; indeed, single murine neurons were found to express up to seven (Bisogni et al., 2018). Until recently, the only crystal structure available, zebrafish Pcdh19 (PDB ID: 5IU9), seemed to confirm this hypothesis, showing adhesion modalities strikingly similar to those of cPCDHs, with an antiparallel interaction formed between *trans*-homomers encompassing the EC1-EC4 stretch (Cooper et al., 2016). Furthermore, adhesion affinities derived from aggregation assays were also reportedly low (Kahr et al., 2013). However, more recent rigorous biophysical measurements of the adhesive affinities among δ members found these to be unexpectedly strong, with K_d values in the order of single μM digits, the lowest being that of Pcdh19, a striking K_d = 0.48 μM (Harrison et al., 2020). Additionally, while their crystal structures recapitulate the *trans*-homotypic adhesion modality seen for Pcdh19 and cPCDHs, no *cis*-association was observed. Finally, and perhaps most tellingly, some degree of heterotypic binding was observed between δ1 members (Harrison et al., 2020). All of these characteristics are in stark contrast with those of cPCDHs (**Section 1.3.1**), and would suggest that δ-PCDHs have additional roles besides being potential neuronal identifiers. Therefore, the real function of δ-PCDHs is still subject to debate.

While the ECD is reasonably well conserved among the subfamily (Harrison et al., 2020), the ICD is more divergent, although two features are found in all δ-*PCDH* genes: the two short stretches called conserved motif 1 (CM1) and CM2, of unidentified function (Wolverton & Lalande, 2001). Another feature, CM3 (residues: RRVTF), is only present among the δ1 subgrouping, and was found to interact with protein phosphatase 1 alpha (PP1α) (Yoshida et al., 1999), although the functional significance of this interaction has to date been unexplored. Conversely, a WIRS domain is only present in the cytosolic tail of the δ2 subgrouping, and that of some PCDHα members, where it was shown to affect lamellipodia formation and actin cytoskeleton reorganisation in *ex vivo* murine neurons (Fan et al., 2018). Further complicating the picture, and again in stark contrast to cPCDHs, all δ-*PCDH* pre-mRNA undergoes differential splicing, which means that multiple isoforms of each δ-PCDH protein are typically expressed in cells (Wu & Maniatis, 1999). Importantly, this only affects the cytosolic domain, and results in some isoforms altogether lacking the CM regions described above, which hints at the interesting possibility of differential δ-PCDH isoform expression being a regulatory mechanism.

1.3.3. PCDH1

PCDH1 (originally, PC42) is a member of the δ1-PCDH subgrouping. The human *PCDH1* gene, on locus 5q31.3^{-}, comprises 5 exons, encoding a single-pass transmembrane protein with 7 EC repeats and a cytosolic tail (**Figure 1.5**). It was identified nearly 30 years ago that PCDH1

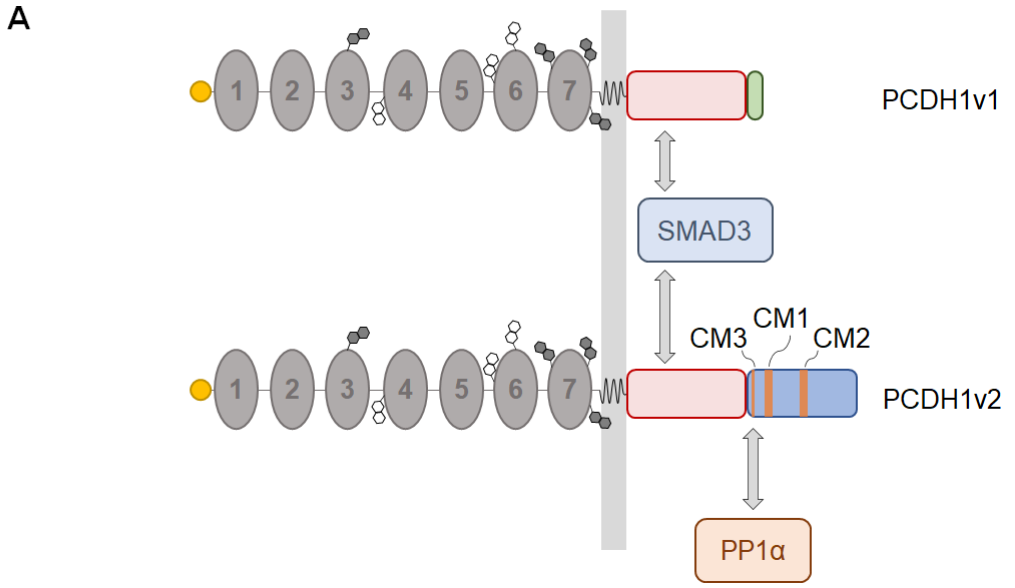

B

	PCDH1v2:	PCDH1v1:
1	MDSGAGGRRCPEAALLILGPPRMEHLRHSPGPGGQRLLLPSMLLALLLLL	MDSGAGGRRCPEAALLILGPPRMEHLRHSPGPGGQRLLLPSMLLALLLLL
51	APSPGHATRVVYKVPEEQPPNTLIGSLAADYGFPDVGHLYKLEVGAPYLR	APSPGHATRVVYKVPEEQPPNTLIGSLAADYGFPDVGHLYKLEVGAPYLR
101	VDGKTGDIFTTETSIDREGLRECQNQLPGDPCILEFEVSITDLVQNGSPR	VDGKTGDIFTTETSIDREGLRECQNQLPGDPCILEFEVSITDLVQNGSPR
151	LLEGQIEVQDINDNTPNFASPVITLAIPENTNIGSLFPIPLASDRDAGPN	LLEGQIEVQDINDNTPNFASPVITLAIPENTNIGSLFPIPLASDRDAGPN
201	GVASYELQAGPEAQELFGLQVAEDQEEKQPQLIVMGNLDRERWDSYDLTI	GVASYELQAGPEAQELFGLQVAEDQEEKQPQLIVMGNLDRERWDSYDLTI
251	KVQDGGSPPRASSALLRVTVLDTNDNAPKFERPSYEAELSENSPIGHSVI	KVQDGGSPPRASSALLRVTVLDTNDNAPKFERPSYEAELSENSPIGHSVI
301	QVKA**N**DSDQGANAEIEYTFHQAPEVVRRLLRLDRNTGLITVQGPVDREDL	QVKA**N**DSDQGANAEIEYTFHQAPEVVRRLLRLDRNTGLITVQGPVDREDL
351	STLRFSVLAKDRGTNPKSARAQVVVTVKDMNDNAPTIEIRGIGLVTHQDG	STLRFSVLAKDRGTNPKSARAQVVVTVKDMNDNAPTIEIRGIGLVTHQDG
401	MA**N**ISEDVAEETAVALVQVSDRDEGENAAVTCVVAGDVPFQLRQASETGS	MA**N**ISEDVAEETAVALVQVSDRDEGENAAVTCVVAGDVPFQLRQASETGS
451	DSKKKYFLQTTTPLDYEKVKDYTIEIVAVDSGNPPLSSTNSLKVQVVDVN	DSKKKYFLQTTTPLDYEKVKDYTIEIVAVDSGNPPLSSTNSLKVQVVDVN
501	DNAPVFTQSVTEVAFPENNKPGEVIAEITASDADSGSNAELVYSLEPEPA	DNAPVFTQSVTEVAFPENNKPGEVIAEITASDADSGSNAELVYSLEPEPA
551	AKGLFTISPETGEIQVKTSLDREQRESYELKVVAADRGSPSLQGTATVLV	AKGLFTISPETGEIQVKTSLDREQRESYELKVVAADRGSPSLQGTATVLV
601	NVLDCNDNDPKFMLSGY**N**FSVMENMPALSPVGMVTVIDGDKGENAQVQLS	NVLDCNDNDPKFMLSGY**N**FSVMENMPALSPVGMVTVIDGDKGENAQVQLS
651	VEQDNGDFVIQ**N**GTGTILSSLSFDREQQSTYTFQLKAVDGGVPPRSAYVG	VEQDNGDFVIQ**N**GTGTILSSLSFDREQQSTYTFQLKAVDGGVPPRSAYVG
701	VTINVLDENDNAPYITAPS**N**TSHKLLTPQTRLGETVSQVAAEDFDSGVNA	VTINVLDENDNAPYITAPS**N**TSHKLLTPQTRLGETVSQVAAEDFDSGVNA
751	ELIYSIAGGNPYGLFQIGSHSGAITLEKEIERRHHGLHRLVVKVSDRGKP	ELIYSIAGGNPYGLFQIGSHSGAITLEKEIERRHHGLHRLVVKVSDRGKP
801	PRYGTALVHLYV**N**ETLA**N**RTLLETLLGHSLDTPLDIDIAGDPEYERSKQR	PRYGTALVHLYV**N**ETLA**N**RTLLETLLGHSLDTPLDIDIAGDPEYERSKQR
851	GNILFGVVAGVVAVALLIALAVLVRYCRQREAKSGYQAGKKETKDLYAPK	GNILFGVVAGVVAVALLIALAVLVRYCRQREAKSGYQAGKKETKDLYAPK
901	PSGKASKGNKSKGKKSKSPKPVKPVEDEDEAGLQKSLKFNLMSDAPGDSP	PSGKASKGNKSKGKKSKSPKPVKPVEDEDEAGLQKSLKFNLMSDAPGDSP
951	RIHLPLNYPPGSPDLGRHYRSNSPLPSIQLQPQSPSASKKHQVVQDLPPA	RIHLPLNYPPGSPDLGRHYRSNSPLPSIQLQPQSPSASKKHQVVQDLPPA
1001	NTFVGTGDTTSTGSEQYSDYSYRTNPPKYPSKQ*LPHRRVTFSATSQAQEL*	NTFVGTGDTTSTGSEQYSDYSYRTNPPKYPSKQ*VGQPFQLSTPQPLPHPY*
1051	*QDPSQHSYYDSGLEESETPSSKSSSGPRLGPLALPEDHYERTTPDGSIGE*	*HGAIWTEVWE*
1101	*MEHPENDLRPLPDVAMTGTCTRECSEFGHSDTCWMPGQSSPSRRTKSSAL*	
1151	*KLSTFVPYQDRGGQEPAGAGSPSPPEDRNTKTAPVRLLPSYSAFSHSSHD*	
1201	*SCKDSATLEEIPLTQTSDFPPAATPASAQTAKREIYL*	

Figure 1.5. PCDH1.

A. Different regions of the proteins are drawn to scale (horizontally), from the relative *NCBI* sequence; EC repeats are classically numbered towards the cell membrane. *N*-glycosylation sites (black = experimentally verified, white = predicted) were retrieved from the *neXtProt* database (ID: NX_Q08174) and approximately placed in the figure. The signal peptide (yellow dot) is cleaved after the sequence matures. CM = conserved motif; double-headed arrow = protein-protein interaction.

B. Numbered amino acid sequences for the two PCDH1 isoforms in **A**. Red = signal peptide; blue = EC repeat; orange = CM region; pink = PDZ-binding site. Bold underlined typeface = glycosylation site; underlined = transmembrane domain; italicised = isoform-specific sequence. The first 1,033 residues are the same in both isoforms. Domain boundaries as per **A**.

exhibits self-adhesive properties in aggregation assays, albeit modest (Sano et al., 1993). Such adhesion was suggested to be responsible for the cell-sorting role of the PCDH1 orthologue in *Xenopus* morphogenesis, with the protein allowing distinct axial or paraxial mesodermal differentiation (Yoder & Gumbiner, 2011). *Trans*-adhesion was hypothesised to be mostly homotypic, due to the preferentially close arrangement of cells expressing fluorescently labelled PCDH1 (Faura Tellez et al., 2016).

During the course of the experiments presented in this thesis, the structure of a partial PCDH1 ectodomain (PDB ID: 6MGA) was solved, and was shown to engage in *trans*-homotypic adhesion involving the antiparallel overlap of four EC repeats shown by the PCDH family, and no *cis*-association (Modak & Sotomayor, 2019). However, later surface-plasmon resonance experiments detected some promiscuity in the binding, showing that the PCDH1 ECD can in fact interact with most other δ1 and a few δ2 members (Harrison et al., 2020). The K_d of homodimerisation was measured as 1.2 µM, the strongest of the δ1 grouping. Interestingly, truncating the ECD to only the first 4 EC repeats more than halves the homodimerization K_d (Harrison et al., 2020), suggesting that the membrane-proximal EC repeats somehow result in a dampening effect on *trans*-adhesion. Importantly, PCDH1 was shown to localise neither at AJs nor at TJs in an epithelial cell line (Faura Tellez et al., 2016).

The cytosolic domain of PCDH1 has a conserved Cys residue at its membrane-proximal region that is palmitoylated which, together with other unidentified residues that undergo the same modification, is important for correctly targeting the protein to the plasma membrane in rat (Fukata & Fukata, 2010). As with all δ-PCDHs, PCDH1 exists as multiple isoforms, the main ones being PCDH1v1 and PCDHv2, which arise due to differential splicing of the immature *PCDH1* transcript after exon 3 (**Figure 3.1**), with PCDH1v2 including exons 4 and 5, while v1 appends a short alternative exon instead. As a result, all isoforms include the same ECD, but only the longest isoform, PCDH1v2, includes the three cytosolic CM regions. The two main *Pcdh1* mRNAs are expressed in a variety of tissues from early (E9.5) murine embryogenesis to adulthood (Redies et al., 2008), and in *Xenopus* embryos (Kuroda et al., 2002). The significance of having different versions of the cytosolic domain is not clear, because it has never been differentially studied in contexts other than the zebrafish, where *pcdh1a* and *pcdh1b* seem to be duplicated because of the teleost-specific genome duplication event (Howe et al., 2013); as a result, both Pcdh1a and Pcdh1b have all three CM sequences (Blevins et al., 2011), rather than being isoforms arising from the same transcript.

Nevertheless, it is likely that different intracellular binding partners can be recruited by each isoform, although only few have been identified to date. The most well documented cytosolic interactor of PCDH1 is SMAD3, a transcription factor activated by activated TGF-β receptors. This interaction was first proposed over 16 years ago by large-scale two-hybrid screens, first a TGF-β-focussed study (Colland et al., 2004), then a proteome-wide study (Rual et al., 2005), and was later corroborated by further two-hybrid and co-immunoprecipitation studies (Faura Tellez et al., 2015). These showed that SMAD3 co-purifies with both PCDH1v1 and v2 in epithelial cells, and that PCDH1 expression levels correlate inversely with SMAD3 activity downstream of TGF-β1 stimulation. This experiment would suggest that PCDH1 modulates TGF-β signalling by sequestering SMAD3; indeed, more recently, impaired Smad3 inhibition due to congenital loss of Pcdh1 was shown to exacerbate airway hyperresponsiveness in mice (Nawijn et al., 2018).

The other known cytosolic interactor of PCDH1 is PP1α, first shown by a two-hybrid assay to interact with the long version of PCDH7 (Yoshida et al., 1999), and then by co-purification with the long, CM3-containing isoform of all δ1-PCDHs (Vanhalst et al., 2005), although the investigators did not try to functionally assess this interaction. Lastly, one review article (Kahr et al., 2013) asserts that PCDH1 interacts cytosolically with the transmembrane receptor RYK, however the mass spectrometric study given as justification for this claim (Berndt et al., 2011) only found one PCDH1 peptide to co-purify with RYK, so the evidence is not as robust as for the other interactors.

The PCDH1 protein has 96% sequence identity to its mouse orthologue (Kuroda et al., 2002), and has been implicated in various human diseases. Much of the research has historically been carried out, by the same academic group, in the context of asthma, since *PCDH1* was first identified as a susceptibility gene for bronchial hyperresponsiveness (BHR), a hallmark of asthma, in a population study (Koppelman et al., 2009). The report was interesting as BHR stems from a loss of epithelial integrity, which could be linked with misfunctioning of a membrane protein such as PCDH1. Later reports identified some *PCDH1* polymorphisms associated with eczema, another atopic disease, linked with asthma (Koning, Postma, et al., 2012; Mortensen et al., 2014). PCDH1 levels were found to decrease in murine lungs after exposure to cigarette smoke (Koning et al., 2014), and increased during the *ex vivo* differentiation of human primary bronchial epithelial cells (Koning, Sayers, et al., 2012). Indeed, PCDH1 knockdown results in impaired cell membrane permeability *in vitro,* even though PCDH1 expression levels or subcellular distribution seem unaltered in asthma patients (Faura Tellez et al., 2016). PCDH1 promoter methylation has been detected in a genomic analysis of pancreatic cancers (Vincent et al., 2011) and triple-negative breast cancers (Vasilatos et al., 2013). Furthermore, aberrant PCDH1 expression was detected in multiple tumour models (Redies et al., 2008), and decreased PCDH1 expression has been identified as predictor of unfavourable survival in a microarray screening of medulloblastomas (Berx & van

Roy, 2009). More recently, the EC1 repeat of PCDH1 was identified as the obligate docking point for *Hantavirus*, a zoonotic infection which causes an untreatable syndrome that results in pulmonary oedema and fatal respiratory failure with cardiogenic shock (Jangra et al., 2018).

1.4. Hypotheses and project aims

There is extensive overlap between neuronal and angiogenic guidance cues (**Section 1.1.4**). A clear biological function for PCDH1 has not been established, but it is a member of a family, the protocadherins, which are necessary for correct axon guidance (**Section 1.3**). It follows that PCDH1 might also be implicated in angiogenesis. In support of this, *Pcdh1* was detected in both neural tissue (Kim et al., 2007), and the endothelium: first in murine lung endothelial cells during adult angiogenesis (Favre et al., 2003), and later at sites of embryonic angiogenesis (Redies et al., 2008).

1.4.1. Project aims

The hypothesis that this project explored is that PCDH1 is involved in regulating angiogenesis. To test this, a set of four project aims was proposed at the outset, and the experiments that addressed these are presented as four separate chapters:

1) To determine whether different PCDH1 expression levels have an impact on angiogenesis, and thus whether the protein takes part in the process (**Chapter 3**): this was assessed by reducing PCDH1 levels by knockdown, and then undertaking *in vitro* assays that model different stages of angiogenesis.

2) To identify a function for the cytosolic domain of PCDH1, and thus shed light on what pathways the protein is involved in (**Chapter 4**): intracellular binding partners were screened by mass spectrometry, and novel findings were corroborated by co-purification.

3) To assess whether the PCDH1 ectodomain has a biological function on the endothelium (**Chapter 5**): this was explored by including the soluble PCDH1 ECD during *in vitro* assays that modulate endothelial tubulogenesis.

4) To assess the effects of Pcdh1 in vessel formation *in vivo* (**Chapter 6**): the vasculature of wild-type and Pcdh1-knockout mouse embryos was compared, to identify any vessel abnormalities resulting from Pcdh1 loss.

CHAPTER 2: MATERIALS AND METHODS

2.1. Reagents and Materials

2.1.1. Commonly used reagents sources

Reagents mentioned throughout the chapter, and not listed in **Table 2.1**, were purchased from Sigma-Aldrich/Merck (Darmstadt, Germany). Similarly, all incubations were carried out at room temperature, unless otherwise stated.

Table 2.1. Common reagents not purchased from Merck (Darmstadt, Germany)

Reagent	**Manufacturer**
Protogel (30%)	National Diagnostics (Atlanta GA, USA)
Gelatin from porcine skin	Fluka Biochemika (Seelze, Germany)
Tris base	Fisher Scientific (Loughborough, UK)
Tris-HCl	Fisher Scientific (Loughborough, UK)
SDS, 20% (w/v) solution	Fisher Scientific (Loughborough, UK)
DMSO	Fisher Scientific (Loughborough, UK)
Ethanol	VWR (Radnor PA, USA)
Methanol	VWR (Radnor PA, USA)
BSA	VWR (Radnor PA, USA)
SOC medium	NEB UK (Herts, UK)
NaCl	Honeywell (Morris Plains NJ, USA)
EDTA	Acros Organics (Geel, Belgium)
L-Glutamine	Gibco/ThermoFisher (Waltham MA, USA)
FBS	Gibco/ThermoFisher (Waltham MA, USA)
0.5% (10X) Trypsin/EDTA solution	Gibco/ThermoFisher (Waltham MA, USA)
Gentamicin/Amphotericin solution	Gibco/ThermoFisher (Waltham MA, USA)
Opti-MEM	ThermoFisher (Waltham MA, USA)
IPTG	ThermoFisher (Waltham MA, USA)
Matrigel Basement Membrane Matrix	Corning (Corning NY, USA)
Marvel dried skimmed milk	Premier Foods (St. Albans, UK)
Heparin	LKT Laboratories (St. Paul MN, USA)
RNAiMAX Lipofectamine	ThermoFisher (Waltham MA, USA)
Promocell supplement kit	Kit #C-39216, Promocell (Heidelberg, Germany)
Human IgG, Fc fragment	EMD Millipore/Merck (Darmstadt, Germany)
Horse serum	Vector Laboratories (Peterborough, UK)
Collagen type I from rat tail	EMD Millipore/Merck (Darmstadt, Germany)
Glutathione agarose slurry	Pierce/ThermoFisher (Waltham MA, USA)
10% formalin-saline	Genta medical (York, UK)
Proteinase K (PCR grade)	Roche Diagnostics (Indianapolis IN, USA)
ProLong Gold antifade mounting medium	ThermoFisher (Waltham MA, USA)
Hydrogen peroxide	ThermoFisher (Waltham MA, USA)
Ethyl cinnamate	Acros/Fisher Scientific (Loughborough, UK)

2.1.2. Commonly prepared solutions

All solutions were made up with deionised water, unless otherwise stated.

Table 2.2. Commonly used solutions and their composition

Name	**Composition**
TBS-T	20 mM Tris base pH7.6, 150 mM NaCl, 0.08% (v/v) Tween-20
PBS (from tablets)	10 mM PO_4^{3-}, 2.68 mM KCl, 140 mM NaCl
TAE buffer	40 mM Tris base, 20 mM acetic acid, 1 mM EDTA
SDS-PAGE sample buffer	50 mM Tris-HCl pH6.8, 10% (v/v) 2-mercaptoethanol, 2% (w/v) SDS, 10% (v/v) glycerol, bromophenol blue
NP-40 (Igepal) lysis buffer	1% (v/v) NP-40, 10 mM Tris base pH7.5, 150 mM NaCl, 1 mM EDTA pH8.0, 0.01% (w/v) NaN_3, 1×protease inhibitors cocktail (#P8340)
SDS-PAGE stacking gel	125 mM Tris-HCl pH6.8, 0.1% (w/v) SDS
SDS-PAGE separating gel	375 mM Tris-HCl pH8.8, 0.1% (w/v) SDS
SDS-PAGE running buffer	25 mM Tris base, 250 mM glycine, 0.1% (w/v) SDS
Immunoblotting (transfer) buffer	25 mM Tris base, 187 mM glycine, 20% (v/v) methanol
Membrane blocking buffer	5% (w/v) Marvel dried skimmed milk in TBS-T
Primary antibody dilution buffer	3% (w/v) BSA in TBS-T (containing 0.01% NaN_3)
E. coli washing buffer	50 mM Tris-HCl pH7.5, 50 mM NaCl, 5 mM $MgCl_2$
E. coli lysis buffer	*E. coli* washing buffer, with freshly added 1 mM PMSF (in methanol) and 1 mM DTT
Glutathione elution buffer	50 mM Tris, 150 mM NaCl, 1 mM PMSF, 10 mM reduced glutathione, pH8.0
Complete DMEM (cDMEM)	DMEM high glucose + 10% (v/v) FBS, 4 mM L-glutamine
Basal M199 (bM199)	1×M199 with Earle's salts, 26 mM $NaHCO_3$
Complete M199 (cM199)	bM199 + 10% (v/v) FBS, 90 mg/L heparin, 4 mM L-glutamine, and 0.1% (v/v) bovine brain extract prepared as described in the literature (Maciag et al., 1979)
Reduced M199 (rM199)	10% (v/v) cM199 in bM199
Promocell-supplemented M199 (PCM199)	bM199 + 10% (v/v) FBS, 4 mM L-glutamine, 2.52% (v/v) Promocell supplement kit #C-39216
FACS buffer	1% (w/v) BSA in PBS (containing 0.1% NaN_3)
IF blocking buffer	3% (w/v) BSA, 10% (v/v) FBS, 0.1% (v/v) Tween-20 in PBS. 0.22 µm-filtered
Gelatin solution	0.1% (w/v) gelatin from porcine skin in PBS
Mammalian cells freezing medium	10% (v/v) DMSO in FBS
Tissue lysis buffer	50 mM Tris-HCl pH8.5, 1 mM EDTA pH8.0, 0.5% (v/v) Tween-20
PTx.2	0.2% (v/v) Triton X-100 in PBS
PTwH	0.2% (v/v) Tween-20, 10 µg/mL heparin in PBS
iDISCO permeabilization solution	2.3 % (w/v) glycine, 20% (v/v) DMSO in PTx.2
iDISCO blocking solution	6% (v/v) horse serum, 10% DMSO in PTx.2

2.1.3. Antibodies and conjugates

Diluents are to be found in the relevant experimental procedure section, in this chapter. In some instances, in place of the standard buffer, primary antibodies for WB were diluted in 3% (w/v) Marvel dried skimmed milk in TBS-T and stored at -20 °C between usage: this is denoted by the * symbol in the table below.

Table 2.3. Primary antibodies

Antibody	Working concentration	Clone ID (Cat. #)	Source
Mouse mAb anti human **PCDH1**	1 µg/mL (WB)	5D5 (H00005097-M01)	Novus Biologicals/ Bio-Techne (Abingdon, UK)
Mouse mAb anti human/mouse **PCDH1**	1:20 i.e. 10 µg/mL (FACS), 1:100 (IF)	B-11 (sc-398263)	Santa Cruz Biotechnology (Heidelberg, Germany)
Rabbit pAb anti human **α-tubulin**	1:1,000 (WB)	(2144)	CST (Leiden, Netherlands)
Rabbit pAb anti **GST**	1:5,000 (WB)	(2622)	CST (Leiden, Netherlands)
Mouse mAb anti **EGFP**	1:2,000 i.e. 1 µg/mL (WB)*	3E1	Cancer Research UK (London, UK)
Mouse mAb anti human **DP**	1:20 (IF, PLA), 1:25 (WB)*	11-5F	Dr Martyn Chidgey, University of Birmingham
Rabbit pAb anti human **DP**	1:1,000 i.e. 1 µg/mL (WB)*	(ab71690)	Abcam (Cambridge, UK)
Mouse mAb anti human **DP**	1:300 (IF)	20B6 (MABT1492)	EMD Millipore
Mouse mAb anti **myc-tag**	1:100 (IF), 1:5,000 (WB)*	9B11 (2276)	CST (Leiden, Netherlands)
Rabbit mAb anti **myc-tag**	1:100 (IF), 1:200 i.e. 65 ng/mL (PLA)	71D10 (2278)	CST (Leiden, Netherlands)
Rabbit pAb anti human **SMAD1/5/9**	1:1,000 i.e. 1 µg/mL (WB)	(ab66737)	Abcam (Cambridge, UK)
Rabbit mAb anti human **SMAD2/3**	1:2,000 (WB)	D7G7 (8685)	CST (Leiden, Netherlands)
Mouse mAb anti **FLAG-tag**	1:1,000 i.e. 1µg/mL (WB)*	M2 (F1804)	Sigma-Aldrich/Merck (Darmstadt, Germany)
Mouse mAb anti human **CD31** (PECAM-1)	1.29 µg/mL (co-culture)	JC/70A (ab9498)	Abcam (Cambridge, UK)
Rat mAb anti mouse **CD31**	1:100 i.e. 5 µg/mL (LSFM)	MEC 13.3 (553370)	BD Biosciences (San José CA, USA)
Rabbit pAb anti human **Plakoglobin/γ-catenin**	1:200 (IF, PLA)	(ab15153)	Abcam (Cambridge, UK)
Rat mAb anti murine **E-Cadherin/Cadherin-1**	4 µg/mL (WB)	ECCD-2 (13-1900)	ThermoFisher (Waltham MA, USA)
Normal mouse IgG	1:300 i.e. 10 µg/mL	(10400C)	Sigma-Aldrich/Merck

(control)	(FACS)		(Darmstadt, Germany)
Mouse IgG (control)	1:7,700 i.e. 65 ng/mL (PLA)	(010-001-298)	Rockland (Limerick PA, USA)
Rabbit IgG (control)	1:15,400 i.e. 65 ng/mL (PLA)	(011-001-297)	Rockland (Limerick PA, USA)

Table 2.4. Secondary antibodies-conjugates

Antibody	**Working concentration**	**Cat. #**	**Source**
Alkaline phosphatase-conjugate goat **anti mouse IgG**	1:500 (co-culture)	A4656	Sigma-Aldrich/Merck (Darmstadt, Germany)
HRP-conjugate goat **anti mouse IgG**	1:5,000 i.e. 200 µg/mL (WB)	P0447	Dako/Agilent (Santa Clara CA, USA)
HRP-conjugate goat **anti rabbit IgG**	1:5,000 (WB)	7074	CST (Leiden, Netherlands)
AF647-conjugate goat **anti rat IgG**	1:300 i.e. 6.7 µg/mL (LSFM)	A-21247	ThermoFisher (Waltham MA, USA)
AF647-conjugate goat **anti rabbit IgG**	1:1,000 i.e. 2 µg/mL (IF)	A-21245	ThermoFisher (Waltham MA, USA)
AF647-conjugate goat **anti mouse IgG**	1:200 i.e. 10 µg/mL (FACS), 1:1,000 (IF)	A-21237	ThermoFisher (Waltham MA, USA)
AF568-conjugate goat F(ab’)$_2$ **anti mouse IgG**	1:1,000 i.e. 2 µg/mL (IF)	A-11019	ThermoFisher (Waltham MA, USA)
AF633-conjugate goat **anti human IgG**	1:200 i.e. 10 µg/mL (FACS)	A-21091	ThermoFisher (Waltham MA, USA)
AF488-conjugate goat **anti mouse IgG**	1:200 i.e. 10 µg/mL (FACS), 1:1,000 (IF)	A-11001	ThermoFisher (Waltham MA, USA)

2.1.4. Oligonucleotides

All oligonucleotides were synthesised by Eurogentec (Southampton, UK) and supplied as 100 µM stocks. Reference for the “direction” column is the coding strand. Oligonucleotides with sequence written partly uppercase and partly lowercase were used in a HiFi Assembly reaction: the lowercase portion annealed one DNA fragment, the uppercase another. Detailed usage information for oligonucleotides used in HiFi assembly reactions is reported in **Table 2.6**.

Table 2.5. Sequences of synthesised oligonucleotides

Name	**Sequence (5’ —> 3’)**	**Direction**	**Usage information**
WV001	CTGCTGGTCATGCAGTGTCT	fwd	Table 2.12
WV002	GCCCCAGGGGTATTTACAAC	rev	Table 2.12
WV003	GGGAGGGAAATGGGTAAGAA	fwd	Table 2.12
WV004	CCAGAAGCCTAGTGGTGAGG	rev	Table 2.12
WV005	ACCCATCCCAGCACAGTTAC	fwd	Table 2.12

WV007	GGGACCCGGTGACTGTATAA	fwd	Table 2.12
WV008	GTGTTGGGTGGCTGTTCCT	rev	Table 2.12
WV009	GGGTGACCCACCACTAGAAA	fwd	Table 2.12
WV010	CAGGGTGCTTAGGTCCTCAC	rev	Table 2.12
WV011	GTTTCCCCGGTTTGACAGAG	fwd	Table 2.12
WV012	GATTTCTGCATTGGCACCTT	rev	Table 2.12
WV013	TACACCCAGCTGTGGATGAG	fwd	Table 2.12
WV015	atcggatctggttccgcgtggatccGTGCGCTACTGCAGACAG	fwd	pGEX-PCDH1_ICD assemblies
WV018	GAGGCCCCAGAATCAGGA	rev	Table 2.12
WV019	GTCTGGCACTCTGCCTCAG	rev	Table 2.12
WV020	gccgctcgagtcgacccgggaattcTCACTCCCACACCTCGGTC	rev	pGEX-PCDH1_ICDv1 assembly
WV021	AGGGCTGCTTTTAACTCTGGT	fwd	Table 2.12
WV022	CCCCACTTGATTTTGGAGGGA	rev	Table 2.12
WV023	CAATGTGCCTGGATGCGTT	fwd	pGEX sequencing
WV024	TGCATGTGTCAGAGGTTTTCA	rev	pGEX sequencing
WV025	cctccaggccACTGTCATAGTAACTGTGCTGG	rev	pGEX-PCDH1_ICDv2 assembly
WV026	ctatgacagtGGCCTGGAGGAGTCTGAG	fwd	pGEX-PCDH1_ICDv2 assembly
WV027	gccgctcgagtcgacccgggaattcTCACAGGTAGATCTCGCG	rev	pGEX-PCDH1_ICDv2 assembly
WV029	ggtgctttgttgcTCCCGGTCGAAACTAAGACTGGATAGGATGG	rev	pWPXL-s2R-PCDH1-myc-P2A-EGFP assemblies
WV030	GTCTTAgtttcgaccgggaGCAACAAAGCACCTACAC	fwd	pWPXL-s2R-PCDH1-myc-P2A-EGFP assemblies
WV031	gccagagtctcatTGACATAAAGATGGACCAAG	rev	pWPXL-s2R-PCDH1-myc-P2A-EGFP assemblies
WV032	catctttatgtcaATGAGACTCTGGCCAACC	fwd	pWPXL-s2R-PCDH1-myc-P2A-EGFP assemblies
WV033	acttgctcttcttGCCTTTGCTTTTGTTTCC	rev	pWPXL-s2R-PCDH1-myc-P2A-EGFP assemblies
WV034	caaaagcaaaggcAAGAAGAGCAAGTCCCCAAAGC	fwd	pWPXL-s2R-PCDH1-myc-P2A-EGFP assemblies
WV035	atcttcttcagaaataagtttttgttcggatccCTCCCACACCTCGGTCCA	rev	pWPXL-s2R-PCDH1-myc-P2A-EGFP assemblies
WV036	atcttcttcagaaataagtttttgttcggatccCAGGTAGATCTCGCGCTTG	rev	pWPXL-s2R-PCDH1v2-myc-P2A-EGFP assembly
WV037	gatcacgagactagcctcgaggtttaaacCAGCTCATGGCCTCTGTTTTG	fwd	pWPXL-s2R-PCDH1v1-myc-P2A-EGFP assembly
WV038	gatcacgagactagcctcgaggtttaaaccagctcATGTCCCCTATACTAGGTTATTGGAAAATTAAG	fwd	pWPXL-s2R-PCDH1-myc-P2A-EGFP assemblies
WV039	tgattatcatatgactagtcccgggaattcTCACTCCCACACCTCGGTC	rev	pWPXL-s2R-PCDH1v1-myc-P2A-EGFP assembly
WV040	tgattatcatatgactagtcccgggaattcTCACAGGTAGATCTCGCG	rev	pWPXL-s2R-PCDH1v2-myc-P2A-EGFP assembly
WV050	TACCTGGCTGCCTTCAATAGA	fwd	Genotyping of Pcdh1-Flox progeny (“del”)
WV051	CCCCTCACCCACAACGCAACTTCC	rev	Genotyping of Pcdh1-Flox

			progeny (“del”)
WV052	TGCCACGACCAAGTGACAGCAATG	fwd	Genotyping of Pcdh1-Flox progeny (“cre”)
WV053	AGAGACGGAAATCCATCGCTCG	rev	Genotyping of Pcdh1-Flox progeny (“cre”)
WV054	ACAACTCCATCGGCGACTAT	fwd	pEGFP-N1-DP(1-1022) sequencing
WV055	CATGCTTGTTCCCTCTGTGG	fwd	pEGFP-N1-DP(1-1022) sequencing
WV056	GTCTGCCTGGACCTGGATAA	fwd	pEGFP-N1-DP(1-1022) sequencing
WV057	TGTCACATGCCTGCATAC	fwd	Genotyping of Pcdh1-Flox progeny (“5’ko”)
WV058	CACAGAGACGAGCTAACAAG	rev	Genotyping of Pcdh1-Flox progeny (“5’ko”)
WV059	ttagtgaaccgtcagatccgctagcGCTACCGGACTCAGATCG	fwd	pEGFP-N1-DPN-Spec assemblies
WV060	tgctcaccatCTGTCGCAGGTGATCCATC	rev	pEGFP-N1-DPN-Spec1 assembly
WV061	cctgcgacagATGGTGAGCAAGGGCGAG	fwd	pEGFP-N1-DPN-Spec1 assembly
WV062	tgattatgatctagagtcgcggccgcTTTACTTGTACAGCTCGTCCATG	rev	pEGFP-N1-DPN-Spec assemblies
WV063	tgctcaccatGGCAGCATTTTCTTTCAGATG	rev	pEGFP-N1-DPN-Spec2 assembly
WV064	aaatgctgccATGGTGAGCAAGGGCGAG	fwd	pEGFP-N1-DPN-Spec2 assembly
WV065	ccatggatccGCCAGGGAGCTGAATGAC	rev	pEGFP-N1-DPN-Spec4 assembly
WV066	gctccctggcggatccATGGTGAGCAAGGGCGAG	fwd	pEGFP-N1-DPN-Spec4 assembly
WV067	GATGTTCTGCAGCTGTCGC	rev	pEGFP-N1-DPN-Spec4 sequencing
VH05	CACGTTTGGTGGTGGCGACC	fwd	pGEX sequencing
VH527	tagtaggaattccagctcATGGCCTCTGTTTTGCCTCTTCCCCTTGCAGCCCTCCTGATTCTGG	fwd	PIG-PCDH1_ECD4 assembly
VH546	TAGTAGGCGGCCGCCaggtgcgttgtcattgacgtccac	rev	PIG-PCDH1_ECD4 assembly
SJGFP	TAGTAGACTAGTTCAAGCTTGAGCTCGAGATCTGAG	rev	GFP-based plasmids sequencing

2.1.5. Plasmids

Plasmids generated as part of this thesis are reported in **Table 2.6**. All were generated by HiFi assembly (**Section 2.5.8**). Where appropriate, insert name is in bold typeface, plasmid backbone in regular typeface. Nucleotide sequencing, carried out either by the Functional Genomics, Proteomics and Metabolomics Facility at the University of Birmingham or by Source BioScience (Nottingham, UK), confirmed correct assembly of each plasmid. Plasmids generated by third parties, and used in this Thesis, are reported in **Table 2.7** instead.

Table 2.6. List of plasmids generated, with cloning strategy

Plasmid name (*description*)	**Cloning strategy**
pGEX-**PCDH1_ICDv1** (*GST-tagged ICD of PCDH1, short isoform*)	Insert PCR-amplified from HUVEC total cDNA with oligos WV015+WV020, then cloned into pGEX-4T-2 backbone (pre-linearised by *Bam*HI-*Eco*RI digest)
pGEX-**PCDH1_ICDv2** (*GST-tagged ICD of PCDH1, long isoform*)	Insert PCR-amplified from HUVEC total cDNA as two separate fragments, with oligos WV015+WV025 and WV026+WV027, then cloned into pGEX-4T-2 backbone (pre-linearised by *Bam*HI-*Eco*RI digest)
pWPXL-**PCDH1_GSTICDv1** (*GST-tagged ICD of PCDH1, short isoform*)	Insert PCR-amplified from pGEX-PCDH1_ICDv1 with oligos WV038+WV039, then cloned into pWPXL backbone (pre-linearised by *Bam*HI-*Eco*RI-HF digest)
pWPXL-**PCDH1_GSTICDv2** (*GST-tagged ICD of PCDH1, long isoform*)	Insert PCR-amplified from pGEX-PCDH1_ICDv2 with oligos WV038+WV040, then cloned into pWPXL backbone (pre-linearised by *Bam*HI-*Eco*RI-HF digest)
pWPXL-**s2R-PCDH1v1-myc**-P2A-EGFP (*Full length PCDH1v1, silently resistant to siRNA duplex #2 and myc-tagged, + free cytosolic EGFP*)	Insert PCR-amplified as 4 separate fragments: A = WV037+WV029 from PIG-PCDH1_ECD B = WV030+WV031 from PIG-PCDH1_ECD C = WV032+WV033 from total HUVEC cDNA D = WV034+WV035 from pGEX-PCDH1_ICDv1 Resistance to siRNA-2 conferred by primer design WV029&WV030. Fragments were joined *via* further PCR-amplification: A to B with oligos WV037+WV031 C to D with oligos WV032+WV035 AB and CD then assembled into pWPXL-myc-2A-EGFP backbone (pre-linearised by *Pme*I-*Bam*HI-HF digest)
pWPXL-**s2R-PCDH1v2-myc**-P2A-EGFP (*Full length PCDH1v2, silently resistant to siRNA duplex #2 and myc-tagged, + free cytosolic EGFP*)	Insert PCR-amplified as 4 separate fragments: A, B, C = as per s2R-PCDH1v1 above E = WV034+WV036 from pGEX-PCDH1_ICDv2 Fragments joined *via* further PCR-amplification: A to B with oligos WV037+WV031 as for v1 C to E with oligos WV032+WV036 AB and CE then assembled into pWPXL-myc-2A-EGFP backbone (pre-linearised by *Pme*I-*Bam*HI-HF digest)
PIG-**PCDH1_ECD4** (*PCDH1 ECD truncated after the fourth EC*	Insert PCR-amplified from PIG-PCDH1_ECD with oligos VH527+VH546, then digested with

repeat, hFc-tagged)	*Eco*RI-HF-*Not*I-HF. Insert then ligated into PIG backbone (pre-linearised by *Eco*RI-HF-*Not*I-HF digest)
pEGFP-N1-**DPN-Spec1** *(Human Desmoplakin truncated after the first Spectrin repeat, EGFP-tagged)*	Insert PCR-amplified from pEGFP-N1-DP(1-1022) as two fragments: A = WV059+WV060 (Spectrin domain) B = WV061+WV062 (EGFP) Assembled all into partial plasmid backbone (pre-linearised by *Acc*I-*Nhe*I-*Not*I-HF digest)
pEGFP-N1-**DPN-Spec2** *(Human Desmoplakin truncated after the second Spectrin repeat, EGFP-tagged)*	Insert PCR-amplified from pEGFP-N1-DP(1-1022) as two fragments: A = WV059+WV063 (Spectrin domains) B = WV064+WV062 (EGFP) Assembled all into partial plasmid backbone (pre-linearised by *Acc*I-*Nhe*I-*Not*I-HF digest)
pEGFP-N1-**DPN-Spec4** *(Human Desmoplakin truncated after the fourth Spectrin repeat, EGFP-tagged)*	Insert PCR-amplified from pEGFP-N1-DP(1-1022) as two fragments: A = WV059+WV065 (Spectrin domains) B = WV066+WV062 (EGFP) Assembled all into partial plasmid backbone (pre-linearised by *Acc*I-*Nhe*I-*Not*I-HF digest). A *Bam*HI site was engineered before the EGFP tag by design of WV066 primer, to allow future full pEGFP-N1 backbone liberation by *Nhe*I-*Bam*HI digest if required.

Table 2.7. List of previously existing plasmids used

Plasmid name (*description*)	**Source and known details**
pGEX-4T-2 *(GST tag, alone)*	Merck (Darmstadt, Germany)
PIG-**PCDH1_ECD** (*PCDH1 ECD, full length, hFc-tagged*)	Dr Victoria Heath, University of Birmingham Assembled by PCR-amplification using HUVEC total cDNA as template
PIG-**PCDH1_ECD3** (*PCDH1 ECD truncated after the third EC repeat, hFc-tagged*)	Dr Victoria Heath, University of Birmingham Assembled by PCR-amplification using HUVEC total cDNA as template
pWPI-**MMRN2_ECD-Fc** (*Human MMRN2 ECD, full length, hFc-tagged*)	Dr Kabir Khan, University of Birmingham
pWPXL *(EGFP, in a lentiviral backbone)*	Dr Victoria Heath, University of Birmingham
pWPXL-myc-2A-**EGFP** *(myc-tag + free cytosolic EGFP, in a lentiviral backbone)*	Addgene #12257 (Cambridge MA, USA)
p**EGFP**-N1 *(EGFP, with MCS on 5')*	Addgene #2491 (Cambridge MA, USA)
pEGFP-N1-**DP(1-1022)** *(*N*-terminus of human Desmoplakin, EGFP-tagged)*	Dr Martyn Chidgey, University of Birmingham
pcDNA-**DP-ABC-GSR-FLAG**	Dr Martyn Chidgey, University of Birmingham

(C-terminus of human Desmoplakin, FLAG-tagged)	
pFLAG-CMV-5c-**DP**, i.e. p931 *(Human Desmoplakin, full length)*	Dr Martyn Chidgey, University of Birmingham Insert between *Not*I-*Kpn*I sites
pBAT-**neo** *(Resistance to G418)*	Dr Martyn Chidgey, University of Birmingham (Tselepis et al., 1998)
pBAT-**EM2** *(Murine E-Cadherin, full length)*	Dr Martyn Chidgey, University of Birmingham (Tselepis et al., 1998)
psPAX2 *(Lentiviral packaging, second generation)*	Addgene #12260 (Cambridge MA, USA)
pMD2.G *(Lentiviral VSV-G envelope protein)*	Addgene #12259 (Cambridge MA, USA)

2.1.6. siRNA duplexes

All duplexes were supplied as a dried powder, synthesised either by Dharmacon (Lafayette CO, USA) or by Ambion/ThermoFisher (Waltham MA, USA). Basepair numbering refers to Hs PCDH1 isoform 1 from *NCBI*, with bp 1 assigned to the adenosine of the main start-of-transcription ATG codon. Only Ambion-sourced siRNA duplexes are sold pre-validated by the company.

Table 2.8. siRNA duplexes used and their target

ID	Sequence of sense strand (5’ —> 3’)	Target bp	Source
s10106	GCCGAACUAUCUGAGAAUAtt	859-877	Ambion
s10107 (“siRNA-1”)	GUGACUUUGUUAUCCAGAAtt	1967-1985	Ambion
s10108 (“siRNA-2”)	GCCUGAGCUUUGAUCGAGAtt	2009-2027	Ambion
HSS181789	CAGAAUGGCACAGGCACCAUCCUA	1981-2004	Ambion
CTM-499124 (“siRNA-3”)	GGGAACAGCGGGAGAGCUAuu	1715-1733	Dharmacon
CTM-504936 (“siRNA-4”)	GCAUAGGGCUAGUGACUCAuu	1172-1190	Dharmacon
Silencer Negative Control siRNA #1 (“NCD”)	Proprietary (cat. #AM4636)	Reportedly no known human transcripts	Ambion

2.1.7. *E. coli* strains

Chemically immunocompetent *E. coli* cells were stored at -80 °C before usage.

Table 2.9. Details of *E. coli* strains used

Strain	Genotype	Application	Antibiotic resistance	Supplier
NEB 5-alpha	*fhuA2 Δ(argF-lacZ)U169 phoA glnV44 Φ80 Δ(lacZ)M15 gyrA96 recA1 relA1 endA1 thi-1 hsdR17*	Plasmid preparation	Amp	NEB UK (Herts, UK)
BL21(DE3)pLysS	F^-, *ompT*, *hsdS*$_B$ (r_B^-, m_B^-), *dcm*, *gal*, *λ(DE3)*, *pLysS*, Cam^R	Protein production	Amp, Cam	Promega (Southampton, UK)

2.2. Cell culture

2.2.1. General mammalian cell culture

All mammalian cells were handled in a hood under sterile laminar flow conditions, and cultured in sterile plastic dishes (Falcon, Franklin Lakes, USA). When not being handled, cells were kept at 37 °C, 5% (v/v) CO_2 and regulated humidity in dedicated incubators (Sanyo Electric Co./Panasonic, Osaka, Japan). All reagents and solutions employed, if not provided sterile, were sterilised either by autoclaving or filtering through 0.22 μm-pore filters (EMD Millipore, Billerica MA, USA). To passage cells, they were washed in PBS, and incubated in 0.05% (w/v) trypsin-EDTA in PBS until completely detached. Trypsin was inactivated by addition of complete growth media. Cells were centrifuged at 195×*g* for 5 min and then re-plated. If cells needed to be stored, the centrifuged pellet was resuspended in freezing medium instead and transferred to a cryovial (Greiner Bio-One, Stonehouse, UK), then moved to -80 °C in a Mr Frosty container (ThermoScientific, Waltham MA, USA), and stored in liquid N_2. When they needed to be revived, vials were submerged in a 37 °C water bath until the contents defrosted, and washed in complete media before plating. Cells were counted manually with the aid of an improved Neubauer haemocytometer (Hawksley, Lancing, UK) under a DM IL LED light microscope (Leica, Milton Keynes, UK). HEK 293T, HaCaT, HBMEC, human dermal fibroblasts, HeLa, and L929 cells were all grown in cDMEM growth medium. L929 cells were centrifuged at gentler speed (150×*g* for 5 min).

2.2.2. HUVEC isolation and culture

HUVEC were isolated from umbilical cords donated for the purpose, obtained from the University of Birmingham's Human Biomaterials Resource Centre (HBRC) under ethical approval (#16-266/16-266E1). Briefly, cords were cannulated at both ends of one of their veins, and flushed with PBS. The flushed vein was then filled with 1 mg/mL collagenase 1A in PBS, and incubated at 37 °C for 20 min. The mixture was then flushed through with PBS *via* one of the cannulae, collected and centrifuged (210×*g*, 6 min). The HUVEC pellet thus isolated was plated and cultured as outlined below, with addition of 10 μg/mL gentamicin + 0.25 μg/mL amphotericin B between isolation and passage 1, and of 100 U/mL penicillin + 100 μg/mL streptomycin between passages 1-2. Isolated HUVEC were cultured in antibiotic-free cM199 medium, on gelatin-coated dishes: each plate was covered in gelatin solution and incubated at room temperature for 20 minutes, discarding the solution afterwards. Cells were typically split in a 1:3 ratio by trypsinisation when they reached ~80-90% confluency. For experiments, only cells between passage 2 and 6 were used. Commercial HUVEC mixtures were treated as isolated HUVEC, but grown in PCM199 instead.

2.2.3. siRNA transfection of HUVEC

siRNA duplexes were first titrated in a range of final concentrations between 50 nM and 80 pM, and delivered at 20 nM in subsequent assays unless otherwise stated; RNAiMAX Lipofectamine was used at a fixed final concentration of 0.3% (v/v). The procedure that follows was adapted to cells seeded on different sizes of plasticware, according to necessity (**Table 2.10**). 10^6 cells were seeded on a 10-cm dish and incubated overnight (16-20 h). The following day, they were washed twice in PBS, then 3.2 mL Opti-MEM was added. Concurrently, a duplex mix was prepared: 10 µL siRNA duplex (400× final transfection concentration) was added to 670 µL Opti-MEM. Similarly, a lipofectamine mix was also prepared: 12 µL was added to 108 µL Opti-MEM. The two mixes were let rest for 10 min, then 120 µL lipofectamine mix was added to the duplex mix, to obtain the final transfection mixture. The latter was incubated for 10 further min, then the whole 800 µL thus obtained was added to the cells covered in Opti-MEM. After 4 h incubation at 37 °C, the mixture was removed and replaced with neat complete medium, and the cells were re-incubated.

Table 2.10. siRNA transfection solutions details

Size of dish	Number of cells	siRNA duplex volume (µL)	Lipofectamine volume (µL)	Total transfection volume in dish (mL)
6-well plate	175,000	2.5	3	1
6-cm dish	360,000	3.6	4.3	1.41
10-cm dish	1×10^6	10	12	4

Ratios between reagent volumes were kept the same as described in the text above.

2.2.4. PEI-based transient transfection

The procedure that follows was adapted to cells seeded on different sizes of plasticware, according to necessity (**Table 2.11**). 3×10^6 HEK 293T cells were seeded in a 10-cm dish and grown overnight. The following day, growth medium was refreshed to 10 mL antibiotic-free cDMEM. Concurrently, a transfection mix was prepared: 9 µg DNA was added to 1 mL Opti-MEM, then 36 µg PEI stock solution (1 mg/mL) was added. The tube was let rest for 10 min after brief, gentle mixing. The mixture was finally added to the cells covered in Opti-MEM, subsequently incubated as usual. Medium was changed to Opti-MEM + 4 mM L-glutamine 24 hours after transfection if producing a secreted protein.

Table 2.11. PEI transfection solutions details

Size of dish	Number of HEK 293T cells	DNA (µg)	Opti-MEM volume	PEI (µg = µL)	cDMEM (mL)
6-well plate	0.3×10^6	1	100 µL	4	2
6 cm	1×10^6	3	300 µL	12	3
10 cm	3×10^6	9	1 mL	36	10
15 cm	6×10^6	18	2 mL	72	20

2.2.5. Lentiviral transduction of HUVEC

1×10^6 HEK 293T cells were plated in a 6-cm dish, and triply-transfected following the PEI-based protocol (**Section 2.2.4**) the next day. The plasmids used were: psPAX2 (1.1 µg), pMD2.G (0.43 µg), and a pWPXL- or pWPI-based plasmid encoding the desired construct (1.5 µg). This transfection medium, and all cells in contact with it, were treated as hazardous (BSL-2) thereafter. 48 h after transfection, the HEK 293T supernatant containing the virions was filtered through a 0.45-µm mesh and supplemented with sterilised HUVEC growth supplements (either the commercial Promocell mix, or bovine brain extract + heparin, accordingly) and polybrene to a final concentration of 8 µg/mL. The viral supernatant was applied to a 6-cm dish of HUVEC. The following day, these were trypsinised and transferred onto a 10-cm dish for another 48 h, at which point they could be used for analysis by flow cytometry and/or desired assays.

2.3. Assays modelling angiogenesis *in vitro*

The *in vitro* assays that follow typically involved plating the desired number of HUVEC, followed by (siRNA) transfection 24 hours afterwards, and the start of the assay proper after a further 48 hours. To minimise inter-experimental technical variation while retaining biological significance, after attempting different strategies, it was decided to keep culturing HUVEC as separate isolates, and mixing them in equal numbers at the moment of plating them before transfection. Therefore, a typical experiment involving three biological replicates would comprise three instances of the same experiment carried out on different days using cells from the same three HUVEC isolates, separately grown and mixed each time only when plating for transfection.

2.3.1. Matrigel assay

70 µL ice-cold Matrigel was deposited in a well of a 12-well-plate, previously wetted with PBS to aid spreading. The plate was incubated for 5 min at 37 °C to solidify the matrix. HUVEC were then seeded onto the Matrigel layer at an optimal density of 180,000/well, and incubated at 37 °C. Pictures of each well were taken with the aid of an IncuCyte live-cell analysis system (Essen BioScience/Sartorius, Göttingen, Germany), using the 4× objective. Each well (condition) in a plate was divided in nine fields of view of equal area, four of which were selected for analysis – the same four positions for all conditions. Alternatively, plates were imaged manually on an EVOS Cell Imaging System (ThermoFisher, Waltham MA, USA), similarly identifying 9 fields of view per well. Images were analysed on *ImageJ* 1.51 (Schneider et al., 2012) with the “Angiogenesis Analyzer” plugin, v 1.0.c – 03 Dec 2013 (Carpentier et al., 2012). The number of fully formed intercellular junctions (“loops”) in each field of view thus obtained was recorded as the average of its four measurements.

2.3.2. Chemotaxis assay

FluoroBlok cell culture inserts with 8 µm pore-PET membrane (Corning, Corning NY, USA) were coated with gelatin solution and placed in a 24-well-plate. In parallel, HUVEC were incubated in reduced M199 (rM199) for 1 hour. 40,000 cells were seeded in rM199 on top of the inserts, placing 700 µL cM199 underneath it, and incubated for 5 hours. Inserts were washed in PBS and fixed in chilled 4% (w/v) PFA for 20 min, then cut out using a scalpel. They were finally placed between two glass slides, resting on a few drops of Vectashield mounting medium with DAPI (Vector Laboratories, Peterborough, UK). Slides were then imaged on an IX81 motorised inverted microscope (Olympus, Tokyo, Japan) and fluorescent nuclei counted manually. Each time, the membrane was divided in 15 fields of view of equal area; the number of nuclei at the bottom of the membrane in each field of view was counted manually, and the average of the 15 measurements was recorded. This was expressed as a percentage to the average number of nuclei at the bottom of the membrane in the negative control. The percentages (X) were then transformed such that $Y=\arcsin(X)$, and the transformed values (Y) were analysed via a one-way ANOVA test, followed by (Dunnett's) multiple comparisons test between the average of either PCDH1 duplex to the average of the control. Alternatively, slides were imaged manually on an EVOS Cell Imaging System, identifying 4 fields of view per membrane. In such cases, the data is reported un-transformed.

2.3.3. Spheroid sprouting assay

Spheroids were assembled overnight by incubating 1,000 HUVEC in 20 μL of a 0.24% methylcellulose/cM199 mixture, in an upside-down 60-well-plate (Nalge Nunc, Rochester NY, USA). Spheroids were collected by centrifugation at 160×*g* for 5 min, then resuspended in 0.8 mg/mL rat-tail collagen in 20% methylcellulose/M199. The ice-cold mixture was polymerised by rapid addition of 0.2 N NaOH to a final concentration of 0.016 N, followed by plating into a 24-well-plate and incubation at 37 °C. After 20 min, 100 μL complete growth medium was added to the top of the gel. After 16 h incubation at 37 °C, the gel was washed in twice in PBS, fixed 10 min with 10% formalin-saline, and pictures were then taken with an EVOS cell imaging system (ThermoFisher, Waltham MA, USA). Sprout length was measured using the "Straight Line" tool of the *ImageJ* software, followed by the "Measure" command. The number of sprouts on each spheroid was counted manually.

2.3.4. Co-culture assay

30,000/well human dermal fibroblasts, passage 3-4, were seeded in a 12-well-plate and grown in cDMEM, refreshed after 72 h. After 24 further hours, the cDMEM was discarded and 20,000 HUVEC were plated on top of the monolayer, in appropriate HUVEC growth medium. The latter was refreshed every 48 h. 3 or 5 days after plating the HUVEC, the cells were washed in PBS and fixed in freezer-cold 70% EtOH for 30 min, then optionally stored at 4 °C. Endothelial CD31 was stained with anti-CD31 (JC/70A, 1.29 µg/mL), 40-60 min, 37 °C, washed off 3× in PBS. To visualise the endothelial network, goat-anti-mouse-IgG-Alkaline Peroxidase (#A4656) was added for 40-60 min at 37 °C, then washed off 3× in PBS and twice in H_2O. Antibody dilutions were in 1% (w/v) BSA in PBS. The signal was visualised by adding SigmaFAST BCIP/NBT substrate (30 min), and recorded as transmitted light images on a Leica MZ16 stereomicroscope, fitted with a PLANAPO 1.0× objective and manual zoom factor 1.6×. Images were analysed with the AngioSys 2.0 software (Cellworks/Caltag Medsystems, Buckingham, UK).

2.3.5. Scratch-wound assay

200,000/well HUVEC were seeded in a 6-well-plate. 24 h afterwards, a scratch was manually performed using a P200 pipette tip (time = 0 h). Pictures were taken with the aid of an IncuCyte live-cell analysis system (Essen BioScience/Sartorius, Göttingen, Germany), using the 4× objective. Alternatively, plates were imaged manually on an EVOS Cell Imaging System, identifying 9 fields of view per membrane, using the 2× objective. The scratched area at each timepoint was manually outlined using the “Segmented Line” tool of the *ImageJ* software. The reported “scratch area” in this thesis for a given timepoint is expressed as a percentage, relative its original area at time = 0 h.

2.4. Protein Biochemistry

2.4.1. Mammalian cell extract harvesting

Cells were washed in PBS, then harvested mechanically using a cell scraper (Fisherbrand, Loughborough, UK) and collecting them into 1 mL PBS on ice. Cells were centrifuged

(2,500×*g*, 2 min), and the pellet resuspended in 10 pellet volumes of ice-cold NP-40 lysis buffer. The tube was vortexed briefly and incubated on ice for 20 min, then centrifuged (20,000×*g*, 15 min, 4 °C). Protein concentration, if required, was estimated with the aid of a commercial BCA protein assay kit (Pierce/ThermoFisher, Waltham MA, USA) as per instructions therein. The supernatant protein lysate was denatured in an equal amount of 2× SDS-PAGE sample buffer.

2.4.2. Pulldown and (co-)immunoprecipitation

Experiments were performed using glutathione agarose (#16100, GE Healthcare, Chicago IL, USA), Protein A-sepharose or Protein G-sepharose (#P9424 or #P3296, Merck, Darmstadt, Germany), according to experimental needs. Typically, 25 µL of a 50% (v/v) beads:buffer slurry would be used for pulldowns or IP on lysates harvested from 6-well-plates, 6-cm dishes, or 10-cm dishes. Beads were always handled on ice, centrifuged gently (~700×*g*, 2 min, 4 °C), and washed 3× in 1 mL lysis buffer before usage, then resuspended in lysis buffer to re-obtain a 50:50 slurry prior to preparing the mix for the experiment. Fresh protein extract or conditioned supernatant, diluted to 1 mL in lysis buffer if necessary, was incubated with washed slurry under end-over-end rotation at 4 °C for 1-2 h; 1 µg antibody was also added, if performing an immunoprecipitation. Beads were washed 3 times in 1 mL lysis buffer washes, then denatured in 2× SDS-PAGE sample buffer, thus releasing bound proteins.

2.4.3. SDS-PAGE of protein samples

Tris-glycine gels of appropriate acrylamide concentration were cast by polymerising an appropriate dilution of Protogel (in either stacking or separating gel buffer) with 0.1% (w/v) APS and 0.1% (v/v) TEMED, according to standard methodology (Sambrook & Russell, 2006); disposable, 1.0 mm-thick mini-cassettes were typically used for convenience (Novex/ThermoFisher, Waltham MA, USA). Denatured protein extracts were heated at 95 °C for 5 min, then quickly centrifuged and loaded on an acrylamide gel, alongside 3 μL relevant prestained protein ladder. Using an XCell SureLock Mini-Cell apparatus (Invitrogen/ThermoFisher, Waltham MA, USA), the samples were run at 90-100 V through the stacking portion of the gel, then at 120 V through the separating portion, and stopped when the dye front reached the base of the gel.

2.4.4. Staining of protein gels

In order to visualise protein bands, SDS-PAGE gels were washed 3×5 min in H_2O, and incubated in Instant*Blue* Ultrafast Protein Stain reagent overnight in the dark with constant, gentle rocking. They were then washed multiple times in H_2O over 2 h to de-stain.

2.4.5. Immunoblotting (Western Blotting)

Unstained SDS-PAGE gels were transferred onto methanol-activated PVDF membranes with pore size 0.45 μm (Immobilon-P/Millipore, Billerica MA, USA) in a wet-transfer tank, assembling a “sandwich” comprising absorbing sponges and 3MM Whatman chromatography paper (Fisher Scientific, Loughborough, UK) around each gel-membrane pair. Transfer was carried out at 30 V for 2 h at 4 °C, in an XCell II Blot Module (Invitrogen/ThermoFisher, Waltham MA, USA). Successful transfer was confirmed by reversible Ponceau S staining. All incubations of the membrane thereafter were carried out with gentle rocking. The membrane was incubated in blocking buffer for 1 h, then briefly rinsed 3× in TBS-T, and incubated overnight with a dilution of the relevant primary antibody at 4 °C. The membrane was washed by incubation in TBS-T for 30 min, swapping the buffer every 6 min. The membrane was incubated 90-120 min with a dilution of the appropriate secondary antibody in membrane blocking buffer, and again washed 30 min in TBS-T as before. The antibody signal was finally revealed by brief incubation with Amersham ECL Western Blotting detection reagent (GE

Lifesciences, Chicago IL, USA), and either developed on Amersham Hyperfilm (GE Lifesciences, Chicago IL, USA) or an Odyssey Fc imaging system (LI-COR Biosciences, Cambridge, UK). In the latter case, to quantify protein expression, regions of interest were drawn around each band, carrying out automated background subtraction. The signal from each protein band was then divided by the signal of its corresponding α-tubulin band, and the relative values thus obtained were normalised to the band of highest intensity.

2.4.6. Batch purification of recombinant, hFc-tagged proteins

HEK 293T cells were transfected (**Section 2.2.4**) with a hFc-fusion construct that allowed secretion of the protein. Given the encountered expression levels and the amount of proteins required, this typically involved transfecting twenty 15-cm dishes at a time. The transfection mixture was swapped to Opti-MEM + 4 mM L-glutamine 24 hours after transfection, which was harvested and refreshed every 48 hours, typically over 2-3 weeks. Collection of a harvest involved centrifugation of the conditioned Opti-MEM (195×*g*, 5 min) and addition of 1 mM EDTA and a few µg PMSF, followed by 0.22-µm filtration and storage at 4 °C. The yield was estimated by Protein A pulldown (**Section 2.4.2**) of 1 mL/harvest, followed by SDS-PAGE (**Section 2.4.3**) and protein staining (**Section 2.4.4**) using known amounts of BSA as standards. The harvested media were pooled to give a total volume of 1.5-2 L, which was then affinity-purified in batch by gravity flow through Protein A-sepharose slurry housed in an Econo-column (#7374011, Bio-Rad Laboratories, Hercules CA, USA) at 4 °C, washed with 50 mL PBS before and after protein flow-through. Fusion proteins were eluted at room temperature by multiple additions of 100 mM glycine (pH2.52), each of which was incubated for 30 min and collected into ice-cold Tris base (pH9), in a 250:100 (v/v) ratio respectively. The fractions thus recovered were mixed and buffer-exchanged into PBS, employing a PD-10 Sephadex-G25M column equilibrated in 25 mL PBS. The proteins were sterilised through a 0.22-µm syringe filter (Millex-GV/Merck, Darmstadt, Germany), then spin-concentrated in a 15-mL ultra-centrifugal filter of 10K MWCO (Amicon/Merck, Darmstadt, Germany), at 3,000×*g*, 4 °C. Purified proteins were stored at 4°C until usage, avoiding prolonged storage to minimise protein degradation. Protein concentration was assessed by means of a BCA assay (**Section 2.4.4**).

2.5. Molecular Biology

2.5.1. DNA gel electrophoresis

Purified DNA samples were diluted in 6X Purple Gel Loading Dye, then loaded onto an agarose-TAE gel submerged in TAE buffer alongside an appropriate DNA size marker (“ladder”). Larger gels (10 cm length) were run at 90 V until satisfactory separation was obtained, then visualised using a GeneGenius Bio Imaging System (Syngene/Biocaon, Bangalore, India). Shorter gels were run similarly, at 50 V.

2.5.2. Total RNA isolation and cDNA synthesis

For standard cDNA preparation, HUVEC of three different passage numbers and isolated from three different umbilical cords were collected by scraping (**Section 2.4.1**). Each third of a 10-cm dish was collected in a separate tube and then further processed separately, allowing the isolation of three technical replicates per plate. In the case of cDNA isolation for microarray purposes instead (**Section 2.5.11**), 20% of a 10-cm dish was scraped to be isolated for immunoblotting purposes, while the remaining 80% was collected for RNA isolation by trypsinisation. In either case, the obtained pellet was treated with the “RNeasy Mini” RNA isolation kit (QIAGEN, Germantown MD, USA), according to the manufacturer’s instruction, starting with resuspension in 350 μL RLT buffer. The RNA samples obtained were treated with the RNase-Free DNase Set while still in the column, according to the manufacturer’s instruction. After final elution in 40 μL RNase-free water, most of the eluate was moved to -80

°C for storage, after taking aside 3 µL to be snap-frozen in dry ice. This aliquot was then diluted with 2 µL 6X Purple Gel Loading Dye (NEB, Herts, UK), and run on a 1% (w/v) agarose-TAE gel (**Section 2.5.1**), to qualitatively check for RNA integrity and the absence of genomic DNA contamination. Gels were visualised on a GeneGenius Bio Imaging System (Syngene/Biocon, Bangalore, India). The concentration of the RNA eluate was measured on a Nanodrop ND-1000 spectrophotometer (ThermoFisher, Waltham MA, USA). If cDNA synthesis was required, 1.4-1.6 µg RNA was used, together with the High-Capacity cDNA Reverse Transcription Kit (ThermoFisher, Waltham MA, USA), in a final reaction volume of 20 µL. Negative control samples, lacking the RT enzyme, were also set up. cDNA samples thus obtained were stored at -20 °C.

2.5.3. Bacterial transformation

Chemically competent cells were thawed from -80 °C on ice, then 1-5 µL (1 pg-100 ng) plasmid or HiFi assembly mixture was added and gently mixed, and incubated on ice for 30 min. The bacteria were heat-shocked at 42 °C for 30 sec (NEB 5-alpha) or 10 sec (BL21(DE3)pLysS), then rested on ice 5 min. 950 µL SOC outgrowth medium was added, and the cells incubated at 37 °C with orbital shaking for 1 h. An appropriate volume of transformed bacteria (100-700 µL) was applied to a LB-agar plate containing the correct antibiotic(s), incubated at 37 °C overnight. Ampicillin was used at a final concentration of 100 µg/mL, chloramphenicol 20 µg/mL, kanamycin 50 µg/mL.

2.5.4. Plasmid isolation

In order to purify plasmid DNA from transformed NEB 5-alpha cells, bacterial colonies were picked and placed in a suitable volume of LB medium containing the appropriate antibiotic(s), and incubated overnight at 37 °C with orbital shaking. For small scale plasmid production, a 3 mL culture was set up; the following morning, this was centrifuged at 5,000×*g* for 10 min and purified with the GeneJET Plasmid Miniprep Kit (ThermoFisher, Waltham MA, USA). For larger scale production, a 2-mL starter culture was prepared and incubated as before for 6-8 h, then inoculated into a 50 mL culture with appropriate antibiotic(s) and incubated overnight. The following morning, the culture was centrifuged (5,000×*g*, 10 min) and purified with the GenElute HP Plasmid Midiprep Kit. [DNA] was measured on a Nanodrop ND-1000, and purified DNA stored at -20 °C.

2.5.5. Restriction digest

Restriction digest mixtures for plasmid fragment isolation purposes, such as for HiFi assemblies, were set up as follows: 5-10 µg DNA, 5 µL 10X buffer (enzyme-dependant), 20 units (each) enzyme, and topped up to 50 µL with H_2O. Smaller reactions were set up to screen plasmid preparations for successful assembly: 100-200 ng DNA, 2 µL 10X buffer, 0.5 units (each) enzyme. Enzymes and relative buffers were supplied by NEB (Herts, UK). Reactions were carried out at 37 °C for 1 hour and, if necessary, Antarctic Phosphatase treatment was immediately performed using 2 µL enzyme (NEB, Herts, UK) for 10 µg DNA. The products were diluted in 6X Purple Gel Loading Dye and run on an agarose-TAE gel (**Section 2.5.1**). If isolating plasmid fragments, these were cut with razor blades and purified with the GeneJET Gel Extraction Kit (ThermoFisher, Waltham MA, USA), eluting in 25 µL H_2O and storing the DNA fragments at -20 °C.

2.5.6. General purpose PCR, including PCDH1 splice variant analysis

Reaction mixtures were assembled on ice in a sterile tissue culture hood with all their components except the template DNA. The REDTaq ReadyMix kit was used, according to manufacturer’s instructions. For endothelial PCDH1 splice variant analysis, template DNA was

HUVEC cDNA (**Section 2.5.2**). Reaction mixtures were: 10 μL 2X REDTaq ReadyMix, 1 μL each 10 μM primers (forward and reverse), 2 μL cDNA previously diluted 1:10, 6 μL H_2O. Typical PCR cycle parameters were as follows: initial denaturation at 94 °C for 1 min, followed by 30-35 cycles of: denaturation (94 °C, 15 sec), annealing (T_a, 2 min, **Table 2.12**), and extension (72 °C, 40 sec/kb). These were followed by a final extension cycle (72 °C, 3 min). All reactions were carried out in Sensoquest thermocyclers (Göttingen, Germany). Primers were designed with the aid of the *Primer3* software (primer3.ut.ee).

Table 2.12. Details of analytical PCR of PCDH1 splice variants

Oligo pair (fwd+rev)	Transcript annealed	Region amplified	T_a (°C)
WV001+WV002	PCDH1v2	4482-4680	52.8
WV003+WV004	PCDH1v1 (but also v3 and v4)	3576-3775	51
WV005+WV019	PCDH1-204	1106-1311	53.7
WV007+WV008	PCDH1-207	55-250	52.9
WV009+WV010	PCDH1-208	36-230	53.4
WV011+WV012	PCDH1v4	14-173	50
WV013+WV018	PCDH1v3	9-132	53.1
WV021+WV022	GAPDH (NM_002046.6)	134-339	52.8

PCDH1v*x* transcripts were retrieved from the *NCBI* database, PCDH1-*xxx* transcripts from *Ensembl*. The region annealed by each primer is reported based on the numbering in the respective sequence since the numbering is not consistent across the two databases (for isoforms present in both).

2.5.7. Preparative PCR, including for HiFi Assembly

In order to produce inserts to clone into plasmids (**Table 2.6**), a high-fidelity Q5 DNA polymerase enzyme (NEB, Herts, UK) was used. For HiFi assembly, primers with appropriate overhangs were designed with the aid of the NEBuilder assembly tool website (https://nebuilder.neb.com/), such as to have a 25-bp overhang compatible with the end of each fragment they annealed. Reaction mixtures were set up on ice under laminar flow as follows: 20 μL 5X Q5 buffer, 2 μL 10 mM dNTPs mix, 1 μL each 100 μM primers (forward and reverse), 1 μL Q5 enzyme (2 units), 20 μL High GC enhancer buffer, and ~500 ng template DNA. The mixture was topped up to 100 μL with H_2O. Cycle parameters were as follows: initial denaturation at 98 °C for 30 sec, followed by 40 cycles of: denaturation (98 °C, 10 sec), annealing (*T*$_a$, 30 sec), and extension (72 °C, 30 sec/kb). These were followed by a final extension cycle (72 °C, 2 min). *T*$_a$ was either calculated by the NEBuilder tool, or set to 5 °C below the primer pair melting temperature. For purification purposes, PCR products were either treated with the QIAquick PCR Purification Kit (QIAGEN, Germantown MD, USA), or run on an agarose-TAE gel. In the latter case, fragment purification was then carried out on the band, excised with razor blades, as per **Section 2.5.5**.

2.5.8. HiFi Assembly

Assemblies were carried using the NEBuilder HiFi DNA Assembly Cloning Kit (NEB, Herts, UK), according to manufacturer's instructions. Reactions were set up with 100 ng vector (longest fragment) and a two-fold molar excess of each insert longer than 200 bp, or a 1:1 molar ratio for shorter inserts. Reactions were carried out at 50 °C for 15 or 45 min, after which 1 µL was used to transform 25 µL NEB 5-alpha cells (**Section 2.5.3**). Purified plasmids from isolated transformant colonies were preliminarily screened by restriction digest, and confirmed by nucleotide sequencing.

2.5.9. DNA ligation

Ligation between an insert and a backbone of blunt-sticky (or compatible sticky) ends was performed with the T4 enzyme kit (NEB, Herts, UK) following manufacturer's instructions. Typically, 1 µL enzyme was used to ligate 50 ng plasmid backbone to a 3:1 molar excess of insert in a 20 µL reaction, carried out at 16 °C overnight and stored at -20 °C. 2 µL ligation mix was used to transform 20 µL NEB 5-alpha cells (**Section 2.5.3**).

2.5.10. Pcdh1-Flox mice and offspring genotyping

For adult mouse genotyping, small ear clippings were performed by Biomedical Services Unit staff as part of routine colony maintenance and husbandry procedures. These were stored at -20

°C, and retrieved from the Unit on a weekly basis. Alternatively, during embryo isolation (**Section 2.7.4**), small portions of the tail or the left hind limb were excised instead. DNA was extracted by overnight incubation of the tissue at 55 °C with shaking in 150 μL tissue lysis buffer with 300 μg/mL PCR-grade Proteinase K. After brief vortexing, the enzyme was inactivated at 100 °C for 12 min, and mixtures thus obtained were stored at +4 °C. 1 μL mixture thus obtained was used as source of template DNA for genotyping reactions, with PCR parameters as follows: initial denaturation at 94 °C for 5 min, followed by 40 cycles of: denaturation (94 °C, 30 sec), annealing (T_a, 30 sec), and extension (72 °C, 1 min). These were followed by a final extension cycle (72 °C, 5 min). The reactions were set up using REDTaq ReadyMix as described in **Section 2.5.6**, using 2 μM oligo stocks instead, to achieve a final primer concentration of 100 nM (each); primer combinations are detailed in **Table 2.13**, the results of the reactions are shown in **Figure 6.1C**.

Table 2.13. Details of genotyping reactions

Reaction	Oligo pair (fwd+rev)	Expected product sizes	Agarose gel	T_a (°C)
del	WV050+WV051	0 bp (WT/Flox), 700 bp (KO)	1.7% (w/v)	52
cre	WV052+WV053	380 bp	1.7% (w/v)	57
5’ko	WV057+WV058	0 bp (KO), 147 bp (WT), 186 bp (Flox)	2.1% (w/v)	49

Oligonucleotide sequences and PCR cycle parameters were obtained from Prof Martijn Nawijn MD, University of Groningen.

2.5.11. Microarray analysis

HUVEC RNA was extracted in triplicates as described in **Section 2.5.2**, and delivered on dry ice to SourceBioScience (Nottingham, UK), who carried out cDNA conversion and the microarray experiments, on a Clariom S platform (ThermoFisher, Waltham, MA, USA). The CEL files thus obtained were analysed with the Transcriptome Analysis Console TAC software version 4.0.2.15 (ThermoFisher, Waltham, MA, USA) which, for statistical analysis, invokes the *limma* module (Ritchie et al., 2015) of the *Bioconductor* R package. All samples passed the platform-specific quality control checks, except for one duplex mixture-treated sample, for which the *thr* value was slightly lower than the *phe* value, however this difference was minimal and all other controls worked as expected, so the sample was kept as part of the analysis. All control spots expression levels were between 4.5 and 5.6. Principal component analysis was run automatically by the software, with unaltered settings. Statistical analysis (two-way ANoVA) was run as follows: “SST-RMA (Gene Level)” analysis with eBayes modification, probeset expression cut-off set to ≥ 50% samples having DABG (Detected Above Background) values < 0.05, positive *vs* negative area-under-the-curve threshold = 70%, minimum *p*-value for gene-level statistical significance = 5%, minimum fold-change <-1.5 or >1.5. All 15 possible two-way comparisons between the 6 treatments were run, e.g. Duplex 1 *vs* NCD, Duplex 2 *vs* NCD, etc. The comparisons lists thus obtained were manually filtered to only include genes with a false discovery rate (FDR) *p*-value < 10%, and to exclude genes for which the coefficient of variance for the signal intensity of the three repeats (COV = standard deviation/average) was over 20%.

Preliminary pathway analysis was undertaken by Dr Zsuzsanna Nagy (University of Birmingham, UK) on most of the comparison lists thus created, with aid of the Ingenuity Pathway Analysis software (QIAGEN, Germantown MD, USA) version 62089861 release date 2021-02-17 (Krämer et al., 2013), creating pathway data for Canonical Pathways, for Diseases and Biofunctions, and for Upstream Regulators. These three datasets, as received, identified each item (i.e. a pathway, or a disease, or a possible upstream regulator) by its *z*-score for a given comparison list, and were manually filtered to only show items that were differentially regulated among different treatments in the following way: either activated by Duplex 1 treatment and blocked by both Duplex 2 and Duplexes mixture treatments, or vice versa, where activated is identified as *z*-score > 0, and blocked as *z*-score < 0.

2.6. Mass Spectrometry

2.6.1. GST-fusion protein purification from *E. coli*

Starter cultures of transformed BL21(DE3)pLysS cells were set up overnight in LB (Miller formulation) containing ampicillin and chloramphenicol, and diluted 1:100 the morning after, in the same medium. Bacterial growth was monitored by recording the OD_{600} value of the culture, taking aliquots regularly and measuring their absorbance in clear polystyrene cuvettes (Fisherbrand, Loughborough, UK) with a UV-Vis spectrophotometer (Camspec, Leeds, UK). When the cells reached mid-log phase (OD_{600} ~0.5), they were induced to produce the desired protein by addition of 0.3 mM IPTG and incubation at the desired temperature with constant shaking. After induction, cells were centrifuged (4,500×*g*, 10 min, 4 °C) and the pellet was resuspended in *E. coli* washing buffer. They were then centrifuged again, and the pellet moved to -80 °C to aid protein release from the cells. The pellet was lysed in ice-cold *E. coli* lysis buffer, 1 mL per 50 mL of culture whence the pellet was derived, and briefly ultra-sonicated on ice in a pulsatile fashion, using a Vibra-Cell Ultrasonic Liquid Processor (Sonics, Newtown CT, USA). Triton X-100 was added to a final concentration of 1% (v/v), then the samples were centrifuged again (21,910×*g*, 10 min, 4 °C) and, thereafter, handled on ice at all times. The clarified supernatant (i.e. the protein extract) was diluted 1:1 in glycerol, and stored at -20 °C. The pellet was denatured with the addition of an equal volume of 2× SDS-PAGE sample buffer and also stored at -20 °C.

To assess the recombinant GST-protein yield, small volumes of protein extract (25, 50, 100, 200 µL) were diluted to a final volume of 1 mL in *E. coli* lysis buffer + 1% (v/v) Triton X-100. 25 µL of 50% (v/v) glutathione slurry (ThermoFisher, Waltham MA, USA), which had previously been washed 3 times in *E. coli* lysis buffer + 1% (v/v) Triton X-100, was then added. Each sample was incubated at 4 °C for 60-75 min with end-over-end rotation, to ensure homogeneous binding to the beads. The latter were then washed 3 times in 1 mL buffer, denatured in 12.5 µL 2× SDS-PAGE sample buffer, and analysed by SDS-PAGE and protein staining. The amount of protein produced was estimated by running the samples alongside defined amounts (1, 5, 10 µg) of BSA diluted in the same buffer.

2.6.2. Mammalian GST-fusion pulldown for mass-spectrometry

Thirty untreated, confluent 10-cm HUVEC dishes were harvested in 100 µL NP-40 lysis buffer each (**Section 2.4.1**) supplemented with the PhosSTOP inhibitors cocktail, then split in equal volume across two tubes. In parallel, glutathione agarose beads, washed in lysis buffer and treated as in **Section 2.6.1**, were incubated with 10 µL of protein lysate previously extracted from *E. coli* cells that had been induced to produce GST-alone protein (pGEX-4T-2 "empty" plasmid). These beads, thereby bound to control GST protein, were used to pre-clear the mammalian lysate, by briefly incubating half with each of the two HUVEC tubes. After such pre-clearing, the beads were discarded and the HUVEC lysates kept on ice.

In parallel, three 10-cm dishes of HEK 293T cells that had been PEI-transfected (**Section 2.2.4**) with either pWPXL-PCDH1_GSTICD construct, v1 or v2, were harvested 48 hours after transfection as described for the HUVEC. A 1:1 mixture was then created by merging the lysates from GST-ICDv1 and v2 transfected cells, lysed in the same volume. The mixture was incubated with 45 µL glutathione agarose slurry, to pull down the GST-fusion proteins; separately, more protein lysate from *E. coli* was also incubated with glutathione agarose, to pull down control, GST-alone protein. After 1 hour incubation, both supernatants were discarded and the beads washed three times.

Finally, these two beads-bound GST samples (GST-empty and GST-ICD mixture) were each incubated in one of the pre-cleared HUVEC lysate supernatant tubes for 1 hour, to pull down endothelial interacting partners. Beads were then washed five times in lysis buffer and denatured in 40 µL, stored until SDS-PAGE.

2.6.3. Pulldown sample preparation for mass-spectrometry

Samples of GST pulldowns from HUVEC lysate, purified as per the previous section, were subjected to SDS-PAGE on a 4-12% Bis-Tris precast gel (Invitrogen/ThermoFisher, Waltham MA, USA). Once run, the gel was washed twice in H_2O, stained in Instant*Blue* for 1 hour, and briefly de-stained. The whole lane of either sample in the stained gel was cut into five pieces of equal height using sterile scalpels, and stored at -80 °C.

To de-stain the sample, each gel lane piece was chopped into minute fragments and incubated for 15 min in 30% (v/v) acetonitrile with vigorous agitation. The solid phase was then subjected to multiple 15 min incubations with agitation in 50% (v/v) acetonitrile, 25 mM NH_4HCO_3. Gel fragments were dehydrated in a vacuum centrifuge for 10 min, then proteins were reduced by incubation at 56 °C for 45 min in 10 mM DTT, 25 mM NH_4HCO_3. The solid phase was alkylated by submerging in 55 mM iodoacetamide, 25 mM NH_4HCO_3 for 45 min in the dark, and washed off afterwards for 10 min in 25 mM NH_4HCO_3 with shaking followed by 2×5 min washes in 50% (v/v) acetonitrile, 25 mM NH_4HCO_3. Gel fragments were again dehydrated in a vacuum centrifuge, then rehydrated for 1 h in a minimal volume of 12.5 ng/µL Trypsin Gold (#V528A, Promega, Southampton, UK) in NH_4HCO_3, from a 1 µg/mL stock in 50 mM acetic acid. Excess trypsin solution was discarded and gel fragments covered in 25 mM NH_4HCO_3 at 37 °C for 16 hours. Formic acid was added to [final] = 0.5% (v/v), and the solution was collected. To extract remaining peptides from the solid phase, the latter was further incubated twice in 50 µL 50% (v/v) acetonitrile, and once more in acetonitrile, with vigorous agitation, obtaining four aliquots from each original gel piece. In each case, the four aliquots were merged and dehydrated by vacuum centrifugation over 140 min, then resuspended in 10 µL 0.1% (v/v) formic acid. Samples were stored at -20 °C until analysis.

2.6.4. Proteomics analysis

The five samples prepared from each treatment (GST-control and GST-ICD) were analysed in two separate runs, using roughly half the volume each time. Mass spectrometry was carried out on a Q-Exactive HF Orbitrap instrument (ThermoFisher, Waltham MA, USA) by the Advanced Mass Spectrometry Facility of the University of Birmingham, who also carried out peptide assignment through the Andromeda search engine (Brasch et al., 2011). Keratin peptides were then removed from the GST-ICD list of hits as potential contaminants, together with peptides also found in the GST-control list of hits and all PCDH1-derived peptides. Furthermore, proteins for which only one peptide was detected were also disregarded.

2.7. Fluorescence-based Assays

2.7.1. Flow cytometry

Cells to be analysed by flow cytometry were washed three times in PBS and collected by incubation with 0.48 mM EDTA in PBS at 37 °C until detached, then centrifuged. Hereafter, cells were always handled on ice. The cell pellet was resuspended in FACS buffer and cells were manually counted, then centrifuged again and resuspended in a dilution of primary antibody (**Table 2.3**) in FACS buffer for 30 min, aiming for 1-2×10^6 cells/mL. Cells were pelleted, resuspended in FACS buffer, and pelleted again, then resuspended in a dilution of fluorophore-conjugated secondary antibody in FACS buffer for at least 20 min in the dark. Cells were filtered through a 50-µm nylon mesh (Celltrics, Sysmex, Norderstedt, Germany), and analysed on a CyAn ADP flow cytometer (Beckman Coulter, Brea CA, USA), rejecting cell doublets/aggregates by their larger forward scatter width:height ratio.

2.7.2. Immunofluorescence

13 mm-diameter glass coverslips were rinsed in 1 M HCl overnight, then washed in 70% (v/v) EtOH, and in three separate, large H_2O containers, then deposited onto a 10-cm dish. Here they were coated in appropriate protein: 0.1% (w/v) gelatin in H_2O for 30 min for HUVEC, 50 µg/mL poly-lysine in H_2O for 2 h otherwise, with gentle rocking. Coverslips were briefly rinsed in H_2O and then deposited onto a paper tissue, air dried, and sterilised by UV irradiation for 2 h, then placed inside tissue-culture plates of desired size. These were kept at 4 °C until usage for a maximum of 2 weeks.

Cells were plated onto coverslips and grown for the desired amount of time, optionally treated as per experimental needs. Henceforth, all PBS-based buffers included 1 mM Ca^{2+} and 500 µM Mg^{2+} to minimise cell detachment from the coverslips. These were rinsed twice in PBS, then fixed in warm 10% formalin-saline at 37 °C for 10 min. After three washes in PBS, coverslips were quenched in 50 mM NH_4Cl in PBS for 10 min and rinsed off twice in PBS afterwards. Permeabilisation, if necessary, was performed for 4 min on a drop of 0.1% (v/v) Triton X-100 in PBS, placed on a strip of Parafilm, followed by two rinses in PBS. Coverslips were blocked in IF blocking buffer for 30-60 min, then incubated overnight at 4 °C in a dilution of primary antibody in IF blocking buffer, in a moistened chamber. Incubations happened in the dark hereafter. After three washes in IF blocking buffer, cells were incubated 1 h in fluorophore-conjugated secondary antibody dilution in IF blocking buffer, and rinsed off twice in IF blocking buffer. If nuclear staining was required, the coverslips were incubated 5 min in 2 µg/mL DAPI in PBS, rinsed off twice in IF blocking buffer. Finally, coverslips were washed once in PBS, twice in H_2O, and deposited face-down onto a glass slide, on a drop of ProLong mounting medium. Slides were stored in the dark for 48 h before imaging on a Leica DM6000 B epifluorescence microscope fitted with a 40× oil-immersion Plan Apo objective (1.25 NA), and a mercury epifluorescence light source with appropriate excitation/emission filters set. Data was visualised and analysed in with the *ImageJ* software, as described previously (**Section 2.3**).

2.7.3. Proximity ligation assay

800,000 HaCaT cells were plated into 6-cm dishes, incubated for 24 hours, then transduced with PCDH1 virions (as per **Section 2.2.5**). After 24 further hours, the cells were trypsinised and plated onto 6-well-plates (400,000 cells/well) with poly-lysine-coated, 13-mm coverslips in them (**Section 2.7.2**), using cDMEM without phenol red to reduce autofluorescence. After 48 hours, coverslips were washed, fixed, quenched, and permeabilised as per the regular immunofluorescence protocol (**Section 2.7.2**). The coverslips were henceforth treated with the Duolink In Situ Red Starter Kit Mouse/Rabbit (Merck, Darmstadt, Germany), as per the manufacturer's instructions. Primary antibodies used are to be found in **Table 2.3**, identified by the “PLA” tag, and were used on Parafilm overnight as per the regular immunofluorescence protocol. Annealing, ligation, and amplification of PLA probes, as well as all washes, were carried out as per the kit's instructions, in a humidity chamber that consisted of a plastic tip box with wet tissues at the bottom and plastic pipette tips as vertical supports for the coverslips. Coverslips were placed on glass slides resting on one drop of supplied mounting medium, sealed in place with clear nail varnish, and imaged as per the regular immunofluorescence protocol.

2.7.4. Whole-mount mouse embryo vasculature staining, and clearing

The procedure that follows is based on the iDISCO+ 2016 protocol (https://idisco.info/, Renier et al. (2014)), adapted to visualise the intact vasculature of mouse embryos. Antibodies used are identified by the “LSFM” tag in **Table 2.3**. Uteruses from dams euthanised at E13.5 by cervical dislocation were collected into ice-cold PBS by Biomedical Services Unit staff.

Embryos were isolated using a combination of forceps and scissors while being kept submerged in cold PBS, then fixed in 10% formalin-saline at 4 °C overnight. They were moved to room temperature for 1 h, then washed in PBS with shaking 3×30 min.

Methanol-based sample pre-treatment: To dehydrate, embryos were incubated in an increasing MeOH/H_2O series (v/v): 20%, 40%, 60%, 80%, 100%, 100%, 1 h each. Embryos, chilled to 4 °C, were incubated overnight at room temperature in 33% (v/v) MeOH in DCM with shaking. After two washes in MeOH, samples chilled to 4 °C were bleached in freshly made 5% (v/v) H_2O_2 in MeOH, overnight at 4 °C. Rehydration followed: 1-hour washes in a decreasing series of MeOH/H_2O (v/v): 80%, 60%, 40%, 20%, PBS.

Immunolabeling step: after 2×1 h washes in PTx.2, samples were incubated 1.5 days in iDISCO permeabilization solution at 37 °C, followed by 1.5 days in iDISCO blocking solution at 37 °C. CD31 antibody incubation was in 5% (v/v) DMSO, 3% (v/v) horse serum in PTwH for 3 days at 37 °C. Samples were washed at room temperature in PTwH for 5 times until the next day, when they were incubated at 37 °C for 3 days in AF647-conjugated secondary antibody diluted in 3% (v/v) horse serum in PTwH. All incubations hereafter were carried out in the dark. Five PTwH washes at room temperature were carried out across the following 24 hours.

Immunolabeling was followed by dehydration, again achieved in an increasing series of MeOH/H_2O washes (v/v): 20%, 40%, 60%, 80%, 100%, 100%, 1 h each, with the option of prolonging the last wash to overnight if required. After 3 h in 33% (v/v) MeOH in DCM with shaking, samples were incubated twice in DCM for 15 min with shaking, and finally stored in dibenzyl ether. Dr Victoria Heath carried out these final dehydration steps for two of the embryos.

2.7.5. Light-sheet fluorescence microscopy imaging of mouse embryos

Light-sheet imaging of whole, cleared mouse embryos was carried out using an UltraMicroscope II (Miltenyi Biotec, Bergisch Gladbach, Germany) equipped with Olympus MX10 zoom body (0.8× magnification) and a 2× air objective (0.5 NA) fitted with a 5.7 mm-working distance dipping cap (0.153× magnification). Embryos were imaged in ethyl cinnamate positioned resting on one side, so as to be illuminated sagittally. Whole sample *z*-stacks were captured with a step size of 2 μm, using dual sided illumination (6 sheets in total) with 639 nm laser excitation (70 mW laser diode), resulting in approximately 2,500 planes per stack. Fluorescence emission was detected by a sCMOS camera (Andor Zyla 5.5, Oxford Instruments Technology, Shanghai, China) with an exposure time of 200 ms through a 680/30 single band pass filter (Semrock, Lake Forest IL, USA). Data was rendered in three dimensions with the *Vision4D* software 4.3.0 (arivis, Munich, Germany), or visualised in two dimensions in *FIJI* (Schindelin et al., 2012).

2.7.6. Two-dimensional vasculature analysis of light-sheet data

Analysis was undertaken, blinded to genotype, on maximum intensity projections (MIP) along the *z* axis, created on *FIJI*. Organ arrangement depended on the precise physical positioning of each embryo at the time of death, so projections were created by locating the same anatomical landmarks in each embryo to use as reference points, rather than by using the same starting and ending slice in all. For visualisation purposes, projections were created using an appropriate number of *z*-planes, whereas in the case of automated region of interest (ROI) analysis for vascular bed branching characterisation, the same total number of *z*-planes per MIP was used, to ensure consistency. After automatic brightness/contrast adjustment, uneven background was rendered uniform by applying the “Rolling Ball Background Subtraction” plugin, with radius = 1,000 px. Each MIP was then segmented using the “Find a tree” function of the “Angiogenesis

Analyzer" plugin. Information of the network thus obtained was then retrieved with the "Analyze Skeleton (2D/3D)" function; the number of loops was identified by automatically colouring in each section with the "Fill" function of Microsoft Paint, and manually counting the number of filled-in sections. In the case of aortic arch luminal thickness measurement, projections were created using an appropriate number of *z*-planes that allowed identification of the required anatomical features, on a per-embryo basis; measurement was carried out using the "Straight Line" tool.

2.7.7. Three-dimensional vasculature analysis of light-sheet data

Analysis was undertaken, blinded to genotype, on three-dimensional ROIs, using the built-in Analysis Pipeline panel in the *Vision4D* software. Pipelines consisted of initial denoising (Discrete Gaussian method) and background correction (Automatic method, with Correction option set to preserve bright objects) steps, followed by segmentation by the Blob Finder algorithm (Split sensitivity = 0%). Other settings for each step depended on the ROI selected: Denoising and background correction diameters = 4 µm, blob finder blur diameter = 12 µm, probability threshold 5% were selected for the medullar brain ROI; denoising diameter = 25 µm, background correction diameter = 5 µm, blob finder blur diameter = 25 µm, probability threshold 3-5% were selected for the ROI around the trunk. The total object volume and surface areas were identified in the Objects Table thus generated.

CHAPTER 3: STUDIES OF PCDH1 FUNCTION USING *IN VITRO* MODELS OF ANGIOGENESIS

3.1. Introduction

The aim of the experiments presented in this chapter was to examine whether PCDH1 plays a role in angiogenesis, using primary human umbilical vein endothelial cells (HUVEC) as the main *in vitro* model. Because PCDH1 is expressed in blood vessels (Favre et al., 2003; Redies et al., 2008), and because many neuronal guidance proteins are co-opted as angiogenic sensors by blood vessels (**Section 1.1.4**), it was reasoned that PCDH1 might be involved in angiogenesis. To explore this possibility, the experiments presented here made extensive use of siRNA duplexes to knock down PCDH1. PCDH1 expression was first confirmed in different HUVEC isolates by PCR, immunoblotting, immunofluorescence, and flow cytometry. The involvement of PCDH1 in angiogenesis was then explored by means of various *in vitro* assays that mimic different stages of the process. To this end, PCDH1 protein levels were reduced exploiting short interfering RNA (siRNA) technology. Experiments included: plating cells on substrates that stimulate intercellular connections, monitoring cell migration towards growth factors or other cells, and assessing the protrusions formed by a spheroid of cells embedded in a solidified matrix. Different *PCDH1*-targeting duplexes each resulted in different outcomes in most assays, all of which were lost when using many *PCDH1*-targeting duplexes together as a mixture. Microarray experiments therefore analysed the transcriptome of siRNA-treated HUVEC, to study off-target transcriptomic changes elicited by individual duplexes.

3.2. PCDH1 is expressed in HUVEC

In order to study the functions of PCDH1 in angiogenesis, the first step was to determine whether *PCDH1* transcript levels are detectable in HUVEC, and which of the multiple splice variants reported so far (Koning, Sayers, et al., 2012) are actively transcribed in this setting. To this end, RNA was isolated from different HUVEC preparations, taking care to digest any genomic DNA potentially carried over. The RNA was then used as a template to synthesise total cellular cDNA, which was subjected to PCR using oligos that differentially annealed known *PCDH1* transcripts (**Table 2.12**, **Figure 3.1**). The designed primers spanned exon-exon junctions, when possible, to avoid the chance of genomic DNA amplification altogether. PCR products thus obtained were analysed on agarose-TAE gels, summarised in **Figure 3.2**. Most reported PCDH1 mRNAs were amplified, with the exception of PCDH1-207 (for which the whole gel shows no bands) and of PCDH1v3. Negative control lanes (lanes 4 to 7) were empty in all cases, confirming only cDNA generated from mRNA transcripts (and not from genomic DNA) was amplified. PCDH1v1 was the most abundant of all amplified fragments, based on relative band brightness, but precise relative expression analysis would require a quantitative-PCR approach. PCDH1v3 shows a very prominent band appearing at around 200 bp, which is not the expected size; this band might have arisen because the oligos annealed some other mRNA sequence (or transcript). Though it appears quite faintly in the gels, PCDH1v4 is present and is not recognised by the PCDH1 antibody used, as the isoform lacks the first EC domains. The same can be said for the very short transcript PCDH1-208. Importantly PCDH1v4, sharing the same 3’ UTR as PCDHv1 (and PCDH1v3), might potentially be amplified by the same primers that recognise that major transcript. However, as can be inferred from **Figure 3.2**, the levels of PCDH1v4 transcript were remarkably low with respect to those of PCDH1v1, even after 35 cycles of PCR amplification, suggesting most of the signal from primer pair WV003+WV004 is due to PCDHv1. Given that both PCDH1v1 and PCDH1v2 are actively transcribed, the conclusion is that both versions of the intracellular domain (ICDv1 and ICDv2) are present in HUVEC.

To confirm that detectable mRNA expression corresponded to detectable levels of PCDH1 protein, flow cytometry experiments were set up with an anti-PCDH1 antibody that recognises an epitope in the extracellular domain (ECD). These experiments were carried out using both

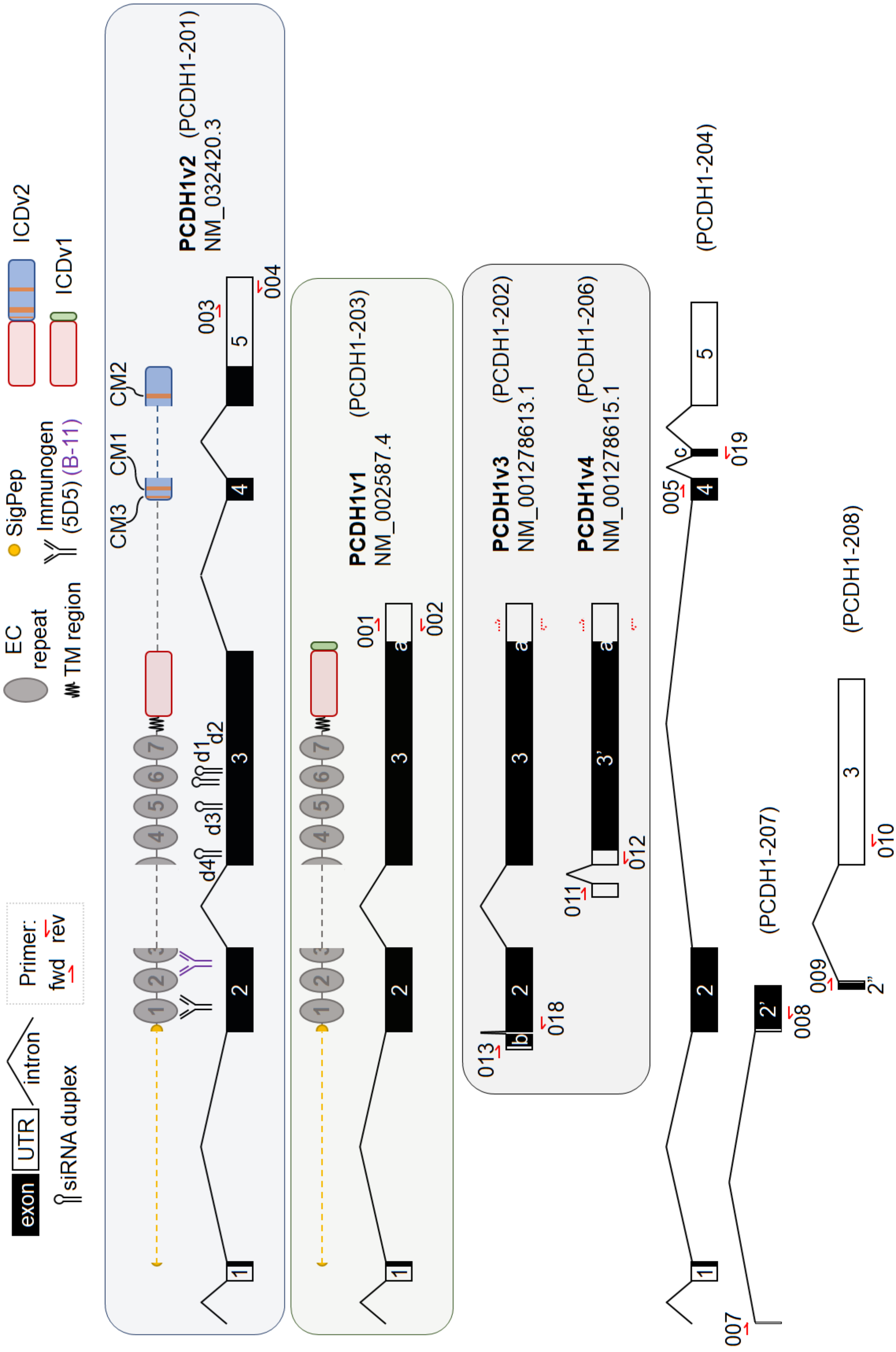

Figure 3.1. RT-PCR panel to identify endothelial Hs *PCDH1* transcripts.
(Caption overleaf)

(Continued from previous page)
Sequences were retrieved from the *NCBI* database (NM_*x*), or *Ensembl* (PCDH1-20*x*) if not present in the former. Exons are drawn to scale to each other, introns are drawn to scale to each other. Shorter exon variants are given apostrophes. Primers used (**Table 2.12**) are not drawn to scale, and their number is written next to their symbol, omitting the initial “WV”. Dotted arrows represent possible annealing sites of primers on transcripts other than the one intended. siRNA duplexes (**Table 2.8**) are not drawn to scale, but are similarly placed where they anneal. SigPep = signal peptide, CM = conserved motif.

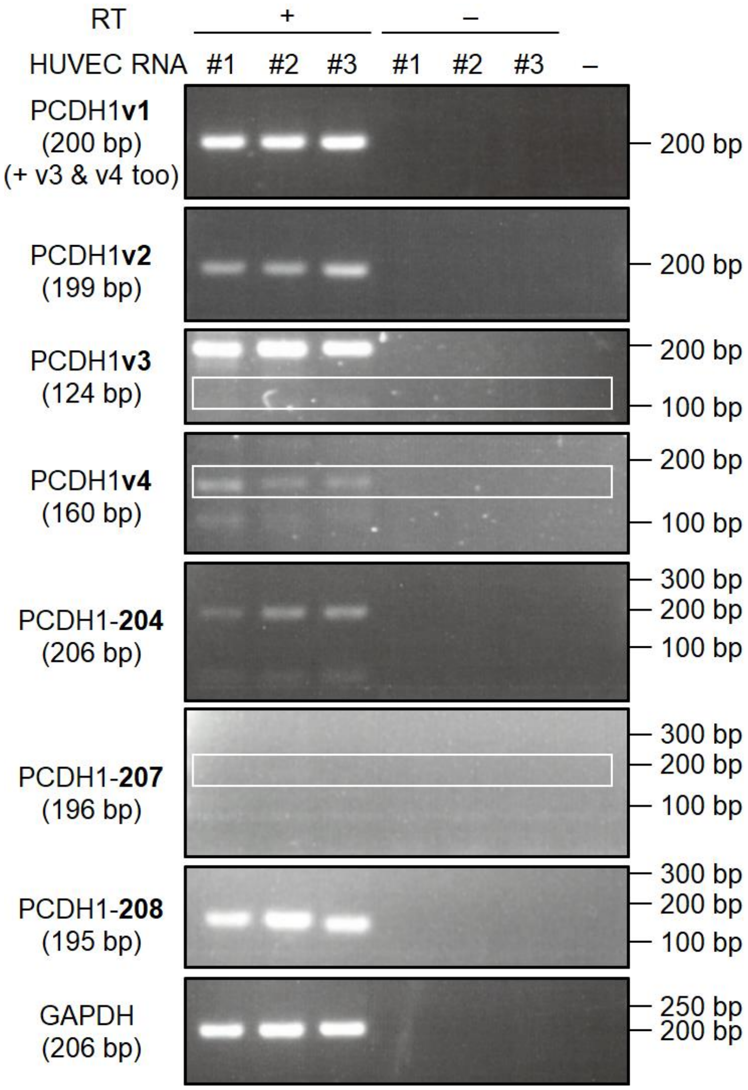

Figure 3.2. Assessing different PCDH1 isoforms in HUVEC.
Total RNA was isolated and reverse transcribed from three different HUVEC preparations (#1-3 lanes), and RNase treated. Reverse-transcription reactions were carried out both with RT enzyme (+ lanes) and without (– lanes). The cDNA was then probed with various primer pairs in separate PCR experiments. 35 cycles were run for each *PCDH1* primer pair, 25 cycles for GAPDH. PCR products were then separated by gel electrophoresis on 2% (w/v) agarose-TAE gels. A negative control was set up in each case (rightmost lane), with H_2O instead of cDNA. The expected product size from each primer pair is given in brackets, and the area where it would appear on the gel is marked in a white box if multiple/no bands are present, to aid interpretation.

HUVEC and HaCaT, a human keratinocyte cell line (Boukamp et al., 1988) with easily detectable levels of PCDH1. Indeed, in these conditions, the presence of PCDH1 was detected endogenously on the surface of both HaCaT cells (**Figure 3.3A**) and HUVEC (**Figure 3.3B**), as assessed by an increase in mean fluorescence from cells treated to isotype control IgG to cells treated to anti-PCDH1 antibody. The latter was also used to probe the subcellular localisation of PCDH1 in immunofluorescence experiments (**Figure 3.3C**), which showed endogenous PCDH1 localising, as expected, in the proximity of the cell membrane in HUVEC monolayers grown on gelatin. These experiments confirm that PCDH1 is detectably expressed in HUVEC, which served as the basis for the assays in this chapter.

3.3. siRNA duplexes reduce PCDH1 levels in HUVEC

To assess PCDH1 function in angiogenesis, a useful approach is to reduce the protein's levels by siRNA-mediated knockdown, and engage the cells in assays that model different stages of the angiogenic process. Any differences observed between these cells and cells treated to a negative control siRNA (NCD) would be due to the reduction in cellular PCDH1 levels. *PCDH1*-targeting duplexes are commercially available, however an appropriate concentration to be used is first needed to be evaluated, in order to minimise any potential off-target effects. To this end, HUVEC were transfected with a range of duplex concentrations, attained by means of serial dilutions, between 50 nM and 80 pM. Two, separate duplexes were used, siRNA-1 and siRNA-2, each independently targeting all major *PCDH1* transcripts (**Figure 3.1**). The cells were harvested 48 h post transfection, and the protein lysate was analysed by SDS-PAGE under reducing conditions, followed by immunoblotting. The same membrane was cut appropriately, allowing the same lysate to be probed for PCDH1 and α-tubulin, to ensure even loading and enable quantification, an approach routinely employed throughout the thesis. The results are shown in **Figure 3.4A**: as compared to NCD-treated cells, PCDH1 levels were decreased.

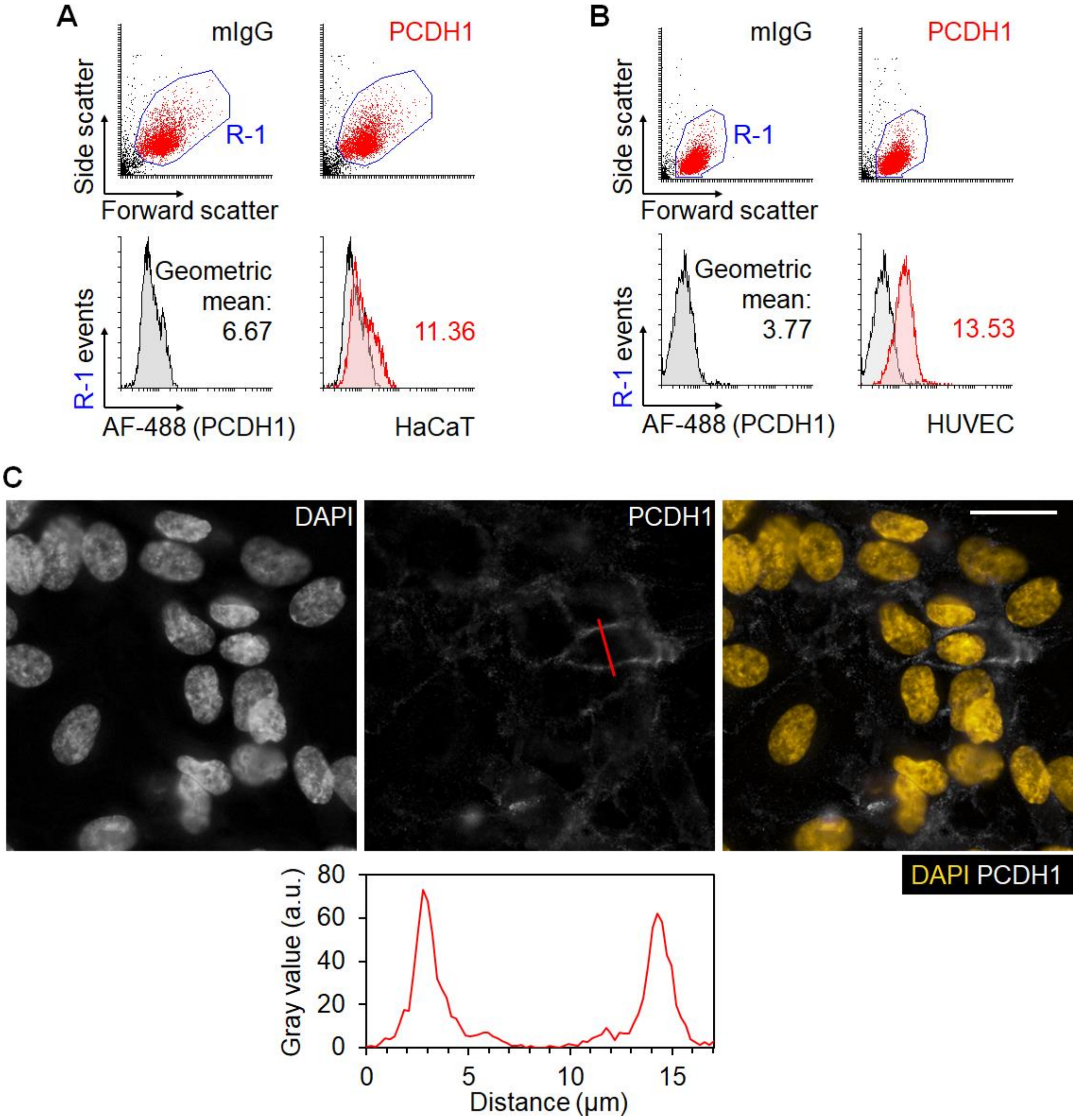

Figure 3.3. Endogenous PCDH1 localises to the plasma membrane of human cell lines and primary cells.

A. Flow cytometry analysis of HaCaT cells incubated with whole mouse IgG or anti-PCDH1 antibody, detected with anti-mouse-AF488. All histograms are gated to their R-1 region.

B. Flow cytometry analysis of a HUVEC isolate, treated as in **A**.

C. Immunofluorescence of a HUVEC isolate grown on a glass coverslip for 24 h. The fixed monolayer was treated with anti-PCDH1 antibody, and visualised by an AF488-conjugate on an epifluorescence microscope. Contrast was improved using the *ImageJ* software, with the Subtract Background plugin set to a rolling ball radius = 100 px (23.04 µm). The histogram below the images shows the pixel intensity value along the red bar, measured with the Plot Profile function of *ImageJ*. White scalebar = 25 µm.

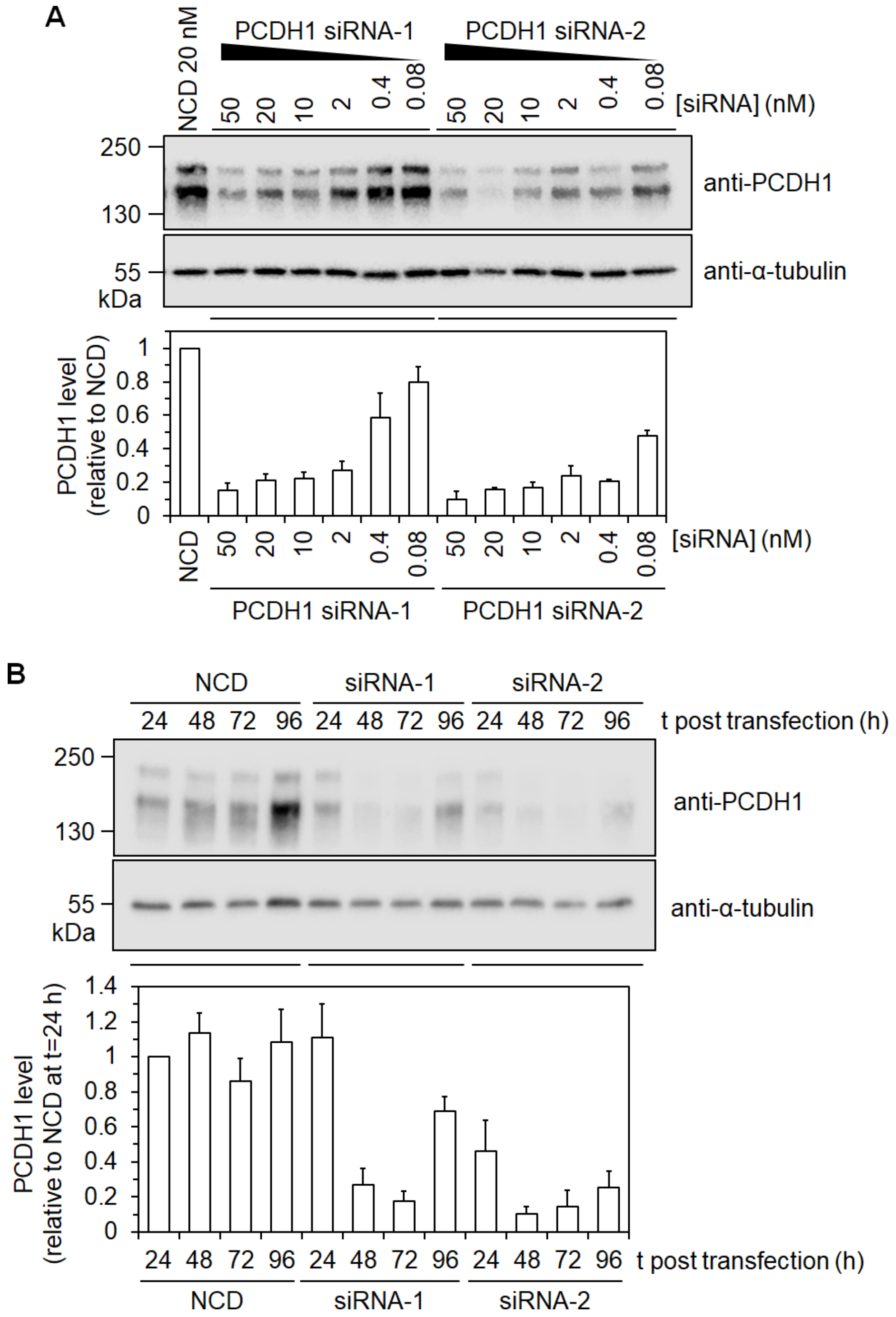

Figure 3.4. siRNA transfection temporarily knocks down PCDH1.
A. HUVEC were transfected with given amounts of *PCDH1*-targeting siRNA duplex, and harvested after 48 h. Protein lysates were separated by SDS-PAGE and immunoblotted. Below, LI-COR analysis showing the average PCDH1 signal from three replicates. Error bars = s.e.m.
B. Protein lysates of HUVEC transfected with 20 nM siRNA duplexes and harvested at different timepoints. Below, LI-COR analysis showing the average PCDH1 signal from three replicates. Error bars = s.e.m.

Specifically, they decreased with increasing concentrations of either of the two duplexes, which targeted the PCDH1 transcripts in two different regions. Reductions of PCDH1 levels by 10-80% across the range of dilutions were achieved, confirming the duplexes were effective even at very low concentrations. siRNA-2 seemed more potent than siRNA-1, as even at 80 pM concentration it achieved 50% PCDH1 reduction and, in general, it resulted in lower levels of PCDH1 at a given concentration. It was evident that PCDH1 appeared as two bands: this was not surprising, as all transcripts share the epitope for the monoclonal antibody used for immunoblotting (**Figure 3.1**). We propose these two bands corresponded to the two main isoforms of the protein, PCDH1v1 and PCDHv2, and appear in the region of the respective predicted molecular weight given their transcript length. Based on these data, the siRNA duplexes were delivered at 20 nM in most ensuing experiments, unless otherwise stated, as a compromise between minimising off-target effects and obtaining a robust PCDH1 knockdown. In fact, to assess the duration of the effect and confirm a good timepoint to start the assays, PCDH1 levels after knockdown in HUVEC were then monitored over time. Cells were transfected with the same siRNA duplexes, and protein samples harvested after 1 to 4 days. As can be seen in **Figure 3.4B**, maximal knockdown of PCDH1 (80-90%) happened between 48 and 72 hours after transfection and, again, siRNA-2 appeared somewhat more potent than siRNA-1. Bearing this in mind, most short-term assays were started 48 hours post transfection, allowing them to take place within the window of minimal PCDH1 levels. Knockdown levels were also assessed in live cells, by means of flow cytometry experiments probing endogenous surface expression 48 hours post transfection: protein levels appeared to decrease on both HaCaT cells (**Figure 3.5A**,**B**) and HUVEC (**Figure 3.5C**,**D**), as assessed by a reduction in surface fluorescence in siRNA-treated cells with respect to NCD-treated cells.

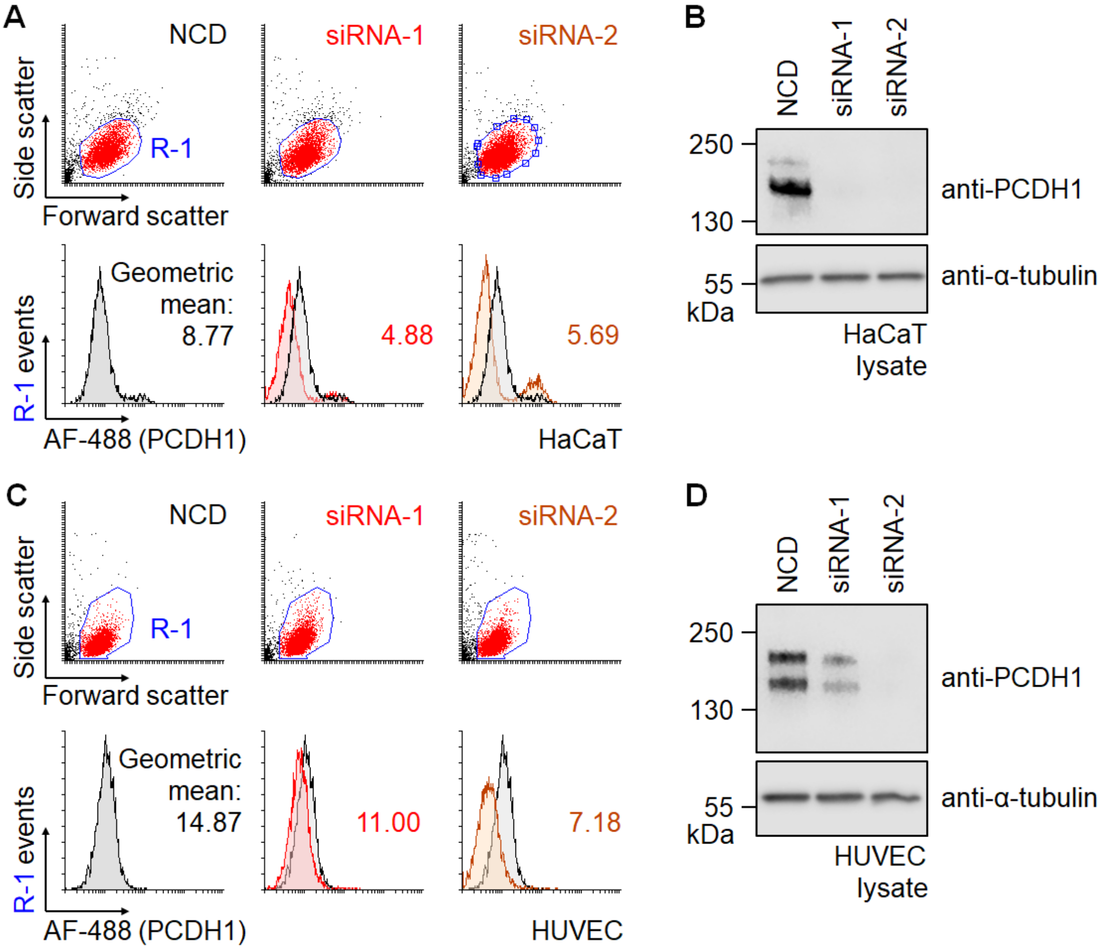

Figure 3.5. Flow cytometry visualises endogenous PCDH1 knockdown in different cell types.

A. Flow cytometry analysis of HaCaT cells transfected with 20 nM siRNA duplexes (NCD or *PCDH1*-targeting) and collected 48 h after. The NCD histogram is overlayed onto all other histograms, gated to their R-1 region. Cells incubated with whole mouse IgG from a mock (no-plasmid) transfection were used as unstained sample, to obtain a fluorescence signal baseline from the cytometer.

B. An immunoblot showing PCDH1 levels in total protein lysate from a separate aliquot of cells that underwent the treatment in **A**.

C. Flow cytometry analysis of a HUVEC isolate that underwent the same treatment as in **A**. Representative images from two repeats.

D. An immunoblot showing PCDH1 levels in total protein lysate from a separate aliquot of cells that underwent the treatment in **C**.

3.4. siRNA-mediated PCDH1 knockdown can be circumvented by synonymous substitution

To confirm that the observed levels of protein knockdown were due to targeted transcript degradation, lentiviral plasmids were assembled encoding myc-tagged versions of the two main *PCDH1* transcripts, harbouring silent mutations in the region annealed by siRNA-2. These constructs would also allow not only to selectively overexpress one isoform with functionally unaltered amino acid sequence, but could also be used to confirm the outcomes observed in any *in vitro* assays as being specifically due to PCDH1 knockdown, by allowing rescuing of any phenotype by means of reinstating PCDH1 expression. These constructs also resulted in proportional expression of free cytosolic EGFP as a marker of successful transduction, as PCDH1 and EGFP were part of the same transcript, separated by a short sequence encoding a self-cleaving viral peptide. Lentiviral transduction of HUVEC with these constructs was therefore carried out, followed by PCDH1 knockdown as previously. As expected, such engineered PCDH1 expression withstood knockdown by siRNA-2, as probed by flow cytometry (**Figure 3.6A**): the top-right quadrants in the plots, showing transduced (EGFP) and stained (PCDH1) cells, presented roughly the same population whether cells were treated with NCD or with siRNA-2. This appeared to recapitulate when protein levels were assessed by immunoblotting (**Figure 3.6B**), with PCDH1 levels unchanged as assessed with either anti-PCDH1 or anti-myc antibodies. This held for both the short version (PCDH1v1) and long version (PCDH1v2) of the protein, as they only differ in regions not targeted by either duplex. Conversely, these analyses confirm that knockdown performed by siRNA-1 was still effective at reducing PCDH1 levels, with flow cytometry analysis showing the percentage of cells in the top-right quadrant reduced by 80-90% with respect to NCD upon knockdown: this was expected given that the virions assembled for transduction were only mutated in the region targeted by

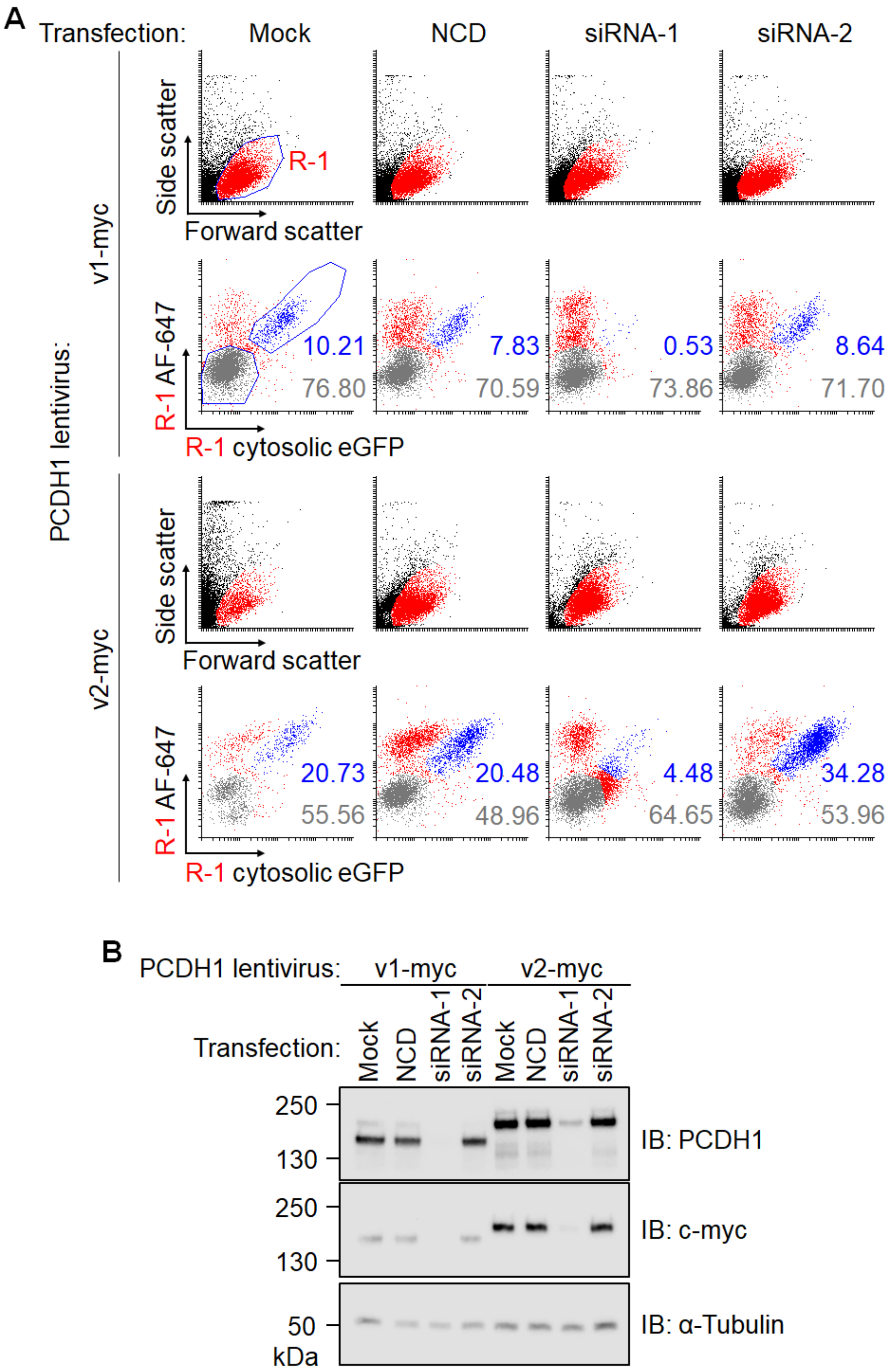

Figure 3.6. Transduced mutant PCDH1 withstands knockdown in HUVEC.
A. Flow cytometry analysis of HUVEC infected with a lentivirus encoding a version of PCDH1 silently-mutated to avoid targeting by PCDH1 siRNA-2. 48 hours after siRNA transfection, cells were detached, then incubated with anti-PCDH1 and AF647-conjugate antibodies. Free, cytosolic EGFP marks transduction. The percentages of double-positive (blue) and double-negative (grey) cells are written on the plots. Representative images from two repeats.
B. Immunoblot of a separate aliquot of cells that underwent the labelling treatment in **A**, harvested and lysed afterwards instead.

siRNA-2. These observations were confirmed by assessment of PCDH1 staining in fixed HUVEC monolayers grown on gelatin (**Figure 3.7**): transduced cells treated with siRNA-2 showed membrane-localised PCDH1, as assessed by anti-myc immunolabeling. Such signal was seemingly unchanged across PCDH1v1- and PCDH1v2-transduced cells, and between cells treated with NCD or siRNA-2, but was virtually absent for all cells treated with siRNA-1. Furthermore, the PCDH1 signal appeared particularly reinforced at membrane-membrane interfaces, with weaker staining in areas of cells not in contact with other cells. These experiments confirmed that PCDH1 could confidently and selectively be targeted for knockdown in HUVEC using these siRNA duplexes, as well as enabling select isoform overexpression and, potentially, validate the following assays.

3.5. PCDH1 knockdown impairs *in vitro* connectivity between HUVEC

To test whether PCDH1 is involved in the tubular differentiation stage of angiogenesis, a commonly employed functional *in vitro* assay was undertaken, involving HUVEC forming networks of intercellular tubules when deposited on a basement membrane preparation, Matrigel, that is purified from Engelbreth-Holm-Swarm (EHS) murine sarcoma cells. siRNA-mediated knockdown of PCDH1 was performed on HUVEC, then these cells were seeded onto Matrigel-coated plates, and images taken after 12 and 24 hours were analysed to count the number of fully formed loops within the networks that arose (**Figure 3.8A**). The data clearly showed that knockdown (**Figure 3.8B**) reduced network formation on Matrigel in HUVEC, with both duplexes achieving 80-90% reduction in loop numbers after 12 hours (**Figure 3.8C**), and over 90% after 24 hours (**Figure 3.8D**). Such analysis suggests that PCDH1 is involved in the differentiation stage of tubulogenesis in HUVEC, as modelled by this assay.

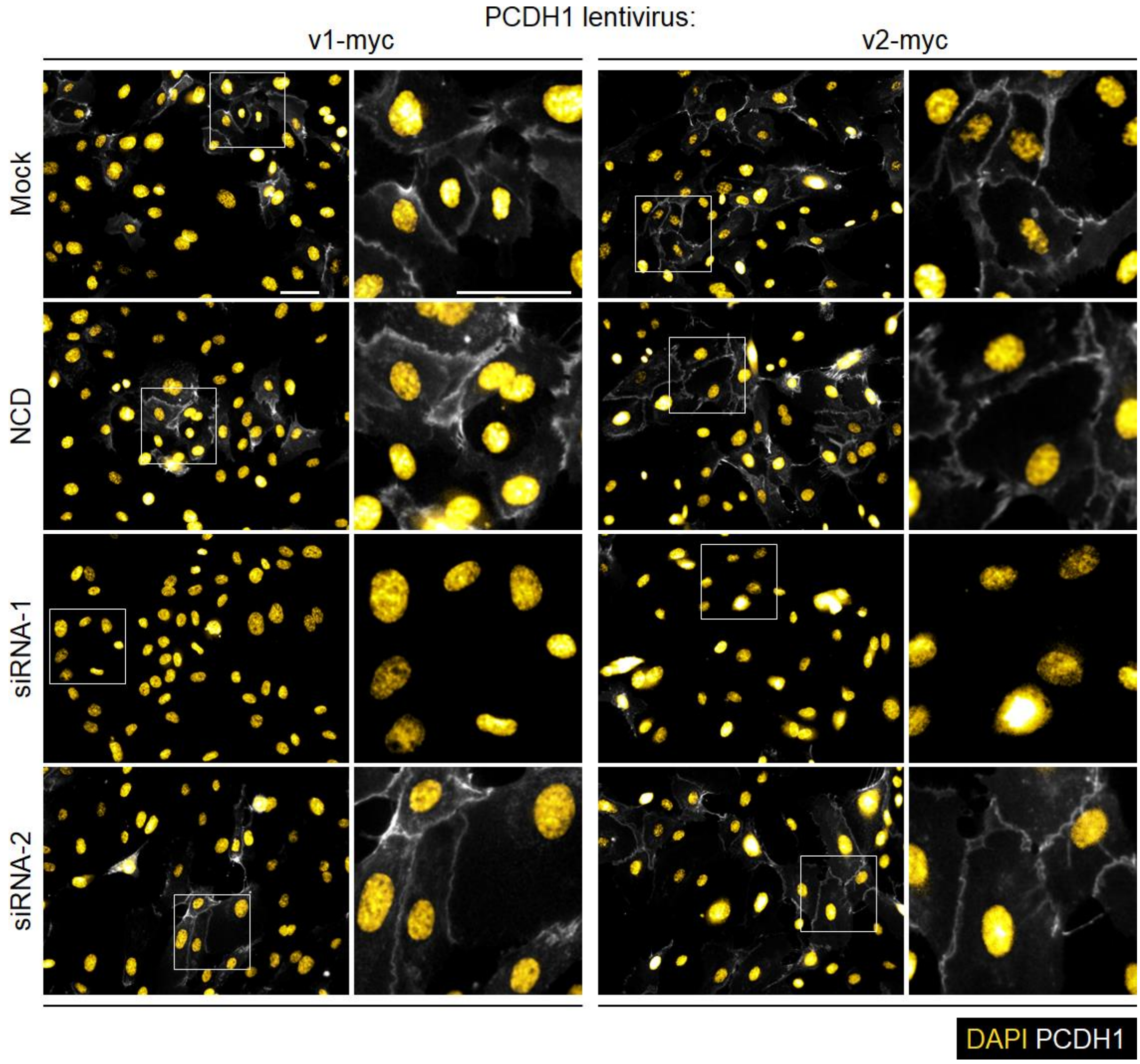

Figure 3.7. Transduced mutant PCDH1 resists knockdown, localises to the plasma membrane.
Immunofluorescence of HUVEC infected with a lentivirus encoding a version of PCDH1 silently-mutated to avoid targeting by PCDH1 siRNA-2. 48 hours after siRNA transfection, cells were collected and plated on glass coverslips. The monolayer was fixed after 24 h, and treated with anti-PCDH1 antibody, visualised by an AF647-conjugate on an epifluorescence microscope. Representative images from two repeats. White scalebars = 50 μm.

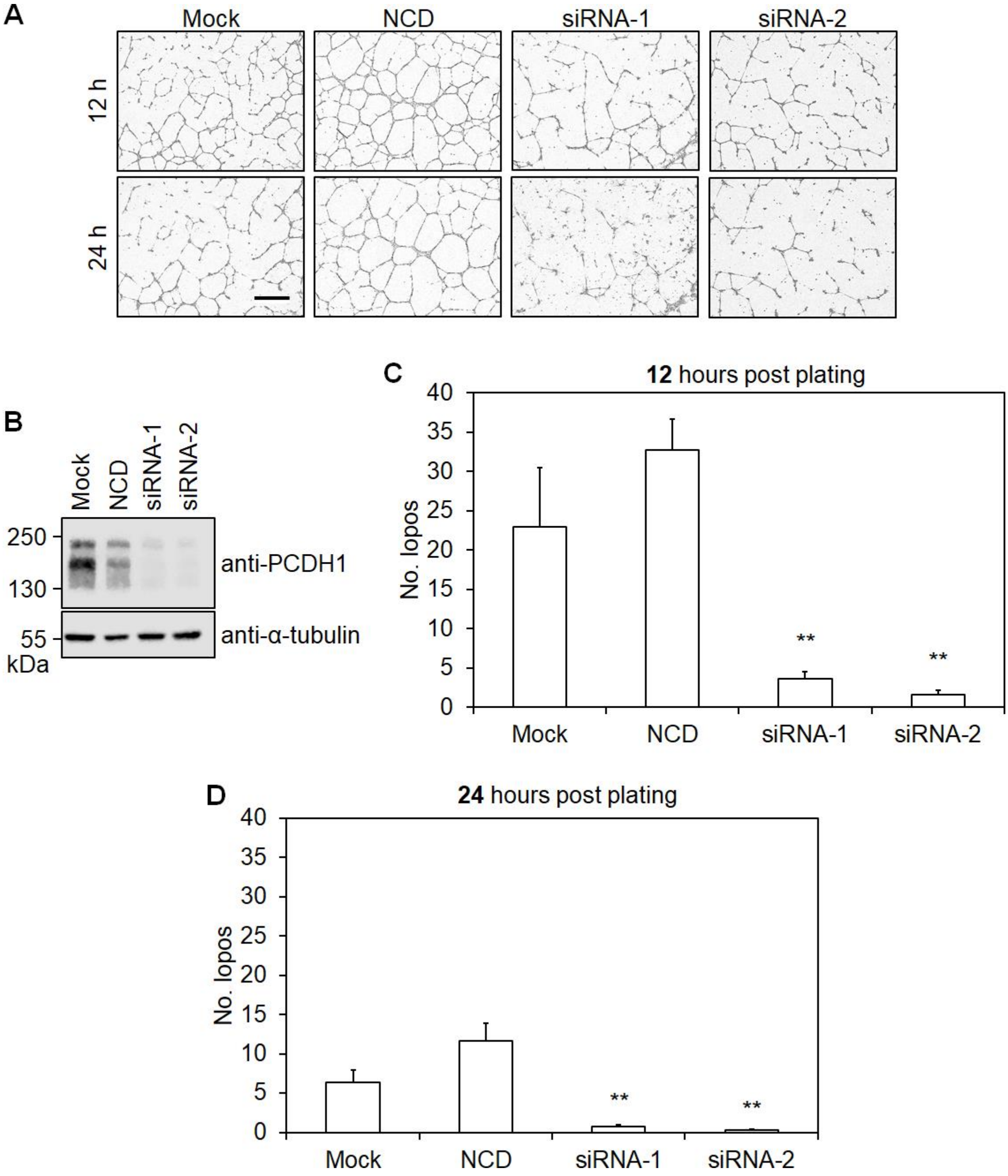

Figure 3.8. PCDH1 knockdown impairs HUVEC connectivity on Matrigel.

A. Endothelial networks formed by HUVEC plated on Matrigel, 48 h after siRNA transfection. Representative images from three repeats, showing the same field of view at two timepoints after plating. Scalebar = 800 µm.

B. Immunoblot confirming PCDH1 knockdown in protein lysate of a separate aliquot of HUVEC used in **A**. Representative images from three repeats.

C. Analysis of mean loop number per field of view, as measured by the Angiogenesis Analyzer plugin for the *ImageJ* software. Stars represent statistical significance with respect to NCD treatment (** = p<0.01), as assessed by one-way ANoVA test followed by Tukey's post-hoc test. Error bars = s.e.m.

D. Data analysis for the t = 24 h post plating timepoint of the experiments described in **C**.

3.6. PCDH1 knockdown impairs *in vitro* motility of HUVEC

To model endothelial cell motility *in vitro*, a scratch-wound assay was chosen: this involved manually inflicting a scratch to an established HUVEC monolayer, and monitoring the time taken by the cells to reseal it. When this was performed to HUVEC that had undergone PCDH1 knockdown (**Figure 3.9A**), the surface area still scratched after 15 hours was ~12% larger for cells treated with siRNA-1 than it was in control conditions (**Figure 3.9C**), and 15% larger after 24 hours (**Figure 3.9D**), suggesting siRNA-1 treatment slowed cell migration. Incidentally, this meant that after 24 hours, cells treated with siRNA-1 had resealed the same surface area that control-treated cells had already resealed after 15 hours. On the other hand, siRNA-2 treatment did not seem to affect the amount of scratched area at either time, despite PCDH1 knockdown being as effective at the time of plating as that obtained *via* siRNA-1 (**Figure 3.9B**).

In a related but different *in vitro* assay exploring chemotactic motility, HUVEC that had undergone siRNA transfection were deprived of FBS for 1 hour, after which they were plated in the same conditions on top of a perforated plastic membrane. This created two separate but intercommunicating compartments, the top having HUVEC and growth medium with reduced serum content, the bottom having complete growth medium. After 5 hours, the bottom of the plastic membrane was imaged, and the number of cells that had transmigrated through its pores was counted. Control conditions revealed that HUVEC only transmigrated if there was a gradient of serum across the membrane (**Figure 3.10A,B**), as expected. Experimental conditions revealed that treatment with either *PCDH1* siRNA reduced the number of transmigrated cells by 25% on average (**Figure 3.10C,D**), albeit not in a statistically significant fashion on account of the baseline variation between experimental repeats. These two assays, taken together, suggested that the ability of HUVEC to follow chemotactic gradients was somewhat reduced upon loss of PCDH1.

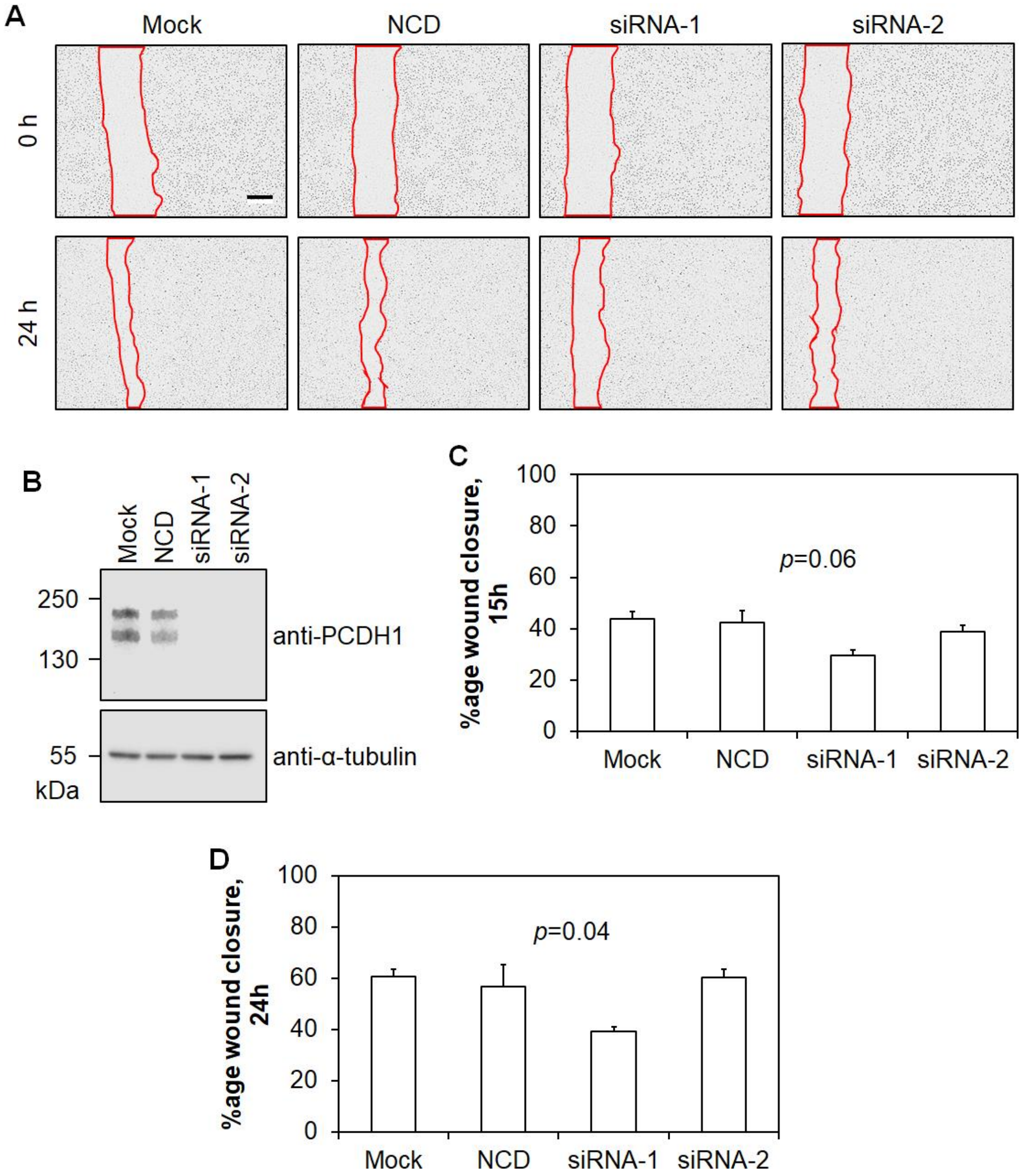

Figure 3.9. PCDH1 knockdown by siRNA-1 increases scratch-wound recovery time for HUVEC.

A. Wound recovery by HUVEC, scratched 48 h after siRNA transfection. Representative images from three repeats, showing the same field of view at the moment of scratching and 24 h afterwards. The scratched area, red, was outlined manually in the *ImageJ* software. Scalebar = 800 µm.

B. Immunoblot confirming PCDH1 knockdown in protein lysate of a separate aliquot of HUVEC used in **A**. Representative images from three repeats.

C. Analysis of mean scratch-wound recovery over 15 h. Each treatment is expressed as percentage of the area still scratched with respect to its originally scratched area at t = 0. Statistical significance was assessed by one-way ANoVA test, and post-hoc analysis revealed no significant difference between any treatment pairs. Error bars = s.e.m.

D. Data analysis for the t = 24 h post plating timepoint of the experiments described in **C**.

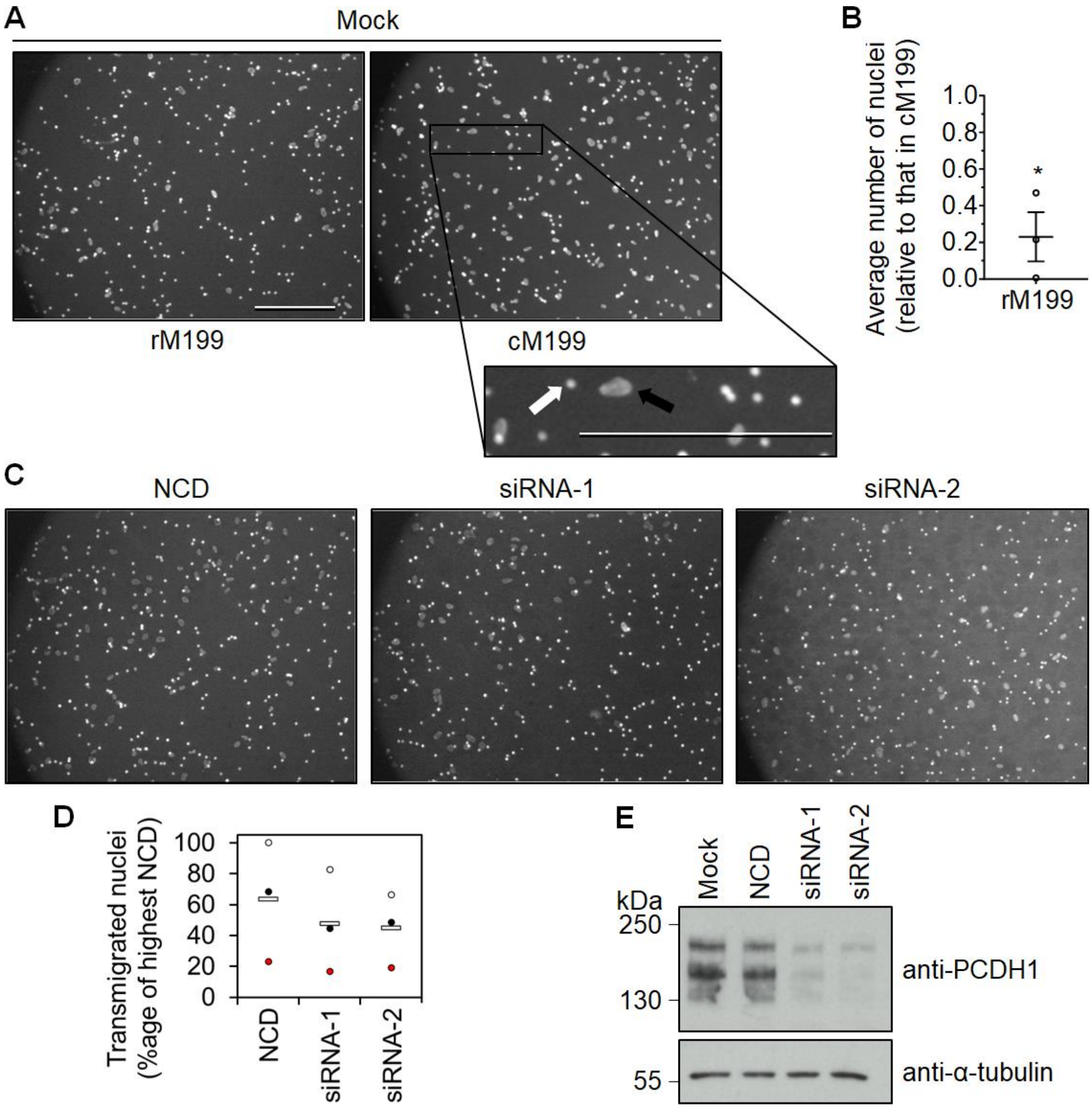

Figure 3.10. PCDH1 knockdown impairs chemotaxis through a porous membrane.

A. Bottom side of FluoroBlok membranes, where a mock-transfected HUVEC isolate was allowed to migrate for 5 h towards medium with 10% (cM199) or 1% (rM199) FBS, after 1 h starvation in rM199. The enlarged view shows the difference between membrane pores (white arrow) and DAPI-stained cell nuclei (black arrow). Representative images from three repeats, each of which was averaged across 15 such fields of view for analysis. Scalebars = 200 µm.

B. Analysis of the number of transmigrated nuclei in **A** as a percentage relative to those transmigrated towards cM199. The star represents statistical significance (* = $p<0.05$), as assessed by paired *t*-test conducted on the arcsine-transformed percentages. Bars = mean±s.e.m.

C. Bottom side of FluoroBlok membranes, where a siRNA-transfected HUVEC isolate was allowed to migrate for 5 h towards cM199, after 1 h serum starvation. Representative images from three repeats, each of which was averaged across 15 such fields of view for analysis.

D. Analysis of the number of transmigrated nuclei in **C** as percentages. The highest value of NCD-treated cells that transmigrated was set to 100%, and all other values were scaled accordingly. Statistical significance assessed by one-way ANoVA test conducted on the arcsine-transformed percentages. White bars = average for a given treatment; dot colour = experimental repeat.

E. Immunoblot confirming PCDH1 knockdown in protein lysate of a separate aliquot of HUVEC used in **A** and **C**. Representative images from three repeats.

3.7. PCDH1 knockdown does not alter endothelial sprouting, nor tubulogenesis *in vitro*

The next stage of the angiogenic process to be examined was cellular sprouting, modelled by endothelial spheroids embedded in collagen. siRNA-mediated knockdown of PCDH1 was performed in HUVEC, and spheroids were assembled overnight by the hanging drop method. These were added to a collagen-methyl cellulose mixture, which was quickly solidified by pH lowering, effectively embedding them in a semi-solid matrix. The spheroids were allowed to sprout overnight, then they were fixed and imaged on a transmitted light microscope (**Figure 3.11A**). Manual analysis of the spheroids in these collagen matrices revealed that siRNA-1 treatment reduced the number of sprouts per spheroid by 75% (**Figure 3.11B**), and both the individual (**Figure 3.11C**) and combined (**Figure 3.11D**) length of these sprouts, by 64% and 89% respectively. Recapitulating what observed previously (**Figure 3.9**), however, treatment by siRNA-2 left these parameters statistically unchanged, or even increased them by over 10%, preventing clear conclusions from being drawn. For this reason, this particular assay was only carried out once in these conditions.

Finally, this pattern of siRNA duplex-based inconsistencies manifested itself again in the last *in vitro* assay undertaken, involving automated assessment of the endothelial network formed over 72 hours by HUVEC plated on an established monolayer of dermal fibroblasts (**Figure 3.12A**). Combined tubule length (**Figure 3.12B**), as well as the number of junctions and branches formed as part of the network (**Figure 3.12D**), were reduced by ~40% in networks of cells treated with siRNA-1, and left statistically unchanged in networks of cells treated with siRNA-2, with respect to NCD-treated cells. This discrepancy, again, occurred despite both duplexes resulting in comparably effective PCDH1 knockdown (**Figure 3.12C**), as assessed by immunoblotting 24 hours after the assay was started.

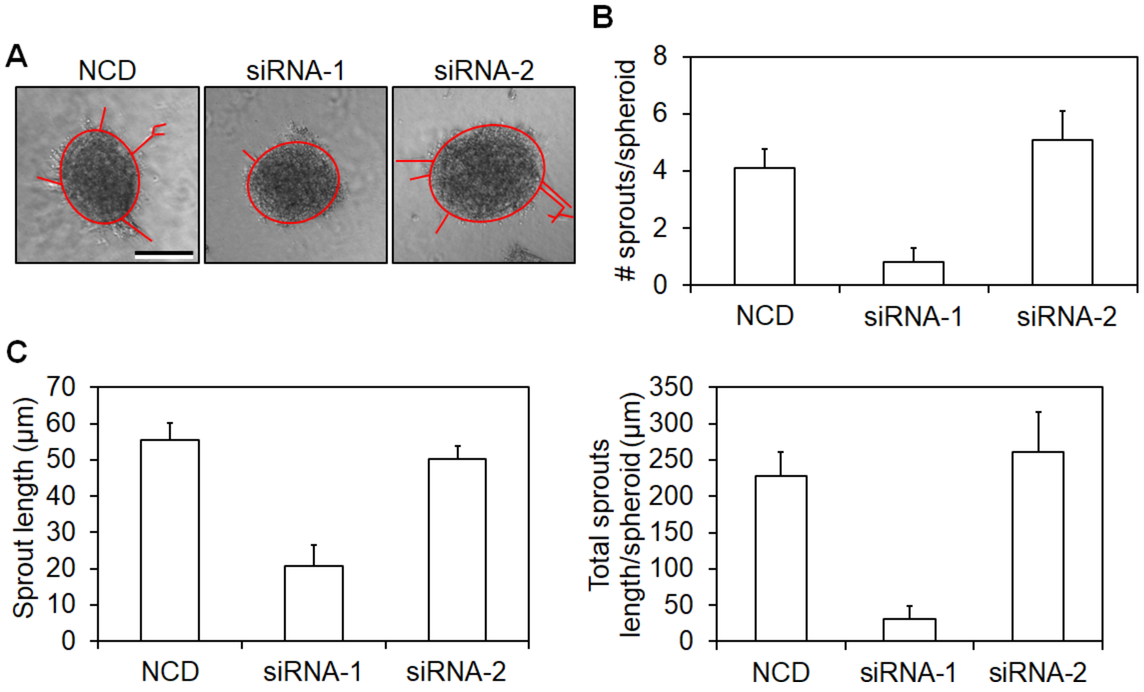

Figure 3.11. PCDH1 knockdown by siRNA-1 impairs HUVEC spheroid sprouting through collagen.

A. Spheroids grown overnight from a single HUVEC isolate, 48 h after siRNA knockdown. The representative images shown here were taken 6.5 h after embedding the spheroids in collagen and incubating them in cM199. Scalebar = 100 µm.

B. Analysis showing the average number of sprouts per spheroid from the experiment in **A**. Error bars = s.e.m. from 10 different spheroids in each condition. Data not assessed for statistical significance, as it was derived from only one biological replicate.

C. Average sprout length (left) and average combined sprouts lengths (right) from the experiment in **A**, as retrieved with the Measure feature in the *ImageJ* software. Error bars = s.e.m. from 10 different spheroids in each condition. Data not assessed for statistical significance, as it was derived from only one biological replicate.

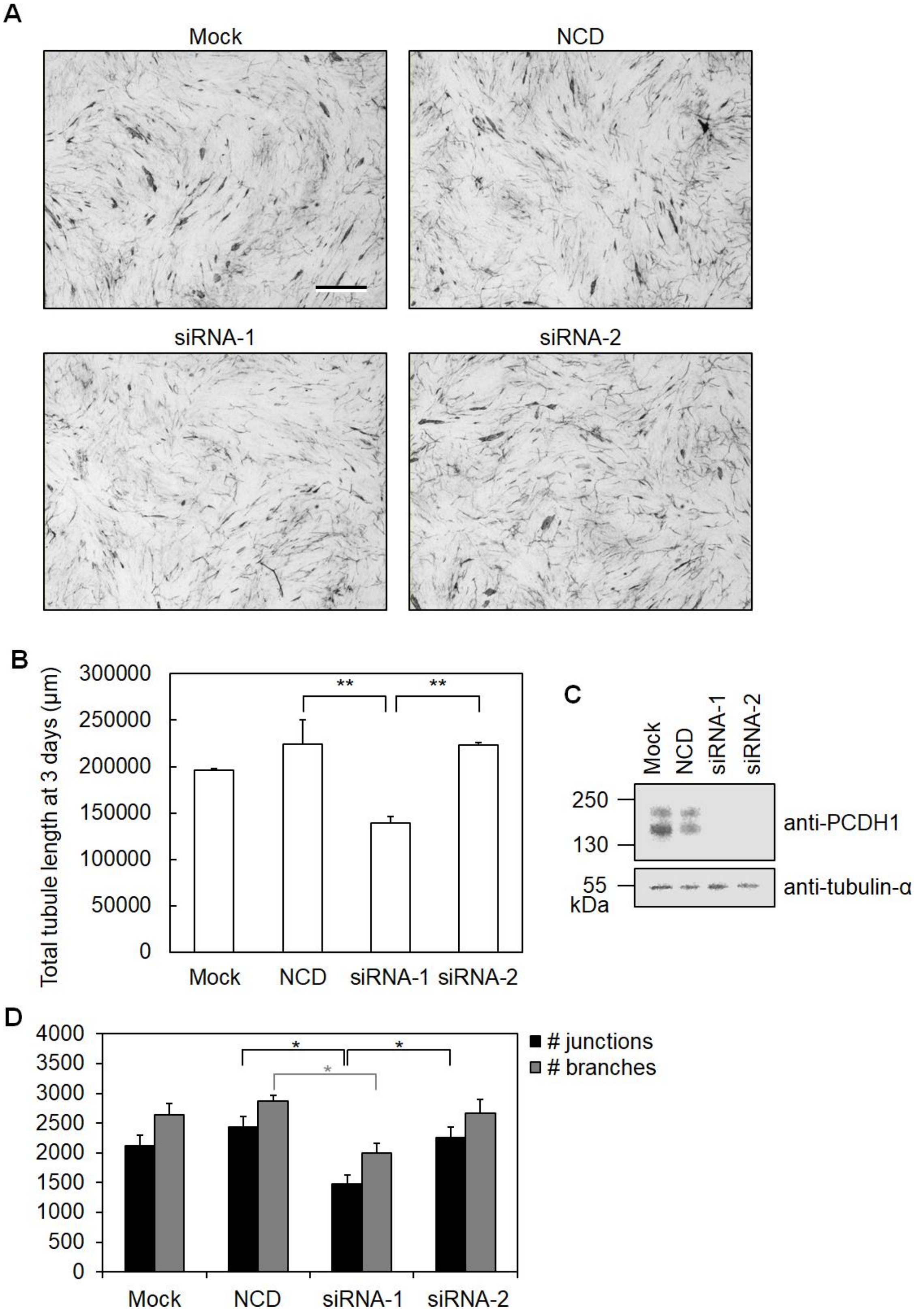

Figure 3.12. PCDH1 knockdown by siRNA-1 reduces connectivity between HUVEC plated on a fibroblast layer.
(Caption overleaf)

A. CD31-stained networks, as formed over three days by HUVEC plated on a 2-day-old layer of human dermal fibroblasts. 24 hours prior to plating, the HUVEC had undergone siRNA transfection with duplexes delivered at 50 nM, to offset the longer duration of this assay. HUVEC were grown in PCM199. Representative images from three repeats. Scalebar = 1 mm.
B. Total length of endothelial tubules, as analysed by the AngioSys software. Stars represent statistical significance (** = $p<0.01$), as assessed by one-way ANoVA test followed by Tukey's post-hoc test. Average of three repeats, error bars = s.e.m.
C. Immunoblot confirming PCDH1 knockdown in protein lysate of a separate aliquot of HUVEC used in **A**. This aliquot was lysed 72 h post transfection, given the longer duration of this assay. Representative images from three repeats.
D. Average number of junctions and branches of the endothelial networks in **B**, as analysed by the AngioSys software. Stars represent statistical significance (* = $p<0.05$), assessed as in **B**.

3.8. PCDH1 knockdown by a mixture of duplexes shows no effect in *in vitro* angiogenesis assays

Because both siRNA-1 and siRNA-2 resulted in comparable knockdown, yet only siRNA-1 resulted in phenotypic outcomes assessed by scratch-wound, spheroid, and co-culture assays (**Sections 3.5-3.7**), one possible reason was that the effects seen were mediated by off-target knockdown effects, despite both siRNA duplexes being checked against the reference genome to avoid the very possibility. To test this hypothesis, two new siRNA duplexes, siRNA-3 and siRNA-4, were designed and commercially synthesised, each of which also targeted most PCDH1 transcripts, albeit at different sequences from the previous two duplexes (**Figure 3.1**). These new duplexes were employed in a titration experiment, similar to that undertaken for the previous ones (**Figure 3.4A**). Immunoblotting revealed that HUVEC treated with siRNA-3 or siRNA-4 at the same concentration, 20 nM, displayed similar levels of PCDH1 knockdown (**Figure 3.13A**). A Matrigel assay was therefore attempted with these newly synthesised duplexes (**Figure 3.13A**), however this assay also returned discording results, with siRNA-4 resulting in 60% reduction in the number of loops with respect to NCD-treated HUVEC, while siRNA-3 left this measurement unaffected (**Figure 3.13D**).

Reasoning that this result might also be due to off-target effects by one of the newer duplexes, a knockdown experiment was carried out using the four duplexes combined, each at one quarter of the concentration it had been previously used at. Using this mixture would minimise off-target effects by single duplexes even further, as each individual duplex would be used at an ever lower concentration, while retaining potent knockdown effects overall by keeping unchanged the total [siRNA]. Immunoblotting of HUVEC treated in this manner revealed the mixture to be as effective at knocking down PCDH1 as previous duplexes singularly taken (**Figure 3.14A**). Therefore, most *in vitro* assays thus far described were repeated using this

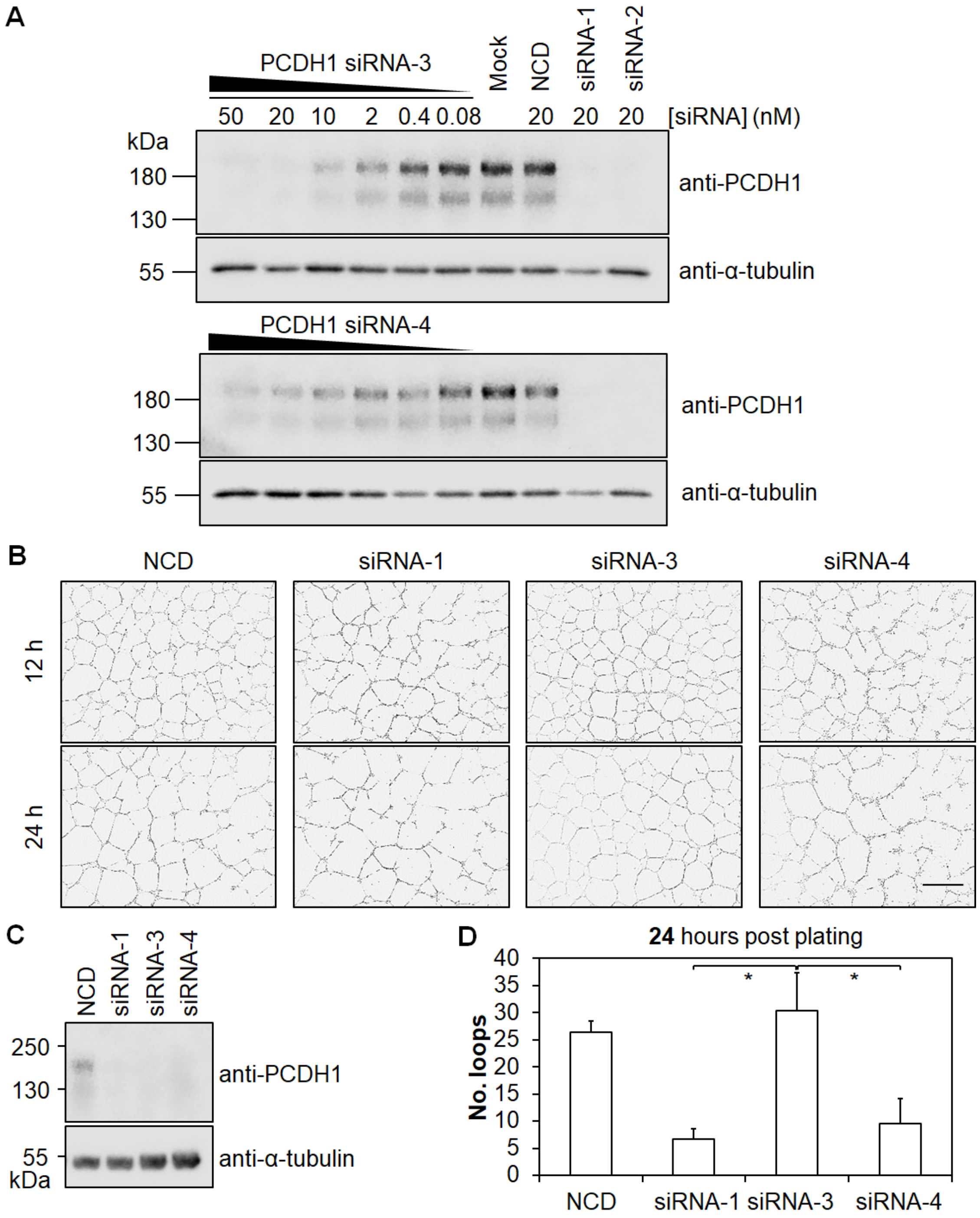

Figure 3.13. Only one of two other PCDH1 siRNA duplexes impairs HUVEC connectivity on Matrigel.

A. HUVEC were transfected with given amounts of *PCDH1*-targeting siRNA duplex, and harvested after 48 h. Protein lysates were separated by SDS-PAGE and immunoblotted.

B. Endothelial networks formed by HUVEC plated on Matrigel, 48 h after siRNA transfection. Representative images from three repeats, showing the same field of view at two timepoints after plating. Scalebar = 800 µm.

C. Immunoblot confirming PCDH1 knockdown in protein lysate of a separate aliquot of HUVEC used in **B**. Representative images from three repeats.

D. Analysis of mean loop number per field of view, as measured by the Angiogenesis Analyzer plugin for the *ImageJ* software. Stars represent statistical significance (* = p<0.05), as assessed by one-way ANoVA test followed by Tukey's post-hoc test. Error bars = s.e.m.

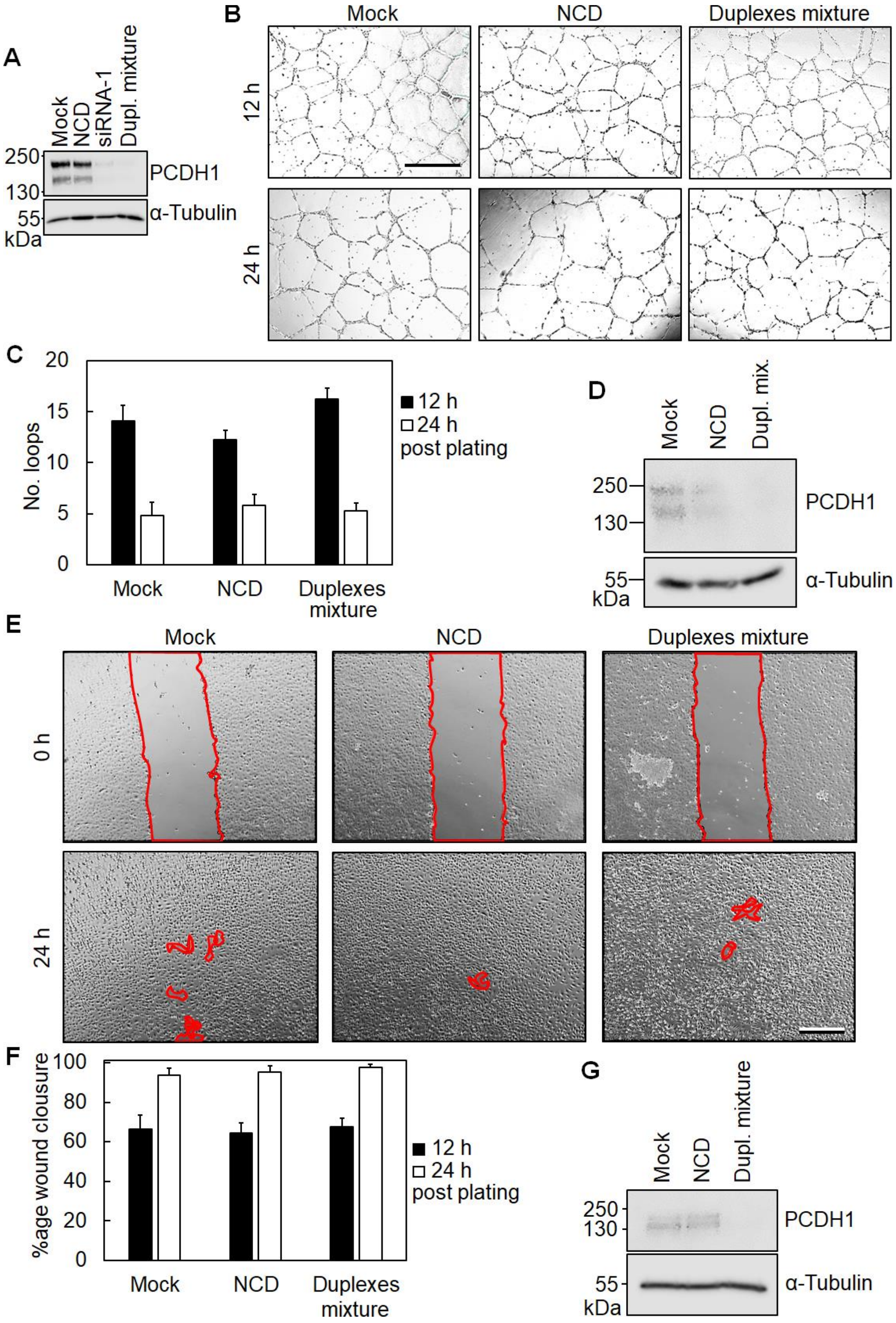

Figure 3.14. PCDH1 knockdown by mixed siRNAs does not impact endothelial connectivity on Matrigel, nor scratch-wound recovery time. *(Caption overleaf)*

A. Immunoblot confirming PCDH1 knockdown in protein lysate HUVEC treated with a 20 nM mixture of four different *PCDH1*-targeting siRNA duplexes, each used at 5 nM.
B. Endothelial networks formed by HUVEC plated on Matrigel, 48 h after siRNA transfection with the mixture of siRNA duplexes used in **A**. Representative images from three repeats. Scalebar = 800 μm.
C. Analysis of mean loop number per field of view, as measured by the Angiogenesis Analyzer plugin for the *ImageJ* software. Error bars = s.e.m., measured over the three repeats described in **B**.
D. Immunoblot confirming PCDH1 knockdown in protein lysate of a separate aliquot of HUVEC used in **B**. Representative images from three repeats.
E. Wound recovery by HUVEC, scratched 48 h after siRNA transfection. Representative images from three repeats. The scratched area, red, was outlined manually in the *ImageJ* software. Representative images from three repeats. Scalebar = 500 μm.
F. Analysis of mean scratch-wound recovery over 12 h and 24 h. Each treatment is expressed as percentage of the area still scratched with respect to its originally scratched area at t = 0 h. Error bars = s.e.m., measured over the three repeats described in **E**.
G. Immunoblot confirming PCDH1 knockdown in protein lysate of a separate aliquot of HUVEC used in **E**. Representative images from three repeats.

mixture for PCDH1 knockdown in HUVEC, which showed no impact in endothelial connectivity on Matrigel (**Figure 3.14B-D**), spheroid sprouting parameters (**Figure 3.14E-G**), chemotactic transmigration (**Figure 3.15A-C**), nor scratch-wound recovery time (**Figure 3.15D-G**) with respect to NCD-treated cells. Such dilution-dependant loss of phenotypic outcomes suggests that the results observed by carrying out *in vitro* assays with single siRNA duplexes were indeed discordant due to off-target effects arising from individual duplexes.

3.9. cDNA microarrays reveal hundreds of transcriptomic changes upon PCDH1 knockdown in HUVEC

Obtaining a clearer picture of exactly which transcripts are affected by siRNA knockdown with a given duplex would allow assessment of which siRNA treatment resulted in off-target effects. With no notion of which non-*PCDH1* mRNA transcripts could be targeted, an unbiased screening approach was set up, where overall transcriptomic changes in HUVEC after knockdown were profiled using DNA microarrays. To this end, total RNA was extracted from HUVEC transfected with either siRNA-1 or siRNA-2 used on their own, as per **Sections 3.3-3.7**, and with the mixture of all four duplexes as used in **Section 3.8**. Effective knockdown was confirmed by immunoblotting (**Figure 3.16A**). These RNA samples were commercially converted to cDNA and used on a Clariom S microarray platform. Preliminary Principal Component Analysis (PCA) was undertaken, which reduced to three dimensions the overall changes across the 21,449 transcripts assessed by the platform. This analysis showed that the experimental repeats of each treatment successfully clustered together (**Figure 3.16B**). Furthermore, NCD treatment seemed to affect the overall transcriptome more extensively than previously anticipated: NCD-treated cells were positioned further away from any *PCDH1*-targeting duplex treatment than mock-treated cells were. Intriguingly, siRNA-2 samples were positioned closer to samples of NCD-treated cells than siRNA-1 samples were, with the

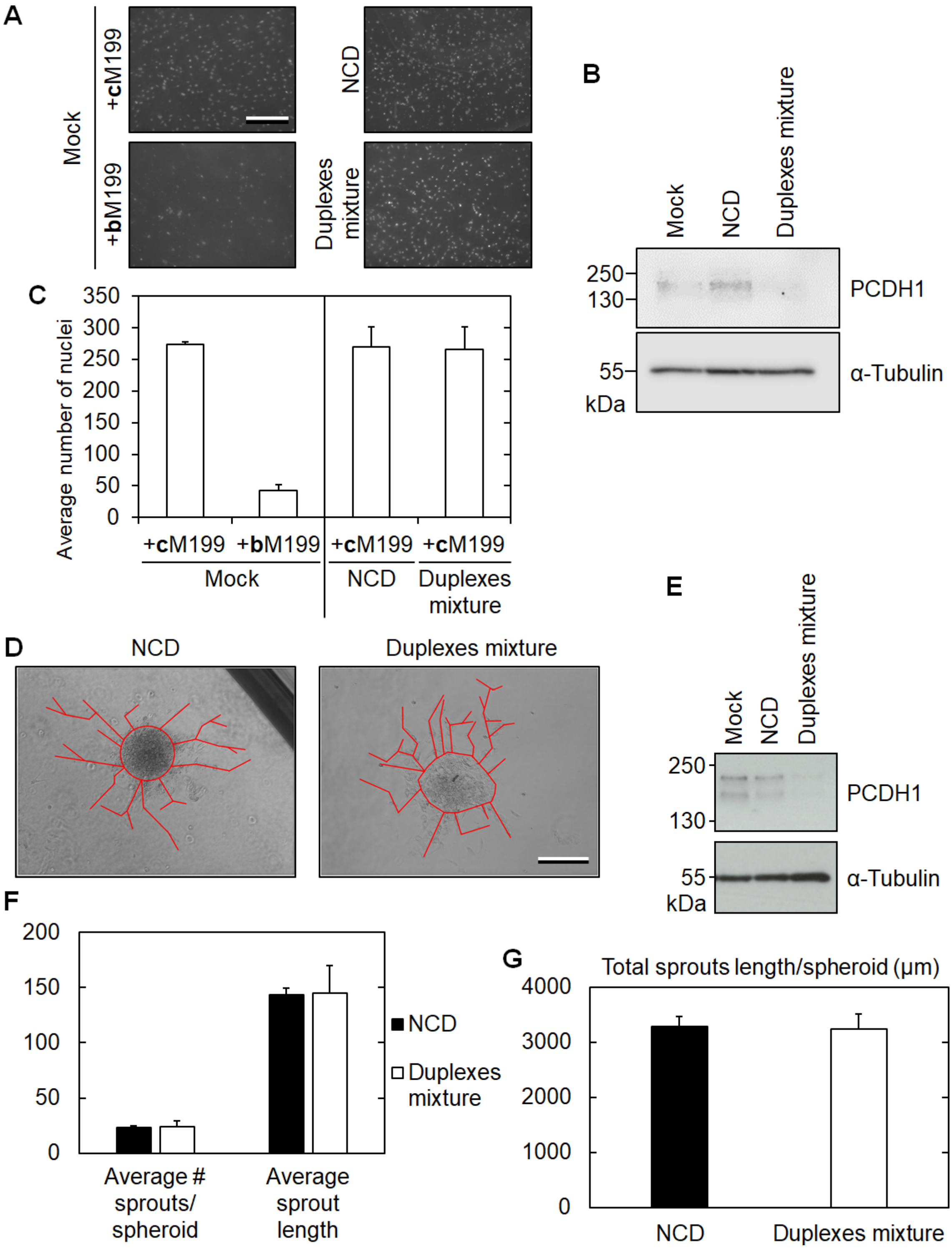

Figure 3.15. PCDH1 knockdown by mixed siRNAs does not impact endothelial chemotaxis through a porous membrane, nor sprouting through collagen.

A. Bottom side of FluoroBlok membranes, where siRNA-transfected HUVEC were allowed to migrate for 5 h towards cM199, after 1 h serum starvation. Representative images from three repeats, each of which was averaged across 3 such fields of view for analysis. Scalebar = 800 μm.

B. Immunoblot confirming PCDH1 knockdown in protein lysate of a separate aliquot of HUVEC used in **A**. Representative images from three repeats.

(Continued from previous page)
C. Analysis of the number of nuclei transmigrated towards growth factors below the porous membrane. Error bars = s.e.m., measured over the three biological repeats described in **A**.
D. HUVEC spheroids were grown overnight, 24 h after siRNA knockdown, and embedded into collaged 24 after that. They were allowed to sprout for 17 h, then fixed and imaged. Scalebar = 200 μm. Representative images from three repeats. Red outlines were manually overlaid with the *ImageJ* software, to allow sprout analysis.
E. Immunoblot confirming PCDH1 knockdown in protein lysate of a separate aliquot of HUVEC used in **D**. Representative images from three repeats.
F. Analysis showing the average number of sprouts per spheroid, and its average length. Error bars = s.e.m., measured over the three biological repeats described in **D**.
G. Analysis showing the average combined length of sprouts per spheroid, complementing the data shown in **F**. Error bars = s.e.m.

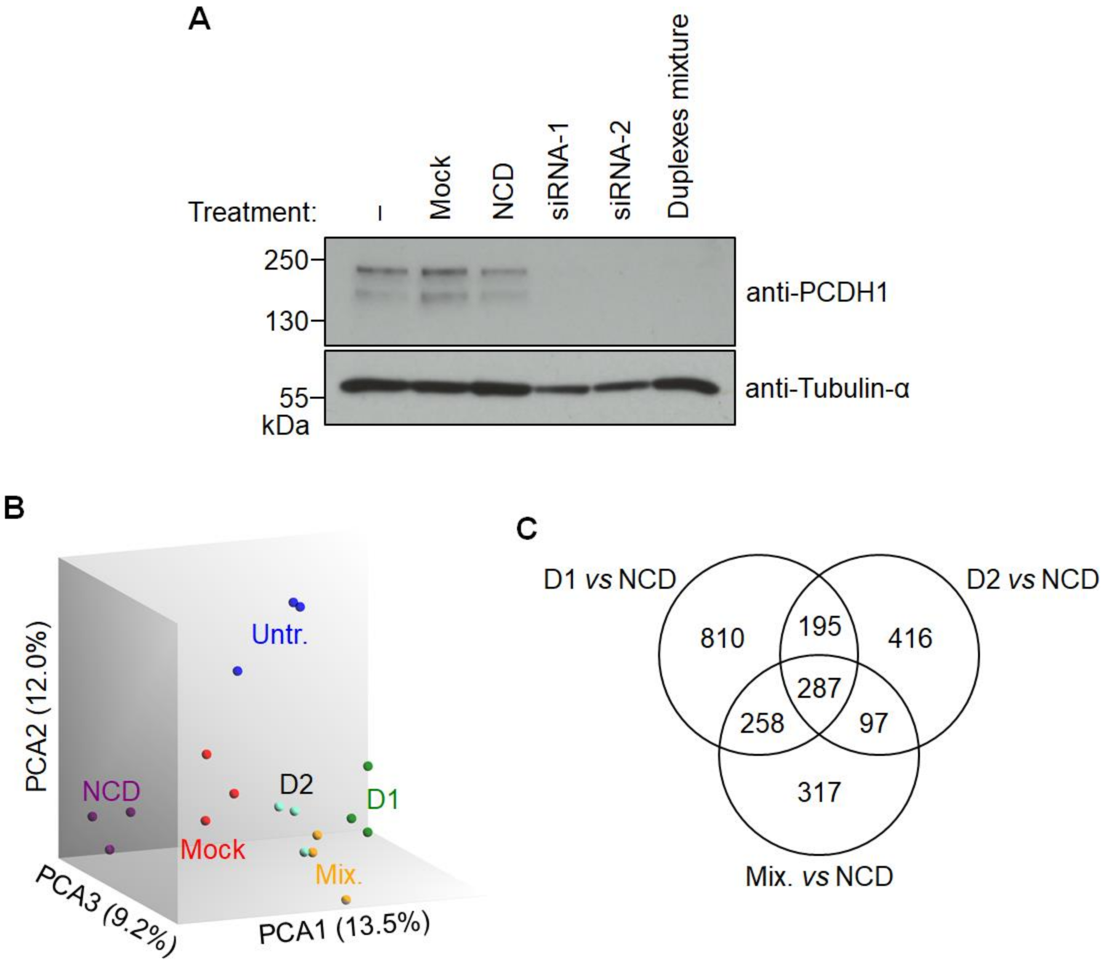

Figure 3.16. DNA microarrays show proteome changes in HUVEC after PCDH1 knockdown.
A. Immunoblot confirming PCDH1 knockdown in protein lysate of a separate aliquot of HUVEC used for RNA isolation. Representative images from the three repeats.
B. Three-dimensional Principal Component Analysis (PCA) plot for the 18 samples submitted for the microarray experiment. The label for the D2 datapoints is written in black to aid visualisation. D1 = siRNA-1-treated cells; D2 = siRNA-2-treated cells.
C. Venn diagram showing the number of transcripts commonly affected across duplex-treated samples, each as compared to the NCD-treated samples. A total of 21,449 transcripts were analysed.

mixture-treated samples positioned between the two; this suggested that siRNA-2 had a smaller impact in terms of overall transcriptomic changes than siRNA-1 did, with respect to NCD treatment, and that dilution of each single duplex upon mixing resulted in reduced off-target effects. However, this analysis was only used as a qualitative confirmation that all treatment points could be included for the subsequent investigation; no conclusions were drawn at this stage. Comparisons between each of the 15 possible pairings of treatments were created, followed by two-way ANoVA and post-hoc analysis to assess the statistical significance of expression changes between each pair. A change in expression of at least 1.5-fold with a *p*-value of 5% was deemed significant. Interestingly, comparing mock treatment with NCD treatment revealed 438 genes being affected (by up- or down-regulation in either sample), and even mock or NCD treatments resulted in 662 or 1381 genes, respectively, being affected as compared to untreated HUVEC (**Table 3.1**). This highlights the potential for substantial differences from the basal HUVEC phenotype being induced by lipofectamine and NCD treatments themselves. As expected, there was some degree of overlap between the transcriptomic changes observed, with e.g. 287 transcripts affected by all of siRNA-1, siRNA-2, and the duplex mixture (**Figure 3.16C**). Unexpectedly, there was more extensive overlap between siRNA-1 and the duplex mixture (545 genes) than there was between the latter and siRNA-2 (383 genes). However, such analysis is limited in that it only compares transcript numbers, although these could be upregulated in one comparison and downregulated in another, and still count as being “affected” in both subsets, and therefore does not necessarily reflect true overall similarity.

3.10. Pathway analysis suggests anti-angiogenic role for PCDH1

To compare the treatments more closely, pathway analysis was undertaken on each of the siRNA duplex treatments (D1, D2, or Mix.) against the NCD treatment. This sophisticated type

Table 3.1. Summary of transcriptomic changes upon PCDH1 knockdown.

Treatment A	Treatment B	Transcripts affected	Downregulated in A wrt B	Upregulated in A wrt B
D1	D2	829	501	328
D1	Mock	659	385	274
D1	NCD	1550	803	747
D1	Untreated	1266	757	509
D2	Mock	333	159	174
D2	NCD	995	443	552
D2	Untreated	1048	570	478
Mixture	D1	559	261	298
Mixture	D2	421	276	145
Mixture	Mock	444	242	202
Mixture	NCD	959	437	522
Mixture	Untreated	1239	659	580
Mock	NCD	438	169	269
Mock	Untreated	662	354	308
NCD	Untreated	1381	759	622

Changes were considered significant if the difference was at least 1.5-fold ($\log_2$ scale).

of analysis can predict potential pathways or molecular effectors as being activated (positive *z*-score) or inhibited (negative *z*-score) by comparing the experimental transcript levels to the known, literature-reported effects that a given pathway/effector has on the transcriptome. Overall, around 200 diseases, 150 molecular pathways, and 4,000 upstream regulators were predicted to be affected with respect to NCD by all three siRNA treatments. In all three cases, 65-90% of the entries were affected in the same fashion (up- or down-regulated) by all three treatments: this was expected, because siRNA-1 and siRNA-2 did elicit the same phenotype in some of the *in vitro* assays (**Sections 3.5**, **3.6**). However, because siRNA-1 conferred a more profound phenotype in most *in vitro* assays than siRNA-2 and the siRNA mixture, the analysis focused on entries affected in the opposite way by siRNA-1 and by siRNA-2 (or the mixture), i.e. considering only entries that were activated by siRNA-1 and inhibited by both siRNA-2 and mixture, or vice versa. siRNA-1 was predicted to significantly (*z*-score > 2 or < -2) inhibit cell proliferation, cell migration, cell survival, and vessel growth with respect to NCD treatment, although no specific biochemical pathways were highlighted as statistically impacted (**Figure 3.17**); conversely, siRNA-2 and the mixture were found to stimulate these cell functions. Therefore, if the absence of *in vitro* phenotypes among mixture-treated samples observed in some assays was due to cell motility being promoted upon PCDH1 loss, this would suggest that basal PCDH1 expression in fact has anti-angiogenic effects. It follows that siRNA-1 treatment, by way of off-target effects, must result in upregulation of transcripts that promote a quiescent-like, anti-angiogenic phenotype.

A separate pathway analysis identified individual upstream regulators that would result in phenotypic changes like those observed by specific siRNA treatments (**Figure 3.18**): over 40% of the statistically significant comparisons were found to be regulators related to inflammatory mechanisms, nearly all of which seem to be inhibited by siRNA-1 and activated by siRNA-2

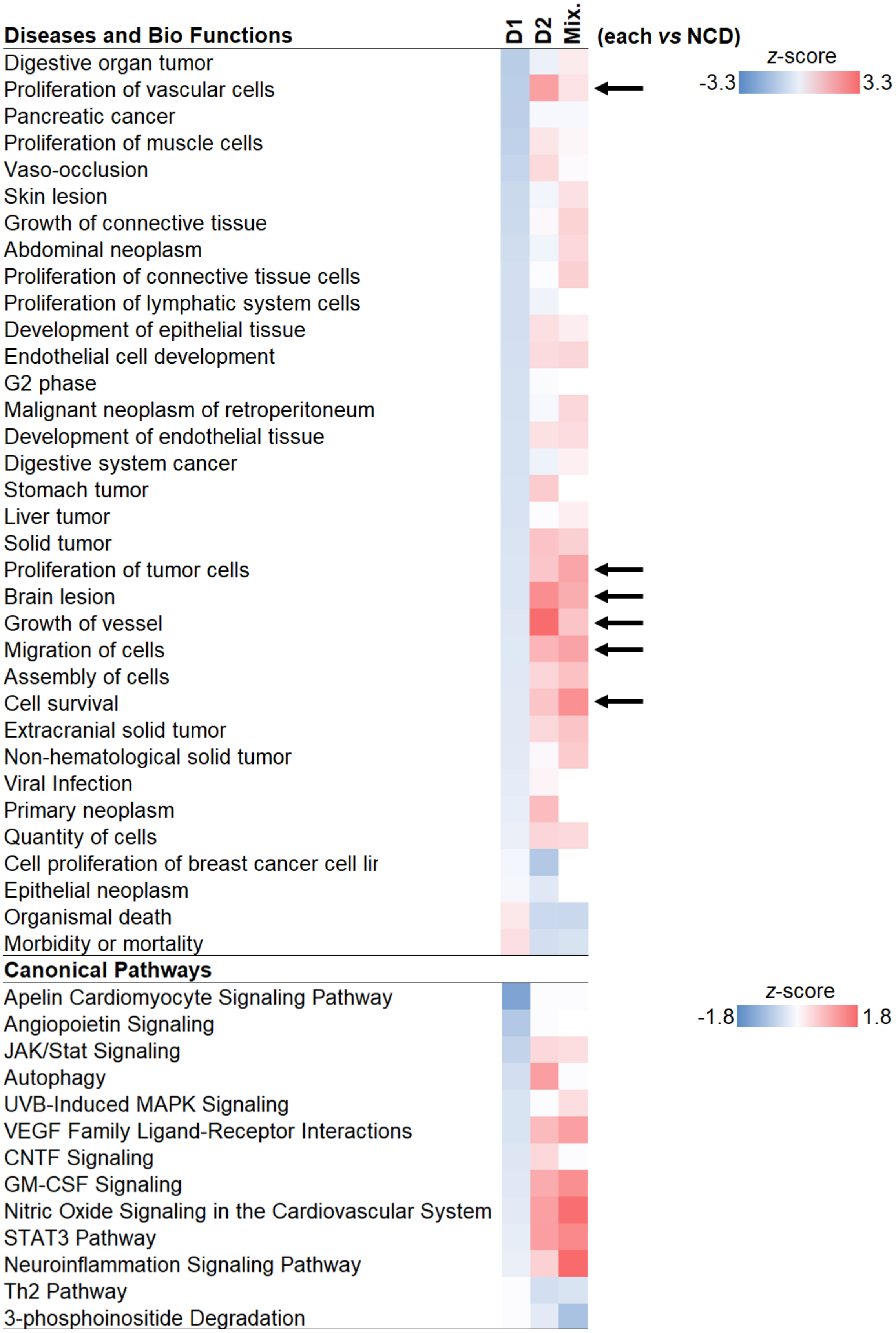

Figure 3.17. Pathways predicted to be affected by *PCDH1* siRNA treatment in HUVEC. Each sample (bold) was compared to the NCD treatment, and the *z*-score of the comparison is

(Continued from previous page)
represented by a shade of blue (predicted inhibition) or red (predicted activation). Black arrows denote rows where at least one of the samples had *z*-score over 2, or below -2. Diseases/pathways are only shown if their *z*-score for the D1 samples had opposite sign to those of D2 and Mix. A total of 725 diseases and 254 pathways were assessed.

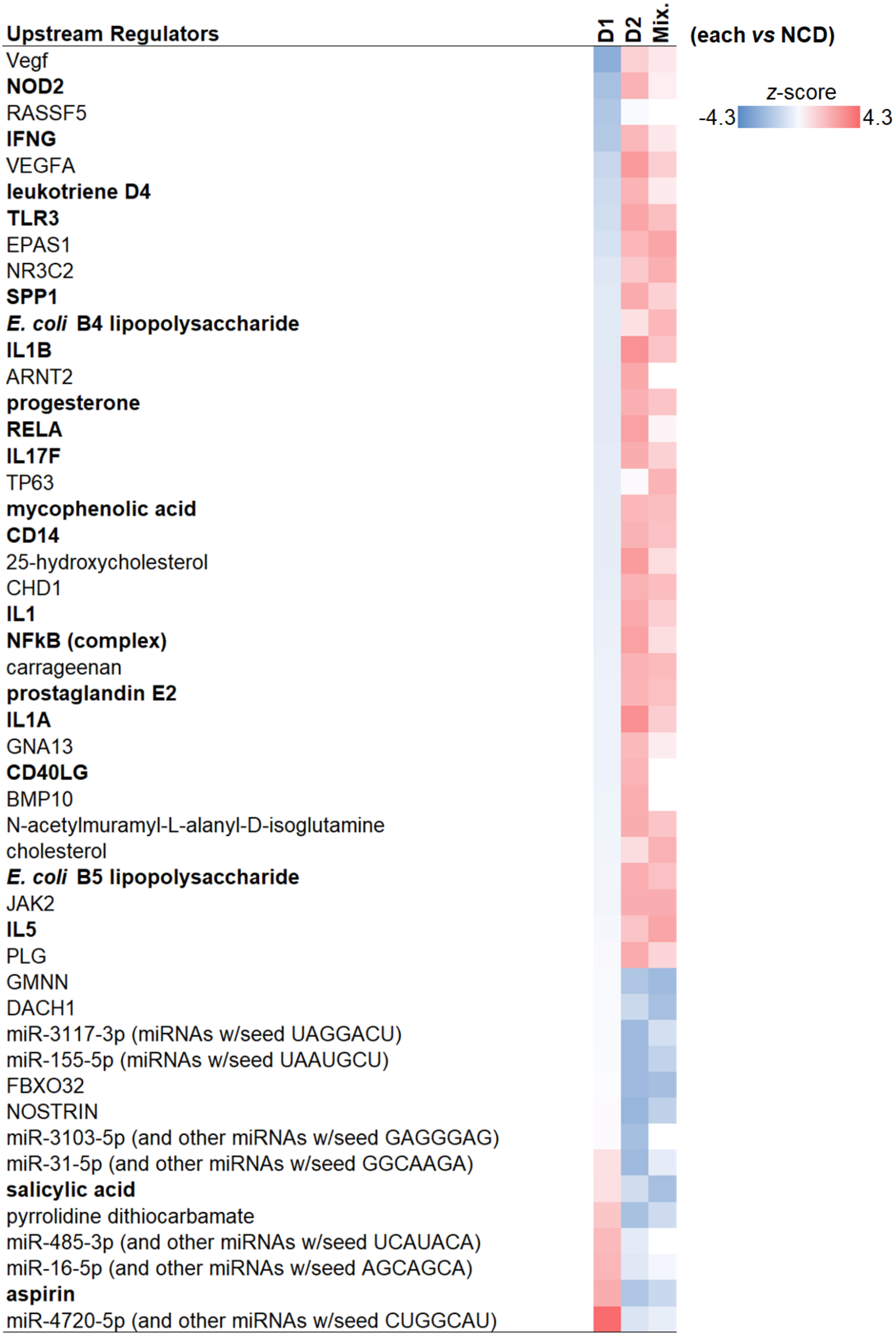

Figure 3.18. Upstream regulators predicted to result in the transcriptomic changes observed with *PCDH1* siRNA treatment in HUVEC. *(Caption overleaf)*

(Continued from previous page)
Each sample was compared to the NCD treatment, and the *z*-score of the comparison is represented by a shade of blue (predicted inhibition) or red (predicted activation). Regulators are only shown if their *z*-score for the D1 samples had opposite sign to those of D2 and Mix. A total of 4,029 regulators were assessed. Furthermore, only regulators that resulted in at least one of the comparisons having a significant *z*-score are shown. Bold typeface denotes regulators that are associated with inflammation in the literature.

and the mixture. This suggests that off-target effects by siRNA-1 might also reduce the inflammation-like cell response of HUVEC to siRNA-treatment. Among these was DACH1, a transcription factor that was predicted to be slightly activated by siRNA-1 but inhibited by siRNA-2 (and mixture), which is known to impair cancer cell motility and angiogenesis (Chen et al., 2015; Chu et al., 2014; Han et al., 2015). Thus it is possible that downregulation of DACH1 mediates the pro-angiogenic changes predicted for siRNA-2 and mixture treatment (**Figure 3.17**). However, the gene-specific expression data for *DACH1* in the microarrays show that it is in fact upregulated in siRNA-2 samples, with respect to NCD samples, and downregulated in the siRNA-1 and mixture samples (**Figure 3.21**). This discrepancy highlights that the lists of predicted pathways, and any conclusions drawn from them, remain speculative.

3.11. Each *PCDH1* siRNA affects multiple angiogenesis-related genes

Next, transcript expression levels were compared as two-way combinations, to try and establish clear differences between the duplexes singularly taken and the siRNA mixture. In the first instance, the average transcriptome of siRNA-mixture-treated HUVEC was compared to that of either siRNA, singularly taken. When viewed on a volcano plot, which displays both differences in expression and their statistical significance (**Figure 3.19**), the mixture seemed to in fact strongly downregulate many transcripts that were not downregulated by either siRNA, because more genes have negative fold-change value than positive. This was explained as arising from the combined effects of the four siRNAs that make up the mixture, each of which must have resulted in some degree of off-target effects. Because the pathway analysis (**Section 3.10**) suggested that cell migration was affected by the duplexes, the *UniProt* database was searched to identify whether any of the differentially expressed genes are known to regulate cell motility/chemotaxis. This resulted in the identification of 17 such genes, among the most

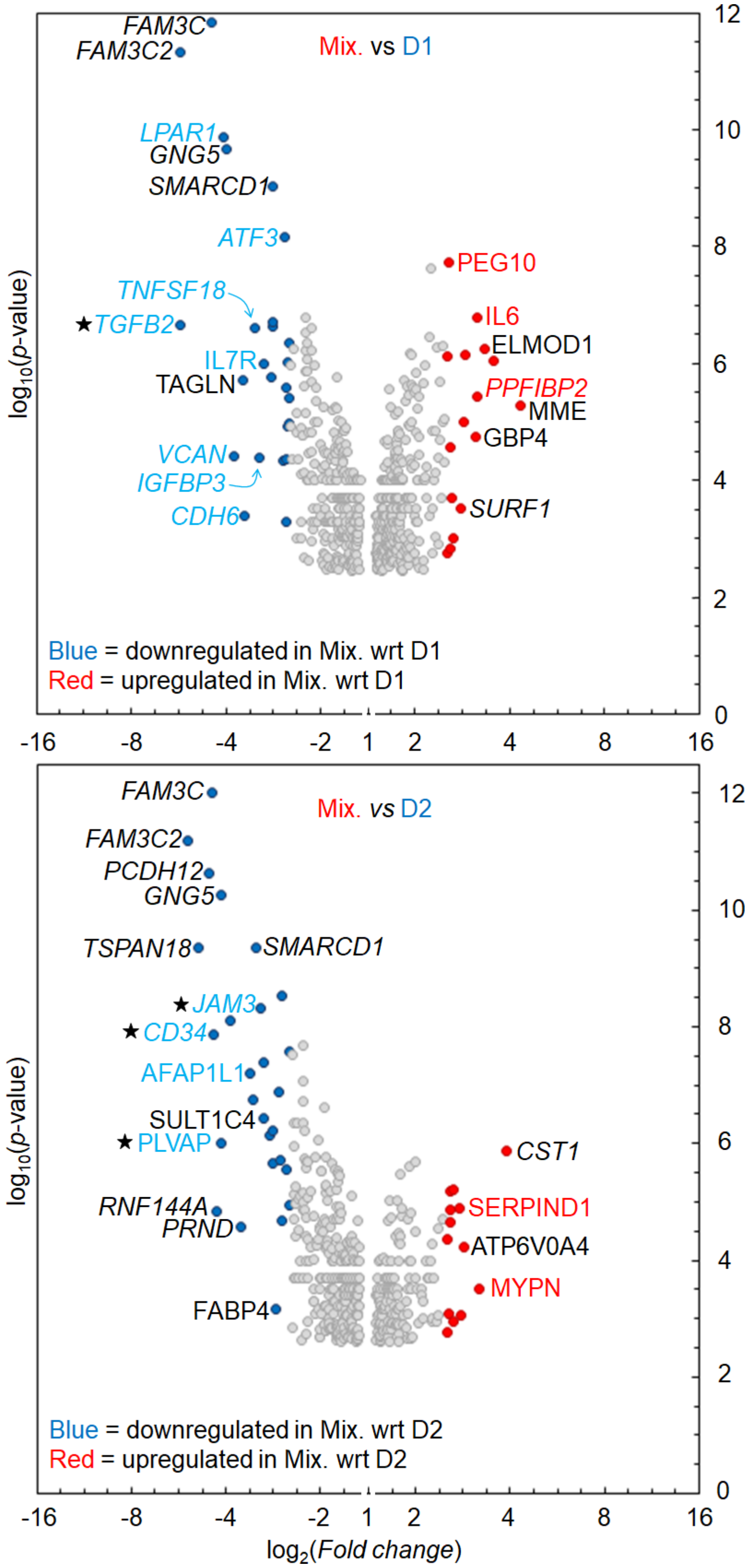

(Figure continues on to next page)

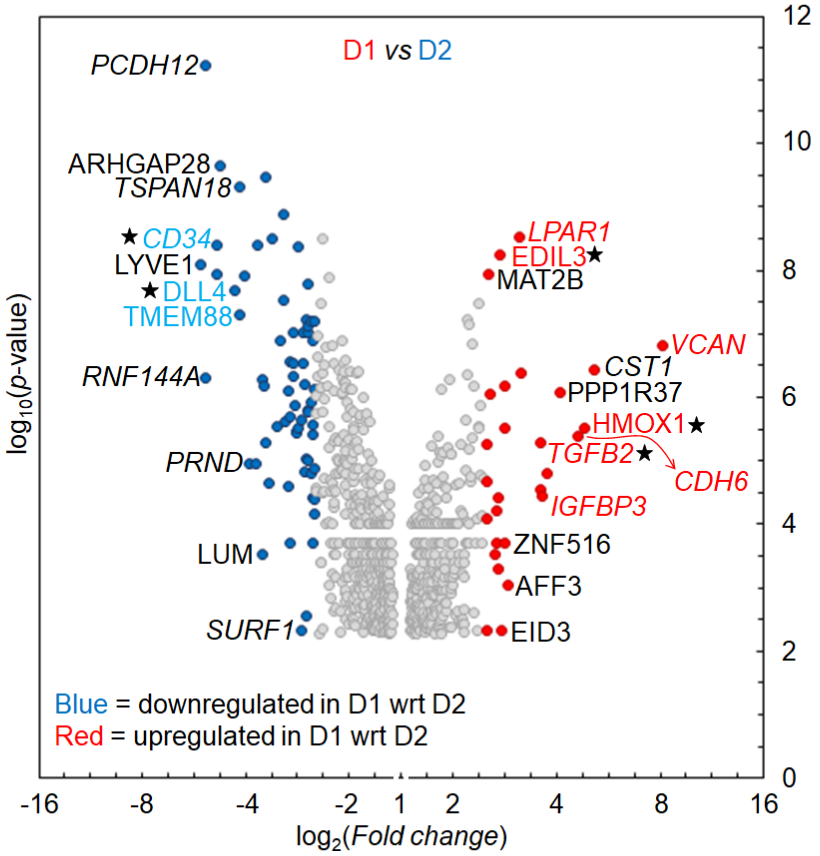

Figure 3.19. Two-way HUVEC transcriptome comparisons between selected duplex treatments.
Plots showing, as dots, individual transcripts from a given treatment comparison, with fold-changes expressed as their logarithmic value. Only transcripts that differ in expression level by at least 1.5-fold in either comparison are shown. Dots are coloured if they differ by at least 2.5-fold. Select transcripts are written next to their position in the plot, with transcripts occurring in more than one plot (either here or in **Figure 3.20**) written in italics. Transcripts are written in coloured typeface if they are associated with chemotaxis/cell adhesion, with a black star next to their symbol if they are associated with angiogenesis, as per the *UniProt* database.

extremely up- or down-regulated. Interestingly, of these motility-related genes, siRNA-1 looked to be upregulating genes with known growth/proliferation effects (*TNFSF18*, *TGFB2*, *IGFBP3*) and inflammation-related genes (*IL7R*), pathways which were also identified earlier (**Section 3.10**); conversely, *IL6*, a potent inflammation mediator, seemed downregulated. However, when comparing siRNA-1 against siRNA-2 treatment, most of these genes did not reappear, suggesting that they were in fact affected by the mixture i.e. siRNA-3 and siRNA-4 specifically. The exceptions were *TGFB2* and *IGFBP3*, which again appeared upregulated by siRNA-1 treatment as compared to siRNA-2, suggesting these two genes are strongly affected by siRNA-1 specifically, in line with the earlier pathways analysis findings (**Section 3.10**). Comparing all plots together highlights that many transcripts are known to play a role in angiogenesis (star symbols), including *DLL4* and *CD34*, which were specifically downregulated by siRNA-1 (as compared to NCD) but not by siRNA-2, as can be seen in the D1 *vs* D2 plot. In contrast, some were downregulated by siRNA-2 but not siRNA-1, such as *HMOX1*. Because varying the expression level of any of these genes could have profound effects on the angiogenic potential of HUVEC, it was not possible to determine which, if any one, conferred the *in vitro* phenotypes observed upon siRNA-1 treatment. This underscores that the phenotypes observed in the *in vitro* assays are in all cases the average of multiple, concurrent transcriptional effects, each of which with potentially opposite outcomes when taken in isolation. The balance of these, as offset by a specific siRNA treatment both in terms of desired (*PCDH1*-targetting) and undesired (off-target) effects, is complex to predict and assign even given access to the full transcriptomic changes taking place in the cells.

3.12. The *PCDH1* siRNA mixture strongly downregulates Sema-3D, Periostin, and E-selectin

Finally, comparison between mixture and NCD treatments (**Figure 3.20**), together with

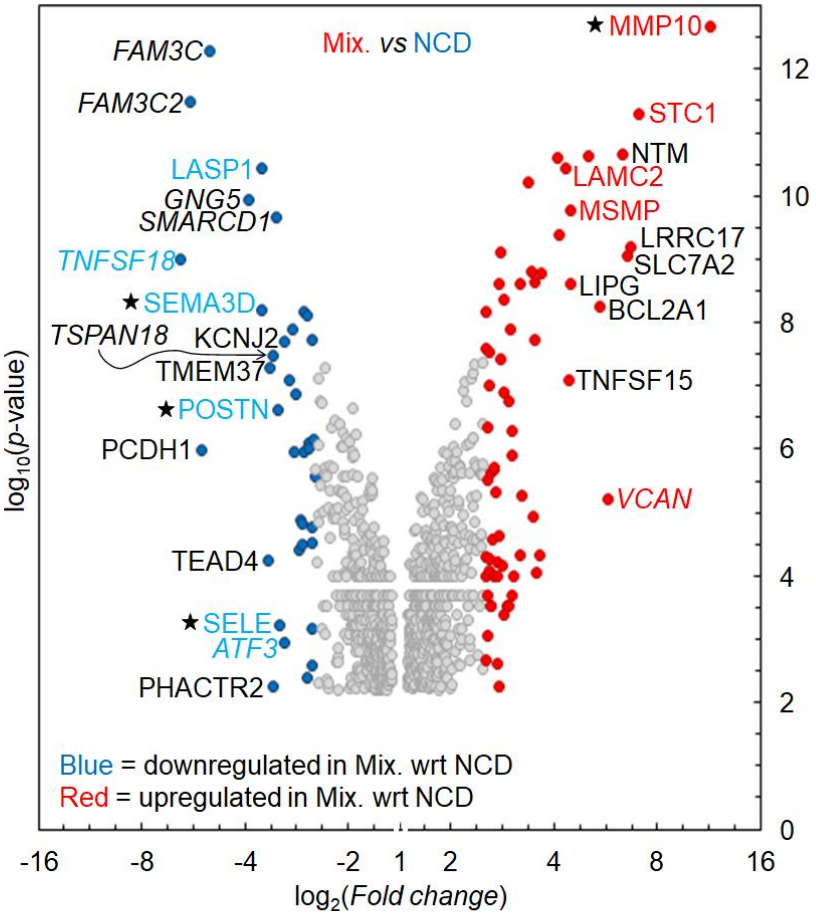

Figure 3.20. HUVEC transcriptome comparison between Mixture and NCD treatments. Plots showing, as dots, individual transcripts from a given treatment comparison, with fold-changes expressed as their logarithmic value. Only transcripts that differ in expression level by at least 1.5-fold in either comparison are shown. Dots are coloured if they differ by at least 2.5-fold. Select transcripts are written next to their position in the plot, with transcripts occurring in more than one plot (including those in **Figure 3.19**) written in italics. Transcripts are written in coloured typeface if they are associated with chemotaxis/cell adhesion, with a black star next to their symbol if they are associated with angiogenesis, as per the *UniProt* database.

confirming *PCDH1* knockdown, showed that the mixture also resulted in large upregulation of MMP10 and downregulation of Sema-3D, among others. MMP upregulation is a hallmark of the early angiogenic stages (**Figure 1.1**), and Sema-3D functions as a repulsive chemotactic cue during angiogenesis (Hamm et al., 2016), much like Sema-3E (**Table 1.1**). This would support the idea that chemotaxis is promoted by siRNA-mixture treatment (**Section 3.10**). Conversely, however, siRNA mixture treatment also resulted in downregulation of E-selectin, which is known to promote chemotaxis and angiogenesis *in vitro* (Koch et al., 1995), and of Periostin, which promotes pathological angiogenesis in human (Bernardes et al., 2020; Zheng et al., 2020) and dog (Alfino et al., 2021) tumours, and in human retinopathy (Kubo et al., 2020). Furthermore, these four genes are also upregulated and downregulated in the same fashion, although to a lesser extent, by both siRNA duplexes (**Figure 3.21**), suggesting these are not mixture-specific effects, rather that they are enhanced in this setting. Nevertheless, they were impacted by the siRNA mixture even more strongly than *PCDH1*, as evident from their larger fold-changes, which suggests that they might play at least complementary roles in the cell processes that are elicited by artificially reducing PCDH1 levels by knockdown.

3.13. Discussion

Work in this chapter attempted to assess whether PCDH1 is involved in angiogenesis. PCDH1 expression in HUVEC was confirmed both at the level of mRNA and protein, by RT-PCR and by fluorescence-based and biochemical assays respectively. Endogenous PCDH1 levels were temporarily reduced in HUVEC by siRNA transfection, which could be circumvented by overexpression of a PCDH1 mutant. Different siRNAs targeted at PCDH1 reduced endothelial chemotaxis and connectivity *in vitro*, but only one of these siRNAs affected sprouting, tubulogenesis, and scratch-wound recovery time. Delivering these duplexes diluted, as part of a four-siRNA mixture, resulted in the loss of these phenotypes. A microarray experiment,

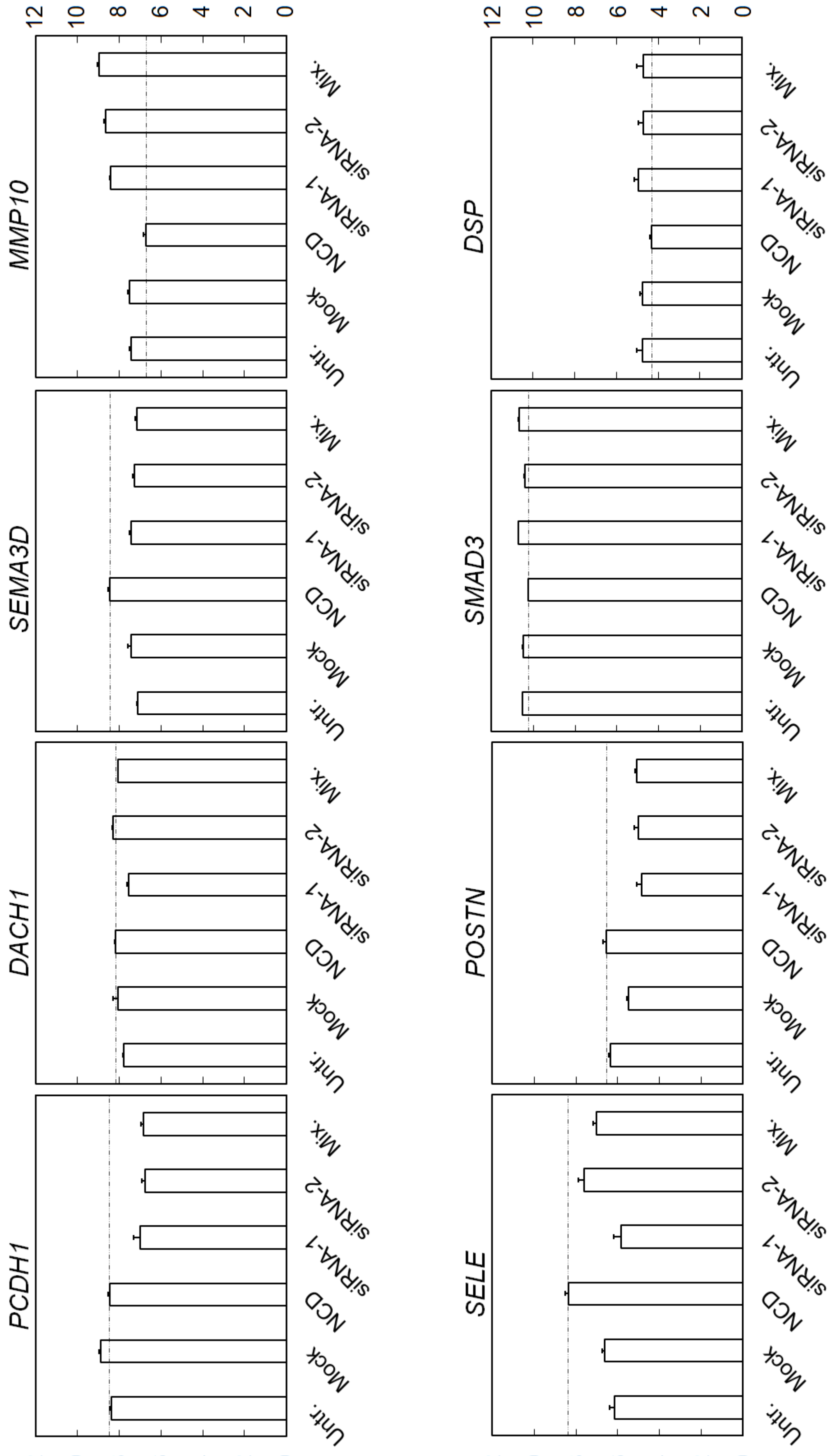

Figure 3.21. Microarray transcript levels ($\log_2$) of selected genes in siRNA-treated HUVEC.

(Continued from previous page)
Transcript levels ($\log_2$) of selected genes are shown as average value of 3 repeats + s.e.m. The dotted line represents the average transcript value for the NCD treatment. The genes of SMAD3 and Desmoplakin (*DSP*) are reported as these proteins are of interest for **Chapter 4**.

designed to assess the transcriptome of HUVEC treated with the above duplexes, highlighted a complex interplay of factors, and suggested that PCDH1 has a modestly anti-angiogenic role.

3.13.1. PCDH1 expression in HUVEC

Between the *NCBI* and *Ensembl* databases, at least seven *PCDH1* splice variants are reported (**Figure 3.1**), identified both computationally and by purposely designed RACE experiments, undertaken both in human (Koning, Sayers, et al., 2012) and murine (Koning et al., 2014) lung tissue. RACE (rapid amplification of cDNA ends) experiments can identify all expressed transcripts relating to a single gene regardless of their 5’ or 3’ sequences, by using a gene-specific primer and a degenerate 5’ or 3’ primer, appropriately (Frohman et al., 1988). By design, therefore, it is a very tissue-specific assay and, even in the original study, not all splice variants were detected in all cell systems used (Koning, Sayers, et al., 2012). It was therefore important here to assess which of these transcripts are present in HUVEC, because some of the reported sequences might be lung epithelium-specific or, simply, not expressed in ECs. This assessment was undertaken by reverse transcriptase-PCR with transcript-specific primers (**Figure 3.1**), which revealed that five transcripts were expressed in HUVEC, including those of the two major isoforms PDCH1v1 and v2 (**Figure 3.2**). It is unclear why the primer pair for PCDH1v3 resulted in a 200 bp product, considering one of the primers for that reaction (WV013) does not anneal any other *PCDH1* transcripts. Furthermore, a primer-*BLAST* search for the primer pair of that reaction only yields non-*PCDH1* transcripts over 600 bp or below 50 bp. To speculate, if this band is not due to contamination and/or sample mishandling in all its three repeats, it could represent a different, hitherto unidentified PCDH1 splice variant; this would have to be confirmed by 3’ RACE or RNA-Seq experiments in HUVEC. This highlights a limitation of this RT-PCR approach, in that it would not have identified any unreported *PCDH1* transcripts that might be unique to ECs. Immunoblotting confirmed that the two main isoforms of PCDH1 could be detected, in line with previous biochemical reports in other cell systems (Faura Tellez et al., 2015). Furthermore, immunofluorescence confirmed their localisation at the cell membrane (**Figure 3.3**), as previously shown (Faura Tellez et al., 2016).

3.13.2. Characterising PCDH1 knockdown in HUVEC

Monitoring PCDH1 levels by immunoblotting over time allowed to confirm that siRNA duplexes resulted in maximal protein knockdown in the time window between 48-72 h after transfection (**Figure 3.4B**). These findings are in in concordance to kinetic studies of siRNA knockdown in the literature (Bartlett & Davis, 2006). Based on the respective transcripts, the two main PCDH1 isoforms are predicted to appear at around 114.7 and 133.7 kDa, yet they appear to be ~200 and ~220 kDa by reducing, denaturing PAGE instead: it is likely that endothelial PCDH1 is glycosylated, increasing its apparent size on gels. In support of that idea, there are experimental reports of four *N*-linked glycosylation sites (Asn305, Asn720, Asn813, Asn818) from mass-spectrometry studies (R. Chen et al., 2009; Danzer et al., 2012) and three other predicted glycosylation sites (Asn403, Asn618, Asn662; *UniProt* ID: Q08174) which, together, could account for the observed masses. PNGase F treatment of HUVEC lysate prior to immunoblotting would reveal whether this is the case, as the enzyme cleaves nearly all GlcNac–>Asn bonds (Tachibana et al., 1982). Knockdown was also confirmed by flow cytometry (**Figure 3.5**) when, for the only time throughout the project, one of the duplexes (siRNA-1) resulted in ostensibly less efficacious knockdown than the other: it is unclear why this would be the case, but the occurrence might be due to erroneous over-dilution of the siRNA stock (later discarded) prior to transfection, rather than there being any underlying biologically-relevant reasons. Nonetheless, this confirmed that flow cytometry detection directly correlated with immunoblotting detection, because in that instance the geometric mean of siRNA-1-treated cells was lower than that of cells treated with siRNA-2, mirroring their fainter bands in the immunoblot (**Figure 3.5C**). Silent mutations in the siRNA-2-targetted sequence were envisaged to allow PCDH1 overexpression that withstood knockdown (**Section 3.4**): immunoblotting confirmed this, and also unequivocally established that the two PCDH1 bands routinely observed in PCDH1 immunoblots were due to the two main isoforms, which co-migrated, and were knocked-down, with the overexpressed proteins.

3.13.3. Angiogenesis-mimicking *in vitro* assays upon PCHD1 knockdown

Five assays were employed, each of which tried to reproduce *in vitro* different steps of the angiogenic process (**Section 1.1.2**). Embedding a spheroid into a growth media-collagen matrix models the early angiogenic step of ECs eliciting filopodial projections into the abluminal milieu. For this assay, the final concentration of collagen was chosen as 1.6 mg/mL, which is complemented by the stiffness provided by 0.24% methyl cellulose, as a compromise between avoiding cell detachment but still allowing filopodia intrusion. Similar concentrations have been used by others (Blacher et al., 2014; Heiss et al., 2015), and small variations in the collagen content do not seem to dramatically affect cell invasiveness (Liu et al., 2020). Plating ECs on Matrigel instead is generally agreed to represent the latter stages of angiogenesis, by modelling cell differentiation, as HUVEC in this assay form capillary-like structures that have tight junctions but are likely not hollow (Staton et al., 2009). Importantly, most of the assays employed here took place over the course of a few hours, so that cell proliferation was not a confounding factor in their interpretation. To corroborate the observations from these short-term assays, longer experiments were undertaken, whereby ECs were plated on an established layer of fibroblasts. The latter mimic the stromal cells that surround ECs *in vivo*, and release extracellular matrix components that stimulate EC assembly in structures, likely lumenised (Bishop et al., 1999), that are more heterogeneous than those seen on Matrigel, and reminiscent of true capillaries. Complementing these assays, perhaps the most physiologically relevant assessment of the outcomes of Pcdh1 loss involved analysis of the vasculature during murine embryonic angiogenesis (**Chapter 6**).

These assays were carried out in HUVEC upon PCDH1 knockdown, obtained in the first instance by transfection with two different siRNA duplexes, used separately. These both resulted in the same phenotype when HUVEC were plated on Matrigel (**Section 3.5**) or when they were presented with bovine serum gradients (**Section 3.6**), but only siRNA-1 resulted in statistically different outcomes affecting HUVEC spheroid sprouting, monolayer wound recovery, and vessel-like assembly on fibroblasts (**Section 3.7**). Similarly, only one of two further duplexes, siRNA-3 and siRNA-4, resulted in phenotypic impairment of HUVEC sprouting on Matrigel, and the above assays resulted in no phenotypic differences when NCD-treated HUVEC were compared to HUVEC treated to an equimolar mixture of the four siRNAs mixed together (**Section 3.8**). Therefore, because PCDH1 knockdown by siRNA-1, and to a lesser extent siRNA-4, resulted in phenotypic outcomes in many *in vitro* assays when used alone, but not when diluted as part of a mixture, it was concluded that those initial observations were due to unexpected off-target effects mediated by the duplex. It is unclear why siRNA-1 should elicit any transcript-specific off-target effects, when a *BLAST* search for its sequence (**Table 2.8**), with thymidines replacing uracils, only retrieves *PCDH1* transcripts. However, it is recognised there is some scope for mis-targeting by siRNA duplexes due to their 3’ end being somewhat less critical in determining hybridisation specificity (Elbashir et al., 2001), which can result in sequence-determined but off-target effects (Carthew & Sontheimer, 2009). An alternative that would be very hard to investigate might be that siRNA-1 physically binds other proteins, thus altering their behaviour (Semizarov et al., 2003). A further alternative could be that transfection with siRNA-1 simply results in non-specific responses that alter cell behaviour, including impairing angiogenesis; this hypothesis would indeed be hard to distinguish experimentally from that of sequence-specific off-target effects.

3.13.4. Microarrays reveal several transcriptomic changes upon PCDH1 knockdown

To try to assess what off-target effects resulted from transfection of HUVEC with the above PCDH1 siRNAs, siRNA-treated cells were lysed and their mRNA pool was converted to cDNA, allowing for microarray analysis of their transcriptome. Computational pathway analysis (**Section 3.10**) revealed that, while most of the pathways were affected in the same direction by siRNA-1, siRNA-2, and the siRNA mixture, some were indeed predicted to be differentially affected. Among these, interestingly, cell migration/proliferation/survival pathways were predicted to be stimulated by the siRNA mixture, suggesting an anti-angiogenic role for endogenous PCDH1. However, these transcriptomic changes must translate into a moderate effect size, because pro-angiogenic outcomes were not apparent from the *in vitro* assays of this chapter, whereupon one would expect to observe increased motility in siRNA mixture-treated samples as compared to NCD treatment. Among the modulated upstream effectors was *DACH1* (**Figure 3.18**), a generally anti-angiogenic transcription factor predicted to be activated by siRNA-1. Interestingly given the implication of PCDH1 in TGF-β signalling (Faura Tellez et al., 2015), *DACH1* is one of the SMAD4 effectors that enable suppression of pro-proliferative signals downstream of TGF-β1 binding *in vitro* (Wu et al., 2003). Recently, however, Dach1 was shown to instead stimulate EC migration and coronary angiogenesis (Chang et al., 2017; Raftrey et al., 2020), and the effect of *DACH1* activation in HUVEC specifically remains to be established.

Given the large number of transcripts affected by each duplex and by the mixture (**Figure 3.16C**), a clear off-target candidate transcript could not be established. However, pair-wise comparisons of differentially affected transcripts in given treatments (**Section 3.11**) did highlight that many of the most strongly affected transcripts have a recognised role in cell motility and angiogenesis, suggesting that modulation of any (or of any combination) of these could have important consequences for HUVEC phenotypes. For example, the observed upregulation of *HMOX1* in siRNA-1 sample with respect to siRNA-2 samples (**Figure 3.20**) could result in anti-angiogenic behaviour, given the link between HMOX1-synthesised CO solute and antiangiogenic *in vitro* effects (Ahmad et al., 2015); this would result in suppression of angiogenesis, as observed in our *in vitro* assays. Downregulation of DLL4, also seen upon siRNA-1 treatment in the same comparison, could reinforce this, given the role of DLL4 in preventing tip cell behaviour and migration (**Section 1.1.2**). Likewise, comparison of siRNA-mixture and NCD treatments allowed the identification of other genes that were affected to a large degree by the mixture, many of which play recognised roles in angiogenesis and cell motility processes (**Section 3.12**) and may, therefore, impact HUVEC biology alongside the loss of PCDH1. However, because the phenotypic effect size (if any) might not necessarily correlate linearly to the level of up- or down-regulation of a given gene, studies targeting each of these individually in HUVEC would be required to assess whether they are of any relevance to explain the predicted activation of cell motility pathways upon siRNA mixture treatment.

If PCDH1 does indeed exert a physiological anti-angiogenic effect, one possibility that arises is that endogenous PCDH1 levels might need to be reduced to enable starting of the angiogenic programme. Therefore, PCDH1 expression should correlate with endothelial quiescence: this could be probed by comparing proliferating HUVEC to HUVEC from established monolayers, and analysing PCDH1 expression *via* immunoblotting. In this framework the expectation would be that proliferating HUVEC should display more abundant PCDH1 expression. In a targeted attempt at elucidating the function of PCDH1, the next chapter describes the identification of potential intracellular binding partners of the protein that might serve as downstream effectors.

CHAPTER 4: DETERMINING THE CYTOSOLIC INTERACTING PARTNERS OF PCDH1

4.1. Introduction

The aim of the experiments described in this chapter was to identify the interacting partners of the intracellular domain (ICD) of PCDH1 in the endothelium. Broadly, this involved expressing and isolating both the short (ICDv1) and full-length (ICDv2) versions of its cytosolic domain by affinity purification, using them as baits in a pulldown assay that had HUVEC lysate as the source of interactions, and then detecting by mass spectrometry the prey proteins that co-purified with the baits. Once a candidate interactor was found, a series of biochemical experiments identified which of its domains were responsible for co-purification with PCDH1, by means of overexpressing the PCDH1 ICD and presenting it with overexpressing lysates of each domain separately. Furthermore, both proteins localised around the cell membrane as assessed by immunofluorescence, and a proximity ligation assay between the two yielded the characteristic fluorescent signal expected from two proteins that co-localise within 25 nm.

Many transmembrane proteins act as angiogenic signal transducers by means of their cytosolic domain and related interactors, most notably VE-Cadherin, whose ICD interacts with a range of cytosolic proteins and allows both outside-in and inside-out signalling in endothelial cells (ECs), mainly to mediate their quiescence in fully formed vessels (Vestweber, 2008). The experiments in this chapter assessed whether a similar role for the PCDH1 ICD could be identified. The two main isoforms of PCDH1 arise from differential splicing of the immature *PCDH1* transcript after exon 3 (**Figure 3.1**). As a result, the known protein-protein interaction sequences termed Conserved Motif 1, 2, and 3 (CM1, CM2, CM3) are only present in the full-length PCDH1v2. Nonetheless, PCDH1v1 harbours a short stretch that is unique to it, therefore the initial screening experiments of this chapter included both isoforms for completeness. The only known cytosolic interactors of PCDH1 are SMAD3, which interacts with both PCDH1 isoforms (Faura Tellez et al., 2015), and PP1α, which interacts with CM3 and, as such, only with the longer isoform (Vanhalst et al., 2005). The second half of this chapter focuses on Desmoplakin (DP), which is here proposed as an interactor of PCDH1: there are no reports of DP associating with PCDH1, nor are there reports of PCDH1 associating with desmosomes.

4.2. The PCDH1 cytosolic domain was produced in mammalian cells to avoid degradation

In order to produce recombinant PCDH1 ICD for analysis by mass spectrometry, bacterial expression constructs encoding either its short (v1) or long (v2) version fused to a GST tag were first assembled, using HUVEC total cDNA as a template for the PCDH1 sequences and appropriately designed primers (**Table 2.6**). These constructs were transformed into an *E. coli* strain optimised for protein production under control of the *lac* operon. Production of GST-ICDv1 was induced in small batches of bacteria at different temperatures and for different amounts of time, to identify expression conditions that resulted in the highest yield. The GST-ICDv1 protein was purified from each bacterial mixture by means of glutathione beads pulldown, and expression conditions were compared on a stained SDS-PAGE gel (**Figure 4.1A**). Substantial protein degradation was observed in all conditions, even after only 2.5 hours induction, and even when inducing at lowered temperature. A host of degraded products under 55 kDa in size appeared in all conditions and, although a clear band in the expected 47 kDa region was noted in most conditions, further purification of this species could not be achieved by means of size-exclusion chromatography. On average, more prolonged production times did not increase yield, which remained stable at around 20 μg undegraded protein/100 mL bacterial culture; longer production time instead resulted in more severe degradation, with overnight production at room temperature resulting in no detectable levels of intact protein. In contrast, GST-alone production by the same bacteria resulted in one clean band, and roughly five times higher yield. GST-ICDv1 protein aggregation was also evident from the gel, with bands at

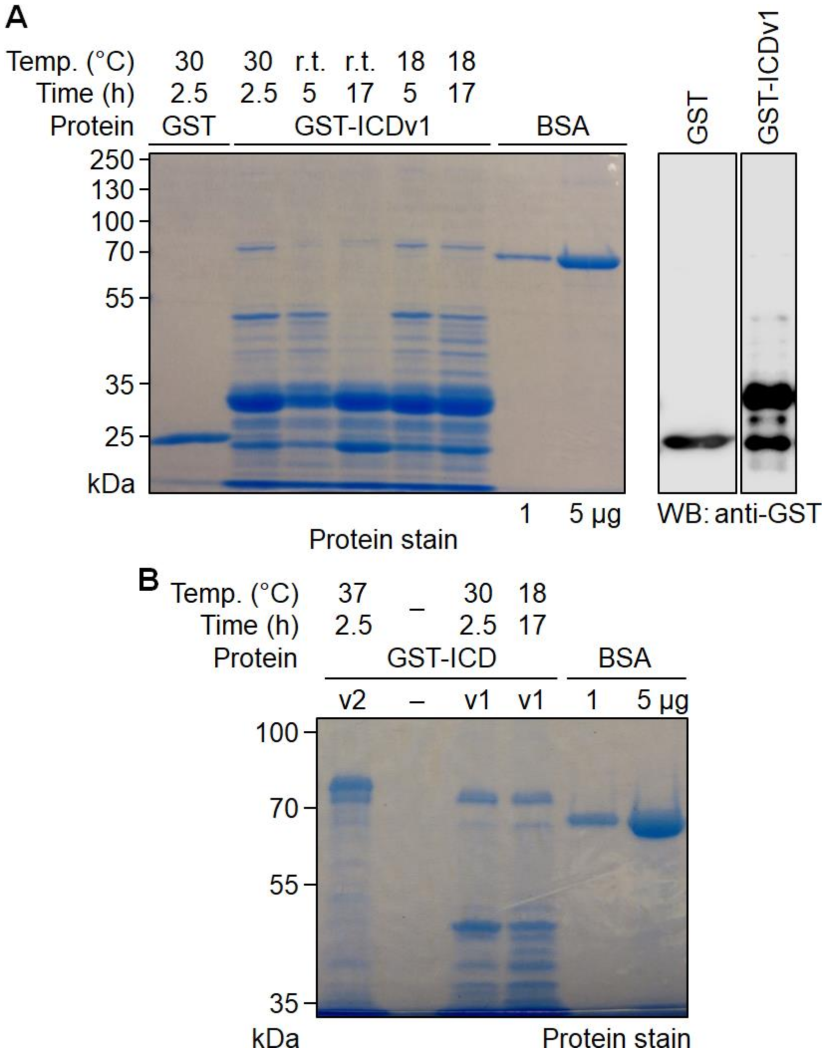

Figure 4.1. The two PCDH1 GST-ICDs can be expressed in *E. coli* cells, but degrade before affinity purification.

A. Stained, reducing SDS-PAGE gel of glutathione pulldowns executed on 100 µL BL21(DE3)pLysS cell extracts. Cells were transformed with either GST-ICDv1 or an empty GST plasmid, grown to log phase, and induced with IPTG for different lengths of time and at different temperatures, as indicated. Predicted GST-ICDv1 size = 47 kDa. For reference, known amounts of BSA were loaded alongside, as indicated. On the right: anti-GST blot of selected lanes from the gel on the left.

B. Stained, reducing SDS-PAGE gel of glutathione pulldowns executed on 100 µL cell extract of BL21(DE3)pLysS cells transformed with a GST-ICDv2 plasmid, grown and induced as in **A**. Predicted GST-ICDv2 size = 66 kDa. Two 100 µL cell extract samples from **A** (GST-ICDv1) were also pulled down and loaded, for comparison. For reference, known amounts of BSA were loaded alongside, as indicated.

around 70 kDa appearing in most conditions, and withstanding denaturation. A trial production of GST-ICDv2 resulted in ever more extensive protein degradation, and similar high-molecular-weight bands of unclear nature, again as assessed by glutathione pulldowns (**Figure 4.1B**). Production was therefore transferred to a mammalian host instead, HEK 293T cells, after assembling suitable pWPXL-based constructs that allowed transfection. Trial GST pulldown of cells 48 hours after transfection showed the degradation phenomenon was ameliorated for both the short and long ICD versions, albeit not entirely resolved (**Figure 4.2**). The yield was similar for the two, at around 5 μg protein/10-cm dish transfected with 9 μg DNA. Though this was lower than could in principle have been attained by bacterial production, these trial experiments established that the mammalian approach represented a viable alternative for GST-ICD protein production and isolation.

4.3. Mass spectrometry of GST-ICD pulldowns identifies Desmoplakin as a candidate endothelial interactor

Having established a method to generate recombinant versions of the PCDH1 ICD, the next step was to use them to identify potential binding partners in ECs. Preparation of GST-ICD proteins in mammalian hosts for mass spectrometry was carried out as described in the previous section, scaling up production appropriately. Cell lysates containing the two proteins were mixed in a 1:1 ratio, and the mixed proteins were purified by glutathione affinity purification. HUVEC lysate, pre-cleared of GST binding proteins, was then added, to present endothelial binding partners to the isolated GST-ICDs. This process was separately repeated using GST protein isolated from *E. coli* as previously described (**Figure 4.1A**), to be used as a control sample. After denaturation of the glutathione beads, proteins were separated by SDS-PAGE (**Figure 4.3A**), and the stained gel was chopped into small fragments, allowing trypsin digestion. The peptides thus obtained were extracted from the gel with formic acid and

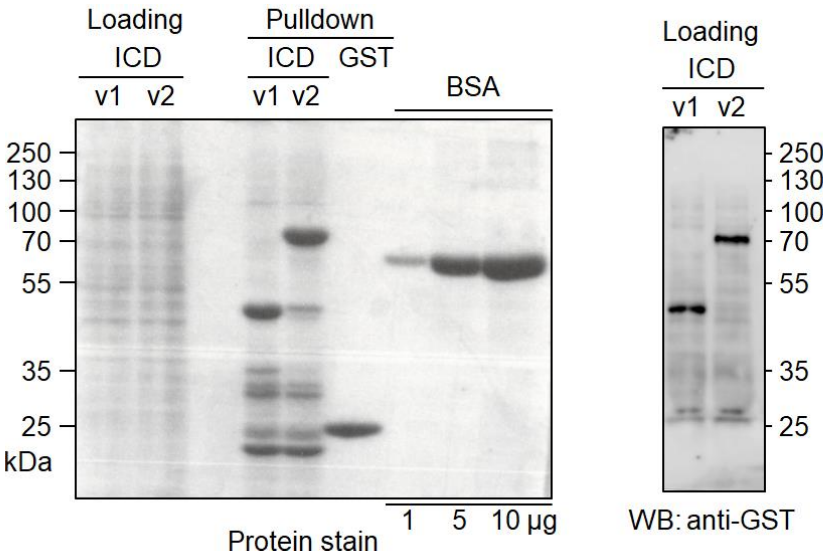

Figure 4.2. The two PCDH1 GST-ICDs can be expressed in HEK 293T cells, with less degradation than in *E. coli*.
Left: Stained, reducing SDS-PAGE gel of glutathione pulldowns executed on cell extracts from a 10-cm dish of HEK 293T transfected with 9 µg either GST-ICDv1 or v2. Cells were lysed 48 hours after transfection. The loading controls only have 0.25% of the lysate. The lysate for the GST pulldown was obtained from suitably transformed *E. coli*. For reference, known amounts of BSA were loaded alongside, as indicated. Right: anti-GST blot of loading lanes from the gel on the left.

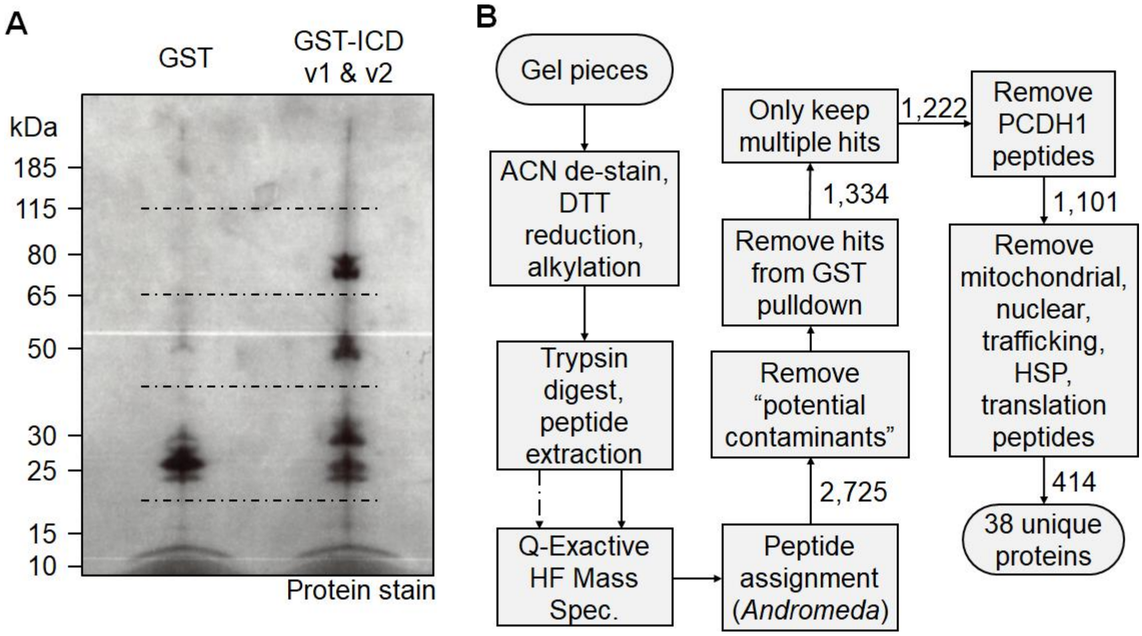

Figure 4.3. Mass spectrometry profile of mammalian GST-ICDs interactors.

A. Stained, reducing SDS-PAGE gel of glutathione pulldowns executed on GST-alone or GST-ICDs (v1+v2, 1:1) HEK 293T lysates, followed by addition of pre-cleared HUVEC lysate from fifteen 10-cm dishes each. Each lane was cut into five pieces (roughly along the horizontal segmented lines), which were then chopped into minute fragments and used in **B**.

B. Brief overview of the proteomic analysis workflow undertaken on the gel fragments produced in **A**. Each of the ten samples produced was analysed twice on the mass spectrometer. Spectrometer operation and peptide assignment were carried out by the Advanced Mass Spectrometry Facility of the University of Birmingham. Numbers alongside arrows indicate the number of peptides in the GST-ICDs hit-list after each step, subcellular localisation and function were consulted on the *UniProt* database. ACN: acetonitrile; DTT: dithiothreitol; HSP: heat shock protein.

analysed, in two separate runs, on an Orbitrap mass spectrometer (**Figure 4.3B**). All keratin peptides were highlighted as "potential contaminants" by the peptide assignment engine, and were thus removed from the list of hits, as it was assumed that they arose from contamination due to sample handling. Peptides appearing in the GST control pulldown, and proteins for which only one peptide was recorded, were manually discarded, again on assumptions of contamination. Furthermore, peptides of proteins known to reside in well-defined subcellular compartments (mitochondria, nucleus) were also removed, together with peptides of heat shock proteins: it was not envisaged that these would feasibly interact with PCDH1 physiologically, but rather that they must have associated with, among other proteins, PCDH1 as a result of the sudden high osmotic pressures and temperature change experienced when the cells were lysed, despite handling the lysates on ice. Finally, peptides associated with protein trafficking and/or translation were also manually removed, reasoning that these must have complexed with immature PCDH1 peptides still being translated at the time of lysate preparation, and would not normally associate with mature PCDH1 proteins at the cell membrane. A summary of the remaining proteins that were detected is presented in **Table 4.1**. The protein from which most peptides were detected was Desmoplakin (82 peptides in total), a cytosolic member of the desmosomal complex. Many recognised members of this subcellular complex were also detected, with a total of 69 other desmosome-related peptides, reinforcing the idea of a putative endothelial interaction between PCDH1 and Desmoplakin (DP). For this reason, the investigations that ensued focussed on corroborating and exploring this interaction.

4.4. Desmoplakin co-purifies with PCDH1

To confirm the findings of the mass spectrometry experiment by other techniques, PCDH1 was immunoprecipitated from HUVEC to assess whether DP would co-purify. The immunoblots (**Figure 4.4A**) were difficult to interpret because, despite successful PCDH1 immuno-

Table 4.1. PCDH1-ICD mammalian interactome.

Gene name	Protein name	Peptides found
DSP	**Desmoplakin**	**82**
CBR1	Carbonyl reductase [NADPH] 1	65
CBR3	Carbonyl reductase [NADPH] 3	35
JUP	**Junction plakoglobin**	**22**
TUBA1C;TUBA1A;TUBA1B	Tubulin alpha-1	20
DSC1	**Desmocollin-1**	**19**
DSG1	**Desmoglein-1**	**18**
ACTB	Actin, cytoplasmic 1	12
FAM98A	Protein FAM98A	12
C16orf13	UPF0585 protein C16orf13	11
GAPDH	Glyceraldehyde-3-phosphate dehydrogenase	8
PRDX1	Peroxiredoxin-1	8
RCC2	Protein RCC2	8
TUBB4B	Tubulin beta-4B chain	8
ENO1	Alpha-enolase	7
PPM1G	Protein phosphatase 1G	7
PKP1	**Plakophilin-1**	**6**
CKAP4	Cytoskeleton-associated protein 4	5
LGALS7	Galectin-7	5
S100A9	Protein S100-A9	5
TGM3	Protein-glutamine gamma-glutamyltransferase E	5
SERPINB12	Serpin B12	4
SBSN	Suprabasin	4
YWHAZ	14-3-3 protein zeta/delta	3
ALPK2	Alpha-protein kinase 2	3
CFL1	Cofilin-1	3
DSC3	**Desmocollin-3**	**3**
KPRP	Keratinocyte proline-rich protein	3
PRDX2	Peroxiredoxin-2	3
FAM98B	Protein FAM98B	3
POF1B	Protein POF1B	3
TUBB	Tubulin beta chain	3
C7orf43	Uncharacterized protein C7orf43	3
ABI1	Abl interactor 1	2
AHCY	Adenosylhomocysteinase	2
MYH9	Myosin-9	2
CDSN	**Corneodesmosin**	**1**
FAT3	Protocadherin Fat 3	1

List of intracellular PCDH1 interactors obtained by mass spectrometry, and refined as per **Section 4.3**, with the number of unique peptides found for each. Names of known desmosome-associated proteins are in bold.

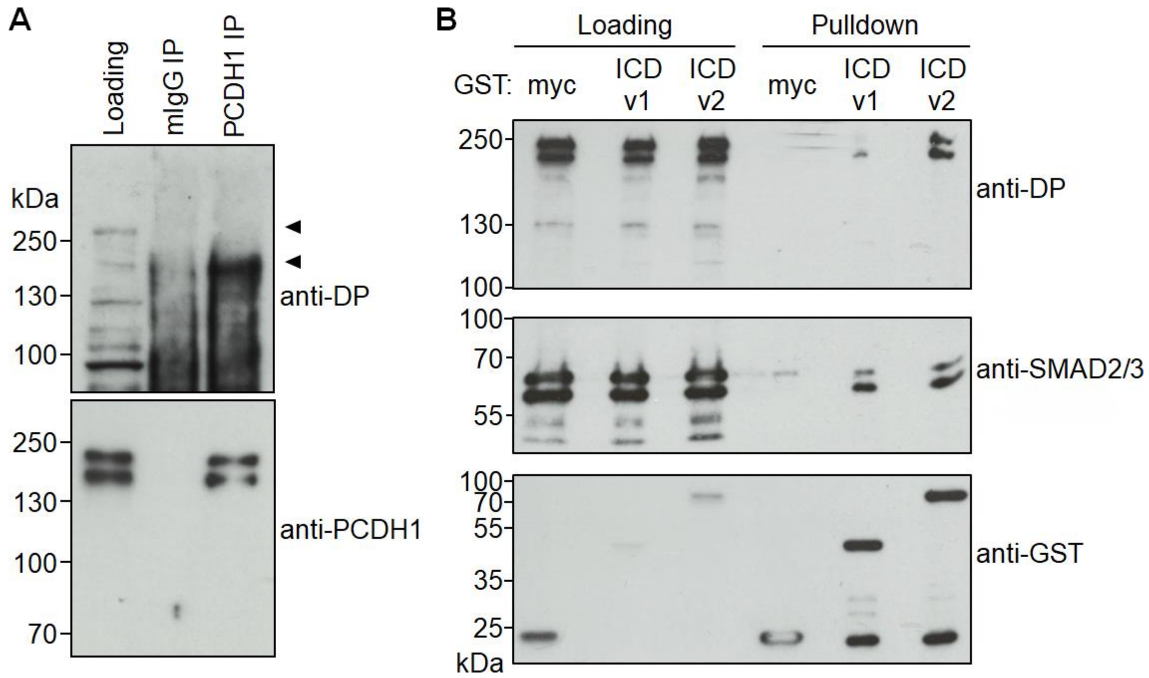

Figure 4.4. Desmoplakin co-purifies with endogenous PCDH1 and overexpressed GST-ICDv2.
A. Immunoblotted SDS-PAGE gel loaded with immunoprecipitations from untreated HUVEC cell lysate: 11×10-cm confluent HUVEC dishes were lysed, merged, and split across two tubes, one to be immunoprecipitated with 1 µg mouse-anti-PCDH1 antibody and the other with 1 µg mouse IgG protein as control. The "Loading" lane was loaded with ~1% of the total cell lysate used as input. Arrowheads indicate the expected size of the two DP isoforms.
B. Immunoblotted SDS-PAGE gel loaded with glutathione pulldowns from lysates of HEK 293T cells transfected with a GST-fusion protein: myc as control, PCDH1-ICDv1 or v2. "Loading" lanes were loaded with ~1% of the total cell lysate used as input. 90% of the final pulldown volume was loaded on the gel to be probed for DP and SMAD2/3, and the remaining 10% on another gel, to be probed for GST. Representative blots from three repeats.

precipitation, the DP signal was smeared down most of the gel lane, with multiple non-specific bands appearing. Nonetheless, DP signal did seem to appear around the expected sizes for the DP doublet (around 250 kDa), while the control lane presented no such signal, suggesting at least some degree of co-immunoprecipitation. Because of such difficulties in dealing with endogenous DP levels in HUVEC, a separate experiment was designed to test whether endogenous DP co-purified with GST-ICDs in transfected HEK 293T cells instead. The immunoblot immediately showed that DP expression levels were clearly higher in this cell line than in HUVEC (**Figure 4.4B**), resulting in a much clearer signal in loading lanes carrying whole cell lysate. DP was successfully co-purified with the GST-ICD construct in this setting, consolidating the mass spectrometry findings. Furthermore, unlike the earlier spectrometric data, this co-purification experiment could return isoform-specific information, as the lysates from either transfection (ICDv1 and v2) were blotted separately. It was apparent that the co-purification signal of endogenous DP was much stronger for ICDv2, suggesting the interaction between PCDH1 and DP is mediated by amino acid sequence(s) only present in the longer isoform, although a faint signal was still identifiable in the ICDv1 lane, which prevented discounting interaction altogether. These pulldown samples were also probed for the R-SMAD couple SMAD2 and SMAD3, given reports of co-immunoprecipitations between PCDH1 and SMAD3 in primary human epithelial cells (Faura Tellez et al., 2015). The immunoblot showed clear signals of co-purification for both PCDH1 isoforms. The antibody used as probe recognises both SMAD2 and SMAD3 as a doublet and, while both bands appeared in the case of PCDH1v1 and v2, the upper band (SMAD2) was also present in the lane where control GST-myc protein was loaded, suggesting SMAD2 interacts with GST itself. In contrast, the lower band (SMAD3) was only detected in the presence of PCDH1 ICD, confirming previous reports in the literature that SMAD3 interacts with both PCDH1 isoforms (Faura Tellez et al., 2015).

4.5. Close interaction of Desmoplakin with PCDH1 is confirmed by proximity-sensitive fluorescence assays in cell lines

Mass spectrometry, pulldown, and co-immunoprecipitation experiments, as outlined in the previous sections, only confirmed the PCDH1-DP interaction taking place between cell lysates. To verify that this is the case in cells too, assays based on immunofluorescence were next carried out. Initial experiments undertaken in HUVEC as the model system failed to yield convincing fluorescence signals, so it was decided to employ other cells instead. Immunofluorescence in HEK 293T cells grown on glass coverslips, and transfected with the full length PCDH1v2-myc construct previously described (**Section 3.4**), confirmed that both transfected PCDH1 and endogenous DP localised to the cell membrane region (**Figure 4.5A**). The fluorescence signal was absent in control coverslips treated with no primary antibodies, confirming that signal was due to specifically bound secondary antibody-fluorophore conjugates rather than unwashed, otherwise immobilised fluorophores. This experiment further supported the previously reported observation (**Section 3.4**) of endothelial PCDH1 signal being highest at sites of intercellular membrane contact. These observations were recapitulated in HaCaT (a keratinocyte cell line) transduced with the same plasmid, and then similarly immunostained for myc, again clearly detecting both overexpressed PCDH1v2 and endogenous DP (**Figure 4.5B**). Automated analysis of the spatial profiles of the signals revealed similar subcellular distributions for the two proteins, again strongly localised to membrane-membrane interfaces.

These observations are however subject to the resolution limit of the microscope, which is subject to the physical phenomenon of the diffraction of light. This limitation renders the positions of different sources of light, such as those of fluorescently labelled antibodies, impossible to identify accurately below 200-250 nm in the range of wavelengths employed for

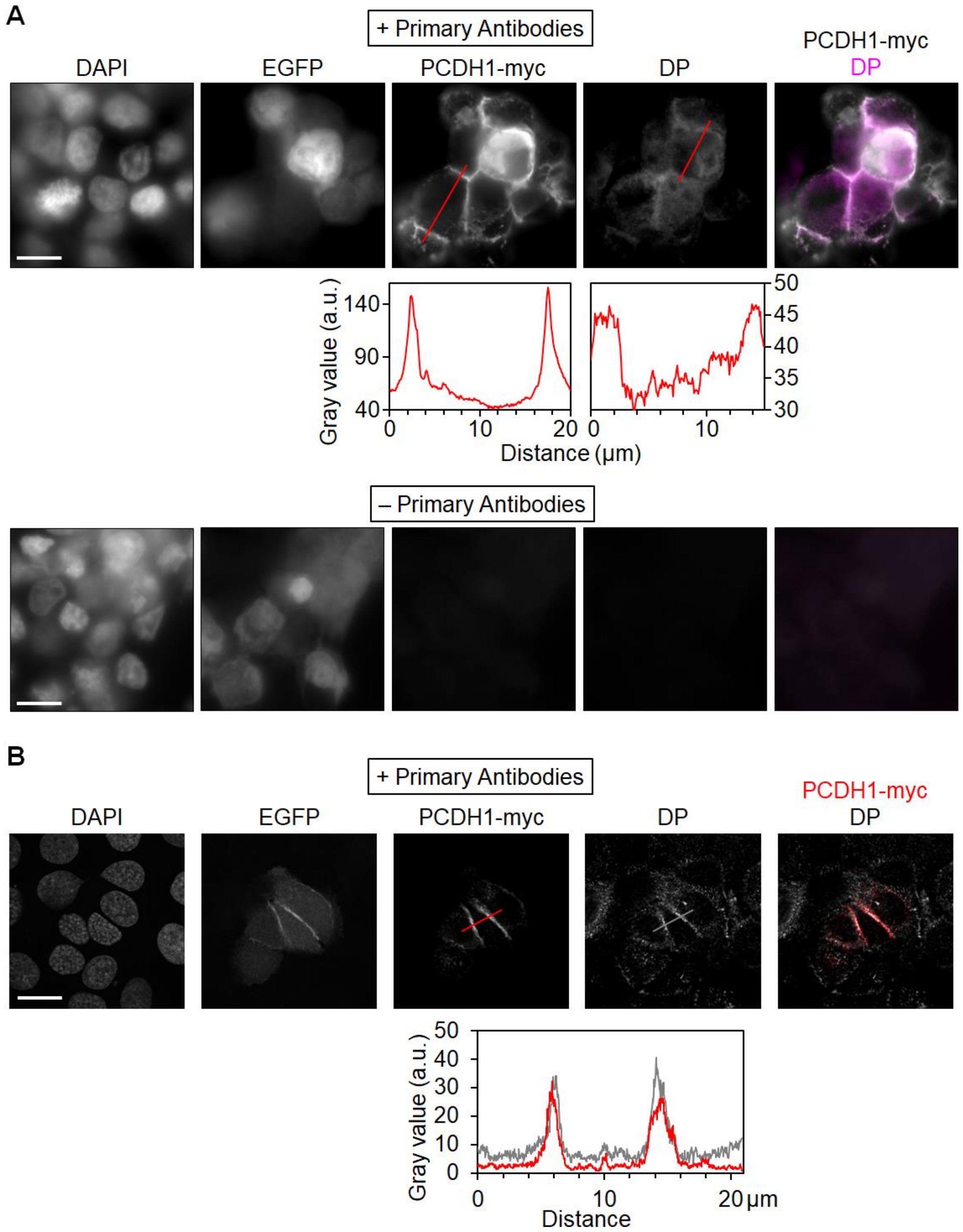

Figure 4.5. PCDH1-myc and Desmoplakin both localise near the plasma membrane.
A. Immunofluorescence of HEK 293T cells PEI-transfected with the PCDH1v2-myc-2A-EGFP plasmid. The fixed cells were treated with anti-myc and anti-DP antibodies, visualised by AF568- and AF647-conjugates respectively, on an epifluorescence microscope. Histograms below images show the pixel intensity value along the red bar, measured by the Plot Profile function of *ImageJ* from its bottom-right end. White scalebar = 10 µm.
B. Immunofluorescence of HaCaT cells transduced with virions harbouring the same plasmid used in **A**. The same staining strategy as in **A** was also employed, but coverslips were imaged on a Zeiss 880 confocal microscope instead. White scalebar = 20 µm.

fluorescence microscopy. Therefore, any pair of fluorescent molecules in a radius of 250 nm will appear to "co-localise", however true protein-protein interactions typically happen in spatial ranges at least one order of magnitude smaller. It follows that standard fluorescent imaging of immunolabelled samples cannot conclusively prove interaction. To overcome this limitation, a commercially sourced kit for proximity ligation assays (PLA) was employed on samples of HaCaT cells transduced as above. Immunolabelling carried out as per the PLA protocol ensures, by design, that fluorescence signal appears only if the two probed proteins are within 25 nm of each other. Standard microscopes were therefore sufficient to image coverslips of HaCaT cells that had undergone PLA (**Figure 4.6**), revealing that fluorescent puncti were observable only around EGFP-positive (i.e. transduced) cells treated with anti-DP and anti-myc antibodies, or in control conditions treated with anti-DP and anti-Plakoglobin antibodies – Plakoglobin being a known interacting partner of DP in the cytosolic region of desmosomal assemblies. The PLA signal in PCDH1v2-transduced cells appeared largely to occur in areas between the nuclei, suggesting cell membrane localisation. Puncti were observed both in PCDH1v2- and PCDH1v1-expressing cells, albeit much less dense in the latter case, an observation that mirrors that made from biochemical analyses (**Section 4.4**). Overall, these experiments support the hypothesis of an interaction between PCDH1 and DP.

4.6. The Head domain of DP co-purifies with PCDH1

The next step consisted of mapping this interaction to a more precise region of the DP protein, which is extremely large, comprising over 2,800 amino acids. Differential splicing of *DSP* transcripts results in DP normally being expressed as two separate isoforms, full-length DPI and shortened DPII (**Figure 4.7A**), which differ only in the length of the central coiled-coil, the "rod" domain. The rod domain allows for self-dimerisation, in a similar fashion to that observed among intermediate-filaments proteins (Green et al., 1992), and has not been reported to interact

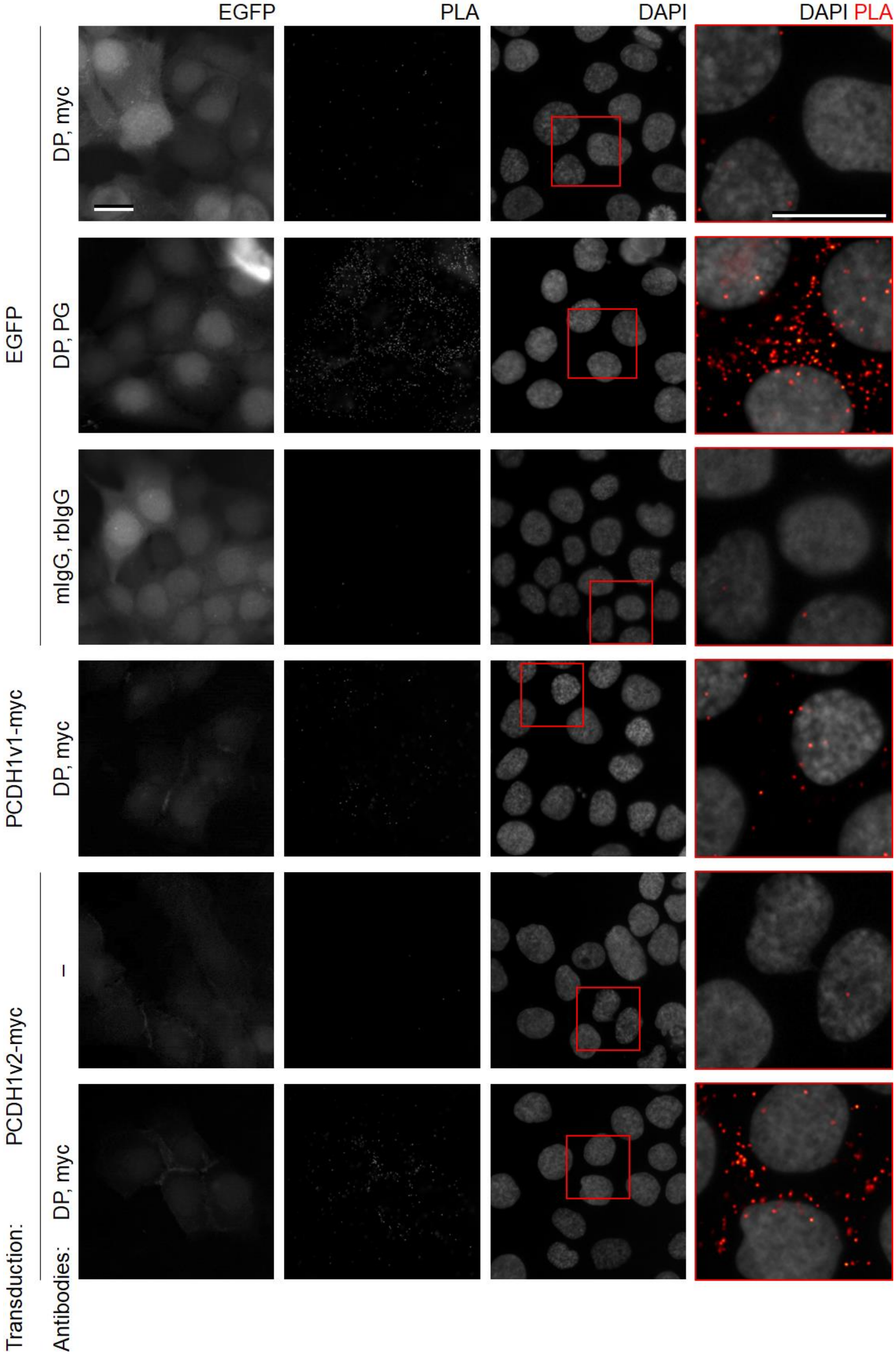

Figure 4.6. PCDH1-Desmoplakin interaction in HaCaT results in PLA signal.

(Continued from previous page)
Proximity ligation assay carried out on HaCaT cells transduced with virions harbouring PCDH1, and fixed 2 days after infection. As controls, HaCaT were instead transduced with EGFP only, and incubated with different primary antibodies (first three rows). As a further control, primary antibodies were also omitted altogether (fifth row). The right-most quadrants are enlarged views of the red insets to their left, and are a merge of signals from the DAPI and PLA channels. Representative images from three repeats. Scale bars = 20 μm. mIgG: mouse IgG; PG: Plakoglobin (γ-catenin); rbIgG: rabbit IgG.

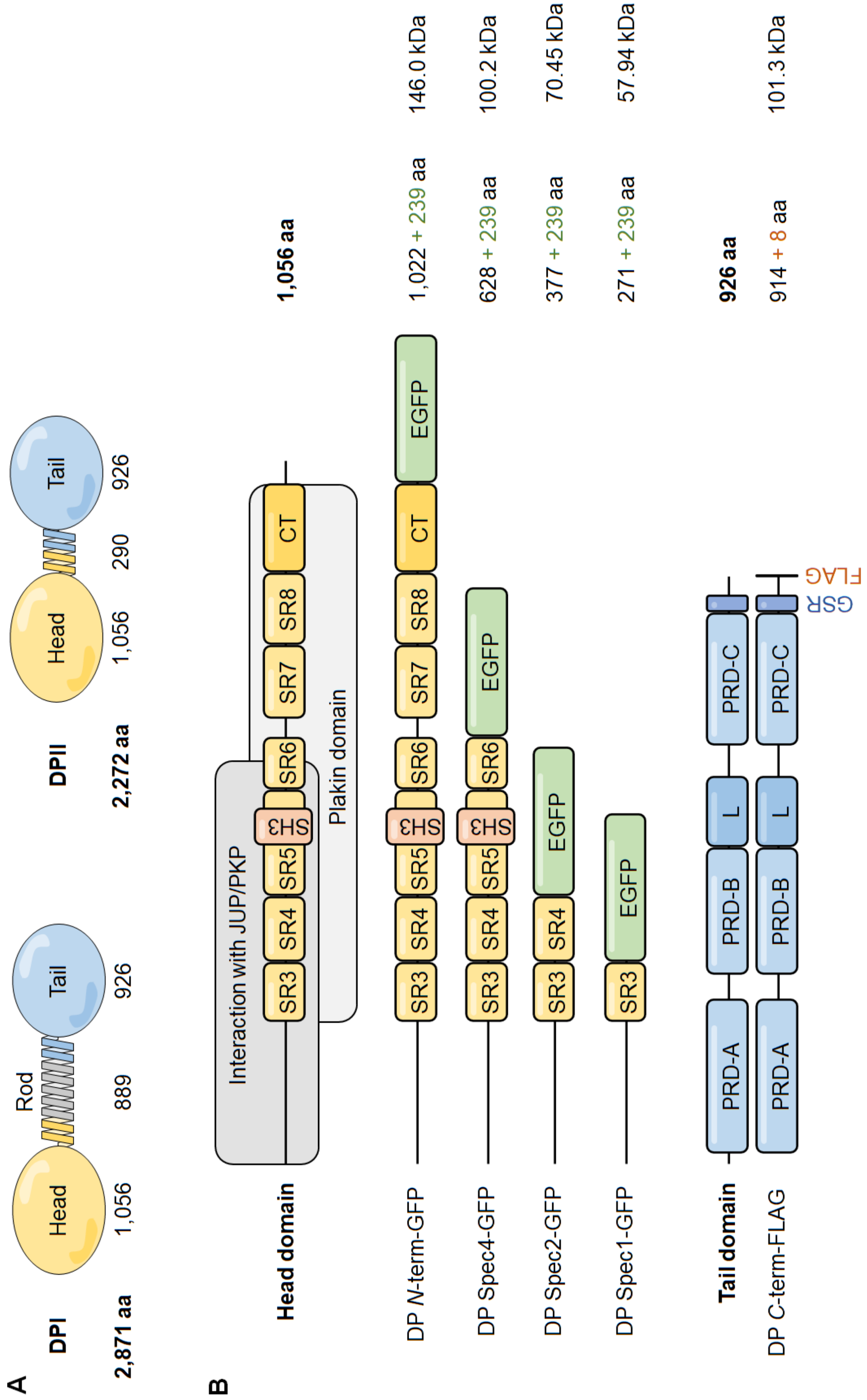

Figure 4.7. Human Desmoplakin structure and related plasmids. *(Caption overleaf)*

(Continued from previous page)
A. Diagrammatic representation of the two human Desmoplakin isoforms, DPI and DPII, arising from differential splicing of the central rod domain. As a result, the two globular domains at either end, the *N*-terminal Head domain and the *C*-terminal Tail domain, remain unchanged across the two isoforms and are both probed by all anti-DP antibodies used in this Thesis. The amino acid length of each domain is reported.
B. A more detailed view of the two globular domains of human Desmoplakin. The colour scheme is consistent with that used in **A**, and features are drawn to scale based on amino acid length. Plasmids encoding parts of or entire domains, as used in this chapter, are also shown. The official numbering of Desmoplakin's Spectrin repeats, reported in the Figure, is based on sequence homology to those of Plectin (Al-Jassar et al., 2011). For ease, however, plasmids are named after the total number of repeats they code for *e.g.* the "Spec4" plasmid produces a partial Desmoplakin protein truncated after the fourth Spectrin repeat, SR6. The predicted molecular size of each truncation is given after its amino acid length. Tail domain nomenclature is after Kang et al. (2016). JUP: junction plakoglobin (γ-catenin); L: linker; PKP: plakophilin; PRD: plakin repeat domain; SH3: SRC Homology 3; SR: Spectrin repeat.

with other proteins, so it was not considered as a reasonable candidate for mediating interaction with PCDH1. Their rigid molecular arrangement makes it possible for DP dimers to orient themselves linearly in the cytosol, with the *N*-terminus towards the cell membrane, and the *C*-terminus towards the intermediate filaments. The attention was then focussed on the two globular domains at each of these ends, the *N*-terminal Head domain and the *C*-terminal Tail domain. The former is a known protein-protein interaction site, and is reported to bind Plakoglobin (γ-catenin) and Plakophilin (**Figure 4.7B**); it is comprised of seven divergent Spectrin repeats, each bearing sequence similarity to those of Plectin (Al-Jassar et al., 2011), another very large desmosomal protein. At the other end of DP is the Tail domain, slightly smaller, which is comprised of three repeating domains (A to C) and is the site of intermediate filaments binding.

To further probe the nature of the PCDH1-DP interaction, pulldown experiments were carried out after transfecting HEK 293T cells with plasmids expressing either the *N*-terminus (Head) or the *C*-terminus (Tail) of DP, tagged to GFP and FLAG, respectively (**Figure 4.8A**). Given that previously a more robust interaction of DP was observed with PCDH1v2, these experiments focussed on this isoform. The DP cell lysates were each added to GST-ICDv2 bound to glutathione beads; immunoblotting revealed that GST-ICDv2 pulldown resulted in co-purification of the DP *N*-terminus (**Figure 4.8B**). In contrast, no signal was detected in control pulldowns, i.e. those carried out between the ICD and GFP alone, and between GST-myc and the DP *N*-terminal domain. Furthermore, by immunoblotting the pulldown carried out between GST-ICDv2 and the DP *C*-terminus, no signal was detected other than in the input whole cell lysate (**Figure 4.8C**). Therefore, because only the Head domain co-purified with the PCDH1 cytosolic domain, this experiment confirmed the idea that DP orients itself in the cytosol with its *N*-terminal end towards the inner side of the cell membrane, so as to direct itself

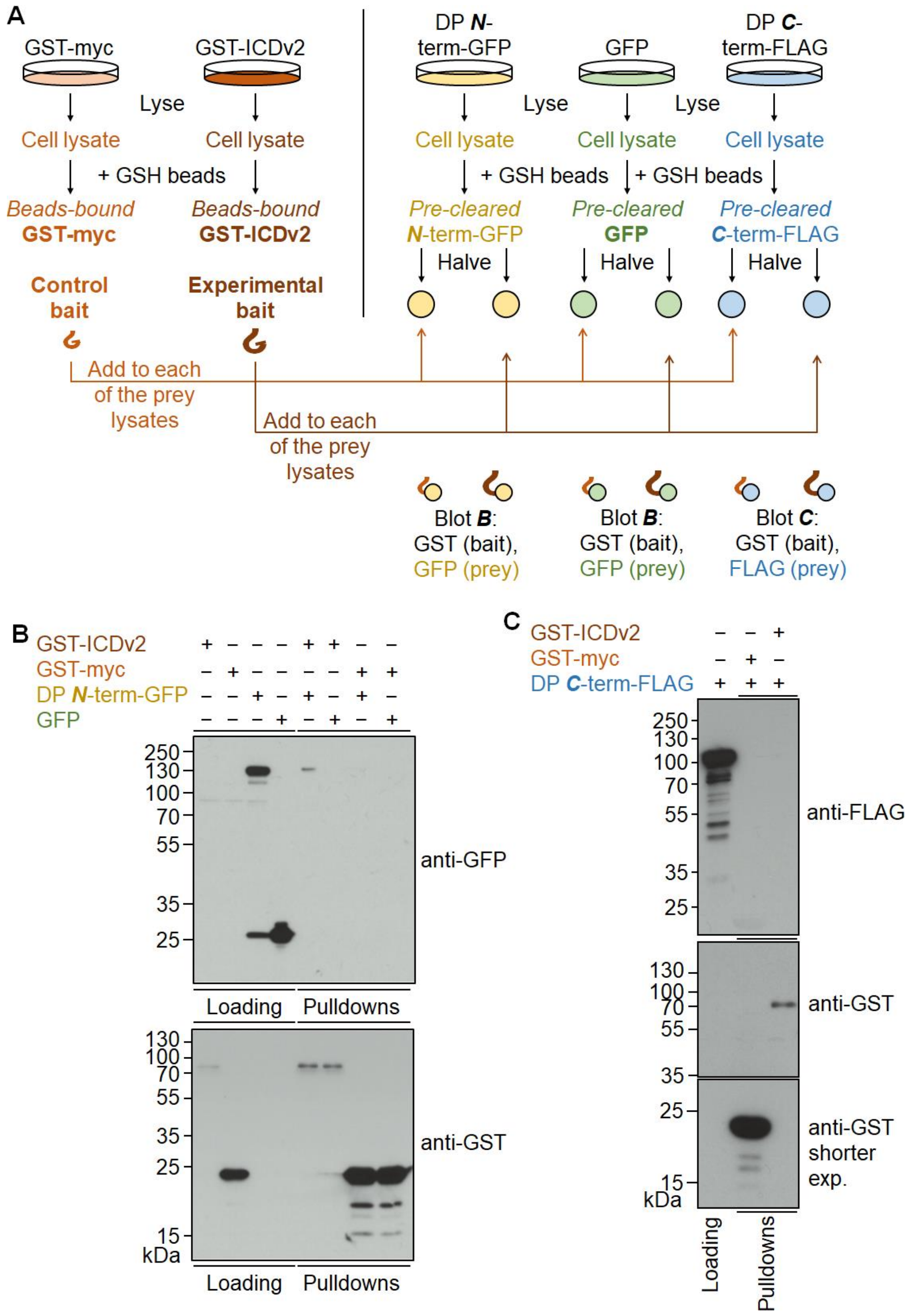

Figure 4.8. PCDH1 GST-ICDv2 pulls down the *N*-terminus of Desmoplakin.
(Caption overleaf)

(Continued from previous page)
A. Scheme of the experimental procedure. HEK 293T cells were separately transfected, and lysates were incubated with GSH beads, to bind the GST-tagged "bait" proteins (left), or to pre-clear the "prey" lysates (right). The beads bound to the GST proteins were then added evenly across the pre-cleared lysates, and finally denatured.
B. Immunoblotted SDS-PAGE gels loaded with glutathione pulldowns from lysates of singly-transfected HEK 293T cells. Lysates from 10-cm dishes were either purified (GST-fusions) or pre-cleared (GFP-fusions) with GSH-agarose beads. Each pulldown was then performed by adding GFP lysate to GST-bound beads: given expression differences, 15 times less GFP-alone lysate was used than GFP-DP lysate, to achieve similar protein concentration. The gel to be probed for GST was loaded with 12% final pulldown volume, the remainder was loaded on the gel to be probed for GFP. "Loading" lanes in the GFP gel were loaded with ~1% of the total cell lysate as isolated. Representative blots from three repeats.
C. Immunoblotted SDS-PAGE gels loaded with glutathione pulldowns from lysates of singly-transfected HEK 293T cells. DP-FLAG lysate from a 10-cm dish was pre-cleared as in **B**, and then added to GST-bound beads as prepared in **B**. Gels were loaded as in **B**.

towards the cytosolic tail of PCDH1.

4.7. The *N*-terminal half of the DP Head domain is required for co-purification with PCDH1

Having established that PCDH1 ICD interacts with the Head domain of DP, the next aim was to further delineate the binding site within this large *N*-terminal domain, which is over 1,000 amino acids in length. Constructs were assembled encoding different truncated versions of this domain (**Figure 4.7B**), to map this interaction more precisely. These constructs encompassed the very *N*-terminus of the protein, and were truncated *C*-terminally after the first (Spec1), the first two (Spec2), or the first four (Spec4) of the seven Spectrin repeats that comprise the Head domain. In all cases, the *C*-terminal GFP tag was retained. Because large differences in expression among this new set of constructs were noted, different volumes of lysates from transfected HEK 293T were loaded in the following experiment, to obtain balanced GFP-fusion protein loading amounts across all truncations. The immunoblots of the pulldowns thus undertaken (**Figure 4.9**) showed the *N*-terminus again co-purifying with the GST-ICDv2 constructs, as previously noted (**Figure 4.8B**). The Spec4-GFP construct also co-purified, but signal failed to be detected for the two shorter constructs. Therefore, by showing that truncation of the DP Head domain down to just the first two SR resulted in failed co-purification, this experiment suggests that interaction between PCDH1 and DP involves the first three or four Spectrin repeats of DP.

4.8. Discussion

Work in this chapter aimed at identifying endothelial cytosolic interactors of PCDH1. Production of the long (ICDv2) and short (ICDv1) isoforms of PCDH1 was carried out in HEK 293T cells to minimise degradation. Mass spectrometric analysis identified a desmosomal

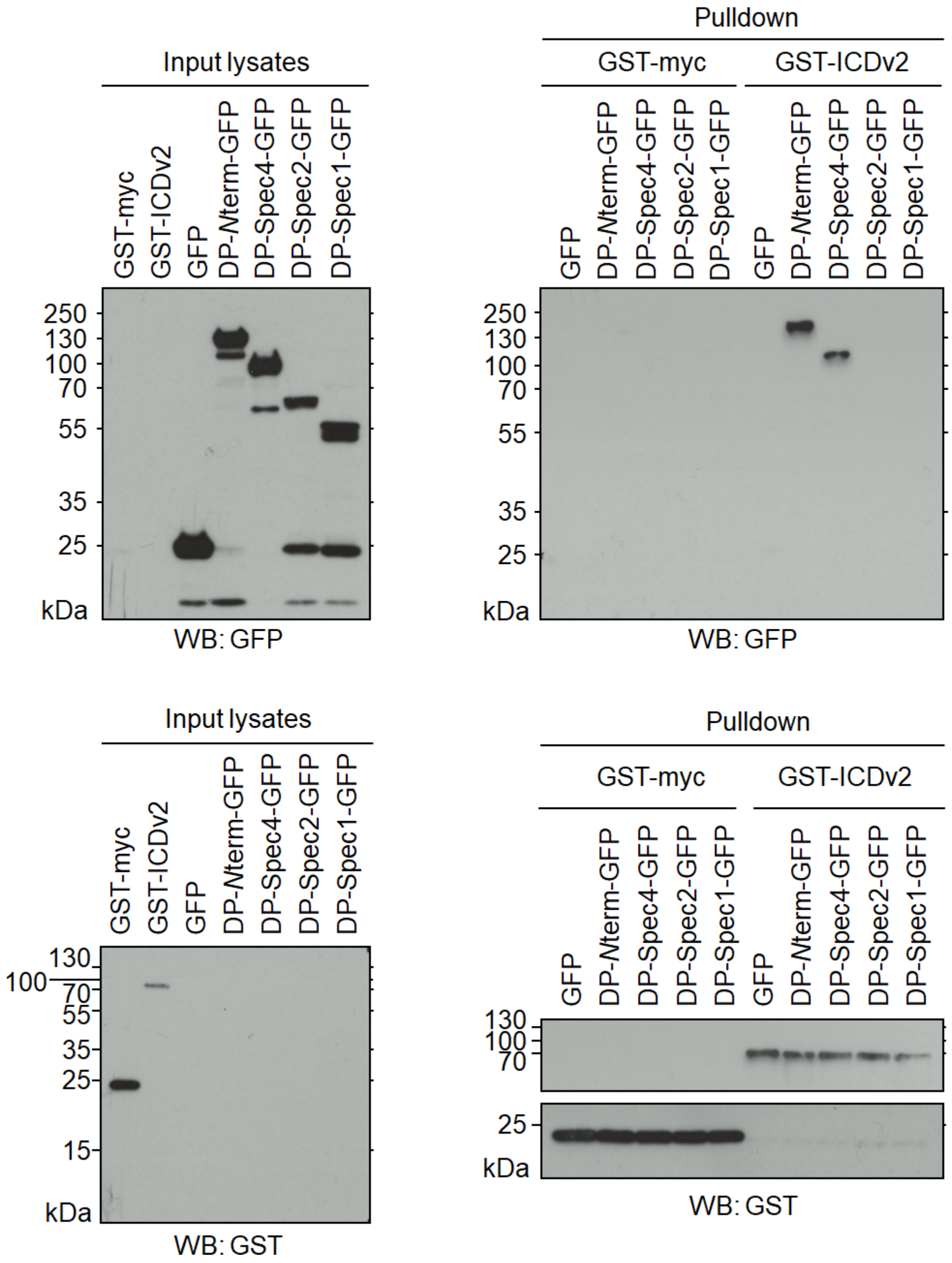

Figure 4.9. The first four Spectrin repeats of DP are required for interaction with PCDH1. Immunoblotted SDS-PAGE gels loaded with glutathione pulldowns from lysates of singly-transfected HEK 293T cells. Lysates from 10-cm dishes were either purified (GST-fusions) or pre-cleared (GFP-fusions) with GSH-agarose beads. Each pulldown was then performed by adding GFP lysate to the GST-bound beads: given expression differences, 50 times less GST-myc lysate than GST-ICDv2 lysate was used, to achieve similar protein concentration. Similarly, 20 times less GFP-alone and GFP-Spec4 lysates were used than GFP-DP lysate, and half as much GFP-Spec2 and GFP-Spec1 lysates were used. "Input" gels, left, were loaded with ~2% of the total cell lysate used for pulldowns. Representative blots from three repeats.

protein, Desmoplakin (DP), as the most abundant candidate interactor. Co-purification of PCDH1 and endogenous DP in HUVEC proved difficult, but pulldown and fluorescence-based assays in HEK 293T and HaCaT cells corroborated the findings. Pulldowns of truncated versions of DP located the interaction between PCDH1v2 and the first three/four Spectrin repeats of DP. Overall, these findings put forth a novel interaction between DP and PCDH1, suggesting a previously unknown association between PCDH1 and the cytoskeleton.

4.8.1. Mass spectrometry identifies DP as PCDH1 interactor

PCDH1 ICD production in *E. coli* resulted in significant degradation of both isoforms (**Figure 4.1**). In line with this, the calculated Instability Index (Guruprasad et al., 1990) of GST-ICDv1 is 45.96, suggesting some degree of instability arising from its amino acid sequence. Furthermore, the GST-ICDv2 Instability Index is even larger (59.03), and indeed its band was even less noticeable in stained pulldown gels than that of ICDv1. These observations suggest that ICD degradation is at least is part due to intrinsic instability, which is supported by the fact that ICD production in HEK 293T also resulted in some degree of degradation, despite increasing the yield significantly (**Figure 4.2**). Given the exploratory nature of the mass spectrometric experimental setup that followed purification, degradation *per se* was not deemed too significant a problem because, while the ICDs might have degraded or been cleaved at any point of their primary sequence, the GST tag would still have to be intact to allow affinity purification – and any distally-shortened ICD peptides would at most result in artificial enrichment of a subset of proteins that interact with the GST-proximal sequence but, overall, all possible interactors would still be detected. One drawback of producing the proteins in mammalian cells is the fact that any interactors detected cannot be ascribed as specifically endothelial despite having added HUVEC lysate to the isolated GST-ICDs, because any interactors could have been carried over from the original HEK 293T system; this would be supported by the observation that ECs do not express Desmogleins nor Desmocollins (Garrod et al., 2002), members of which families were in fact detected (**Table 4.1**), suggesting at least some degree of HEK 293T carry-over. While DP has been reported in numerous mass spectrometry datasets as “contaminant” (*cf.* CRAPome entry for *DSP* gene, Mellacheruvu et al. (2013)), all members of the desmosomal complex were also detected in this dataset, some of which, such as PKP1 and DSC3, were only considered contaminants in < 5% of the reported datasets; this gave more confidence in pursuing DP as a potential interactor. In fact, because DP interacts, albeit indirectly, with the intermediate filaments, some of the many keratin peptides that were automatically discarded as contaminants by the peptide assignment software (**Figure 4.3B**) might have truly co-purified with the GST-ICD as part of entire desmosomal complexes. Curiously, neither SMAD3 nor PP1α, the known PCDH1 interactors, appeared in our mass spectrometry study, suggesting that the binding half-life and/or strength are too small to allow detection by such means.

4.8.2. Corroborating the putative PCDH1-DP interaction

Endogenous DP co-immunoprecipitation with PCDH1 was difficult to assess in HUVEC (**Figure 4.4A**). This is likely due to a combination of low endothelial expression levels of DP, and its poor solubility. Indeed, although DP has been successfully imaged by immunofluorescence in fixed vascular ECs (Kowalczyk et al., 1998; Zhou et al., 2004), such studies have only attempted co-immunoprecipitation in overexpressing systems; interestingly, DP was reported to show stronger signal in lymphatic than blood endothelia (Ebata et al., 2001). Furthermore, in the case of HUVEC specifically, DP has also been reported not to solubilise with standard lysis buffers, instead crashing out as part of the insoluble pellet (Valiron et al., 1996); however, pellet lysis with urea-based buffers, or even SDS sample buffer, was not successful in our case, and therefore DP co-purification was conclusively shown in ICD-transfected HEK 293T instead (**Figure 4.4B**), followed by dual-colour immunofluorescence (**Figure 4.5**) and a proximity ligation assay (**Figure 4.6**) in HaCaT cells. An interesting experiment would involve carrying out a proximity ligation assay between endogenous PCDH1 and endogenous DP in HUVEC monolayers, to address the question of whether PCDH1 and DP interact in the endothelium. However, this would require antibodies directed against the intracellular domains of PCDH1, which are not commercially available (Koning, Sayers, et al., 2012).

4.8.3. Identifying the PCDH1-DP interaction domains

Finally, pulldown experiments showed that the DP Head domain co-purifies with PCDH1-ICDv2, whereas the DP Tail domain does not (**Figure 4.8**). It was indeed expected that only one or the other co-purify with ICDv2, because the DP rod domain that connects the two domains is rigid, preventing simultaneous interaction of both domains. Specifically, the Head domain was the more likely candidate, as it has an array of documented interacting proteins (Kowalczyk et al., 1997; Kowalczyk et al., 1999), whereas the Tail domain only interacts with the intermediate filaments, using binding sites (PRD, **Figure 4.7**) very specific to intermediate filaments proteins (Kang et al., 2016). Truncations of DP showed that the first four Spectrin repeats of the Head domain are needed for interaction with PCDH1-ICDv2 (**Figure 4.9**), which was also expected as the aforementioned interactions between DP and Plakoglobin or Plakophilin were confirmed using constructs spanning only the first 584 aa of DP, i.e. from the very *N*-terminus to the middle of the fourth Spectrin repeat (SR6, **Figure 4.7**).

The sequence of the PCDH1 ICD that interacts with DP still remains to be established. Pulldown experiments with truncations of the PCDH1 ICD could help to identify this region more precisely. Similarly, whether this interaction is direct cannot be concluded from the experiments presented here. To this end, extensive purification of PCDH1 and DP separately, followed by *in vitro* binding assays based on biophysical properties e.g. isothermal titration calorimetry, surface plasmon resonance, or analytical ultracentrifugation would be required.

4.8.4. Roles for a PCDH1-DP interaction

It is hard to speculate as to what the significance of this interaction might be, because experiments thus far have been aimed at confirming the interaction rather than elucidating its function. It is unclear whether this interaction takes place alongside, or is mutually exclusive with, the interactions between PCDH1 and its known cytosolic partners, SMAD3 (Faura Tellez et al., 2015) and PP1α (Vanhalst et al., 2005): neither is known to associate specifically with cell-junctional complexes, so structural recruitment of either to the desmosome *via* PCDH1 appears unlikely. In fact, given that both SMAD3 and DP can associate with both PCDH1 isoforms, concurrent interaction at membrane-proximal sequence of the PCDH1 ICD appears sterically unlikely. Because PCDH1 is known to sequester SMAD3 downstream of TGF-β1 (Faura Tellez et al., 2015), this in turn would mean that association of PCDH1 with DP prevents association of PCDH1 with SMAD3, functionally dampening the response to TGF-β1 in cells with abundant DP expression. This would seem logical, as high DP levels typically meet the demand for structural rigidity in response to mechanical stress (Garrod & Chidgey, 2008), where fast transcriptional response to cytokine signalling such as is rendered available by the SMAD pathway (Lebrin et al., 2005) might not be considered a priority. Conversely, lineages such as ECs, which need to quickly exit quiescence and be able to respond to chemokines and growth factor gradients, have lower levels of DP expression which, in this framework, would allow faster response to TGF-β1 signalling as SMAD3 is not sequestered by PCDH1. Very similarly, VE-cadherin was found to inhibit endothelial proliferation by inhibiting TGF-β effector phosphorylation, including SMAD3 (Rudini et al., 2008), so this proposed TGF-β-dampening effect provided by PCDH1 could enrich the response elicited by VE-cadherin. If this was true, PCDH1 purification in TGF-β-stimulated cells might result in co-purification of TGF-receptors, as happens with VE-cadherin (Rudini et al., 2008). Furthermore, PCDH1 expression should correlate with quiescence in ECs, which could be probed by comparing protein levels between established HUVEC monolayers and dividing cells. For example, PCDH12 mediates quiescence in flow-exposed HUVEC and HAEC, and is downregulated upon SMAD6 knockdown (Ruter et al., 2021), so a similar phenotype might be observed for PCDH1 and SMAD3.

Desmosomes, given their “hyperadhesive” nature (Garrod & Chidgey, 2008), engage in remarkably tight adhesion to provide structural robustness; PCDH1 (like other δ1-PCDH) also forms remarkably strong *trans*-homodimers (Harrison et al., 2020), so a structural role in cell-cell adhesion mediated by the PCDH1 (extracellular-transmembrane) and DP (cytoskeletal) axis seems apt. Experiments such as aggregation assays could be undertaken to probe the level of intercellular adhesion between PCDH1-positive cells in the presence and absence of DP, and might show whether the complex has structural significance. It would seem appropriate to speculate that PCDH1, like VE-cadherin (Schmelz et al., 1994), is part of the endothelial cell-specific junctional complex termed *complexus adhaerens* (**Section 1.2.4**); however, it remains unknown whether PCDH1 specifically resides within any adhesion complexes proper, or just associates with DP. Reports have shown that PCDH1 does not localise at adherens, nor tight, junctions in epithelial cells (Faura Tellez et al., 2016), so if PCDH1 is part of any other adhesion complex, desmosome-like assemblies are the obvious alternative. Super-resolution microscopy imaging of PCDH1, DP, and a transmembrane desmosomal protein such as Desmocollin or Desmoglein could investigate potential co-localisation.

VE-cadherin interacts with DP and plakoglobin (Kowalczyk et al., 1998), so interaction of PCDH1 with plakoglobin, as well as DP, seems possible. Cytosolic involvement of PCDH1 with the cytoskeleton could already be hypothesised based on both isoforms having a PDZ domain-binding site at their extreme *C*-terminus (Demontis et al., 2006). Notably, however, this sequence cannot mediate interaction with DP, as the latter lacks a PDZ domain. This means that PCDH1 could also interact with other members of the cytoskeleton, even concurrently to its interaction with DP. DP is known to interact with both Plakophilin and Plakoglobin through the same region, i.e. the same one identified to mediate interaction with PCDH1. Therefore, concurrent interaction of DP with all three proteins seems unfeasible; more likely, a subset of DP proteins interacts with PCDH1, and a different subset with the other cytosolic desmosomal proteins.

CHAPTER 5: INVESTIGATING THE BIOLOGICAL FUNCTION OF SOLUBLE PCDH1 EXTRACELLULAR DOMAIN

5.1. Introduction

The aim of the experiments described in this chapter was to investigate whether the extracellular domain (ECD) of PCDH1 exhibits any biological function related to angiogenesis. This was assessed *in vitro*, by means of sprouting assays that involved HUVEC and the addition to their culture media of soluble, recombinant PCDH1 ECD. Preliminary studies showed that self-binding of the ECD, which was investigated by flow cytometry analysis of HUVEC incubated with fluorescently-labelled recombinant ECD, was undetectable.

All the main PCDH1 isoforms (**Figure 3.1**) share the same extracellular sequence, subdivided in 7 extracellular cadherin (EC) repeats, so splice variants were not a concern for these experiments. Nevertheless, in a similar vein to the Desmoplakin truncations presented in Chapter 4, different truncations of the ECD were purified, to try to assess which EC repeats are necessary for binding. The idea behind these experiments arose because binding of the recombinant ECD of different proteins to the surface of endothelial cells can result in angio-inhibitory effects, as shown in similarly designed assays with other proteins (Kertesz et al., 2006; Suchting et al., 2005), including other PCDH proteins (Korzystka, 2018). Rigorous biophysical measurements (Harrison et al., 2020), published after our experiments took place, showed that PCDH1 exhibits largely preferential homotypic *trans*-binding through its first four EC repeats: the K_d for this self-adhesion was calculated as 1.2 μM (135 ng/mL), suggesting even small amounts of the soluble ECD should readily result in binding, further supporting the rationale for these experiments.

5.2. Cloning, expression and purification of recombinant ECD truncations

In order to purify recombinant, soluble PCDH1 ECD, a mammalian expression construct encoding the entire domain as a soluble, hFc-fusion protein (ECD-Fc) was transiently transfected in HEK 293T cells, grown in protein-free complete medium. Preliminary affinity purification however resulted in an impractically low protein yield. Motivated by the fact that the crystal structure of PCDH1 suggested that the four most plasma membrane-distal EC repeats of the PCDH1 ECD alone retain adhesive properties (Modak & Sotomayor, 2018), a smaller construct was created, encoding only these four EC repeats, similarly fused to a *C*-terminal hFc tag (ECD4-Fc, **Figure 5.1B**). The purification strategy involved transient transfection of large numbers of HEK 293T cells, followed by batch affinity chromatography, buffer exchange to PBS, and concentration (**Figure 5.1A**). Truncating the ECD after the fourth EC repeat resulted in improved yield (**Figure 5.1C**), so experiments in this chapter were mostly carried out using this shortened fusion protein instead of the full length. As a putative negative control, an even shorter construct encoding only the three most membrane-distal EC repeats of PCDH1 fused to hFc (ECD3-Fc, **Figure 5.1B**) was employed, reasoning that further truncation would result in reduced adhesive properties, and thus observable biological activity, if any.

5.3. Soluble ECD does not bind the endothelial cell surface by flow cytometry

To assess whether soluble PCDH1 ECD binds endogenously expressed PCDH1 on the surface of endothelial cells, the full length ECD and truncations thereof (**Figure 5.1B**) were expressed as hFc fusions. The tag was then probed with a fluorophore-conjugated secondary antibody raised against human IgG (**Figure 5.2A**), which includes the hFc region. The observed surface fluorescence of HUVEC incubated with PCDH1 ECD-Fc, ECD4-Fc, or ECD3-Fc as assessed by flow cytometry was not different from that of HUVEC incubated with hFc alone (**Figure 5.2B**). In contrast, although modestly, endothelial fluorescence above control levels was recorded for MMRN2-Fc, the binding of which to both CLEC14A and CD93 on the HUVEC cell surface is known to be detectable by similar methods (Khan et al., 2017). Given the

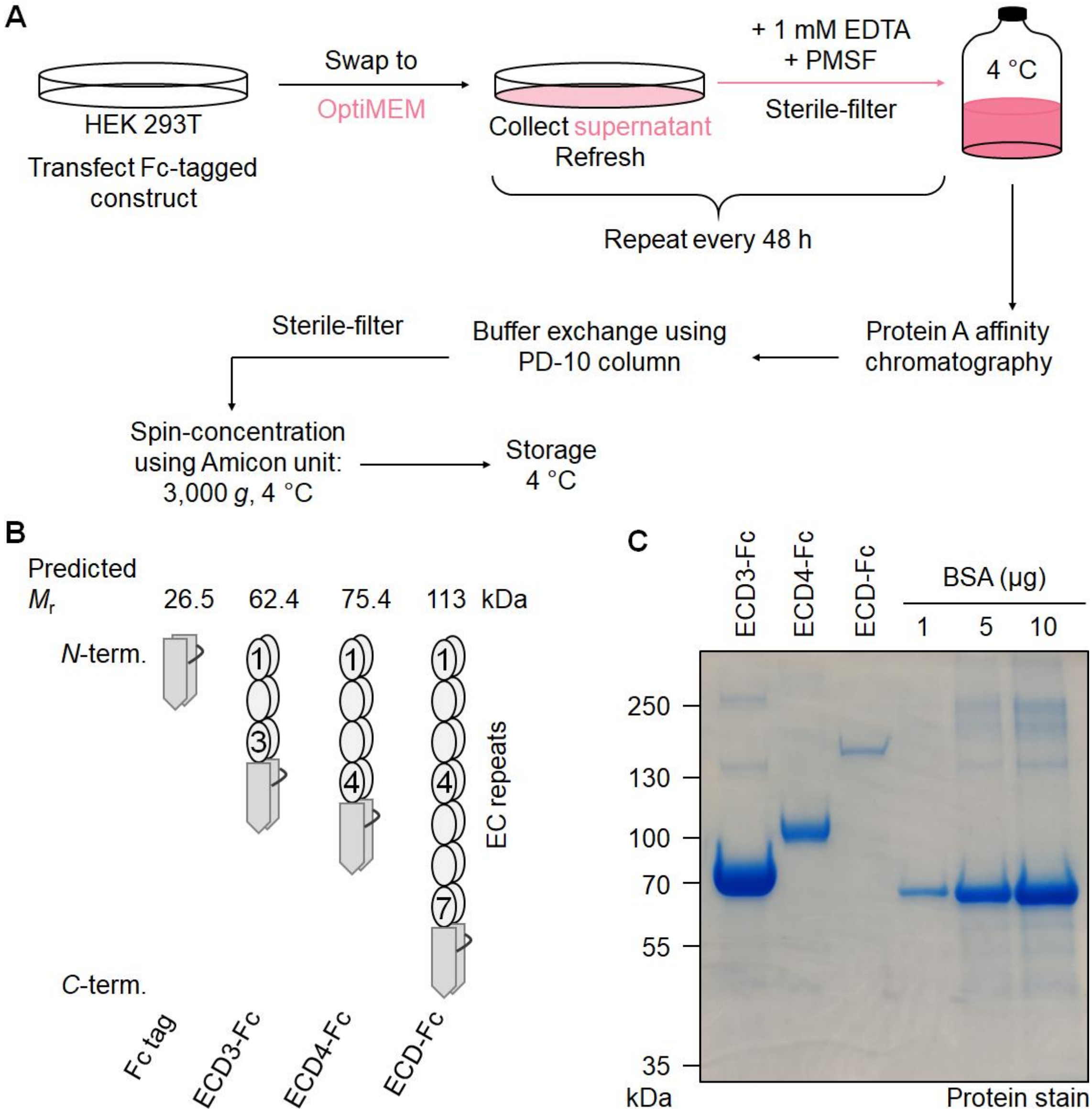

Figure 5.1. Expressing and purifying different PCDH1 ECD fusion proteins.
A. Workflow for the purification of PCDH1 ECD truncations. Typically, 20 dishes of HEK 293T cells (1.2×10^{8} cells) were PEI-transfected, allowing the supernatant with the secreted fusion protein to be collected and refreshed multiple times. These merged harvests, typically 1.5-2 L, were batch-purified by gravity-based affinity chromatography, and eluted at room temperature in low-pH glycine, neutralised with Tris base. This buffer was swapped to PBS by filtration through Sephadex G-25, and the sterile protein was centrifuge-concentrated through a 10-kDa-cut-off filter.
B. Summary of ECD fusion proteins purified in experiments throughout the chapter, drawn to scale and with their predicted monomeric molecular weight. The hFc tag forms dimers *via* disulfide bonds (dark grey line, not to scale) between hinge regions.
C. Stained, reducing SDS-PAGE gel of Protein A pulldowns showing relative expression of ECD fusion proteins. The same number of HEK 293T cells was transfected with each construct, and the protein isolated from 2 mL of media was loaded. For reference, known amounts of BSA were loaded alongside, as indicated.

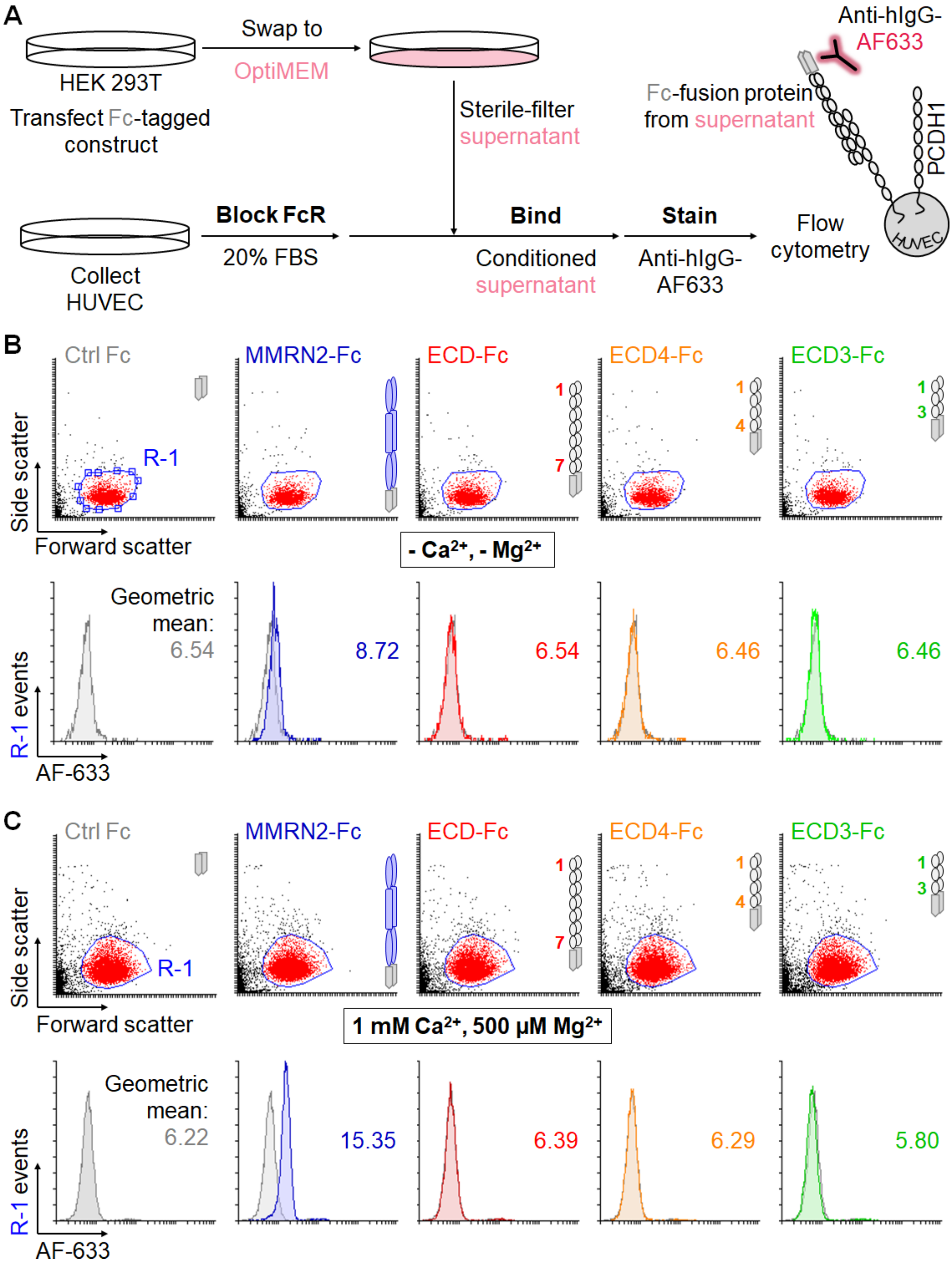

Figure 5.2. Soluble PCDH1-ECD truncations do not display binding to HUVEC surface by flow cytometry.
A. Experimental workflow and schematic of proposed molecular interaction. Blocking of Fc receptors (FcR) and fluorescent staining were carried out in FACS buffer. During the binding step, HUVEC were resuspended in neat Opti-MEM containing the relevant fusion protein, freshly collected. hFc tags dimerise in oxidising solutions (see **Figure 5.1B**).
(Continued overleaf)

(Continued from previous page)
B. Flow cytometry analysis of the experiment described in **A**. The negative control (hFc) histogram is overlayed onto all other histograms. HUVEC incubated with conditioned Opti-MEM from a mock transfection carried out without any plasmids were used as unstained sample, to obtain a fluorescence signal baseline from the cytometer.
C. Repeat of the experiment in **B**, with addition of Ca^{2+} and Mg^{2+} during the blocking, binding, and staining steps of the protocol.

eponymous requirement of Ca^{2+} for adhesion among the Cadherin superfamily members, and preliminary reports that the same holds for the δ-protocadherin subfamily (Bisogni et al., 2018), the experiment was repeated in the presence of 1 mM Ca^{2+} and 500 µM Mg^{2+} at each staining step (**Figure 5.2C**). The trend followed that of the first experiment, with MMRN2-Fc detectably binding the HUVEC cell surface, but no significant fluorescence shift in any of the PCDH1 ECD samples, indicating no detectable binding.

5.4. Soluble PCDH1 ECD truncations do not impair HUVEC sprouting on Matrigel

To study whether the PCDH1 ECD can affect angiogenesis, an *in vitro* Matrigel assay was set up adding the relevant fusion protein as part of the cell growth medium. It was hypothesised that adding a soluble form of the adhesive portion of PCDH1 in high concentrations would disrupt the endogenous homotypic interactions of PCDH1, and in turn affect tube formation. When the experiment was carried out with HUVEC grown in standard cM199 medium (**Figure 5.3A**), there was a reduction in the number of fully closed intercellular junctions (“loops”) formed by cells treated with ECD4-Fc, as compared to that of HUVEC treated with hFc alone (**Figure 5.3B**). Furthermore, a higher concentration of fusion protein (200 µg/mL) resulted in a more profound reduction in number of loops formed than that at lower protein amounts (50 µg/mL), hinting at a molecular mechanism whereby the provided soluble PCDH1 ECD truncation binds the endogenous endothelial PCDH1 ECD and proceeds to impede sprouting in a concentration-dependent manner. In contrast, when the experiment was repeated with a commercially sourced mix of HUVEC isolates grown in PCM199 (**Figure 5.3C**), no such reduction was observed, either on addition of ECD4-Fc or ECD3-Fc. As a general trend, supplementing with PCDH1 ECD truncation at any concentration down to 1 µg/mL seemed to in effect increase the number of intercellular loops formed, as compared to those formed in the

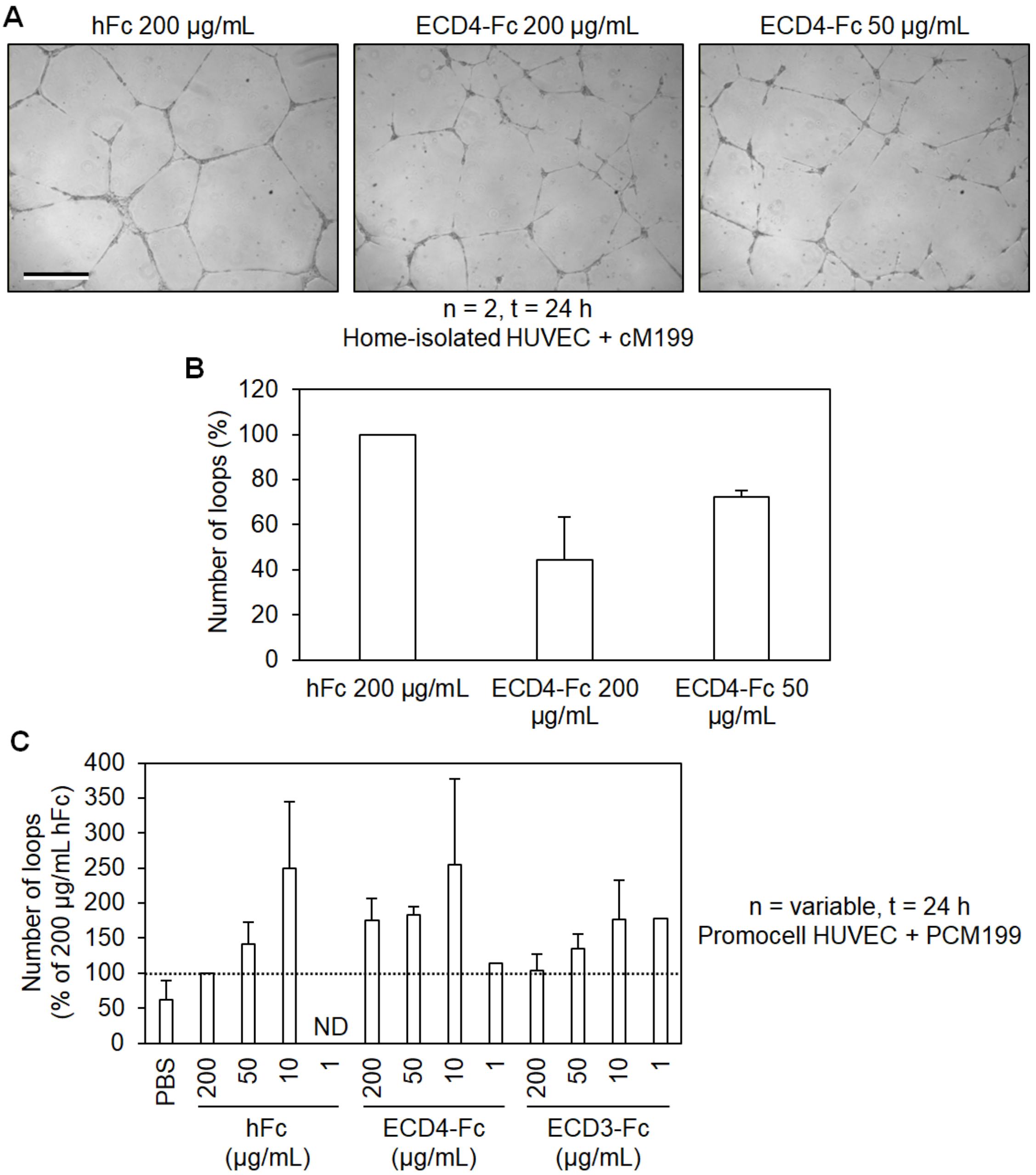

Figure 5.3. Soluble ECD4-Fc and ECD3-Fc do not impair HUVEC sprouting on Matrigel.
A. Representative images of two different experiments where ECD4-Fc was included in the medium at the time of plating home-isolated HUVEC on Matrigel. Three different HUVEC isolates were mixed in equal ratios before plating for the experiment. Scalebar = 600 µm.
B. Analysis of the data exemplified in **A**, where the number of loops formed after 24 h was quantified with the Angiogenesis Analyzer plugin for *ImageJ*. The data is expressed as a percentage of the hFc control value, plotted as mean + sem.
C. Analysis of experiments where Fc fusion proteins were included, at various concentrations, in the medium at the time of plating commercially sourced HUVEC on Matrigel. Data analysed as in **B**, expressed as a percentage of the hFc [200 µg/mL] value, plotted as mean and with error bars indicating the SEM. As an additional control, an equivalent volume of PBS was at times used. To minimise fusion protein usage, not all concentrations were probed each time the experiment was repeated; therefore, n differed for given conditions and ranged from 1-5.

hFc treatment. Addition of higher amounts of any given protein, on the other hand, did correlate with a reduction in the number of loops formed as compared to lower amounts of the same protein, again hinting at a concentration-dependent mechanism of some capacity. Importantly, however, increasing the concentration of hFc control protein also had a similar effect, resulting in the formation of fewer loops. These data suggested that under the conditions of this assay adding this soluble protein, comprising the four membrane-distal EC repeats, had no effect on tube formation on Matrigel.

5.5. ECD3-Fc does not impair HUVEC tubulogenesis in co-culture

To check whether PCDH1 ECD can impact angiogenesis in a more physiologically relevant setting, an *in vitro* co-culture assay was set up similarly to Chapter 3: untreated HUVEC were plated onto the established fibroblast monolayer for four days, and ECD3-Fc was added as part of the cell growth medium both at the time of plating and when refreshing the medium halfway through the assay (**Figure 5.4A**). ECD3-Fc was chosen in this instance on the basis of the sprouting assays on Matrigel, where HUVEC behaved comparably when treated with ECD4-Fc or ECD3-Fc (**Figure 5.3C**), and because its higher expression levels (**Figure 5.1C**) would allow for an even higher concentration to be used (400 µg/mL) than in the Matrigel-based assays. Automated analysis of the endothelial network formed in the experiment (**Figure 5.4B**) showed that the length of each tubule was highest in cells treated with control hFc, and reduced after an equimolar ECD3-Fc treatment. However, a comparable reduction was achieved by not adding any protein in the medium (PCM199 treatment), and yet a bigger reduction was apparent by addition of an equivalent volume of PBS, the buffer in which hFc and ECD3-Fc were purified. The number of junctions and branches per vessel followed identical trends (**Figure 5.4C**). Importantly, the supplemented protein did not degrade for the duration of the assay, as confirmed by affinity purification of the conditioned media collected at the end of the

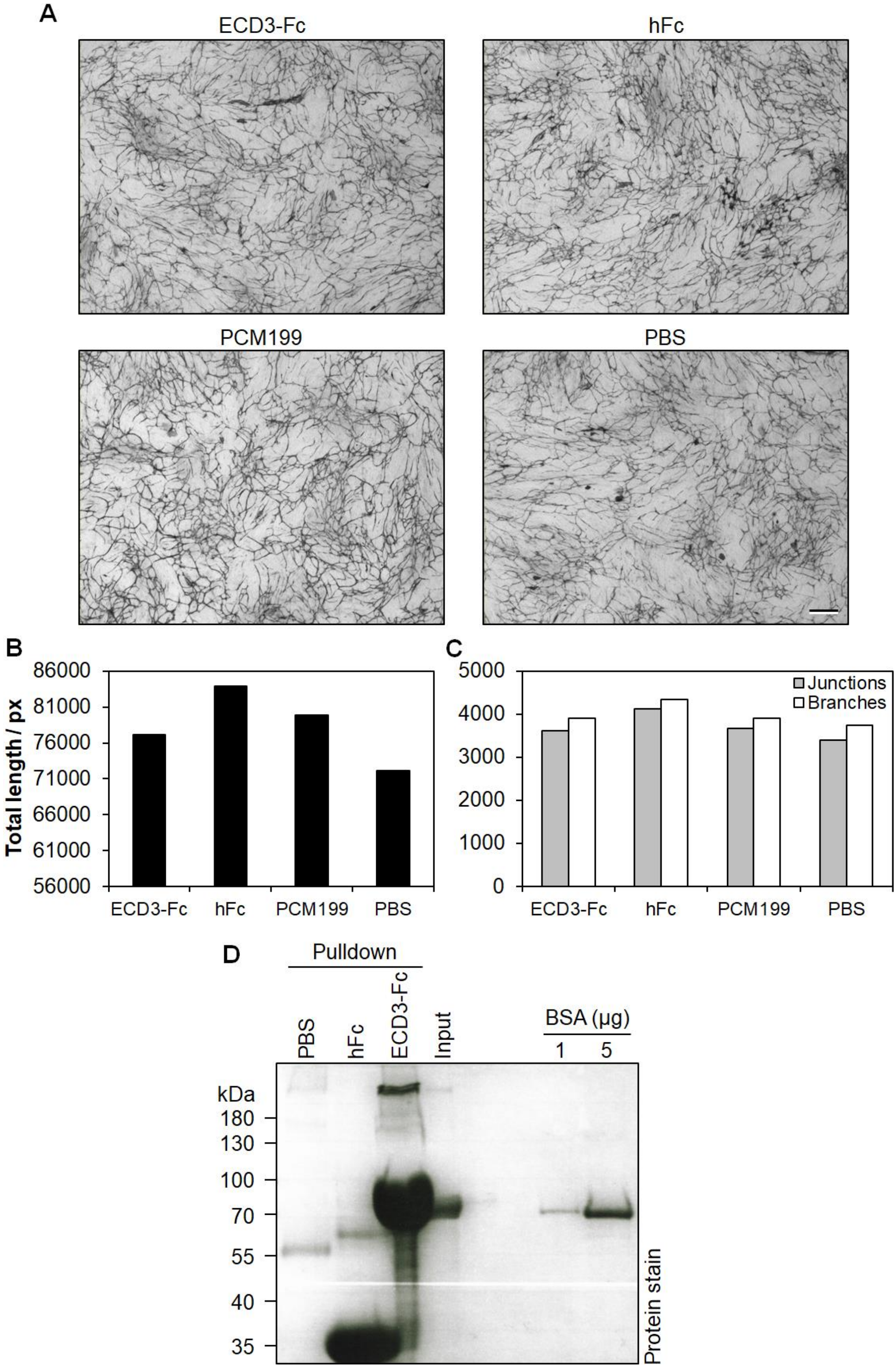

Figure 5.4. Soluble ECD3-Fc does not impair HUVEC tubulogenesis in co-culture.

(Continued from previous page)
A. CD31 staining of a co-culture experiment where ECD3-Fc was added to the medium at the time of plating home-isolated HUVEC on a HDF monolayer that had been grown for five days. Three different HUVEC isolates were mixed in equal ratios at the time of plating. Medium, and fusion protein therein, were refreshed after 48 hours (i.e. 48 hours before fixation). ECD3-Fc was [400 µg/mL] = 6.41 µM, and the hFc control was at equimolar concentration. Conditions with neat medium without fusion protein (PCM199) or with an equivalent volume of PBS were set up as additional controls. Scalebar = 500 µm.
B, C. Analysis of the tubule networks shown in **A**, using the AngioSys 2.0 software.
D. Stained SDS-PAGE gel loaded with Protein A pulldown samples from the conditioned media used in **A**, collected at the end of the assay. The “input” lane was loaded with 2 µL ECD3-Fc protein from the purified batch used to supplement the media. For reference, known amounts of BSA were loaded alongside, as indicated.

experiment, but before fixing the co-culture (**Figure 5.4D**).

5.6. Discussion

Work in this chapter attempted to establish an *in vitro* biological function for the ectodomain of PCDH1 as a recombinant, soluble protein. Production and isolation of truncated forms were successful, although binding to endogenous PCDH1 could not be visualised by flow cytometry. Endothelial networks on Matrigel were impaired by ECD4 supplementation, but this was not recapitulated by commercially sourced cells grown on different media. The outcome of ECD3 addition to HUVEC growing on fibroblasts remains unclear.

5.6.1. PCDH1 ECD production

HEK 293T were chosen as the system to produce PCDH1 ECD to most closely mimic endothelial PCDH1, including appropriate folding and native post-translational modification patterns, as these are pivotal for Cadherin function. However, purification of the full-length PCDH1 ectodomain (ECD-Fc) by affinity chromatography highlighted low production yield (**Figure 5.1C**). This has been reported elsewhere, and seems to be ameliorated by retention of the transmembrane domain in the protein (Bisogni et al., 2018), or growth medium supplementation with high [Ca^{2+}] (Harrison et al., 2020). Other strategies could involve different expression vectors, different signal peptides (Stern et al., 2007), or a brief period of mild hypothermia (Lin et al., 2015). Instead, producing just the first four PCDH1 EC repeats (ECD4-Fc) improved expression (**Figure 5.1C**). Importantly, ECD4 still retains adhesive properties (Modak & Sotomayor, 2018), validating the use of this truncation in functional assays. This truncated protein is 68% the length of ECD-Fc, and excludes most ECD glycosylation sites (**Figure 1.5**), potentially explaining the increased yield. Indeed ECD3-Fc, a further *C*-terminal truncation missing the fourth EC repeat, and thus a further glycosylation site, expressed in even greater amounts (**Figure 5.1C**).

5.6.2. PCDH1 surface binding on HUVEC

Given that endogenous PCDH1 in HUVEC is detectable by flow cytometry (**Figure 3.3**), binding of soluble ECD-Fc to its endothelial counterpart was hypothesised to be detectable with a hFc-specific, fluorophore-labelled secondary antibody (**Figure 5.2A**). Such a strategy was previously employed to visualise binding of MMRN2 fragments to CLEC14A or CD93 on the endothelial surface (Khan et al., 2017). Binding of any of the PCDH1 ECD constructs to HUVEC, however, was not detected by flow cytometry (**Figure 5.2B**), unlike that of MMRN2-Fc. The experiment was repeated including Ca^{2+} and Mg^{2+} in all steps of the protocol, given that (Proto-)Cadherin binding is abolished in the absence of calcium. Again, however, no surface binding by any of the PCDH1 ECD constructs was observed (**Figure 5.2C**). One explanation could be that 1 mM Ca^{2+} was not enough to allow adhesion: PCDH1 self-adhesion has indeed been studied at 2-3 times higher $[Ca^{2+}]$ (Blevins et al., 2011; Harrison et al., 2020; Modak & Sotomayor, 2018), but the calcium K_d of E-CDH is around 30 µM (Koch et al., 1997). Therefore, if the unmeasured calcium K_d for δ-PCDHs is similarly low, 1 mM Ca^{2+} is orders of magnitude larger than required for adhesion.

Another explanation could be that the adhesive self-affinity of PCDH1 is too low to allow it to be captured by flow cytometry. The K_d of PCDH1 ECD4 dimerisation was recently measured as 0.53±0.46 µM (Harrison et al., 2020), which might not suffice for this experimental setup, routinely employed to visualise the much higher-affinity antibody:antigen interaction (K_d ~1 nM, Wilson and Soh (2020)). The affinity between MMRN2 and its binding partners is unmeasured, but withstands denaturation (Khan et al., 2017). Additionally, PCDH1 complexes might not be stable in the fluidics environment of a flow cytometer: E-cadherin dimer strength decreases at higher shear rate (Perret et al., 2002), and if this holds for PCDH1 too, typical cytometer flow rates (1,000s of events/min) could mechanically disrupt the interaction. FACS analysis has failed to register PCDH oligomerisation before (Morishita et al., 2006). On one hand, improving PCDH1 ECD avidity with a multimerising tag might increase experimental sensitivity (Bushell et al., 2008). On the other hand, steric hindrance due to multimerisation, possibly even just from dimerising hFc tags, could prevent the soluble ECD interacting freely with bound ectodomains. Indeed, a pair of dimerised hFc tags, <1 nm apart (Bošnjak et al., 2014), would mimic lateral PCDH proximity, previously shown to hamper adhesion (Harrison et al., 2020). To avoid this issue, an engineered protease recognition site between the ECD and the hFc tag would allow enzymatic isolation of the former as a monomer before flow analysis.

5.6.3. Biological ECD activity on Matrigel

ECD4-Fc was then included when plating HUVEC on Matrigel, impairing intercellular connections formation (**Figure 5.3**). Assuming ECD4-Fc and endothelial PCDH1 did bind in this static setting, competitively blocking endogenous adhesion surfaces must impair cell motility and/or adhesion. The data also suggested dose-dependency for the effect (**Figure 5.3B**), with 200 µg/mL ECD4-Fc (2.7 µM) reducing sprouting twice as much as at 50 µg/mL – concentration choices based on assays with other Protocadherins (Korzystka, 2018) and other guidance-related endothelial proteins (Suchting et al., 2005). It is unclear why a four-fold increase in dosage would result in only a two-fold increase in inhibition. If physical effects such as higher order aggregation and steric hindrance do take place, these would lower the effective concentration. Alternatively, a concentration between those used could be enough to saturate all adhesion surfaces. This is supported by the notion that K_d for PCDH1 homodimerisation (**Section 5.6.2**) is much less than half the molarity of 200 µg/mL ECD4-Fc, but larger than that of 50 µg/mL.

A titration experiment, with ECD4-Fc or ECD3-Fc supplied to HUVEC on Matrigel in decreasing concentrations, tried to assess dose dependency more closely (**Figure 5.3C**); the expectation was that any effects would subside at low enough ECD concentration. Puzzlingly, increasing concentrations of hFc alone resulted in decreasing numbers of loops formed, and addition of the protein buffer (PBS) without protein reduced the number of loops even further. Moreover, the effects of adding either ECD4-Fc or ECD3-Fc were comparable to those elicited by the same amount of control hFc protein. The expectation was for ECD4-Fc to recapitulate the effect previously seen in the same assay (**Figure 5.3B**), and for ECD3-Fc addition to result in no phenotype, lacking the fourth EC repeat.

Conclusions from this experiment are hard to make, given that possible changes in the number of loops are masked by large statistical errors (**Figure 5.3C**), which highlight large experimental variability. Furthermore, unlike preliminary experiments (**Figure 5.3B**), these titrations were carried out using a commercial source of mixed HUVEC isolates, grown in medium that includes 0.5 ng/mL VEGF$_{165}$ among other growth factors. The combined stimulatory effects of these might have masked the phenotypic outcome of recombinant PCDH1 ECD supplementation, particularly if the effect size is modest to begin with – explaining the similar data in control and treated conditions. The large variability across biological repeats, on the other hand, could partly arise from batch variation in the produced fusion proteins and the commercial control hFc – one possible factor contributing to batch variation being the presence of bacterial endotoxin, which would not be removed by standard filtration techniques and has recognised effects on endothelial cells, including ICAM1 upregulation (Wong & Dorovini-Zis, 1992). Lastly, defective recombinant ECD glycosylation, arising as a side-effect of transfection, or if HEK 293T cells lack an essential endothelial glycan-processing enzyme subset, could have affected protein folding and function (Colley et al., 2017). To address some of these issues, the experiment could be undertaken with HUVEC isolates grown in cM199 instead, after cleaving the hFc tag from the soluble ECD to ensure saturation (**Section 5.6.2**). Despite these factors, it remains unclear why addition of PBS alone, or hFc control protein, resulted in larger phenotypic impairment than addition of PCDH1 ECD.

5.6.4. ECD3 activity in HUVEC-fibroblasts co-culture

Lastly, the effects of PCDH1 ECD on tubulogenesis *in vitro* were tested by adding soluble ECD3-Fc to HUVEC on fibroblasts (**Figure 5.4**). Therefore ECD3-Fc was used, as it resulted in a comparable phenotype to ECD4-Fc in the discussed Matrigel experiments (**Figure 5.3C**), and because this shorter truncation expressed in even greater yield (**Figure 5.1C**), allowing ECD addition at even higher concentration. This precaution was taken considering the length of the assay, with HUVEC allowed to grow on the fibroblast monolayer for four days. While ECD3-Fc addition did seem to impair tubule formation when compared to hFc alone, the same volume of neat PBS resulted in even greater reduction of all measured vessel properties, similar to the Matrigel assays (**Figure 5.3C**). It is hard to draw any definitive conclusions as this experiment was performed only once. The expectation however would be for ECD3-Fc not to show any biological effects, given later reports of PCDH1 EC repeats 1-3 failing to bind the PCDH1 ECD altogether (Harrison et al., 2020). The informed choice now would be to undertake the experiment using ECD4-Fc instead.

The experiments reported in this chapter have tried to explore the nature of the PCDH1 ectodomain self-interaction. To assess the effects of Pcdh1 loss *in vivo*, compounding loss of both intracellular (**Chapter 4**) and extracellular (this chapter) interactions, the next step involved studying a murine Pcdh1-deficient model (**Chapter 6**).

CHAPTER 6: INVESTIGATING VASCULAR DEVELOPMENT DURING EMBRYOGENESIS IN MICE LACKING Pcdh1

6.1. Introduction

The aim of the experiments described in this chapter was to assess whether lack of Pcdh1 results in vascular abnormalities in mice. The organisation of CD31-labelled vasculature was assessed in Pcdh1-knockout embryos, rendered optically clear to allow whole-mount imaging. Two- and three-dimensional analyses in knockout and wild-type embryos did not highlight any differences in the extent or topology of the vasculature. Corroborating postnatal angiogenic assays were envisaged at the outset, but could not be undertaken due to time constraints.

Pcdh1 mRNA expression has been assessed by means of *in situ* hybridisation (Redies et al., 2008) in wild-type mouse embryos, with passing references to transcript expression in the endothelium. In this chapter, the vasculature of Pcdh1-KO embryos was studied instead. The approach used to image cleared mouse embryos was based on that previously employed with Smad6-KO mice (Wylie et al., 2018), in which the embryonic vasculature was similarly immunostained, fluorescently labelled, and then imaged by fluorescence light-sheet microscopy. This technique is a recent development of a hundred-year-old imaging method later named selective plane illumination microscopy (Huisken & Stainier, 2009), optimised to allow imaging of large, transparent samples without physically sectioning them – translating in a surge in light-sheet applications among cardiovascular researchers, especially to assess zebrafish development.

6.2. Knockout embryos rederivation

In order to achieve the desired Pcdh1-KO genotype in mice, mouse embryonic stem cells of the C57BL/6J bc;129-*Pcdh1*^{tm2Naw} mouse line ("Pcdh1-Flox") were created by the Nawijn-Koppelman laboratories (University of Groningen, NL). These cells were created by genomic integration of the murine PCDH1 orthologue with its exon 2 flanked by *loxP* sites (**Figure**

6.1A). The latter are short (34 bp) sequences, derived from the P1 bacteriophage (Branda & Dymecki, 2004), that can function as a recognition site for the Cre site-specific recombinase enzyme; once Cre activity is established, having *loxP* sequences at either end of the gene of interest allows to efficaciously and specifically excise the gene according to a high-fidelity mechanism that involves strand cleavage, exchange, and re-ligation around the Floxed sequences. Because the plasmid carried the entire *Pcdh1-Flox* sequence (**Figure 6.1A**), the sequences directly 5' and 3' to exon 2 also worked as two extensive homology arms: these allowed to integrate *Pcdh1-Flox* into the genome *via* homologous recombination, thereby effectively replacing the endogenous Pcdh1 *locus* with the Floxed version. This Pcdh1-Flox line was shipped to the University of Birmingham, and re-derived by implantation into a pseudopregnant mouse, the offspring of which was genotyped to establish the Floxed colony. The increased size of the Pcdh1 *locus* due to the *loxP* sites was used to discriminate successfully Floxed mice by PCR ("del" and "5'ko" reactions, **Section 2.5.10**). Breeding of Pcdh1-Flox mice to Pgk1-Cre mice yielded Pcdh1$^{+/-}$ mice: these arose by establishment of Cre activity under the direction of the near-ubiquitous Pgk1 promoter, resulting in recombination and thus elimination of exon 2 (**Figure 6.1B**). These mice were similarly genotyped by PCR, by identification of a relatively short (700 bp) product that would be undetected in WT or Flox mice due to the much larger distance between annealing sites for the PCR oligos before *Pcdh1-Flox* excision. Mating of these heterozygous-Pcdh1 mice resulted in progeny that included embryos with global, constitutive Pcdh1 loss, as a result of the loss of Pcdh1 exon 2, which codes for most of the protein (**Figure 6.1A**). Timed sacrifice of pregnant dams allowed isolation of such progeny at embryonic day E13.5, which were genotyped as previously described (**Figure 6.1B**), allowing identification of four KO and four WT embryos.

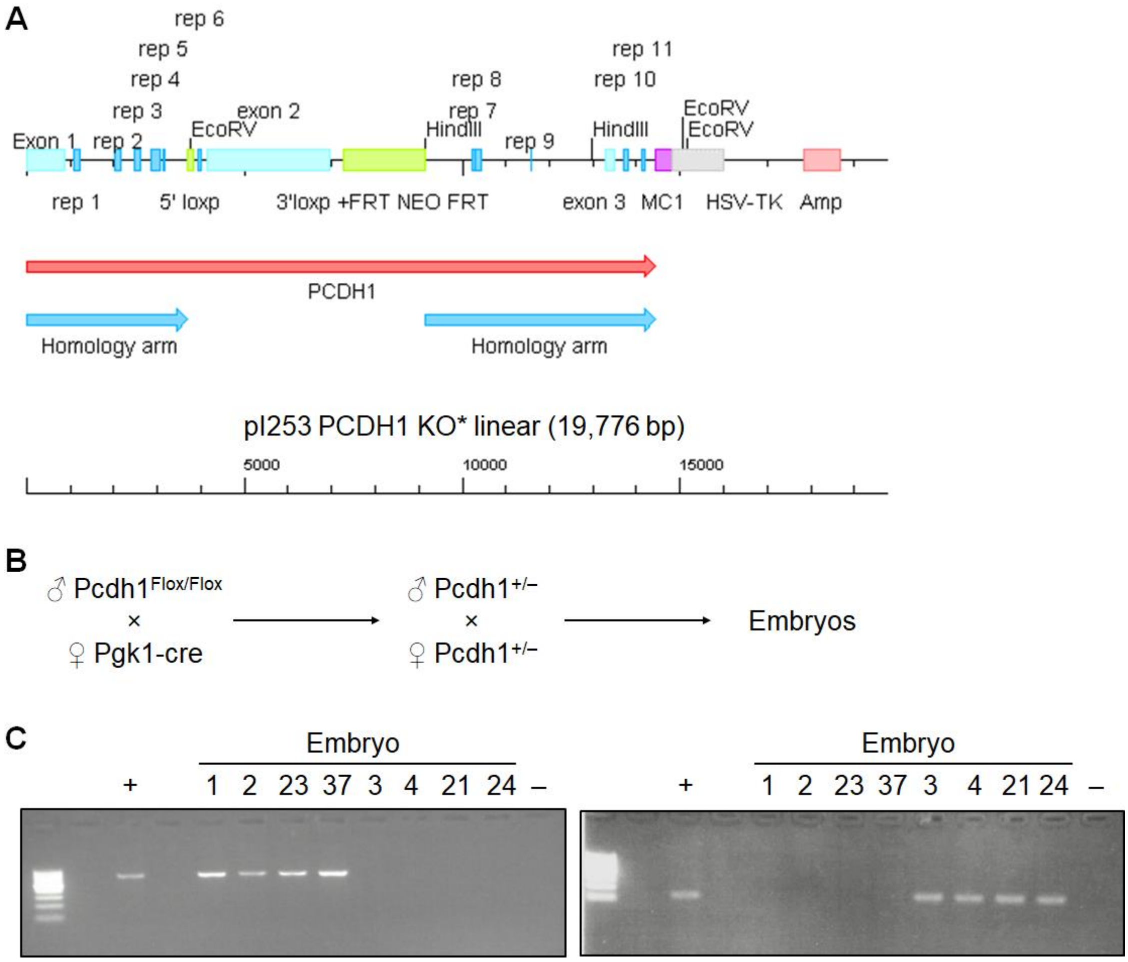

Figure 6.1. Generation of Pcdh1-KO mice.

A. Map of the vector assembled by the Nawijn-Koppelman laboratories (University of Groningen, NL), used to create Floxed Pcdh1 mice (Pcdh1-Flox). These mice were rederived in Birmingham, from embryos provided by the aforementioned laboratory. Note the *loxP* sites flanking exon 2. The neomycin resistance gene is flanked by *FRT* sites, which allow cassette excision by the Flp recombinase, similarly to *loxP* sites (Branda & Dymecki, 2004).

B. Outline of the mating strategy employed to obtain timed Pcdh1-KO embryos. Pcdh1-Flox embryos were obtained as described in **A**, Pgk1-cre does were commercially sourced as the B6.C-Tg(Pgk1-cre)1Lni/CrsJ strain. This mating caused Cre-mediated *loxP* sites recombination in the offspring, from which heterozygous littermates were then cross-mated to obtain Pcdh1-KO embryos.

C. Agarose gels with PCR products of the genotyping reactions for the 8 embryos imaged. On the left is the gel with the “del” reaction products, on the right that with the “5’ko” reaction products. Reaction details are in **Section 2.5.10**. Embryos 1, 2, 3 and 37 were taken forward as Pcdh1-KO (“KO”), whereas embryos 3, 4, 21, and 24 were taken forward as “WT”. As positive controls (+ lane), Pcdh1$^{+/–}$ mice were used. H$_2$O was used for negative control reactions (– lane).

6.3. Light-sheet microscopy allows whole-mount imaging of immunolabelled mouse embryos

Because of the three-dimensional nature of all vascular beds, two-dimensional analysis such as is possible by immunohistochemistry of serial embryo sections only gives partial information; therefore, it was decided to perform three-dimensional analysis of the immunolabelled vasculature to obtain a more complete picture. Although it is possible to extract three-dimensional information from embryo sections by fluorescence confocal microscopy, inherent limitations are the possible deformations due to the sectioning process, the long acquisition times, and the necessary thinness of the sections, together preventing true volumetric information on whole embryos from being obtained. For these reasons, the imaging method of choice was fluorescence light-sheet microscopy, which allows fast, whole-embryo imaging by means of virtual sectioning along the optical axis followed by computational three-dimensional reconstruction. In this technique, the illuminating light is fashioned by means of appropriate optics into a thin sheet, so that only one thin section of the sample is illuminated at any one time, the focal plane. Crucially, the objective that collects the fluorescent emission is orthogonal to the direction of the excitation beam. The light-sheet microscope selected for imaging was an Ultramicroscope II, where the sample rests in a reservoir that is placed on a motorised stage that can move axially (*z* direction), allowing different sections of the embryo to be imaged over time by a static set of light-sheets. Because E13.5 mouse embryos are pigmented, it was necessary to render them optically transparent before imaging, so as to allow both the incoming excitation light to penetrate into the tissue and, likewise, the outcoming emission light to reach the detection device in the microscope without excessive scattering. To this end, a protocol involving the usage of hydrogen peroxide to bleach the embryo, and methanol-dichloromethane to remove water and most lipids, was employed after fluorescent CD31 immunolabelling on freshly isolated WT and KO embryos. As a result, all embryos were cleared to near-complete transparency, with less effective clearing of liver and heart, and poor clearing of the irides (**Figure 6.2**). Nonetheless, this was satisfactory for the purposes of imaging, as very minimal scattering was observed.

Fluorescence imaging yielded a substantial amount of data (50 GB/embryo), comprising thousands of single-plane, two-dimensional images per embryo, which could be computationally assembled through the commercial software *Vision4D* (arivis, Rostock, Germany), allowing to reconstruct the embryonic vasculature in three dimensions (**Figure 6.3**). From a gross anatomical perspective, no obvious differences were noted in the organisation of the main vascular beds when comparing WT and KO embryos. In all cases, the CD31 fluorescence signal was strongest in the largest vessels: intercostal and tail intersegmental vessels and the vasculature around the nasal cavities and of the limbs, as well as in pulmonary arteries, carotids, superficial temporal vessels, and facial veins. The exception was the aorta which, while still very clearly stained, was much less intensely so, likely due to its less superficial and more medial position. Such three-dimensional representations allowed for much easier identification of anatomical features, which was pivotal to enable selection of the same regions for analysis across embryos.

6.4. Two-dimensional analysis of vasculature in Pcdh1-KO embryos

As a preliminary approach, two-dimensional analysis of the data was attempted. First, three regions of interest (ROI) in the embryo were selected for their abundance of smaller vessels, aiming at finding areas where angiogenesis was occurring or had recently occurred. The areas selected were the hindbrain, the area where the medulla becomes the spinal cord, and a small area of the tail around the lumbar vertebrae (**Figure 6.4A**). For the purposes of the

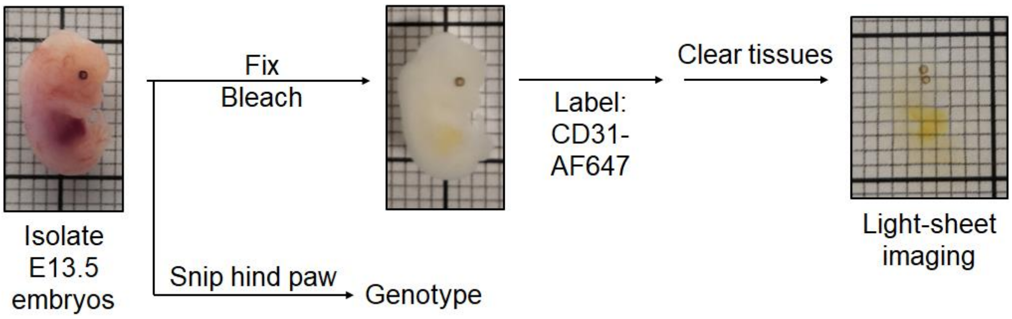

Figure 6.2. Preparation of Pcdh1-KO embryos for fluorescence light-sheet imaging. Schematic of sample preparation for light-sheet imaging. Heterozygous Pcdh1-Flox mice were mated, and dams euthanised 13.5 days after vaginal plug formation. Embryos were isolated, their left hind paw was snipped before fixation to extract DNA, while the rest of the embryo was immunolabelled, mostly following the iDISCO+ procedure (**Section 2.7.4**). Pictures show a representative embryo at each stage of the protocol, resting on a mm-grid for size reference.

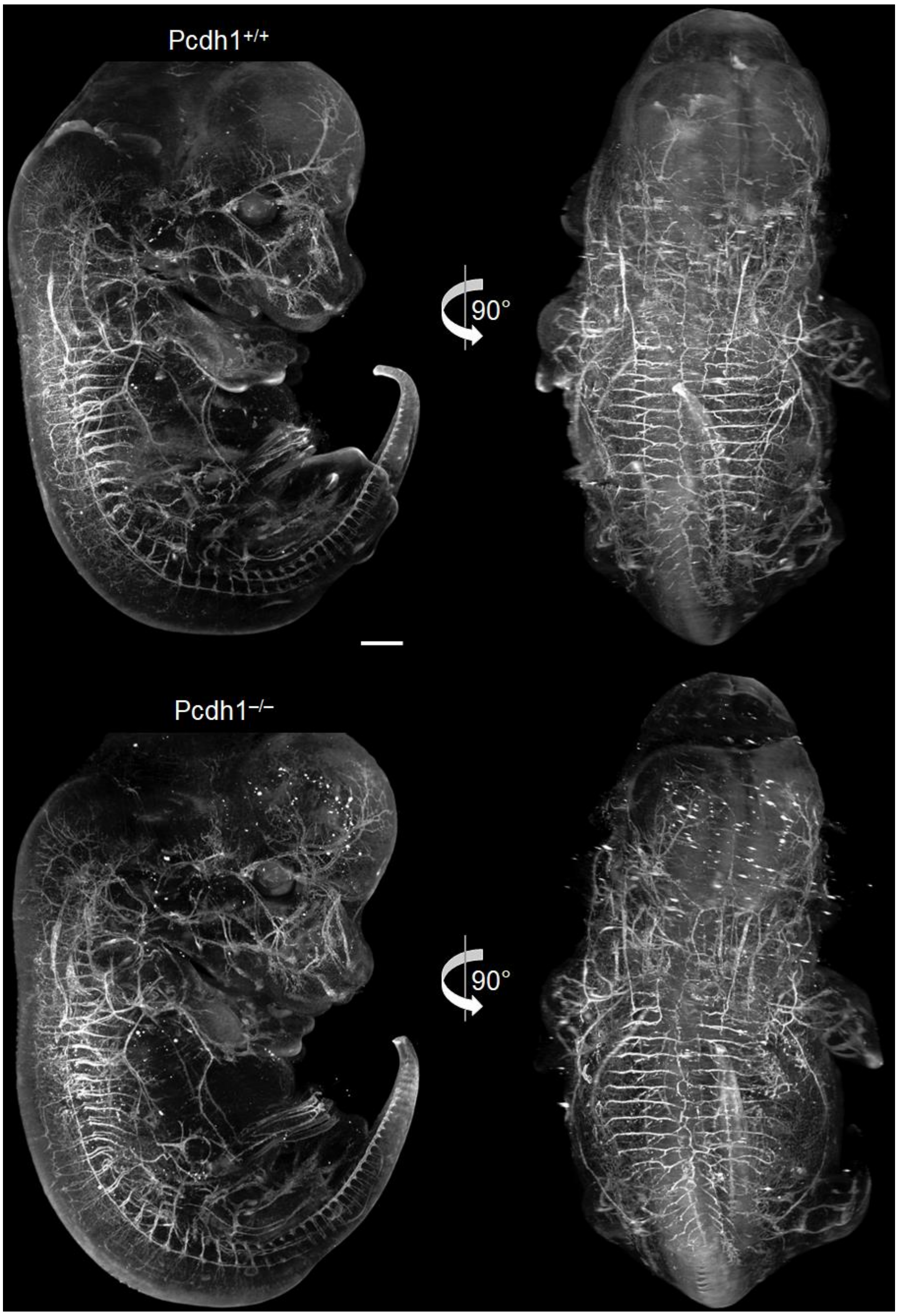

Figure 6.3. Three-dimensional renders of cleared, CD31-labelled mouse embryos.
3D renders of a representative “WT” mouse embryo (top) and of a representative “KO” embryo (bottom). Main vascular beds are easily identifiable in both, and do not differ grossly. Scale bar = 500 µm.

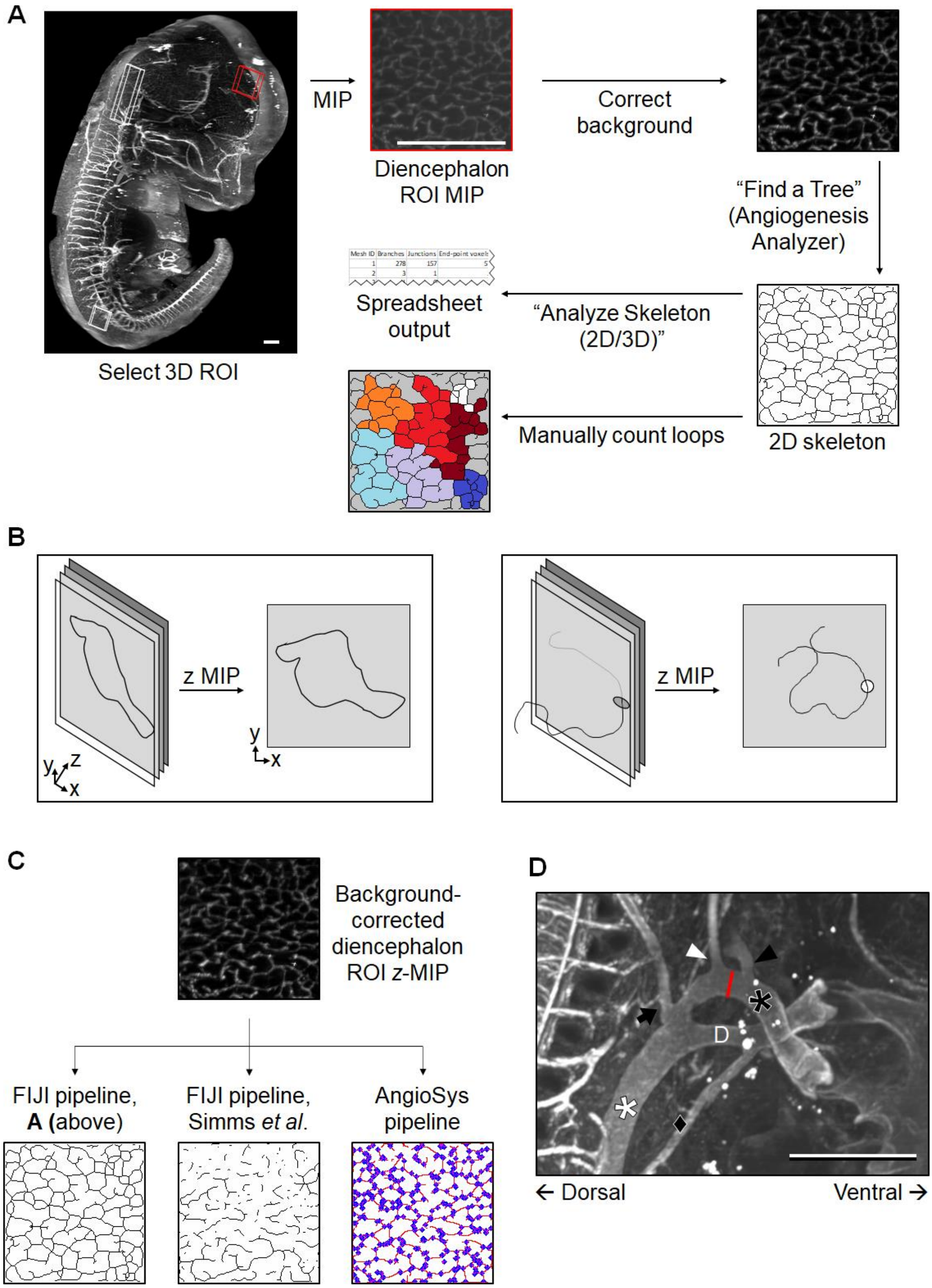

Figure 6.4. Pipelines for MIP (2D) analysis of E13.5 mouse embryo vasculature.
A. 2D mesh analysis pipeline. A maximum intensity projection along the *z*-axis (*z*-MIP) was created, background-corrected, and automatically analysed as detailed in **Section 2.7.6**. The embryo in the initial panel is a 3D render of 300 *z*-planes, tilted to aid visualisation of the thickness of each ROI. The white/red boxes identify the three 3D ROI analysed, the red ROI being selected as an example for further panels. Scale bars = 500 µm.

(Continued from previous page)

B. Looped structures identified in a 2D *z*-MIP can either derive from actual vascular loops (left), or from the superimposition of non-looping, multi-plane structures that appear to loop upon *z*-projection (right).

C. Alternative segmentation approaches for analysis. The result of each segmentation pipeline applied to the same ROI is shown. The central pipeline is taken from Simms et al. (2017).

D. Visualisation of a representative aortic region, with labels identifying the structures used as reference points to assess aortic arch luminal thickness. Structures were identified with the aid of diagrams in the literature (Assemat et al., 2014; Savolainen et al., 2009). Scale bar = 500 µm. Red line = measurement; D = ductus arteriosus; diamond = pulmonary artery; white star = descending aorta; black star = ascending aorta; black arrow = left subclavian artery; black arrowhead = brachiocephalic/innominate artery; white arrowhead = left common carotid artery.

analysis, a maximum intensity projection (MIP) was first created from an appropriate number of *z*-planes per ROI, the minimum sufficient to result in the appearance of looping structures. The number of planes differed for the three ROIs in different positions, but was kept consistent for a given ROI across the different specimens. These loops could either arise as a representation of a truly looping set of vessels, or as artefacts of compressing three-dimensional data onto a single plane – the MIP (**Figure 6.4B**). Various vascular parameters were then quantified using the Angiogenesis Analyzer plugin for *ImageJ*, as this resulted in the most consistent identification of vessels across the tested pipelines (**Figure 6.4C**); the *Angiosys* software could also effectively identify vessels, but the parameters had to be manually identified on a per sample basis, whereas they could be kept consistent for the same ROI across embryos when using Angiogenesis Analyzer. Vessels identified and analysed through this pipeline were 10-20 μm in diameter, which was about the resolution limit of the experiment. Similarly, in a different type of two-dimensional analysis, the luminal thickness of the aortic arch was quantified, also from an appropriately assembled MIP (**Figure 6.4D**); in this case, however, the number of *z*-planes used varied, although not vastly, across embryos, given that the aorta was not always in the same position and orientation, and that the true diameter could only be estimated by including a number of *z*-planes sufficient to encompass its whole thickness.

Automated analysis of vascular features in two dimensions (**Figure 6.5**), as per the pipeline outlined above, yielded no statistical difference in any of: the total number of vessels, the number of extremities (vessels connected to another vessel at only one of their ends), the number of junctions (single points where at least three vessels are joined), the total vessel length, or the average vessel length in the ROI encompassing the junction between the medulla and the spinal cord; similarly, none of these parameters were different between WT and KO groups for the diencephalon ROI, nor the spinal cord ROI either. Furthermore, statistical

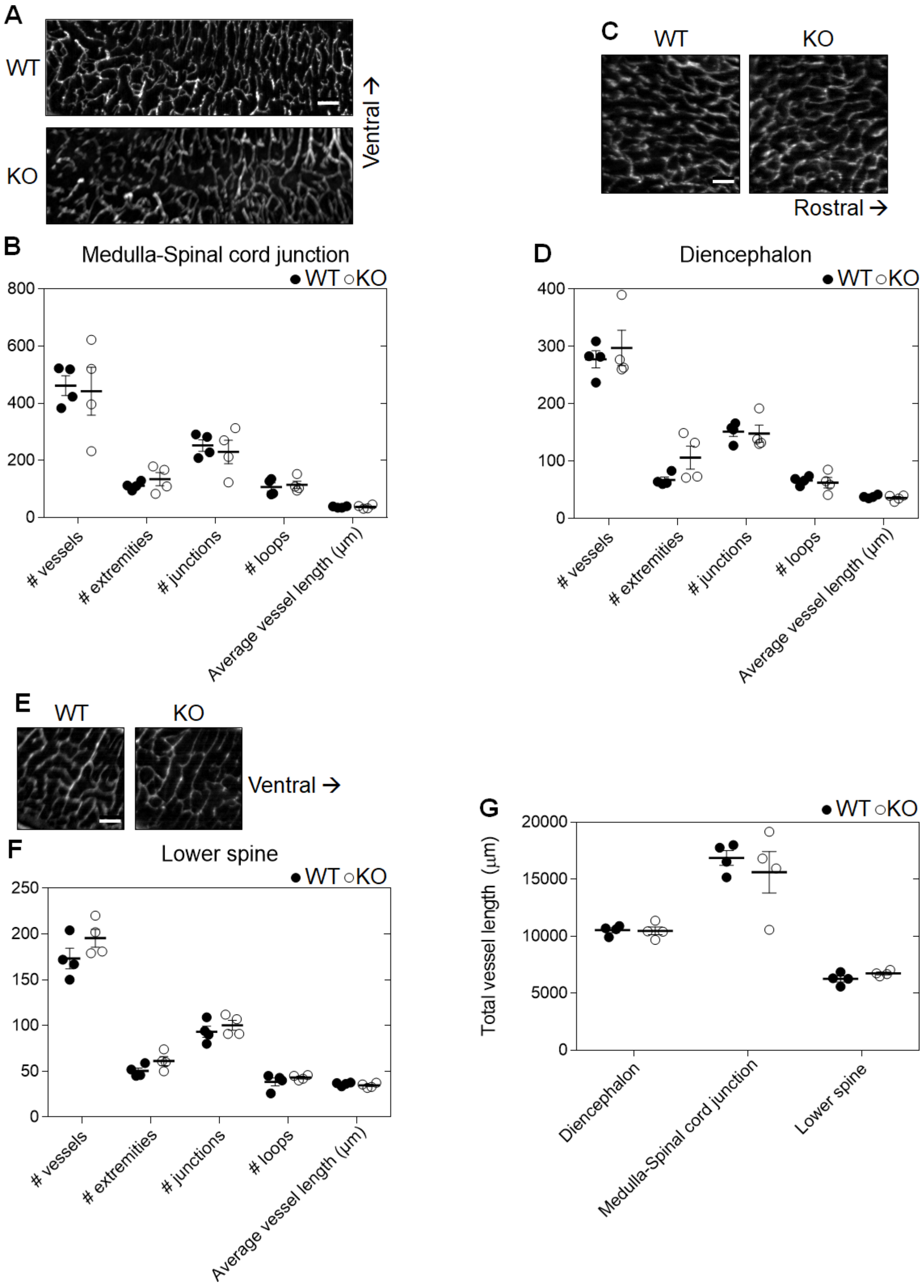

Figure 6.5. Two-dimensional analysis of small-diameter embryonic vasculature.

A, C, E. Representative *z*-MIP used for vascular analysis in the medulla-spinal cord junction (**A**), diencephalon (**C**), and lower spine (**E**) ROIs. These are identified in **Figure 6.4A**. Scale bar = 100 µm.

B, D, F. Summary of the analysis performed in the medulla-spinal cord junction (**B**), diencephalon

(Continued from previous page)
(**D**), and lower spine (**F**) ROIs. Single data points (individual embryos) are shown as circles. Bars identify mean ± s.e.m.
G. Combined length of all vessels in each ROI, analysed and represented as in **B**.

analysis of aortic arch thickness (**Figure 6.6**) also showed no significant difference between WT and KO embryos, with all values within the 90-100 μm range; values in KO embryos, however, varied much more than for WT specimens.

6.5. Three-dimensional analysis of vasculature in Pcdh1-KO embryos

Preliminary, qualitative analysis of MIPs constructed from merging 50 virtual planes in directions other than the *z*-axis again showed no substantial anatomical differences in the organisation of the vasculature between WT and KO embryos (**Figure 6.7**, **Figure 6.8**). Quantitative, three-dimensional vasculature analysis required an ad hoc pipeline to be established in *Vision4D*, the only available piece of software that could analyse the files, given their size. The pipeline that resulted in the most effective and sensitive identification of most vessel structures consisted of pre-processing aimed at correcting uneven background and reducing background noise, followed by signal intensity-based segmentation using the in-built "blob finder" algorithm. Because this algorithm is designed to identify isolated structures, rather than continuous structures such as vessels, its "split" factor was reduced to 0 so as to obtain a continuous surface that encompassed the whole vessel in each case; allowing any degree of splitting invariably resulted in vessels being identified as patchy structures, depending on variations of CD31 immunolabelling signal intensity across their surface. Two drawbacks derived from this choice: first, information on the interconnectivity of the vasculature could not be gathered, because all vasculature was effectively classified as one, contiguous object. Second, the analysis could not be undertaken on whole embryos due to their skin being autofluorescent: with split sensitivity = 0 the outer surface, also identified as an object due to its signal intensity, was classified as contiguous with, and a part of, the total internal vasculature, as one large object. To partly overcome these limitations, three-dimensional analysis was undertaken on smaller, internal ROIs that did not encompass the skin of the

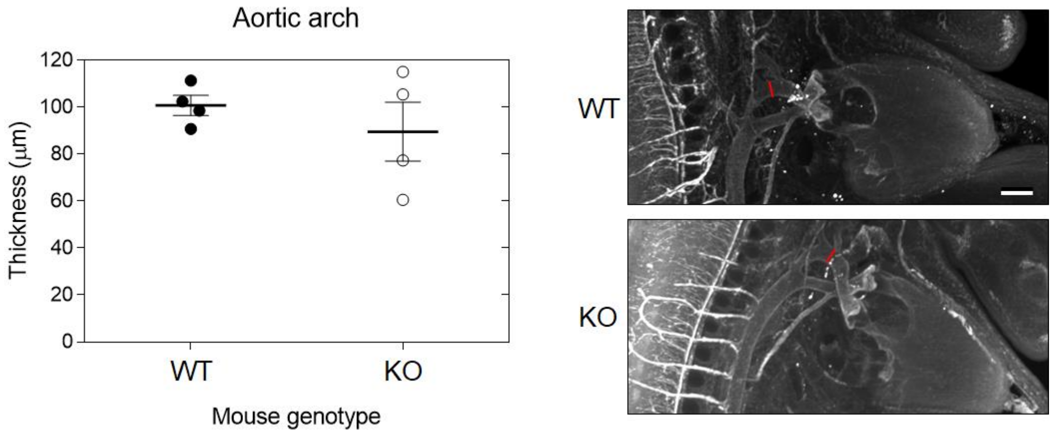

Figure 6.6. Two-dimensional analysis of aortic arch luminal thickness.
Analysis of the internal thickness of the aortic arch, measured between the left common carotid artery and the innominate artery. Single data points (individual embryos) are shown as circles. Bars identify mean ± s.e.m. On the right, representative pictures for each genotype are shown. Scale bar = 200 μm.

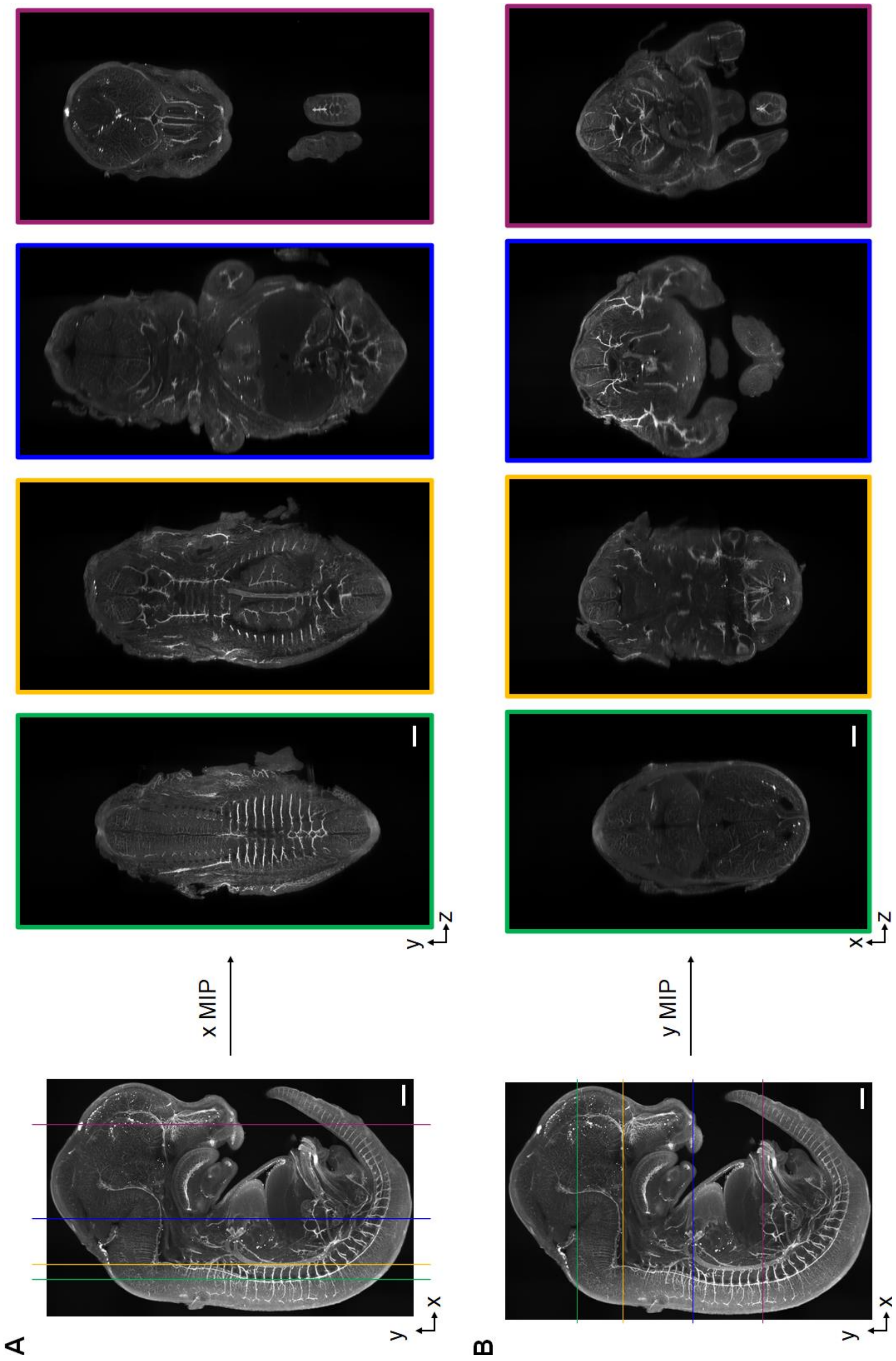

Figure 6.7. Virtual sectioning of a WT embryo.

A. The Vision 4D software allows computational reconstruction of MIP along axes other than the acquisition axis, allowing identification and comparison of the same features across different samples. Here, coronal sections are reconstructed by calculating MIP along the *x* axis of a representative WT embryo. Each section is an *x*-MIP constructed from a stack of 25 *x*-planes at either side of the given coloured line, for a total thickness of 193 µm. Scale bar = 500 µm.
B. Transverse sections of a representative WT embryo, reconstructed as per **A** from a given *y*-MIP of the same thickness. Scale bar = 500 µm.

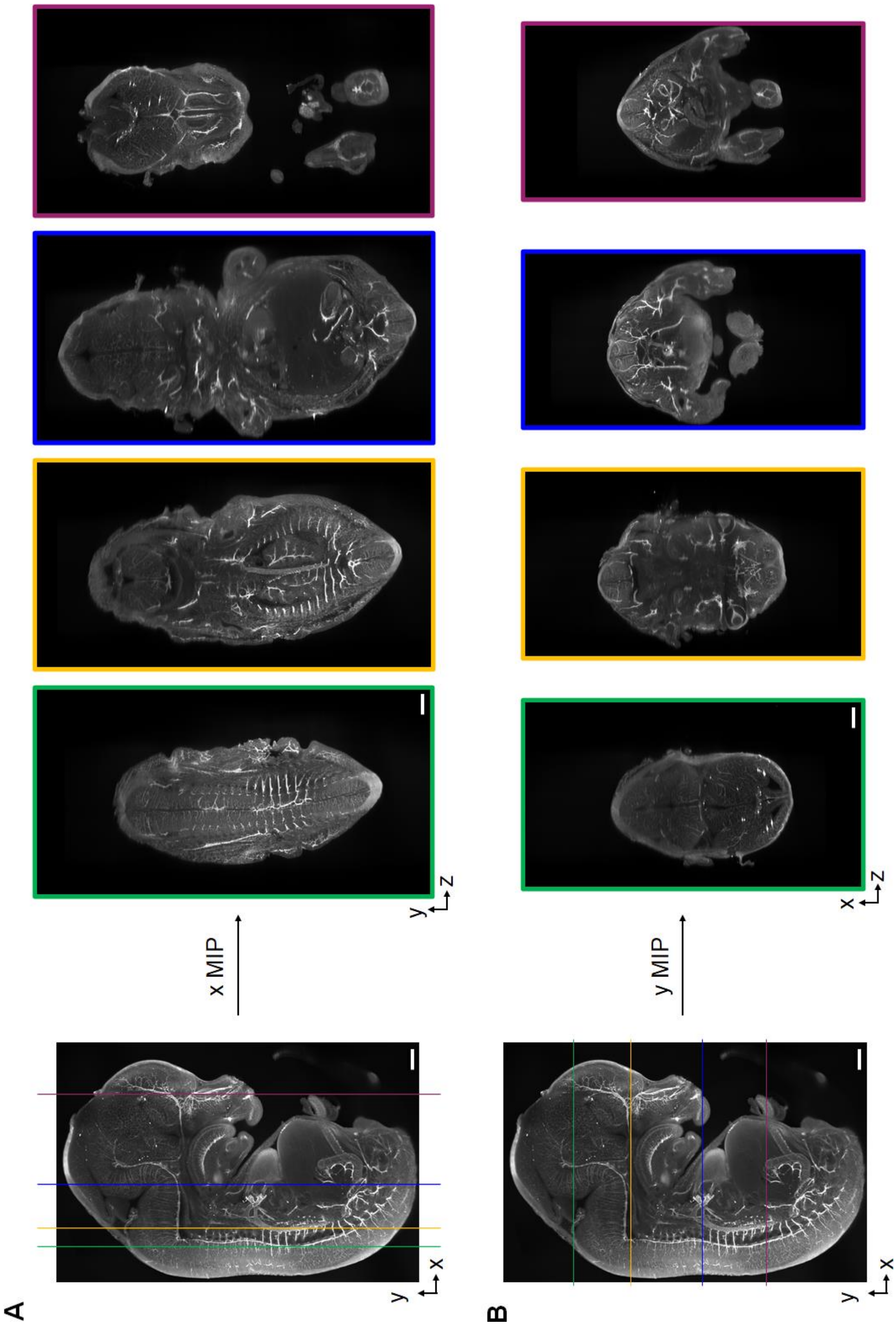

Figure 6.8. Virtual sectioning of a KO embryo.
A. Coronal sections of a representative KO embryo, reconstructed as per **Figure 6.7A** from a given *x*-MIP of the same thickness. Scale bar = 500 µm.
B. Transverse sections of a representative KO embryo, reconstructed as per **A** from a given *y*-MIP of the same thickness. Scale bar = 500 µm.

embryos: a larger ROI around the trunk area that included aorta, intercostal vessels, and pulmonary vasculature; and a much smaller ROI within the medullar portion of the brain (**Figure 6.9A-D**). The size of the trunk ROI was chosen as to maximise the ROI volume without encompassing the embryo's skin, whereas the medullar ROI was chosen to represent an area similarly analysed in two dimensions previously (**Section 6.4**). Analysis of the vasculature segmented as described (**Figure 6.9E-F**) revealed no significant differences between WT and KO vasculature in either ROI, both measured as total vessel surface area and total vessel volume, with most datapoints being fairly clustered, recapitulating preliminary observations from two-dimensional analysis.

Viewed together, the analyses undertaken in this chapter suggest that at E13.5 there are no differences in the physical organisation of the vasculature between WT and Pcdh1-KO mice.

6.6. Discussion

Work in this chapter aimed at assessing the arrangement of vascular beds in Pcdh1-KO mouse embryos. E13.5 embryos, immunolabelled for CD31, were rendered optically clear, allowing whole-mount imaging by fluorescence light-sheet microscopy. Qualitative vascular assessment revealed no gross anatomical abnormalities, and quantitative analysis of CD31 signal both in two and three dimensions highlighted no vascular differences between WT and Pcdh1-KO embryos.

6.6.1. Pcdh1 deletion during mouse embryogenesis

Mating Pcdh1-Flox to Pgk1-Cre mice allowed the generation of mice displaying the desired constitutive, ubiquitous knockout of Pcdh1. Mating Floxed and Pgk1-Cre parents is a commonly employed strategy to obtain global-knockout mice, and relies on the constitutive expression of the Cre transgene downstream of the *Pgk1* promoter, which starts early during

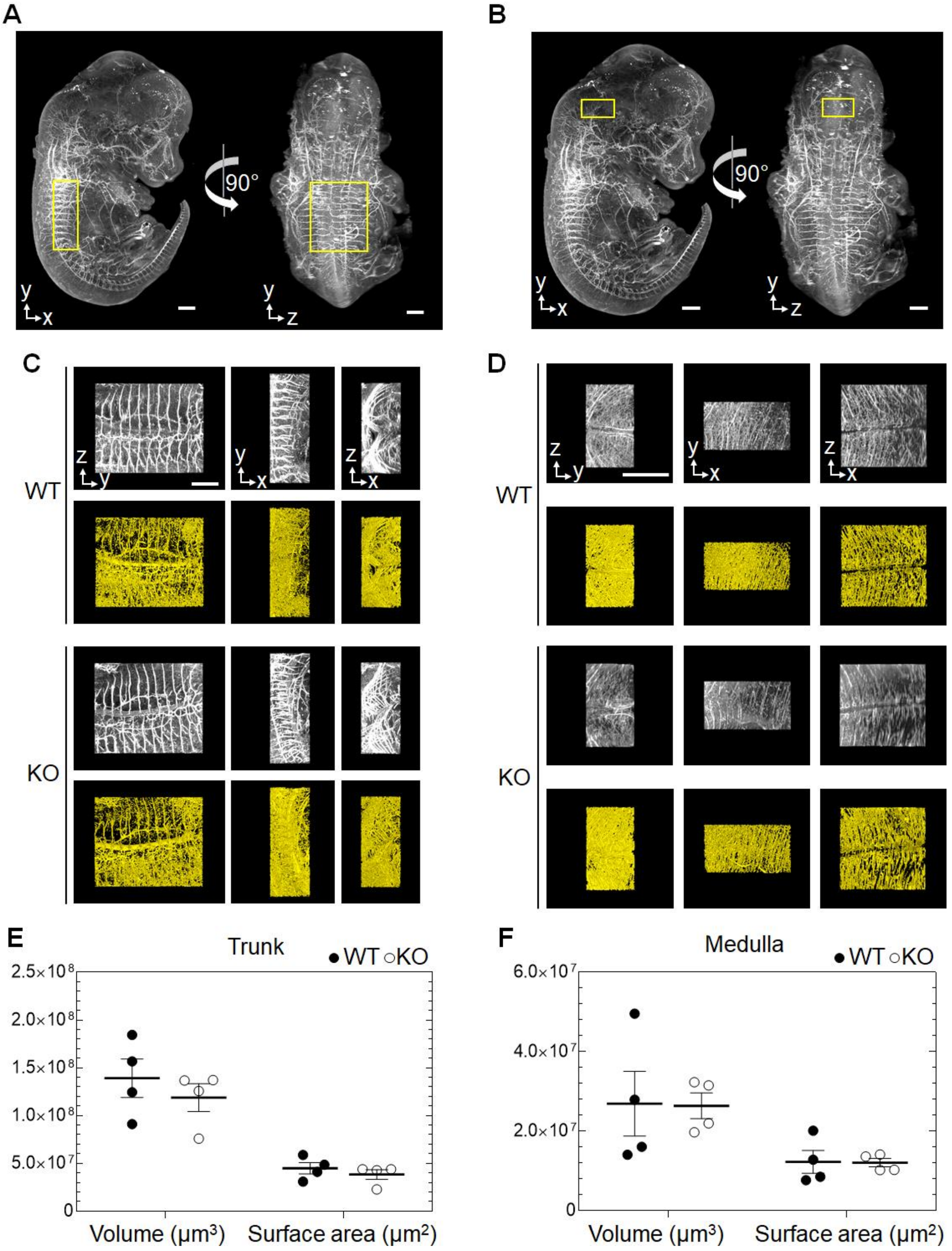

Figure 6.9. Three-dimensional analysis of embryo vasculature.

A, B. Representative 3D render showing, in a yellow outline, the location of the 3D ROIs chosen for vascular analysis in the trunk region around the aorta (**A**) and medulla (**B**). Scale bar = 500 μm.

C, D. 3D renders showing head-on, magnified versions of the ROIs above them (**C**: trunk; **D**: medulla), and the corresponding objects as identified after analysis (yellow). Scale bar = 500 μm.

E, F. Summary of the analyses of the trunk (**E**) and medullar (**F**) ROIs. Single data points (individual embryos) are shown as circles. Bars identify mean ± s.e.m.

oogenesis (Lallemand et al., 1998), and can therefore result in offspring carrying the deletion even without expressing Cre endogenously. The approach is similar to the more common strategy of transgene expression downstream of the *Rosa26* promoter, but is thought to result in increased expression levels (Chen et al., 2011); indeed, as assessed by genotyping PCRs, recombination worked well in all embryos taken forward (**Figure 6.1B**). Mating of Pcdh1-Flox mice to mice harbouring Cre under the direction of a tissue-specific promoter could instead allow deletion of Pcdh1 in only, for example, the endothelium, such as by using Tie2-Cre or VE-Cadherin-Cre mice (Payne et al., 2018). On the other hand, mating of Pcdh1-Flox mice to mice harbouring a tamoxifen-inducible Cre fusion protein, Cre/ERT2, would allow temporal control over the establishment of Pcdh1 knockout, either during pregnancy or adulthood. However, because in the first instance it was desired to assess whether Pcdh1 deletion had any effects global, embryonic deletion was deemed the most appropriate approach, reasoning that it would result in the most extreme phenotype, if any.

The exact developmental stage was selected as embryonic angiogenesis is well underway at E13.5, and *Pcdh1* is actively transcribed (Redies et al., 2008), reasoning that if Pcdh1 is involved in the process, any Pcdh1 loss-related phenotype would be manifest in the developing vasculature at this staging. Furthermore, because of the unclear role of PCDH1 in angiogenesis-mimicking *in vitro* assays (**Chapter 3**) undertaken prior to the experiments in this chapter, it was expected that any effects of Pcdh1 loss *in vivo* likely be modest, and potentially compensated for if assessing the vasculature at later embryonic stages.

6.6.2. Light-sheet imaging

The benefits of light-sheet imaging include avoiding the need to section the sample and thus preserving the intact anatomical organisation of the sample. This cardiovascular research community has recently started to recognise this as a major benefit for assessing an intrinsically three-dimensional structure such as the vasculature; however, applications of light-sheet microscopy to imaging vessel beds have often been confined to the zebrafish, because of its inherent transparency amongst other reasons (Baek et al., 2018; Ding, Lee, et al., 2018; Ding, Ma, et al., 2018). Notably, however, CD31 staining has been carried out previously with success in mouse embryos (Wylie et al., 2018), inspiring the experiments in this chapter. In order to achieve optical transparency, mouse embryos analysed here were cleared for light-sheet imaging through the iDISCO method, which was chosen among a plethora of clearing methods because of the relatively large size of the samples, the relative ease of the procedure and modest autofluorescence levels achieved, the availability and cost-effectiveness of the reagents involved, and because initial trials resulted in efficient CD31 immunostaining; indeed, the benefits of this particular clearing method to prepare samples for the purposes of light-sheet imaging were later summarised in a recent review (Molbay et al., 2021). Suboptimal clearing of the liver and heart (**Figure 6.2**) has been reported before and is a consequence of the high levels of perfusion of these organs, which renders it hard to bleach the haem groups completely despite hydrogen peroxide being used as part of the protocol. Clearing of the eyes is prevented (**Figure 6.2**) by the abundance of melanin instead, which is similarly hard to bleach; noteworthy, the melanin content of the embryo skin is also the likely reason (Molbay et al., 2021) behind its reported faint autofluorescence (**Section 6.5**). These limitations, which cause the apparent lack of CD31 signal in the liver, are however inherent to all clearing methods thus far developed, and further research into other (or additional), more effective haem bleaching or removal techniques is needed before complete optical clarity can be achieved.

6.6.3. Embryonic vasculature analysis

As reported in the previous section, whole-mouse embryonic vasculature analysis had been undertaken before (Wylie et al., 2018) but, notably, in a purely qualitative fashion, i.e. without undertaking any unbiased analysis. Because of the size, organisational complexity, and the differences in vessel calibres, automated analysis of three-dimensional vasculature has typically been confined to smaller organisms such as the developing zebrafish (Kugler et al., 2018; Kugler et al., 2020) or, as of more recently, single organs such as the murine brain (Kirst et al., 2020; Todorov et al., 2020), with other vascular beds invariably requiring analysis pipelines to be designed *ad hoc* (Buglak et al., 2021; Chang et al., 2019; Epah et al., 2018; Lugo-Hernandez et al., 2017). Importantly, there are no standardised, automated pipelines for the analysis of entire murine embryo vasculature. Therefore, given both the complexities mentioned above and the faint level of autofluorescence observed on all samples' skin (**Section 6.5**, **Figure 6.3**), an analysis pipeline had to be developed *ad hoc* here too. The three-dimensional analysis pipelines developed as a result had to take into account all these factors, and were therefore confined to ROIs that did not encompass the skin (**Figure 6.9**), rather than the whole embryo. Another important caveat to the analysis is the fact that the expression of CD31 is not exclusively confined to the surface of blood vessels, in fact appearing on a host of other cells, including platelets and leucocytes that can infiltrate tissues (Pusztaszeri et al., 2006). CD31$^+$ infiltrates could conceivably contribute to the faint levels of autofluorescence observed across the entire embryo, which prevented identification of vessels of diameter smaller than 10-15 μm, despite the illuminating sheet of light used for excitation being 2 μm-thick (**Section 2.7.5**) – which would have greatly minimised out-of-focus emission.

The results of preliminary vascular analysis in two dimensions (**Section 6.4**) were later corroborated by the analyses undertaken in three dimensions (**Section 6.5**). The areas to be analysed in two dimensions were chosen because of their high vascular density (**Figure 6.5**) and, importantly, because *Pcdh1* expression was reported as abundant in these regions at age

E13.5 in the Allen Developing Mouse Brain Atlas (experiment ID: 100058589; Lein et al. (2007)) and in previous publications in the case of the hindbrain of E13 NMRI mouse embryos (Redies et al., 2008). Furthermore, the hindbrain in particular has been proposed as a convenient model structure to assess angiogenesis in developing mice (Fantin et al., 2013). Personal correspondence with the Nawijn-Koppelman laboratories revealed Pcdh1-KO mice to be smaller than their littermates on average, although this was not noted in the embryos at the time of analysis; therefore, such developmental defects must become apparent only after the first two weeks of pregnancy, indeed when embryos increase in size most dramatically, nearly doubling in length during the last week of pregnancy (Theiler, 1989). For this reason, analysis of physiological angiogenesis after E13.5, either at later embryonic stages or postnatally (such as takes place in the retina), could be undertaken to assess whether it is impacted by Pcdh1 loss. Likewise, *in vivo* assays that stimulate ectopic angiogenesis, either by ligation of an artery, or the implantation of tumours or solidified matrices, could also be undertaken in adult mice.

CHAPTER 7: GENERAL DISCUSSION

7.1. General discussion

The data presented in this thesis has clearly shown that PCDH1 is expressed, and can be targeted by individual or mixed siRNA duplexes, in HUVEC (**Chapter 3**), that the cytosolic domain of PCDH1 co-purifies with the first four repeats of the Desmoplakin (DP) Head domain (**Chapter 4**), that truncations of the soluble extracellular domain of PCDH1 are unlikely to affect tubulogenesis *in vitro* (**Chapter 5**), and that global Pcdh1 knockout does not result in impaired vessel formation in E13.5 mouse embryos (**Chapter 6**).

A more speculative conclusion, based on cDNA microarray analysis of HUVEC following PCDH1 knockdown, is that PCDH1 might have an anti-angiogenic role (**Chapter 3**). This is supported by a computational pathway analysis, which highlighted that treating HUVEC with a mixture of *PCDH1*-targetting siRNAs overall results in a similar transcriptomic profile to those known to be elicited if cell proliferation and motility molecular pathways were activated. The nature of this assessment is speculative, but it seems plausible given the lack of anti-angiogenic phenotypes in all *in vitro* assays undertaken with siRNA-mixture. Furthermore, the lack of any overt pro-angiogenic phenotypes, together with the observation of an anti-angiogenic phenotype in some of the *in vitro* assays where PCDH1 knockdown was obtained by transfection of single siRNA duplexes, underscores that this proposed effect would be modest in nature. Importantly, microarray analysis allowed to identify many cell motility-related transcripts that were affected, alongside PCDH1, by the mixture as compared to a negative-control duplex. These included changes that are themselves known to promote angiogenesis such as MMP upregulation and Sema-3D downregulation, which were affected even more strongly by the PCDH1 siRNA mixture that PCDH1 itself, so at present it is unclear whether reductions in PCDH1 levels alone are sufficient to elicit activation of pro-angiogenic pathways. Furthermore, a surprising number of genes were found to be affected by transfection with the negative-control duplex, as compared to vector (Lipofectamine) only transfection or untreated HUVEC. However, because the above conclusions were all drawn using the negative control-treated samples as the baseline, any offset from the “true” HUVEC phenotype was thus incorporated into the analysis.

Taken together, these observations highlight that there are limitations that are inherent to the nature of any *in vitro* assay and that, financial constraints notwithstanding, it is important to profile the transcriptomic changes of the cell system, including transfection- and siRNA-specific changes, that is employed for the purposes of modelling a complex cell process such as angiogenesis. Other limitations might include the usage of HUVEC, which are not microvascular cells, to model a mainly microvascular process such as angiogenesis (Nowak-Sliwinska et al., 2018), and the fact that these assays, by design, do not include the effect of shear stress, which in itself is known to affect gene expression in the endothelium (Topper & Gimbrone Jr, 1999), including that of cell adhesion molecules (Chappell et al., 1998; Morigi et al., 1995; Nagel et al., 1994; Pfenniger et al., 2012). Nonetheless, they are still very useful tools to model *in vitro* single aspects of endothelial cell biology that would not be able to be probed separately, nor as quickly, *in vivo*.

Because some of the *in vitro* assays highlighted an impaired angiogenic response upon PCDH1 knockdown with either siRNA-1 or siRNA-2, and because this phenotype was lost by dilution of these duplexes, the effect size of reducing PCDH1 levels in HUVEC is predicted to be modest. It was therefore not surprising that Pcdh1-KO mice showed no obvious vascular phenotype at E13.5 (**Chapter 6**). However, this assessment only captures the organisation of vascular beds at a specific timepoint. Indeed, adult Pcdh1-KO mice are somewhat growth-impaired, and present a clear phenotype in the lung epithelium (Nawijn et al., 2018), so that later embryological, or even adult, manifestations of a vascular phenotype in Pcdh1-KO mice cannot be excluded. Assessment of postnatal angiogenesis, such as is permitted by the *ex vivo* retinal angiogenesis model, would assess whether this is the case (Stahl et al., 2010). Conversely, because the phenotype of different cell subpopulations undergoing the angiogenic programme is drastically different (**Section 1.1.2**), it is possible that only e.g. tip cells are affected by loss of Pcdh1 which, coupled with a small effect size, would likely result in normalisation of the vasculature over time and thus resolution of any vascular abnormalities. In this case, only assessments of the angiogenic process that resolve subcellular structures would be able to discern whether there are any differences between wild-type and KO mice; such assessments could include confocal imaging of the postnatal retina, or embryonic tissue sections, immunolabelled.

A potential interaction between the intracellular domain (ICD) of PCDH1 and DP was detected by an unbiased mass spectrometry experiment (**Chapter 4**). This was further examined by targeted co-purifications, and a proximity ligation assay, a commercial fluorescence-based assay that relies on physical proximity between the proteins of interest as the limiting factor to yield signal. The original aim was to identify endothelial interacting partners of PCDH1 but, because the PCDH1 ICD was produced in and purified from HEK 293T cells, the interaction was not confirmed to take place in the endothelium. Nevertheless, HUVEC express both PCDH1 (**Section 3.2**) and DP (Valiron et al., 1996), so it is likely that if the two interact in HEK 293T cells, they interact in HUVEC also, and that the interaction is of physiological relevance in the endothelial context, especially if PCDH1 resides in *complexus adhaerentes* alongside VE-cadherin (**Section 1.2.4**). Because DP interaction with the recognised desmosomal cadherins is mediated by Plakoglobin (**Figure 1.3**), it is likely that any interactions between DP and PCDH1 would also be mediated by the same adaptor(s).

Importantly, potential interactions mediated by the extracellular domain were not addressed by the experiments presented here, because investigation around the PCDH1 ectodomain only explored the possibility for self-interaction (**Chapter 5**). Furthermore, in other investigations, extracellular interactors of PCDH1 have only been explored within the δ-PCDH family (Harrison et al., 2020). However, even within the δ-PCDH family there are cases of extracellular interaction with classical cadherins (Biswas et al., 2010; Emond et al., 2011) and, more generally, cadherins can interact with altogether different membrane proteins (Morita et al., 2010). It could therefore be interesting to explore the potential for novel extracellular binding partners of PCDH1, perhaps by semi-high throughput technologies such as the Extracellular Interactome Assay platform (Özkan et al., 2013).

Ultimately, the most insightful experiments in the future could address the biological significance of the proposed interaction between PCDH1 and DP. For example, functional assays comparing the adhesive properties of the possible combinations of PCDH1^{+ve}/PCDH1^{-ve} and DP^{+ve}/DP^{-ve} cells might offer some insight into whether they reside in the same complex and whether they act in a synergistic way, to improve cell adhesion over the basal adhesion levels conferred by PCDH1 alone (Bisogni et al., 2018; Sano et al., 1993). However these assays, together with being qualitative in nature, might also be complicated by the fact that, if the interaction between DP and PCDH1 is mediated by other proteins rather than being direct, those might also be required to be co-expressed to enable binding.

Overall, the work in this thesis supports a number of novel findings, main among which are a novel interaction between PCDH1 and the Head domain of DP, and the potential identification of an anti-angiogenic role for PCDH1. Although the data gathered as part of this thesis gave limited functional information, a tentative biological role for PCDH1 in the endothelium can be proposed (**Figure 7.1**), on the basis of these conclusions and available data in the literature (**Section 1.3.3**). Extracellularly, PCDH1 mediates strong homotypic adhesion in *trans*. In a phalanx (quiescent) cell, SMAD3 and DP can bind the PCDH1 intracellular domain. These interactions are likely mutually exclusive, because mediated by adjacent, or even overlapping, residues in PCDH1. Interaction with DP confers structural rigidity by linking to the intermediate filament cytoskeleton, while sequestration of SMAD3 prevents its heterodimerisation with SMAD4. Upon sensing angiogenic stimuli and TGF-β binding, surface PCDH1 expression could be reduced, thereby liberating SMAD3 and allowing its translocation to the nucleus and thus activation of gene transcription. Similarly, reduced PCDH1 levels liberate DP and result in fewer intercellular interactions, allowing reorganisation of the cytoskeleton, alteration of cell morphology, and enabling responsiveness to chemotactic cues, potentially even PCDH1 ectodomains on other cells. By way of speculation, because disengagement of PCDH1-PCDH1 interactions results in “naked” PCDH1 species on the cell surface, the PCDH1 ECD would then be accessible to membrane-bound proteinases. Such proteins would include MMP10 (**Section 3.12**). Once the PCDH1 ECD is cleaved and degraded, post-translational modification of the PCDH1 ICD would allow interaction with unidentified intracellular signalling partners. Alternatively, a similar cleavage could take place in the cytosolic side, allowing the ICD to translocate to the nucleus. Either way, nuclear translocation (either of the PCDH1 ICD, or of a downstream effector) could affect a number of changes: stimulating MMP10 surface expression, thus establishing a self-reinforcing loop that commits the EC to the angiogenic pathway and allows extracellular matrix degradation; interfering with the expression of PCDH species including PCDH1, such that cell-cell adhesion is further impaired; reducing Sema-3 expression (**Section 3.12**), and perhaps expression of its receptor Plexin-D1, thereby dampening chemo-repulsive forces and allowing chemotaxis to occur; increasing KLF2 expression, further promoting exit from the basal quiescent state. Finally, by virtue of stimulating RHO GTPase expression, cortical reorganisation would be enhanced, such that the intermediate filaments skeleton would be reorganised, and lamellipodia formation would be enabled, further sustaining cell migration. Because the PCDH1 can recognise and bind to copies of itself with specificity and selectivity, and because the first four EC repeats are required for this ability (Harrison et al., 2020), only “naked” (and thus available for binding), full-length PCDH1 proteins would be able to act as chemotactic cue for migrating ECs i.e. PCDH1 would therefore act as migratory cue that allows to impart directionality to tip cells towards other tip cells. This tentative model incorporates and summarises the key findings of the thesis, to show how careful regulation of PCDH1 activity might enable or prevent an angiogenesis-responsive phenotype.

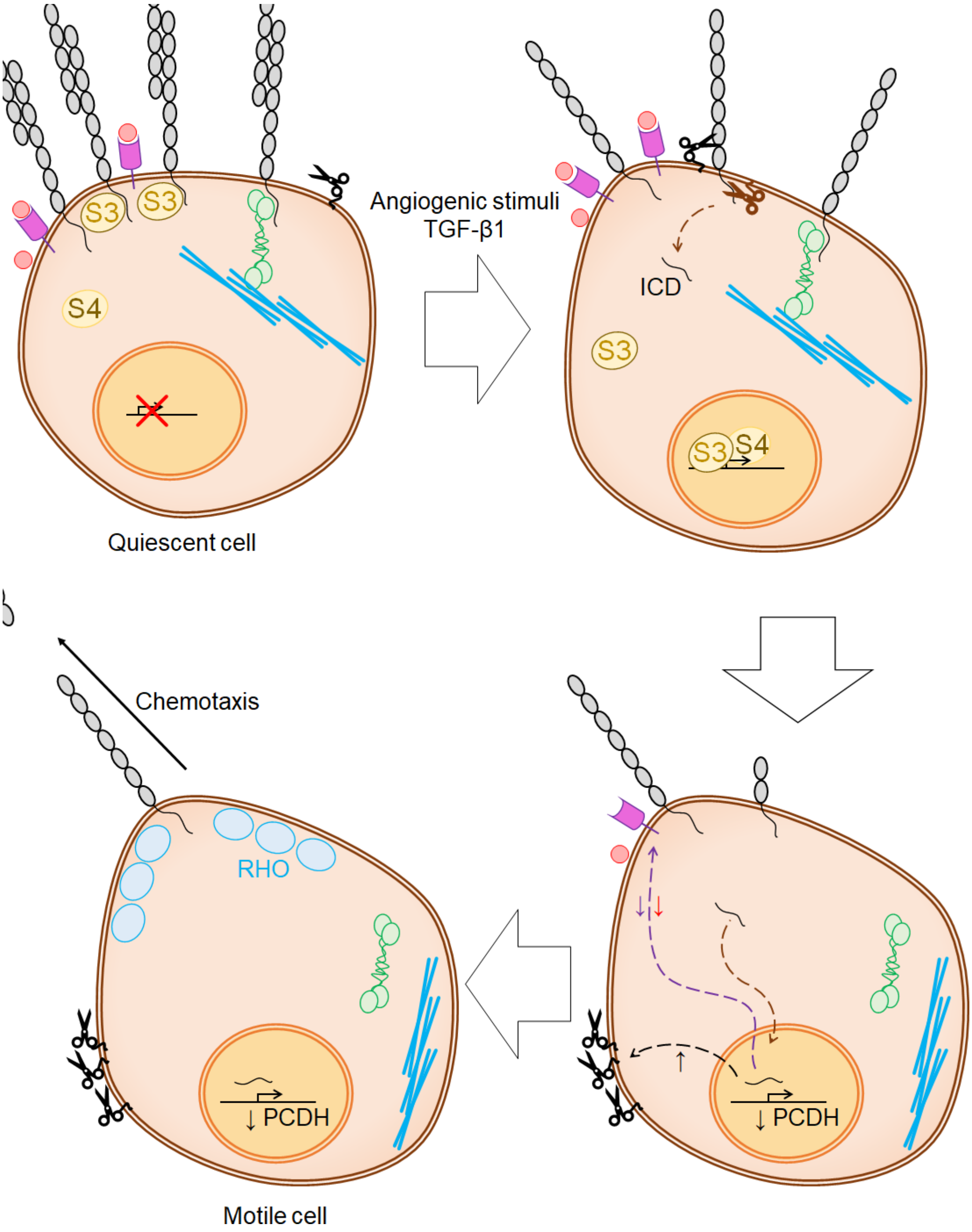

Figure 7.1. Possible biological roles of PCDH1.
Schematic representation of the possible biological roles of PCDH1 in the endothelium. Grey = PCDH1; S3 = SMAD3; S4 = SMAD4; green = Desmoplakin; blue lines = intermediate filaments; purple = Plexin-D1; red = Sema-3; black scissors = MMP10; brown scissors = intracellular protease.

APPENDIX: PLASMID BACKBONES

This appendix reports plasmid backbone maps of the plasmids that were employed and generated throughout the project, presented in the same order as they appear in **Table 2.7**. To avoid cluttering, select restriction sites are only shown if used as part of a cloning strategy, as described in **Table 2.6**.

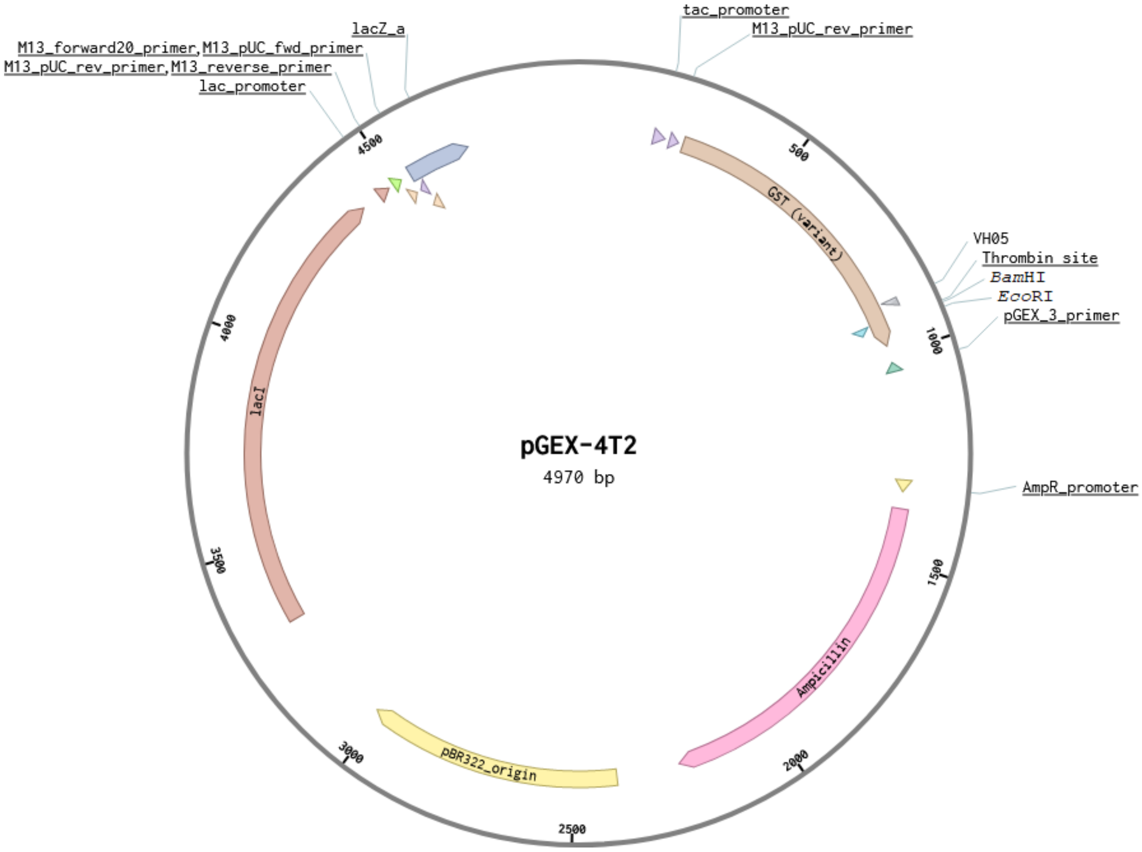

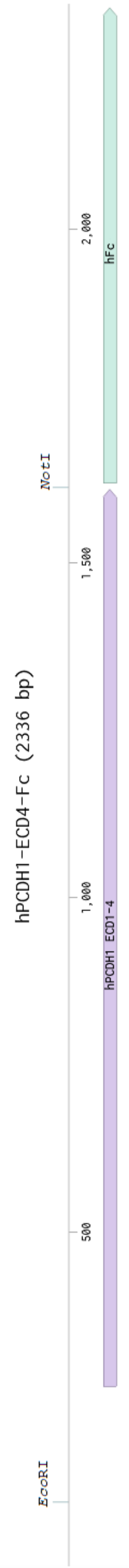

Please note that the full-sequence PIG vector, which is based on a pcDNA backbone (page 216), is not available. *In lieu* of a no-insert PIG vector, therefore, the map above presents the sequenced stretch of the hPCDH1-ECD4-hFc plasmid, which is based on the PIG backbone. As a result, bp numbering of the above is arbitrary.

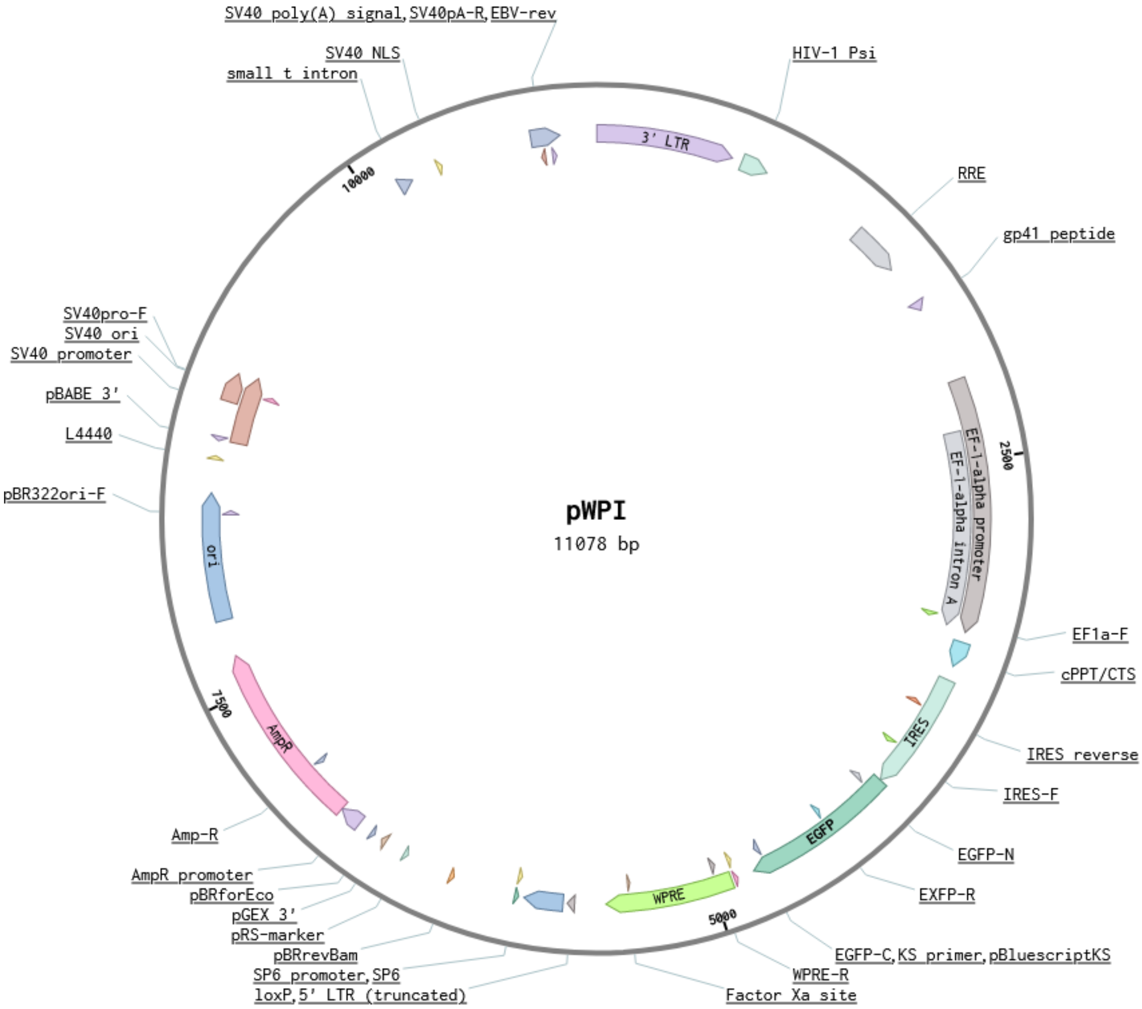
SV40 poly(A) signal, SV40pA-R, EBV-rev
SV40 NLS
small t intron
HIV-1 Psi
RRE
gp41 peptide
SV40pro-F
SV40 ori
SV40 promoter
pBABE 3'
L4440
pBR322ori-F
Amp-R
AmpR promoter
pBRforEco
pGEX 3'
pRS-marker
pBRrevBam
SP6 promoter, SP6
loxP, 5' LTR (truncated)
EF1a-F
cPPT/CTS
IRES reverse
IRES-F
EGFP-N
EXFP-R
EGFP-C, KS primer, pBluescriptKS
WPRE-R
Factor Xa site
3' LTR
EF-1-alpha promoter
EF-1-alpha intron A
IRES
EGFP
WPRE
AmpR
ori
10000
2500
5000
7500
pWPI
11078 bp

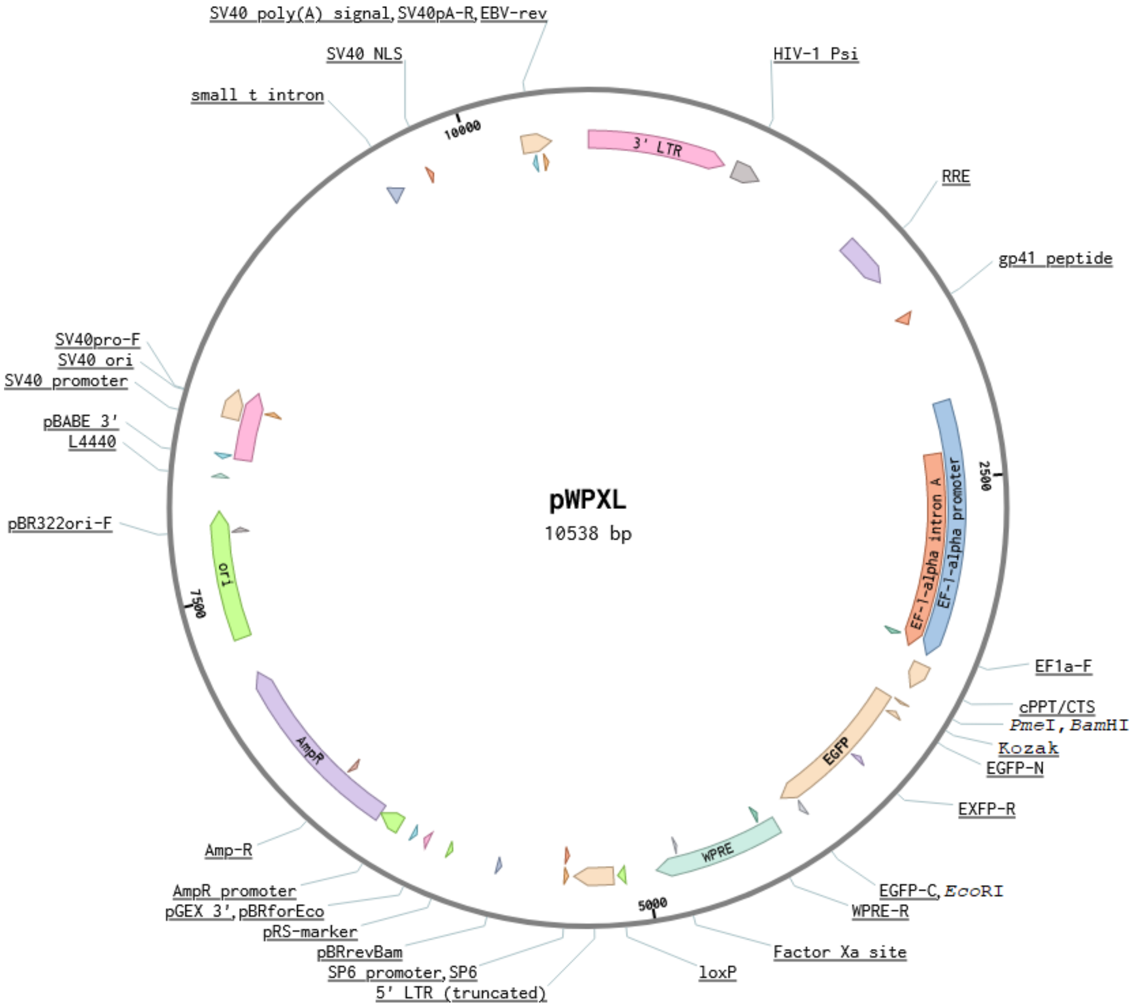
SV40 poly(A) signal, SV40pA-R, EBV-rev
SV40 NLS
small t intron
HIV-1 Psi
RRE
gp41 peptide
SV40pro-F
SV40 ori
SV40 promoter
pBABE 3'
L4440
pBR322ori-F
pWPXL
10538 bp
10000
3' LTR
2500
EF-1-alpha intron A
EF-1-alpha promoter
ori
7500
EF1a-F
cPPT/CTS
PmeI, BamHI
Kozak
EGFP-N
EGFP
EXFP-R
AmpR
WPRE
5000
EGFP-C, EcoRI
WPRE-R
Amp-R
AmpR promoter
pGEX 3', pBRforEco
pRS-marker
pBRrevBam
SP6 promoter, SP6
5' LTR (truncated)
Factor Xa site
loxP

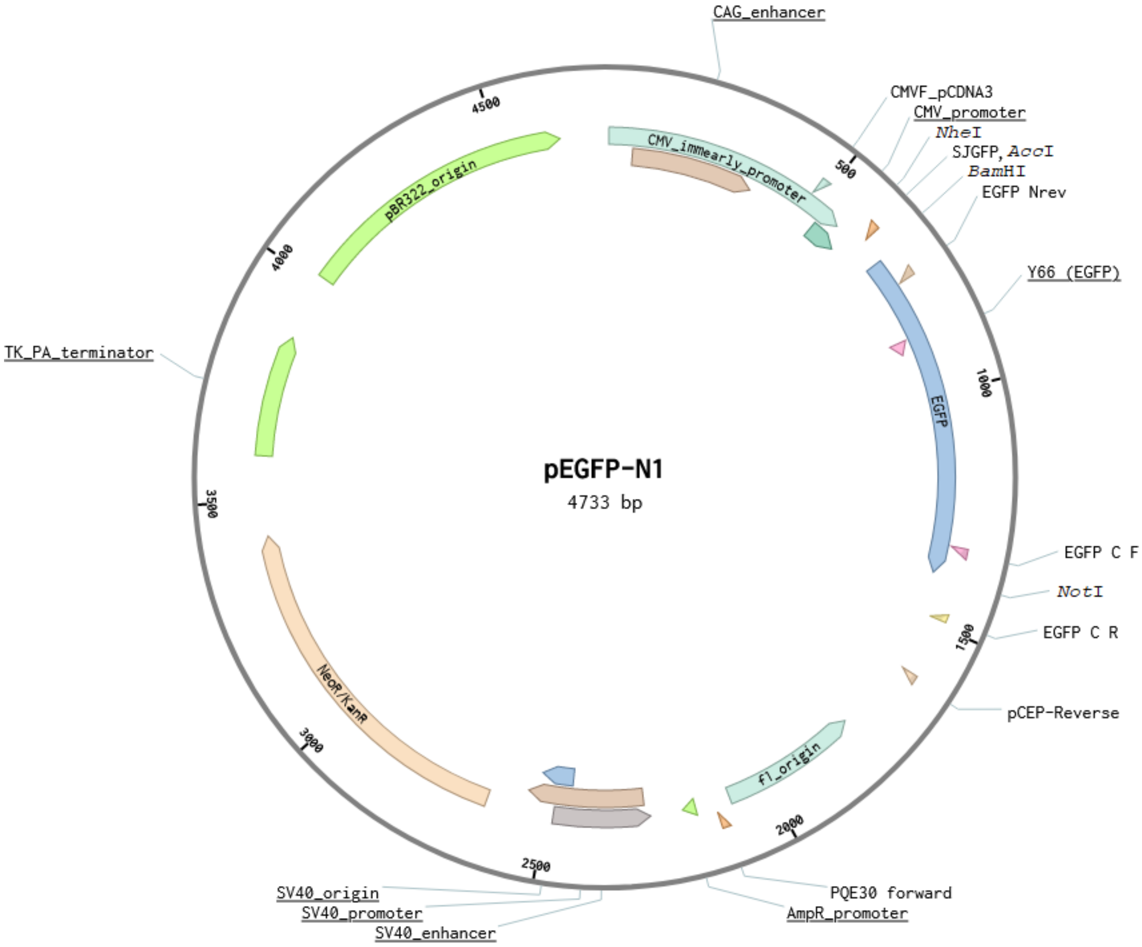
CAG_enhancer
CMVF_pCDNA3
CMV_promoter
NheI
SJGFP, AccI
BamHI
EGFP Nrev
Y66 (EGFP)
EGFP C F
NotI
EGFP C R
pCEP-Reverse
PQE30 forward
AmpR_promoter
SV40_origin
SV40_promoter
SV40_enhancer
TK_PA_terminator
pEGFP-N1
4733 bp
CMV_immearly_promoter
EGFP
f1_origin
NeoR/KanR
pBR322_origin
500
1000
1500
2000
2500
3000
3500
4000
4500

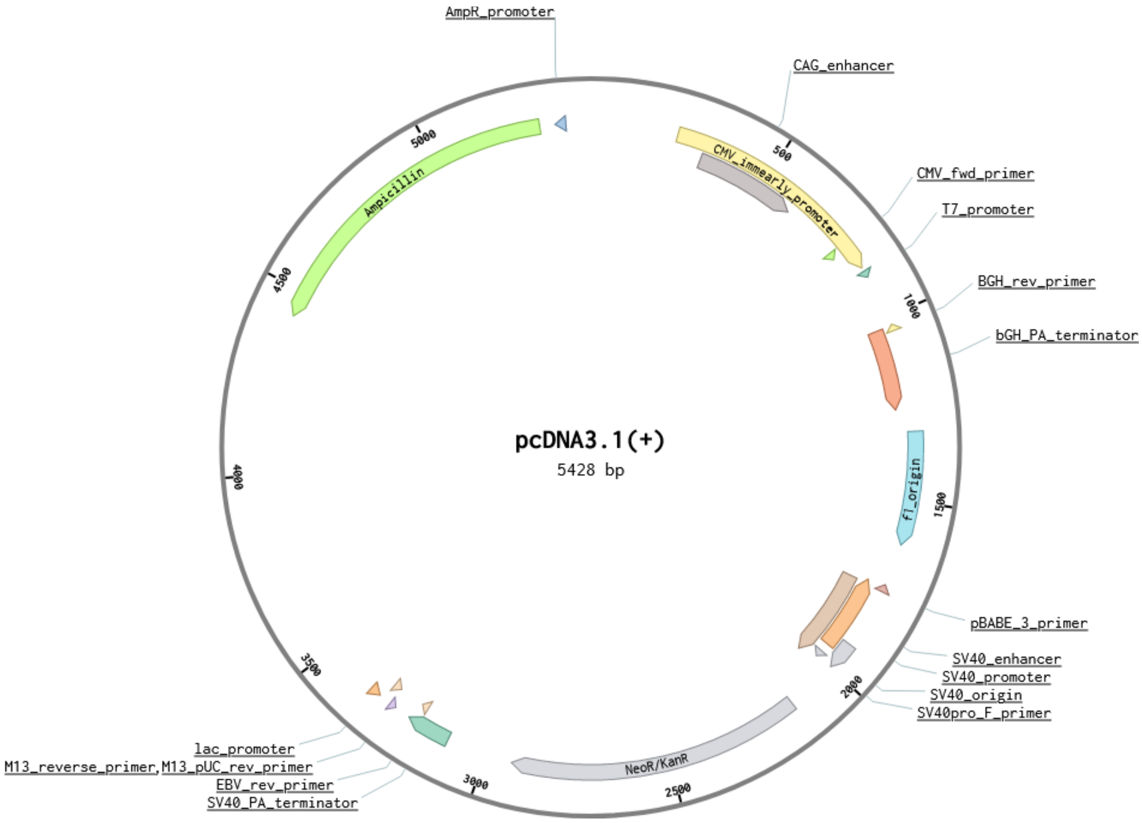
AmpR_promoter
CAG_enhancer
CMV_fwd_primer
T7_promoter
BGH_rev_primer
bGH_PA_terminator
pBABE_3_primer
SV40_enhancer
SV40_promoter
SV40_origin
SV40pro_F_primer
lac_promoter
M13_reverse_primer,M13_pUC_rev_primer
EBV_rev_primer
SV40_PA_terminator
pcDNA3.1(+)
5428 bp
Ampicillin
CMV_immearly_promoter
f1_origin
NeoR/KanR
500
1000
1500
2000
2500
3000
3500
4000
4500
5000

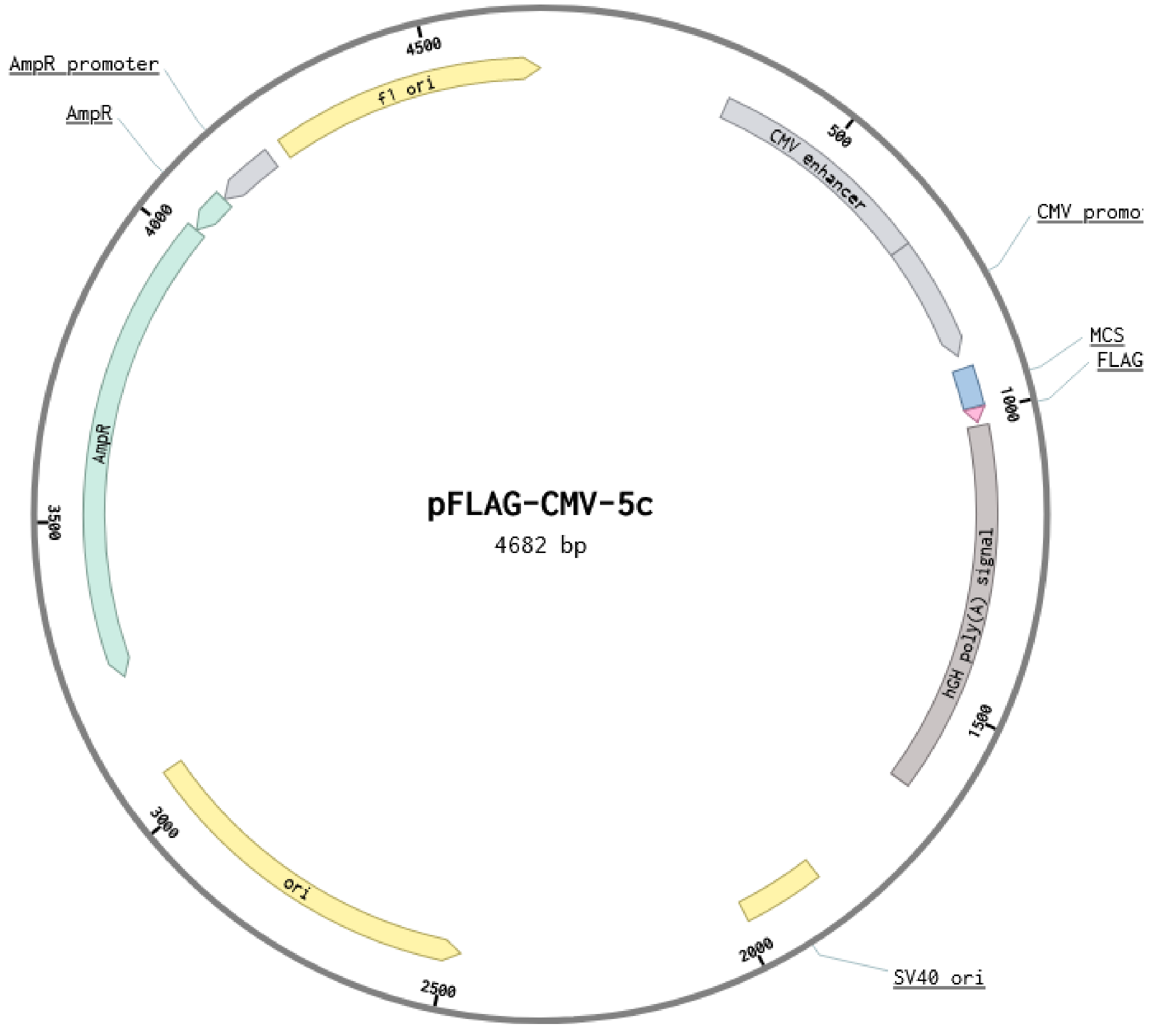
pFLAG-CMV-5c
4682 bp
AmpR promoter
AmpR
f1 ori
4500
500
CMV enhancer
CMV promo
MCS
FLAG
1000
hGH poly(A) signal
1500
SV40 ori
2000
2500
ori
3000
3500
4000
AmpR

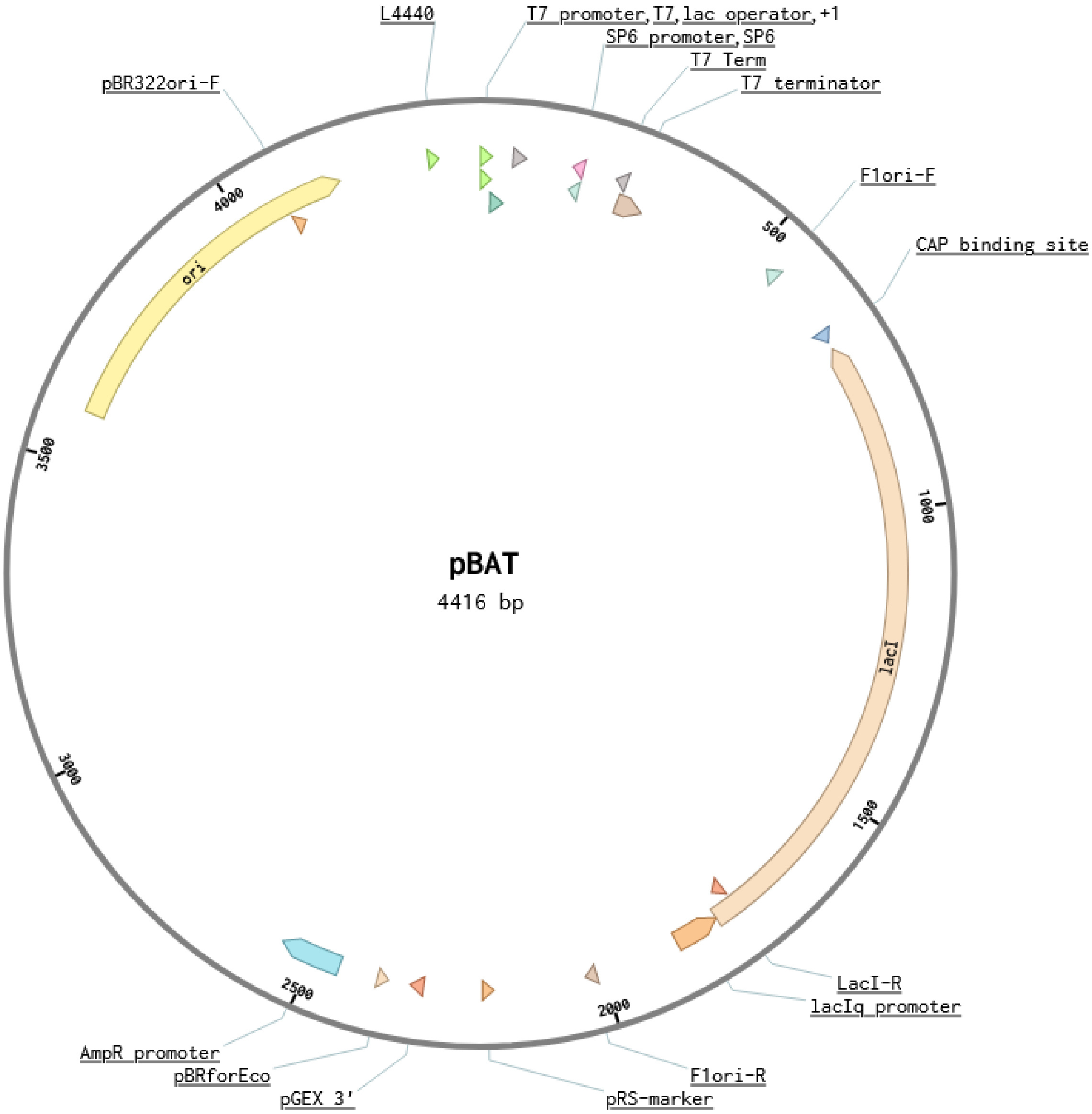
L4440
T7_promoter, T7, lac_operator, +1
SP6_promoter, SP6
T7_Term
T7_terminator
pBR322ori-F
F1ori-F
CAP_binding_site
4000
500
ori
3500
1000
pBAT
4416 bp
lacI
3000
1500
LacI-R
lacIq_promoter
2500
2000
AmpR_promoter
pBRforEco
pGEX_3'
F1ori-R
pRS-marker

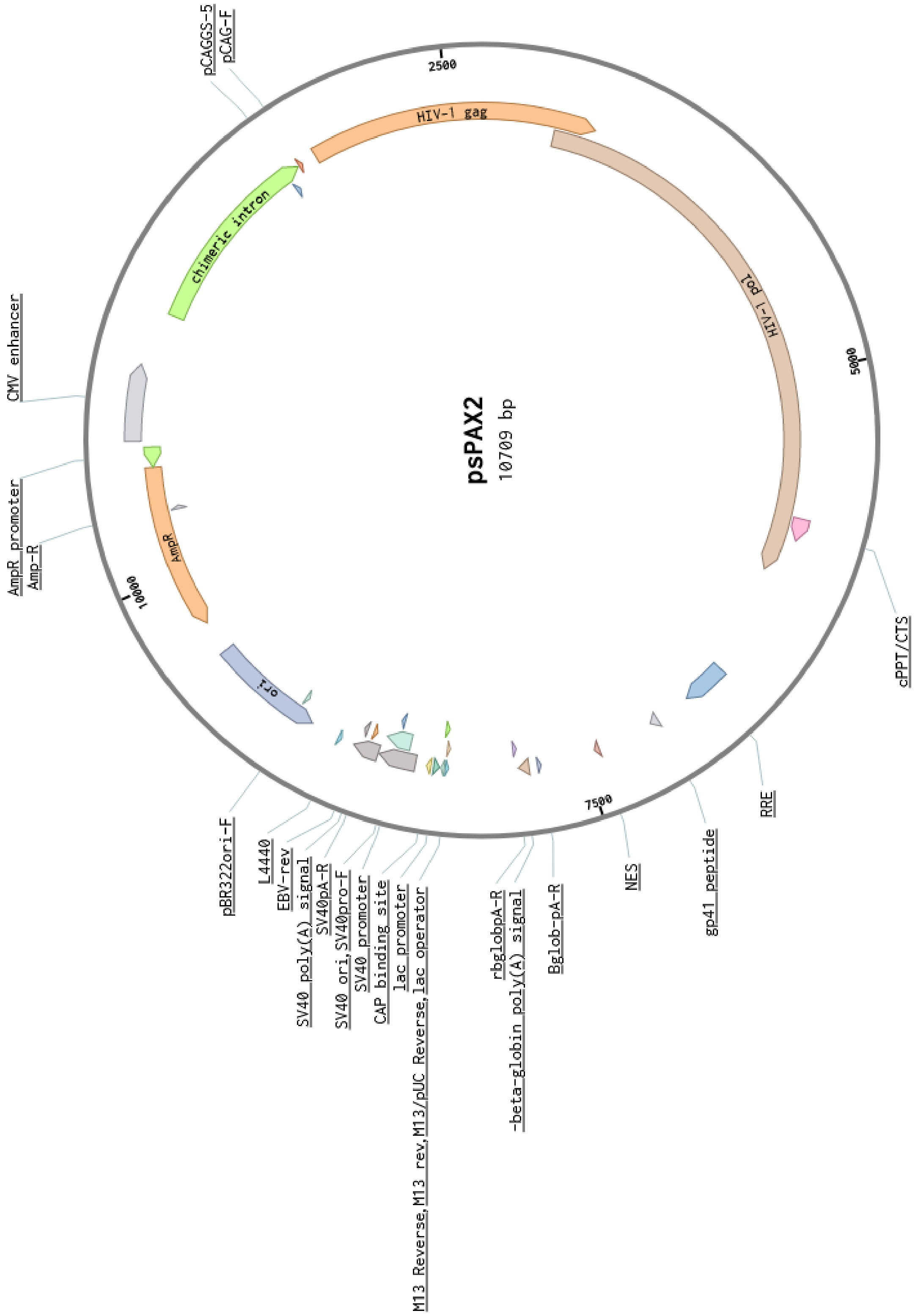
psPAX2
10709 bp
2500
5000
7500
10000
pCAGGS-5
pCAG-F
HIV-1 gag
HIV-1 pol
cPPT/CTS
RRE
gp41 peptide
NES
Bglob-pA-R
rbglobpA-R
-beta-globin poly(A) signal
M13 Reverse,M13 rev,M13/pUC Reverse,lac operator
lac promoter
CAP binding site
SV40 promoter
SV40 ori,SV40pro-F
SV40pA-R
SV40 poly(A) signal
EBV-rev
L4440
pBR322ori-F
ori
AmpR
Amp-R
AmpR promoter
CMV enhancer
chimeric intron

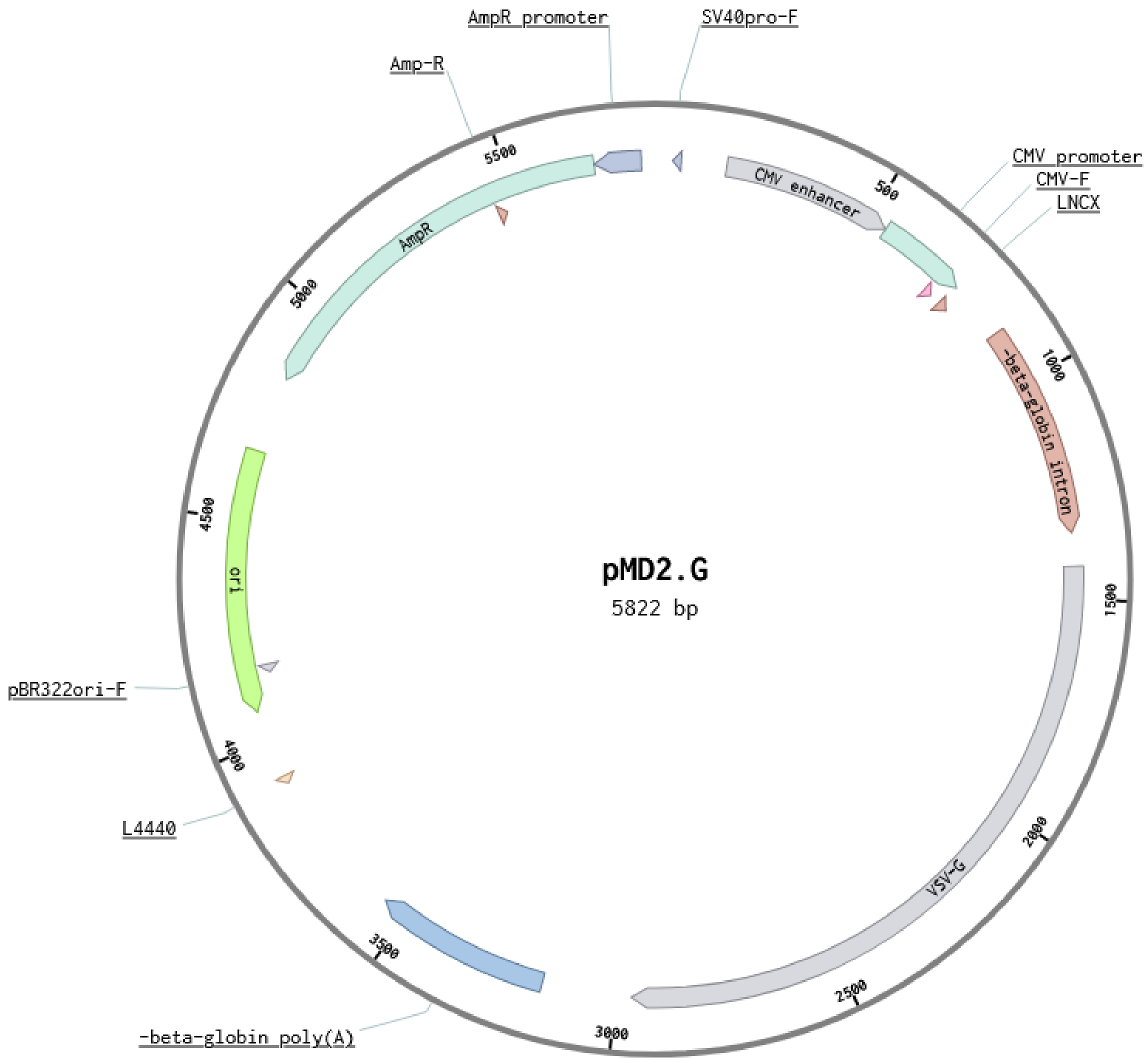
AmpR promoter
SV40pro-F
Amp-R
CMV promoter
CMV-F
LNCX
5500
500
CMV enhancer
AmpR
5000
1000
-beta-globin intron
4500
ori
pMD2.G
5822 bp
1500
pBR322ori-F
4000
L4440
2000
VSV-G
3500
2500
3000
-beta-globin poly(A)

List of references

Affolter, M., Zeller, R., & Caussinus, E. (2009). Tissue remodelling through branching morphogenesis. *Nature Reviews Molecular Cell Biology, 10*(12), 831-842.

Ahmad, S., Hewett, P. W., Fujisawa, T., Sissaoui, S., Cai, M., Gueron, G., . . . Ahmed, A. (2015). Carbon monoxide inhibits sprouting angiogenesis and vascular endothelial growth factor receptor-2 phosphorylation. *Thromb Haemost, 114*(02), 329-337.

Al-Amoudi, A., Castaño-Diez, D., Devos, D. P., Russell, R. B., Johnson, G. T., & Frangakis, A. S. (2011). The three-dimensional molecular structure of the desmosomal plaque. *Proceedings of the National Academy of Sciences, 108*(16), 6480-6485.

Al-Amoudi, A., Díez, D. C., Betts, M. J., & Frangakis, A. S. (2007). The molecular architecture of cadherins in native epidermal desmosomes. *Nature, 450*(7171), 832-837.

Al-Jassar, C., Knowles, T., Jeeves, M., Kami, K., Behr, E., Bikker, H., . . . Chidgey, M. (2011). The Nonlinear Structure of the Desmoplakin Plakin Domain and the Effects of Cardiomyopathy-Linked Mutations. *Journal of Molecular Biology, 411*(5), 1049-1061.

Alberts, B., Johnson, A., Lewis, J., Morgan, D., Raff, M., Roberts, K., & Walter, P. (2015). *Molecular biology of the cell* (6th ed.). New York: Garland Science, Taylor & Francis Group LLC.

Alfino, L. N., Wilczewski-Shirai, K. C., Cronise, K. E., Coy, J., Glapa, K., Ehrhart, E. J., . . . Regan, D. P. (2021). Role of Periostin Expression in Canine Osteosarcoma Biology and Clinical Outcome. *Veterinary Pathology*, 0300985821996671.

Alghanem, A. F., Wilkinson, E. L., Emmett, M. S., Aljasir, M. A., Holmes, K., Rothermel, B. A., . . . Cross, M. J. (2017). RCAN1.4 regulates VEGFR-2 internalisation, cell polarity and migration in human microvascular endothelial cells. *Angiogenesis, 20*, 341-358.

Armulik, A., Abramsson, A., & Betsholtz, C. (2005). Endothelial/pericyte interactions. *Circulation Research, 97*, 512-523.

Assemat, P., Siu, K. K., Armitage, J. A., Hokke, S. N., Dart, A., Chin-Dusting, J., & Hourigan, K. (2014). Haemodynamical stress in mouse aortic arch with atherosclerotic plaques: Preliminary study of plaque progression. *Computational and Structural Biotechnology Journal, 10*(17), 98-106.

Baek, K. I., Ding, Y., Chang, C.-C., Chang, M., Sevag Packard, R. R., Hsu, J. J., . . . Hsiai, T. K. (2018). Advanced microscopy to elucidate cardiovascular injury and regeneration: 4D light-sheet imaging. *Progress in Biophysics and Molecular Biology, 138*, 105-115.

Bartlett, D. W., & Davis, M. E. (2006). Insights into the kinetics of siRNA-mediated gene silencing from live-cell and live-animal bioluminescent imaging. *Nucleic Acids Research, 34*, 322-333.

Bäumer, S., Keller, L., Holtmann, A., Funke, R., August, B., Gamp, A., . . . Vestweber, D. (2006). Vascular endothelial cell–specific phosphotyrosine phosphatase (VE-PTP) activity is required for blood vessel development. *Blood, 107*(12), 4754-4762.

Bazzoni, G., & Dejana, E. (2004). Endothelial Cell-to-Cell Junctions: Molecular Organization and Role in Vascular Homeostasis. *Physiological Reviews, 84*(3), 869-901.

Belardi, B., Son, S., Felce, J. H., Dustin, M. L., & Fletcher, D. A. (2020). Cell–cell interfaces as specialized compartments directing cell function. *Nature Reviews Molecular Cell Biology, 21*(12), 750-764.

Benham-Pyle, B. W., Pruitt, B. L., & Nelson, W. J. (2015). Mechanical strain induces E-cadherin–dependent Yap1 and β-catenin activation to drive cell cycle entry. *Science, 348*(6238), 1024-1027.

Bernardes, S. S., Pinto, M. C. X., Amorim, J. H., Azevedo, V. A. d. C., Resende, R. R., Mintz, A., & Birbrair, A. (2020). Glioma Pericytes Promote Angiogenesis by Producing Periostin. *Cellular and Molecular Neurobiology*.

Berndt, J. D., Aoyagi, A., Yang, P., Anastas, J. N., Tang, L., & Moon, R. T. (2011). Mindbomb 1, an E3 ubiquitin ligase, forms a complex with RYK to activate Wnt/β-catenin signaling. *Journal of Cell Biology, 194*, 737-750.

Berx, G., & van Roy, F. (2009). Involvement of members of the cadherin superfamily in cancer. *Cold Spring Harbor Perspectives in Biology, 1*, 1-27.

Best, B. T. (2019). Single-cell branching morphogenesis in the Drosophila trachea. *Developmental Biology, 451*(1), 5-15.

Beutel, O., Maraspini, R., Pombo-García, K., Martin-Lemaitre, C., & Honigmann, A. (2019). Phase Separation of Zonula Occludens Proteins Drives Formation of Tight Junctions. *Cell, 179*(4), 923-936.e911.

Bishop, E. T., Bell, G. T., Bloor, S., Broom, I. J., Hendry, N. F. K., & Wheatley, D. N. (1999). An in vitro model of angiogenesis: Basic features. *Angiogenesis, 3*(4), 335-344.

Bisogni, A. J., Ghazanfar, S., Williams, E. O., Marsh, H. M., Yang, J. Y. H., & Lin, D. M. (2018). Tuning of delta-protocadherin adhesion through combinatorial diversity. *eLife, 7*, e41050.

Biswas, S., Emond, M. R., & Jontes, J. D. (2010). Protocadherin-19 and N-cadherin interact to control cell movements during anterior neurulation. *Journal of Cell Biology, 191*(5), 1029-1041.

Blacher, S., Erpicum, C., Lenoir, B., Paupert, J., Moraes, G., Ormenese, S., . . . Noel, A. (2014). Cell Invasion in the Spheroid Sprouting Assay: A Spatial Organisation Analysis Adaptable to Cell Behaviour. *PLOS ONE, 9*(5), e97019.

Blanco, R., & Gerhardt, H. (2013). VEGF and Notch in tip and stalk cell selection. *Cold Spring Harbor Perspectives in Medicine, 3*, 1-20.

Blevins, C. J., Emond, M. R., Biswas, S., & Jontes, J. D. (2011). Differential expression, alternative splicing, and adhesive properties of the zebrafish δ1-protocadherins. *Neuroscience, 199*, 523-534.

Bonné, S., Gilbert, B., Hatzfeld, M., Chen, X., Green, K. J., & van Roy, F. (2003). Defining desmosomal plakophilin-3 interactions. *Journal of Cell Biology, 161*(2), 403-416.

Bošnjak, I., Bojović, V., Šegvić-Bubić, T., & Bielen, A. (2014). Occurrence of protein disulfide bonds in different domains of life: a comparison of proteins from the Protein Data Bank. *Protein Engineering, Design and Selection, 27*(3), 65-72.

Boukamp, P., Petrussevska, R. T., Breitkreutz, D., Hornung, J., Markham, A., & Fusenig, N. E. (1988). Normal keratinization in a spontaneously immortalized aneuploid human keratinocyte cell line. *The Journal of cell biology, 106*(3), 761-771.

Branda, C. S., & Dymecki, S. M. (2004). Talking about a Revolution: The Impact of Site-Specific Recombinases on Genetic Analyses in Mice. *Developmental Cell, 6*(1), 7-28.

Brasch, J., Goodman, K. M., Noble, A. J., Rapp, M., Mannepalli, S., Bahna, F., . . . Shapiro, L. (2019). Visualization of clustered protocadherin neuronal self-recognition complexes. *Nature, 569*(7755), 280-283.

Brasch, J., Harrison, O. J., Ahlsen, G., Carnally, S. M., Henderson, R. M., Honig, B., & Shapiro, L. (2011). Structure and Binding Mechanism of Vascular Endothelial Cadherin: A Divergent Classical Cadherin. *Journal of Molecular Biology, 408*(1), 57-73.

Brasch, J., Katsamba, P. S., Harrison, O. J., Ahlsén, G., Troyanovsky, R. B., Indra, I., . . . Shapiro, L. (2018). Homophilic and Heterophilic Interactions of Type II Cadherins Identify Specificity Groups Underlying Cell-Adhesive Behavior. *Cell Reports, 23*(6), 1840-1852.

Brose, K., Bland, K. S., Wang, K. H., Arnott, D., Henzel, W., Goodman, C. S., . . . Kidd, T. (1999). Slit Proteins Bind Robo Receptors and Have an Evolutionarily Conserved Role in Repulsive Axon Guidance. *Cell, 96*(6), 795-806.

Buglak, N. E., Lucitti, J., Ariel, P., Maiocchi, S., Miller, F. J., Jr., & Bahnson, E. S. M. (2021). Light sheet fluorescence microscopy as a new method for unbiased three-dimensional analysis of vascular injury. *Cardiovascular Research, 117*(2), 520-532.

Burgess, R. W., Jucius, T. J., & Ackerman, S. L. (2006). Motor Axon Guidance of the Mammalian Trochlear and Phrenic Nerves: Dependence on the Netrin Receptor *Unc5c* and Modifier Loci. *The Journal of Neuroscience, 26*(21), 5756.

Bushell, K. M., Söllner, C., Schuster-Boeckler, B., Bateman, A., & Wright, G. J. (2008). Large-scale screening for novel low-affinity extracellular protein interactions. *Genome Research, 18*(4), 622-630.

Cao, J., Ehling, M., März, S., Seebach, J., Tarbashevich, K., Sixta, T., . . . Schnittler, H. (2017). Polarized actin and VE-cadherin dynamics regulate junctional remodelling and cell migration during sprouting angiogenesis. *Nature Communications, 8*(1), 2210.

Carmeliet, P., Ferreira, V., Breier, G., Pollefeyt, S., Kieckens, L., Gertsenstein, M., . . . Nagy, A. (1996). Abnormal blood vessel development and lethality in embryos lacking a single VEGF allele. *Nature, 380*, 435-439.

Carmeliet, P., & Jain, R. K. (2011). Molecular mechanisms and clinical applications of angiogenesis. *Nature, 473*, 298-307.

Carmeliet, P., Lampugnani, M.-G., Moons, L., Breviario, F., Compernolle, V., Bono, F., . . . Dejana, E. (1999). Targeted Deficiency or Cytosolic Truncation of the VE-cadherin Gene in Mice Impairs VEGF-Mediated Endothelial Survival and Angiogenesis. *Cell, 98*(2), 147-157.

Carpentier, G., Martinelli, M., Courty, J., & Cascone, I. (2012). *Angiogenesis analyzer for ImageJ.* Paper presented at the 4th ImageJ User and Developer Conference proceedings.

Carthew, R. W., & Sontheimer, E. J. (2009). Origins and Mechanisms of miRNAs and siRNAs. *Cell, 136*(4), 642-655.

Chadjichristos, C. E., Scheckenbach, K. E. L., van Veen, T. A. B., Richani Sarieddine, M. Z., de Wit, C., Yang, Z., . . . Kwak, B. R. (2010). Endothelial-Specific Deletion of Connexin40 Promotes Atherosclerosis by Increasing CD73-Dependent Leukocyte Adhesion. *Circulation, 121*(1), 123-131.

Chang, A. H., Raftrey, B. C., D'Amato, G., Surya, V. N., Poduri, A., Chen, H. I., . . . Red-Horse, K. (2017). DACH1 stimulates shear stress-guided endothelial cell migration and coronary artery growth through the CXCL12–CXCR4 signaling axis. *Genes & Development, 31*(13), 1308-1324.

Chang, C.-C., Ding, Y., Baek, K. I., Ding, X., Wang, D., Li, S., . . . Hsiai, T. K. (2019, 2019/04/14). *Light-sheet Imaging to Characterize Vascular Development in Murine Retina.* Paper presented at the Biophotonics Congress: Optics in the Life Sciences Congress 2019 (BODA,BRAIN,NTM,OMA,OMP), Tucson, Arizona.

Chappell, D. C., Varner, S. E., Nerem, R. M., Medford, R. M., & Alexander, R. W. (1998). Oscillatory Shear Stress Stimulates Adhesion Molecule Expression in Cultured Human Endothelium. *Circulation Research, 82*(5), 532-539.

Chauvet, S., Cohen, S., Yoshida, Y., Fekrane, L., Livet, J., Gayet, O., . . . Mann, F. (2007). Gating of Sema3E/PlexinD1 Signaling by Neuropilin-1 Switches Axonal Repulsion to Attraction during Brain Development. *Neuron, 56*(5), 807-822.

Chen, C.-m., Krohn, J., Bhattacharya, S., & Davies, B. (2011). A Comparison of Exogenous Promoter Activity at the ROSA26 Locus Using a PhiC31 Integrase Mediated Cassette

Exchange Approach in Mouse ES Cells. *PLOS ONE, 6*(8), e23376.

Chen, J., Lu, Y., Meng, S., Han, M.-H., Lin, C., & Wang, X. (2009). α- and γ-Protocadherins Negatively Regulate PYK2. *Journal of Biological Chemistry, 284*(5), 2880-2890.

Chen, K., Wu, K., Jiao, X., Wang, L., Ju, X., Wang, M., . . . Pestell, R. G. (2015). The Endogenous Cell-Fate Factor Dachshund Restrains Prostate Epithelial Cell Migration via Repression of Cytokine Secretion via a CXCL Signaling Module. *Cancer Research, 75*(10), 1992-2004.

Chen, R., Jiang, X., Sun, D., Han, G., Wang, F., Ye, M., . . . Zou, H. (2009). Glycoproteomics Analysis of Human Liver Tissue by Combination of Multiple Enzyme Digestion and Hydrazide Chemistry. *Journal of Proteome Research, 8*, 651-661.

Chen, X., Bonné, S., Hatzfeld, M., van Roy, F., & Green, K. J. (2002). Protein Binding and Functional Characterization of Plakophilin 2: EVIDENCE FOR ITS DIVERSE ROLES IN DESMOSOMES AND β-CATENIN SIGNALING. *Journal of Biological Chemistry, 277*(12), 10512-10522.

Choi, H.-J., Gross, J. C., Pokutta, S., & Weis, W. I. (2009). Interactions of Plakoglobin and β-Catenin with Desmosomal Cadherins. *Journal of Biological Chemistry, 284*(46), 31776-31788.

Choi, H.-J., & Weis, W. I. (2005). Structure of the Armadillo Repeat Domain of Plakophilin 1. *Journal of Molecular Biology, 346*(1), 367-376.

Chu, Q., Han, N., Yuan, X., Nie, X., Wu, H., Chen, Y., . . . Wu, K. (2014). DACH1 inhibits cyclin D1 expression, cellular proliferation and tumor growth of renal cancer cells. *Journal of Hematology & Oncology, 7*(1), 73.

Ciatto, C., Bahna, F., Zampieri, N., VanSteenhouse, H. C., Katsamba, P. S., Ahlsen, G., . . . Shapiro, L. (2010). T-cadherin structures reveal a novel adhesive binding mechanism. *Nature Structural & Molecular Biology, 17*(3), 339-347.

Colamarino, S. A., & Tessier-Lavigne, M. (1995). The axonal chemoattractant netrin-1 is also a chemorepellent for trochlear motor axons. *Cell, 81*(4), 621-629.

Colás-Algora, N., & Millán, J. (2019). How many cadherins do human endothelial cells express? *Cellular and Molecular Life Sciences, 76*(7), 1299-1317.

Colegio, O. R., Van Itallie, C. M., McCrea, H. J., Rahner, C., & Anderson, J. M. (2002). Claudins create charge-selective channels in the paracellular pathway between epithelial cells. *American Journal of Physiology-Cell Physiology, 283*(1), C142-C147.

Colland, F., Jacq, X., Trouplin, V., Mougin, C., Groizeleau, C., Hamburger, A., . . . Gauthier, J.-M. (2004). Functional Proteomics Mapping of a Human Signaling Pathway. *Genome Research, 14*(7), 1324-1332.

Colley, K. J., Varki, A., & Kinoshita, T. (2017). Cellular organization of glycosylation.

Cooper, S. R., Jontes, J. D., & Sotomayor, M. (2016). Structural determinants of adhesion by Protocadherin-19 and implications for its role in epilepsy. *eLife, 5*, e18529.

Cummings, R. D. (2019). "Stuck on sugars – how carbohydrates regulate cell adhesion, recognition, and signaling". *Glycoconjugate Journal, 36*(4), 241-257.

Danzer, C., Eckhardt, K., Schmidt, A., Fankhauser, N., Ribrioux, S., Wollscheid, B., . . . Krek, W. (2012). Comprehensive Description of the N-Glycoproteome of Mouse Pancreatic β-Cells and Human Islets. *Journal of Proteome Research, 11*, 1598-1608.

Davis, M. A., Ireton, R. C., & Reynolds, A. B. (2003). A core function for p120-catenin in cadherin turnover. *Journal of Cell Biology, 163*(3), 525-534.

De Smet, F., Segura, I., De Bock, K., Hohensinner, P. J., & Carmeliet, P. (2009). Mechanisms of Vessel Branching. *Arteriosclerosis, Thrombosis, and Vascular Biology, 29*(5), 639-649.

de Wit, C., & Griffith, T. M. (2010). Connexins and gap junctions in the EDHF phenomenon and conducted vasomotor responses. *Pflügers Archiv - European Journal of Physiology, 459*(6), 897-914.

Demontis, F., Habermann, B., & Dahmann, C. (2006). PDZ-domain-binding sites are common among cadherins. *Development Genes and Evolution, 216*(11), 737-741.

Denzel, M. S., Scimia, M.-C., Zumstein, P. M., Walsh, K., Ruiz-Lozano, P., & Ranscht, B. (2010). T-cadherin is critical for adiponectin-mediated cardioprotection in mice. *The Journal of Clinical Investigation, 120*(12), 4342-4352.

Dilling, C., Roewer, N., Förster, C. Y., & Burek, M. (2017). Multiple protocadherins are expressed in brain microvascular endothelial cells and might play a role in tight junction protein regulation. *Journal of Cerebral Blood Flow & Metabolism, 37*(10), 3391-3400.

Ding, Y., Lee, J., Hsu, J. J., Chang, C.-C., Baek, K. I., Ranjbarvaziri, S., . . . Hsiai, T. K. (2018). Light-Sheet Imaging to Elucidate Cardiovascular Injury and Repair. *Current Cardiology Reports, 20*(5), 35.

Ding, Y., Ma, J., Langenbacher, A. D., Baek, K. I., Lee, J., Chang, C.-C., . . . Hsiai, T. K. (2018). Multiscale light-sheet for rapid imaging of cardiopulmonary system. *JCI Insight, 3*(16).

Drake, C. J., & Fleming, P. A. (2000). Vasculogenesis in the day 6.5 to 9.5 mouse embryo. *Blood, 95*, 1671-1679.

Duguay, D., Foty, R. A., & Steinberg, M. S. (2003). Cadherin-mediated cell adhesion and tissue segregation: qualitative and quantitative determinants. *Developmental Biology, 253*(2), 309-323.

Duncan, G. S., Andrew, D. P., Takimoto, H., Kaufman, S. A., Yoshida, H., Spellberg, J., . . . Mak, T. W. (1999). Genetic Evidence for Functional Redundancy of Platelet/Endothelial Cell Adhesion Molecule-1 (PECAM-1): CD31-Deficient Mice Reveal PECAM-1-Dependent and PECAM-1-Independent Functions. *The Journal of Immunology, 162*(5), 3022-3030.

Ebata, N., Nodasaka, Y., Sawa, Y., Yamaoka, Y., Makino, S., Totsuka, Y., & Yoshida, S. (2001). Desmoplakin as a Specific Marker of Lymphatic Vessels. *Microvascular Research, 61*(1), 40-48.

Elbashir, S. M., Martinez, J., Patkaniowska, A., Lendeckel, W., & Tuschl, T. (2001). Functional anatomy of siRNAs for mediating efficient RNAi in Drosophila melanogaster embryo lysate. *The EMBO Journal, 20*(23), 6877-6888.

Emond, M. R., Biswas, S., Blevins, C. J., & Jontes, J. D. (2011). A complex of Protocadherin-19 and N-cadherin mediates a novel mechanism of cell adhesion. *Journal of Cell Biology, 195*(7), 1115-1121.

Epah, J., Pálfi, K., Dienst, F. L., Malacarne, P. F., Bremer, R., Salamon, M., . . . Brandes, R. P. (2018). 3D Imaging and Quantitative Analysis of Vascular Networks: A Comparison of Ultramicroscopy and Micro-Computed Tomography. *Theranostics, 8*(8), 2117-2133.

Erskine, L., Reijntjes, S., Pratt, T., Denti, L., Schwarz, Q., Vieira, Joaquim M., . . . Ruhrberg, C. (2011). VEGF Signaling through Neuropilin 1 Guides Commissural Axon Crossing at the Optic Chiasm. *Neuron, 70*(5), 951-965.

Esumi, S., Kakazu, N., Taguchi, Y., Hirayama, T., Sasaki, A., Hirabayashi, T., . . . Yagi, T. (2005). Monoallelic yet combinatorial expression of variable exons of the protocadherin-α gene cluster in single neurons. *Nature Genetics, 37*(2), 171-176.

Fan, L., Lu, Y., Shen, X., Shao, H., Suo, L., & Wu, Q. (2018). Alpha protocadherins and Pyk2 kinase regulate cortical neuron migration and cytoskeletal dynamics via Rac1 GTPase and WAVE complex in mice. *eLife, 7*, e35242.

Fanning, A. S., Jameson, B. J., Jesaitis, L. A., & Anderson, J. M. (1998). The Tight Junction Protein ZO-1 Establishes a Link between the Transmembrane Protein Occludin and the Actin Cytoskeleton*. *Journal of Biological Chemistry, 273*(45), 29745-29753.

Fantin, A., Vieira, J. M., Plein, A., Maden, C. H., & Ruhrberg, C. (2013). The embryonic mouse hindbrain as a qualitative and quantitative model for studying the molecular and cellular mechanisms of angiogenesis. *Nature Protocols, 8*(2), 418-429.

Faura Tellez, G., Vandepoele, K., Brouwer, U., Koning, H., Elderman, R. M., Hackett, T.-L., . . . Nawijn, M. C. (2015). Protocadherin-1 binds to SMAD3 and suppresses TGF-β1-induced gene transcription. *American Journal of Physiology - Lung Cellular and Molecular Physiology, 309*, L725-L735.

Faura Tellez, G., Willemse, B. W. M., Brouwer, U., Nijboer-Brinksma, S., Vandepoele, K., Noordhoek, J. A., . . . Koppelman, G. H. (2016). Protocadherin-1 Localization and Cell-Adhesion Function in Airway Epithelial Cells in Asthma. *PLOS ONE, 11*, e0163967.

Favre, C. J., Mancuso, M., Maas, K., McLean, J. W., Baluk, P., & McDonald, D. (2003). Expression of genes involved in vascular development and angiogenesis in endothelial cells of adult lung. *American Journal of Physiology-Heart and Circulatory Physiology, 285*(5), H1917-H1938.

Ferrara, N., Carver-Moore, K., Chen, H., Dowd, M., Lu, L., O'Shea, K. S., . . . Moore, M. W. (1996). Heterozygous embryonic lethality induced by targeted inactivation of the VEGF gene. *Nature, 380*, 439-442.

Ferrara, N., Gerber, H. P., & LeCouter, J. (2003). The biology of VEGF and its receptors. *Nature Medicine, 9*, 669-676.

Flamme, I., von Reutern, M., Drexler, H. C. A., Syed-Ali, S., & Risau, W. (1995). Overexpression of Vascular Endothelial Growth Factor in the Avian Embryo Induces Hypervascularization and Increased Vascular Permeability without Alterations of Embryonic Pattern Formation. *Developmental Biology, 171*(2), 399-414.

Franze, K., & Guck, J. (2010). The biophysics of neuronal growth. *Reports on Progress in Physics, 73*(9), 094601.

Frohman, M. A., Dush, M. K., & Martin, G. R. (1988). Rapid production of full-length cDNAs from rare transcripts: amplification using a single gene-specific oligonucleotide primer. *Proceedings of the National Academy of Sciences, 85*(23), 8998-9002.

Fukata, Y., & Fukata, M. (2010). Protein palmitoylation in neuronal development and synaptic plasticity. *Nature Reviews Neuroscience, 11*, 161-175.

Furuse, M., Sasaki, H., & Tsukita, S. (1999). Manner of Interaction of Heterogeneous Claudin Species within and between Tight Junction Strands. *Journal of Cell Biology, 147*(4), 891-903.

Gabbert, L., Dilling, C., Meybohm, P., & Burek, M. (2020). Deletion of Protocadherin Gamma C3 Induces Phenotypic and Functional Changes in Brain Microvascular Endothelial Cells In Vitro. *Frontiers in Pharmacology, 11*(2029).

Gallicano, G. I., Bauer, C., & Fuchs, E. (2001). Rescuing desmoplakin function in extra-embryonic ectoderm reveals the importance of this protein in embryonic heart, neuroepithelium, skin and vasculature. *Development, 128*(6), 929-941.

Garrett, Andrew M., Schreiner, D., Lobas, Mark A., & Weiner, Joshua A. (2012). γ-Protocadherins Control Cortical Dendrite Arborization by Regulating the Activity of a FAK/PKC/MARCKS Signaling Pathway. *Neuron, 74*(2), 269-276.

Garrod, D. R., & Chidgey, M. (2008). Desmosome structure, composition and function. *Biochimica et Biophysica Acta - Biomembranes, 1778*, 572-587.

Garrod, D. R., Merritt, A. J., & Nie, Z. (2002). Desmosomal cadherins. *Current Opinion in Cell*

Biology, 14(5), 537-545.

Giannotta, M., Trani, M., & Dejana, E. (2013). VE-Cadherin and Endothelial Adherens Junctions: Active Guardians of Vascular Integrity. *Developmental Cell, 26*(5), 441-454.

Giepmans, B. N. G. (2004). Gap junctions and connexin-interacting proteins. *Cardiovascular Research, 62*(2), 233-245.

Gimbrone, M. A., Leapman, S. B., Cotran, R. S., & Folkman, J. (1972). Tumor dormancy in vivo by prevention of neovascularization. *The Journal of Experimental Medicine, 136*, 261 LP - 276.

Gory-Faure, S., Prandini, M. H., Pointu, H., Roullot, V., Pignot-Paintrand, I., Vernet, M., & Huber, P. (1999). Role of vascular endothelial-cadherin in vascular morphogenesis. *Development, 126*(10), 2093-2102.

Götz, M., & Huttner, W. B. (2005). The cell biology of neurogenesis. *Nature Reviews Molecular Cell Biology, 6*, 777.

Graesser, D., Solowiej, A., Bruckner, M., Osterweil, E., Juedes, A., Davis, S., . . . Madri, J. A. (2002). Altered vascular permeability and early onset of experimental autoimmune encephalomyelitis in PECAM-1–deficient mice. *The Journal of Clinical Investigation, 109*(3), 383-392.

Green, K. J., Parry, D. A., Steinert, P. M., Virata, M. L., Wagner, R. M., Angst, B. D., & Nilles, L. A. (1990). Structure of the human desmoplakins. Implications for function in the desmosomal plaque. *Journal of Biological Chemistry, 265*(5), 2603-2612.

Green, K. J., Stappenbeck, T. S., Parry, D. A. D., & Virata, M. L. A. (1992). Structure of Desmoplakin and Its Association with Intermediate Filaments. *The Journal of Dermatology, 19*(11), 765-769.

Grifoni, D., Sollazzo, M., Fontana, E., Froldi, F., & Pession, A. (2015). Multiple strategies of oxygen supply in Drosophila malignancies identify tracheogenesis as a novel cancer hallmark. *Scientific Reports, 5*(1), 9061.

Gu, C., Yoshida, Y., Livet, J., Reimert, D. V., Mann, F., Merte, J., . . . Ginty, D. D. (2005). Semaphorin 3E and Plexin-D1 Control Vascular Pattern Independently of Neuropilins. *Science, 307*(5707), 265-268.

Guruprasad, K., Reddy, B. V. B., & Pandit, M. W. (1990). Correlation between stability of a protein and its dipeptide composition: a novel approach for predicting in vivo stability of a protein from its primary sequence. *Protein Engineering, Design and Selection, 4*(2), 155-161.

Halbleib, J. M., & Nelson, W. J. (2006). Cadherins in development: cell adhesion, sorting, and tissue morphogenesis. *Genes and Development, 20*, 3199-3214.

Hamm, M. J., Kirchmaier, B. C., & Herzog, W. (2016). Sema3d controls collective endothelial cell migration by distinct mechanisms via Nrp1 and PlxnD1. *Journal of Cell Biology, 215*(3), 415-430.

Hämmerling, B., Grund, C., Boda-Heggemann, J., Moll, R., & Franke, W. W. (2006). The complexus adhaerens of mammalian lymphatic endothelia revisited: a junction even more complex than hitherto thought. *Cell and Tissue Research, 324*(1), 55-67.

Han, M.-H., Lin, C., Meng, S., & Wang, X. (2010). Proteomics Analysis Reveals Overlapping Functions of Clustered Protocadherins. *Molecular & Cellular Proteomics, 9*(1), 71-83.

Han, N., Yuan, X., Wu, H., Xu, H., Chu, Q., Guo, M., . . . Wu, K. (2015). DACH1 inhibits lung adenocarcinoma invasion and tumor growth by repressing CXCL5 signaling. *Oncotarget, 6*(8).

Harrison, O. J., Bahna, F., Katsamba, P. S., Jin, X., Brasch, J., Vendome, J., . . . Shapiro, L. (2010). Two-step adhesive binding by classical cadherins. *Nature Structural &*

Molecular Biology, 17(3), 348-357.

Harrison, O. J., Brasch, J., Katsamba, P. S., Ahlsen, G., Noble, A. J., Dan, H., . . . Shapiro, L. (2020). Family-wide Structural and Biophysical Analysis of Binding Interactions among Non-clustered δ-Protocadherins. *Cell Reports*, *30*(8), 2655-2671.e2657.

Harrison, O. J., Brasch, J., Lasso, G., Katsamba, P. S., Ahlsen, G., Honig, B., & Shapiro, L. (2016). Structural basis of adhesive binding by desmocollins and desmogleins. *Proceedings of the National Academy of Sciences, 113*(26), 7160-7165.

Harrison, O. J., Jin, X., Hong, S., Bahna, F., Ahlsen, G., Brasch, J., . . . Honig, B. (2011). The Extracellular Architecture of Adherens Junctions Revealed by Crystal Structures of Type I Cadherins. *Structure, 19,* 244-256.

Haseloff, R. F., Dithmer, S., Winkler, L., Wolburg, H., & Blasig, I. E. (2015). Transmembrane proteins of the tight junctions at the blood–brain barrier: Structural and functional aspects. *Seminars in Cell & Developmental Biology, 38,* 16-25.

Hattori, D., Chen, Y., Matthews, B. J., Salwinski, L., Sabatti, C., Grueber, W. B., & Zipursky, S. L. (2009). Robust discrimination between self and non-self neurites requires thousands of Dscam1 isoforms. *Nature, 461*(7264), 644-648.

Hatzfeld, M. (2007). Plakophilins: Multifunctional proteins or just regulators of desmosomal adhesion? *Biochimica et Biophysica Acta (BBA) - Molecular Cell Research, 1773*(1), 69-77.

Hatzfeld, M., Haffner, C., Schulze, K., & Vinzens, U. (2000). The Function of Plakophilin 1 in Desmosome Assembly and Actin Filament Organization. *Journal of Cell Biology, 149*(1), 209-222.

Heiss, M., Hellström, M., Kalén, M., May, T., Weber, H., Hecker, M., . . . Korff, T. (2015). Endothelial cell spheroids as a versatile tool to study angiogenesis in vitro. *The FASEB Journal, 29*(7), 3076-3084.

Helker, C. S. M., Schuermann, A., Pollmann, C., Chng, S. C., Kiefer, F., Reversade, B., & Herzog, W. (2015). The hormonal peptide Elabela guides angioblasts to the midline during vasculogenesis. *eLife, 4,* 1-13.

Herbert, S. P., Huisken, J., Kim, T. N., Feldman, M. E., Houseman, B. T., Wang, R. A., . . . Stainier, D. Y. R. (2009). Arterial-Venous Segregation by Selective Cell Sprouting: An Alternative Mode of Blood Vessel Formation. *Science, 326,* 294-298.

Herbert, S. P., & Stainier, D. Y. R. (2011). Molecular control of endothelial cell behaviour during blood vessel morphogenesis. *Nature Reviews Molecular Cell Biology, 12,* 551-564.

Hermkens, D. M. A., Stam, O. C. G., de Wit, N. M., Fontijn, R. D., Jongejan, A., Moerland, P. D., . . . de Vries, H. E. (2019). Profiling the unique protective properties of intracranial arterial endothelial cells. *Acta Neuropathologica Communications, 7*(1), 151.

Hirayama, T., & Yagi, T. (2013). Clustered Protocadherins and Neuronal Diversity. In F. van Roy (Ed.), *Progress in Molecular Biology and Translational Science* (Vol. 116, pp. 145-167): Academic Press.

Honig, B., & Shapiro, L. (2020). Adhesion Protein Structure, Molecular Affinities, and Principles of Cell-Cell Recognition. *Cell, 181*(3), 520-535.

Howe, K., Clark, M. D., Torroja, C. F., Torrance, J., Berthelot, C., Muffato, M., . . . Stemple, D. L. (2013). The zebrafish reference genome sequence and its relationship to the human genome. *Nature, 496*(7446), 498-503.

Hug, C., Wang, J., Ahmad, N. S., Bogan, J. S., Tsao, T.-S., & Lodish, H. F. (2004). T-cadherin is a receptor for hexameric and high-molecular-weight forms of Acrp30/adiponectin. *Proceedings of the National Academy of Sciences of the United States of America,* *101*(28), 10308-10313.

Huisken, J., & Stainier, D. Y. R. (2009). Selective plane illumination microscopy techniques in developmental biology. *Development, 136*(12), 1963-1975.

Hulpiau, P., Gul, I. S., & van Roy, F. (2016). Evolution of Cadherins and Associated Catenins. In S. T. Suzuki & S. Hirano (Eds.), *The Cadherin Superfamily: Key Regulators of Animal Development and Physiology* (pp. 13-37). Tokyo: Springer Japan.

Hunt, D. M., Sahota, V. K., Taylor, K., Šimrak, D., Hornigold, N., Arnemann, J., . . . Buxton, R. S. (1999). Clustered Cadherin Genes: A Sequence-Ready Contig for the Desmosomal Cadherin Locus on Human Chromosome 18. *Genomics, 62*(3), 445-455.

Ikenouchi, J., Furuse, M., Furuse, K., Sasaki, H., Tsukita, S., & Tsukita, S. (2005). Tricellulin constitutes a novel barrier at tricellular contacts of epithelial cells. *Journal of Cell Biology, 171*(6), 939-945.

Ivanov, D., Philippova, M., Antropova, J., Gubaeva, F., Iljinskaya, O., Tararak, E., . . . Tkachuk, V. (2001). Expression of cell adhesion molecule T-cadherin in the human vasculature. *Histochemistry and Cell Biology, 115*(3), 231-242.

Ivanov, D., Philippova, M., Tkachuk, V., Erne, P., & Resink, T. (2004). Cell adhesion molecule T-cadherin regulates vascular cell adhesion, phenotype and motility. *Experimental Cell Research, 293*(2), 207-218.

Jangra, R. K., Herbert, A. S., Li, R., Jae, L. T., Kleinfelter, L. M., Slough, M. M., . . . Chandran, K. (2018). Protocadherin-1 is essential for cell entry by New World hantaviruses. *Nature, 563*(7732), 559-563.

Jones, C. A., London, N. R., Chen, H., Park, K. W., Sauvaget, D., Stockton, R. A., . . . Li, D. Y. (2008). Robo4 stabilizes the vascular network by inhibiting pathologic angiogenesis and endothelial hyperpermeability. *Nature Medicine, 14*(4), 448-453.

Juettner, V. V., Kruse, K., Dan, A., Vu, V. H., Khan, Y., Le, J., . . . Malik, A. B. (2019). VE-PTP stabilizes VE-cadherin junctions and the endothelial barrier via a phosphatase-independent mechanism. *Journal of Cell Biology, 218*(5), 1725-1742.

Kahr, I., Vandepoele, K., & van Roy, F. (2013). Delta-protocadherins in health and disease. *Progress in molecular biology and translational science, 116*, 169-192.

Kang, H., Weiss, T. M., Bang, I., Weis, W. I., & Choi, H.-J. (2016). Structure of the Intermediate Filament-Binding Region of Desmoplakin. *PLOS ONE, 11*(1), e0147641.

Kertesz, N., Krasnoperov, V., Reddy, R., Leshanski, L., Kumar, S. R., Zozulya, S., & Gill, P. S. (2006). The soluble extracellular domain of EphB4 (sEphB4) antagonizes EphB4-EphrinB2 interaction, modulates angiogenesis, and inhibits tumor growth. *Blood, 107*(6), 2330-2338.

Khan, K. A., Naylor, A. J., Khan, A., Noy, P. J., Mambretti, M., Lodhia, P., . . . Bicknell, R. (2017). Multimerin-2 is a ligand for group 14 family C-type lectins CLEC14A, CD93 and CD248 spanning the endothelial pericyte interface. *Oncogene, 36*(44), 6097-6108.

Kidd, T., Bland, K. S., & Goodman, C. S. (1999). Slit Is the Midline Repellent for the Robo Receptor in Drosophila. *Cell, 96*(6), 785-794.

Kim, S.-Y., Chung, H. S., Sun, W., & Kim, H. (2007). Spatiotemporal expression pattern of non-clustered protocadherin family members in the developing rat brain. *Neuroscience, 147*(4), 996-1021.

Kim, S.-Y., Yasuda, S., Tanaka, H., Yamagata, K., & Kim, H. (2011). Non-clustered protocadherin. *Cell Adhesion & Migration, 5*(2), 97-105.

Kimmel, C. B., Ballard, W. W., Kimmel, S. R., Ullmann, B., & Schilling, T. F. (1995). Stages of embryonic development of the zebrafish. *Developmental Dynamics, 203*, 253-310.

Kimura, T. E., Merritt, A. J., & Garrod, D. R. (2007). Calcium-Independent Desmosomes of

Keratinocytes are Hyper-Adhesive. *Journal of Investigative Dermatology, 127*(4), 775-781.

Kirst, C., Skriabine, S., Vieites-Prado, A., Topilko, T., Bertin, P., Gerschenfeld, G., . . . Renier, N. (2020). Mapping the Fine-Scale Organization and Plasticity of the Brain Vasculature. *Cell, 180*(4), 780-795.e725.

Kitsukawa, T., Shimizu, M., Sanbo, M., Hirata, T., Taniguchi, M., Bekku, Y., . . . Fujisawa, H. (1997). Neuropilin–Semaphorin III/D-Mediated Chemorepulsive Signals Play a Crucial Role in Peripheral Nerve Projection in Mice. *Neuron, 19*(5), 995-1005.

Kniesel, U., Risau, W., & Wolburg, H. (1996). Development of blood-brain barrier tight junctions in the rat cortex. *Developmental Brain Research, 96*(1), 229-240.

Knudsen, K. A., Soler, A. P., Johnson, K. R., & Wheelock, M. J. (1995). Interaction of alpha-actinin with the cadherin/catenin cell-cell adhesion complex via alpha-catenin. *Journal of Cell Biology, 130*(1), 67-77.

Koch, A. E., Halloran, M. M., Haskell, C. J., Shah, M. R., & Polverini, P. J. (1995). Angiogenesis mediated by soluble forms of E-selectin and vascular cell adhesion molecule-1. *Nature, 376*(6540), 517-519.

Koch, A. W., Farooq, A., Shan, W., Zeng, L., Colman, D. R., & Zhou, M. M. (2004). Structure of the neural (N-) cadherin prodomain reveals a cadherin extracellular domain-like fold without adhesive characteristics. *Structure, 12*, 793-805.

Koch, A. W., Mathivet, T., Larrivée, B., Tong, R. K., Kowalski, J., Pibouin-Fragner, L., . . . Eichmann, A. (2011). Robo4 Maintains Vessel Integrity and Inhibits Angiogenesis by Interacting with UNC5B. *Developmental Cell, 20*, 33-46.

Koch, A. W., Pokutta, S., Lustig, A., & Engel, J. (1997). Calcium binding and homoassociation of E-cadherin domains. *Biochemistry, 36*, 7697-7705.

Koning, H., Postma, D. S., Brunekreef, B., Duiverman, E. J., Smit, H. A., Thijs, C., . . . Koppelman, G. H. (2012). Protocadherin-1 polymorphisms are associated with eczema in two Dutch birth cohorts. *Pediatric Allergy and Immunology, 23*, 270-277.

Koning, H., Sayers, I., Stewart, C. E., de Jong, D., ten Hacken, N. H. T., Postma, D. S., . . . Koppelman, G. H. (2012). Characterization of protocadherin-1 expression in primary bronchial epithelial cells: association with epithelial cell differentiation. *The FASEB Journal, 26*, 439-448.

Koning, H., van Oosterhout, A. J. M., Brouwer, U., den Boef, L. E., Gras, R., Reinders-Luinge, M., . . . Nawijn, M. C. (2014). Mouse Protocadherin-1 Gene Expression Is Regulated by Cigarette Smoke Exposure In Vivo. *PLOS ONE, 9*(7), e98197.

Koppelman, G. H., Meyers, D. A., Howard, T. D., Zheng, S. L., Hawkins, G. A., Ampleford, E. J., . . . Postma, D. S. (2009). Identification of PCDH1 as a novel susceptibility gene for bronchial hyperresponsiveness. *American Journal of Respiratory and Critical Care Medicine, 180*, 929-935.

Korzystka, A. (2018). *In vitro functional studies of the tumour vascular target PCDH7 and identification of novel tumour vascular targets in colorectal cancer.* (PhD). University of Birmingham,

Kostrewa, D., Brockhaus, M., D'Arcy, A., Dale, G. E., Nelboeck, P., Schmid, G., . . . Hennig, M. (2001). X-ray structure of junctional adhesion molecule: structural basis for homophilic adhesion via a novel dimerization motif. *The EMBO Journal, 20*(16), 4391-4398.

Kowalczyk, A. P., Bornslaeger, E. A., Borgwardt, J. E., Palka, H. L., Dhaliwal, A. S., Corcoran, C. M., . . . Green, K. J. (1997). The Amino-terminal Domain of Desmoplakin Binds to Plakoglobin and Clusters Desmosomal Cadherin–Plakoglobin Complexes. *Journal of*

Cell Biology, 139(3), 773-784.

Kowalczyk, A. P., Hatzfeld, M., Bornslaeger, E. A., Kopp, D. S., Borgwardt, J. E., Corcoran, C. M., . . . Green, K. J. (1999). The Head Domain of Plakophilin-1 Binds to Desmoplakin and Enhances Its Recruitment to Desmosomes: IMPLICATIONS FOR CUTANEOUS DISEASE*. *Journal of Biological Chemistry, 274*(26), 18145-18148.

Kowalczyk, A. P., Navarro, P., Dejana, E., Bornslaeger, E. A., Green, K. J., Kopp, D. S., & Borgwardt, J. E. (1998). VE-cadherin and desmoplakin are assembled into dermal microvascular endothelial intercellular junctions: a pivotal role for plakoglobin in the recruitment of desmoplakin to intercellular junctions. *Journal of Cell Science, 111*(20), 3045-3057.

Krämer, A., Green, J., Pollard, J., Jr, & Tugendreich, S. (2013). Causal analysis approaches in Ingenuity Pathway Analysis. *Bioinformatics, 30*(4), 523-530.

Kruger, O., Plum, A., Kim, J. S., Winterhager, E., Maxeiner, S., Hallas, G., . . . Willecke, K. (2000). Defective vascular development in connexin 45-deficient mice. *Development, 127*(19), 4179-4193.

Kubo, Y., Ishikawa, K., Mori, K., Kobayashi, Y., Nakama, T., Arima, M., . . . Yoshida, S. (2020). Periostin and tenascin-C interaction promotes angiogenesis in ischemic proliferative retinopathy. *Scientific Reports, 10*(1), 9299.

Kugler, E., Chico, T., & Armitage, P. (2018, 2018//). *Image Analysis in Light Sheet Fluorescence Microscopy Images of Transgenic Zebrafish Vascular Development.* Paper presented at the Medical Image Understanding and Analysis, Cham.

Kugler, E. C., Frost, J., Silva, V., Plant, K., Chhabria, K., Chico, T. J. A., & Armitage, P. A. (2020). 3D quantification of zebrafish cerebrovascular architecture by automated image analysis of light sheet fluorescence microscopy datasets. *bioRxiv*, 2020.2008.2006.239905.

Kullander, K., Croll, S. D., Zimmer, M., Pan, L., McClain, J., Hughes, V., . . . Gale, N. W. (2001). Ephrin-B3 is the midline barrier that prevents corticospinal tract axons from recrossing, allowing for unilateral motor control. *Genes & Development, 15*(7), 877-888.

Kumar, N. M., & Gilula, N. B. (1996). The Gap Junction Communication Channel. *Cell, 84*(3), 381-388.

Kuroda, H., Inui, M., Sugimoto, K., Hayata, T., & Asashima, M. (2002). Axial protocadherin is a mediator of prenotochord cell sorting in Xenopus. *Developmental Biology, 244*, 267-277.

Lagendijk, A. K., & Hogan, B. M. (2015). VE-cadherin in vascular development: A coordinator of cell signaling and tissue morphogenesis. *Current Topics in Developmental Biology, 112*, 325-352.

Laird, D. W. (2010). The gap junction proteome and its relationship to disease. *Trends in Cell Biology, 20*(2), 92-101.

Lallemand, Y., Luria, V., Haffner-Krausz, R., & Lonai, P. (1998). Maternally expressed PGK-Cre transgene as a tool for early and uniform activation of the Cre site-specific recombinase. *Transgenic Research, 7*(2), 105-112.

Lambert, E., Coissieux, M.-M., Laudet, V., & Mehlen, P. (2012). Netrin-4 Acts as a Pro-angiogenic Factor during Zebrafish Development. *Journal of Biological Chemistry, 287*(6), 3987-3999.

Lambert, O., Taveau, J.-C., Lai Kee Him, J., Al Kurdi, R., Gulino-Debrac, D., & Brisson, A. (2005). The Basic Framework of VE-cadherin Junctions Revealed by Cryo-EM. *Journal of Molecular Biology, 346*(5), 1193-1196.

Lampugnani, M. G. (2012). Endothelial Cell-to-Cell Junctions: Adhesion and Signaling in Physiology and Pathology. *Cold Spring Harbor Perspectives in Medicine, 2*(10).

Lampugnani, M. G., Corada, M., Caveda, L., Breviario, F., Ayalon, O., Geiger, B., & Dejana, E. (1995). The molecular organization of endothelial cell to cell junctions: differential association of plakoglobin, beta-catenin, and alpha-catenin with vascular endothelial cadherin (VE-cadherin). *Journal of Cell Biology, 129*(1), 203-217.

Lampugnani, M. G., Orsenigo, F., Gagliani, M. C., Tacchetti, C., & Dejana, E. (2006). Vascular endothelial cadherin controls VEGFR-2 internalization and signaling from intracellular compartments. *Journal of Cell Biology, 174*, 593-604.

Lampugnani, M. G., Resnati, M., Raiteri, M., Pigott, R., Pisacane, A., Houen, G., . . . Dejana, E. (1992). A novel endothelial-specific membrane protein is a marker of cell-cell contacts. *Journal of Cell Biology, 118*(6), 1511-1522.

Lampugnani, M. G., Zanetti, A., Corada, M., Takahashi, T., Balconi, G., Breviario, F., . . . Dejana, E. (2003). Contact inhibition of VEGF-induced proliferation requires vascular endothelial cadherin, β-catenin, and the phosphatase DEP-1/CD148. *Journal of Cell Biology, 161*(4), 793-804.

Larrieu-Lahargue, F., Welm, A. L., Thomas, K. R., & Li, D. Y. (2010). Netrin-4 induces lymphangiogenesis in vivo. *Blood, 115*(26), 5418-5426.

Larrivée, B., Freitas, C., Suchting, S., Brunet, I., & Eichmann, A. (2009). Guidance of Vascular Development. *Circulation Research, 104*(4), 428-441.

Larrivée, B., Freitas, C., Trombe, M., Lv, X., DeLafarge, B., Yuan, L., . . . Eichmann, A. (2007). Activation of the UNC5B receptor by Netrin-1 inhibits sprouting angiogenesis. *Genes & Development, 21*(19), 2433-2447.

Lebrin, F., Deckers, M., Bertolino, P., & Ten Dijke, P. (2005). TGF-β receptor function in the endothelium. *Cardiovascular Research, 65*, 599-608.

Lechler, T., & Fuchs, E. (2007). Desmoplakin: an unexpected regulator of microtubule organization in the epidermis. *The Journal of cell biology, 176*(2), 147-154.

Lefebvre, J. L., Kostadinov, D., Chen, W. V., Maniatis, T., & Sanes, J. R. (2012). Protocadherins mediate dendritic self-avoidance in the mammalian nervous system. *Nature, 488*(7412), 517-521.

Lein, E. S., Hawrylycz, M. J., Ao, N., Ayres, M., Bensinger, A., Bernard, A., . . . Jones, A. R. (2007). Genome-wide atlas of gene expression in the adult mouse brain. *Nature, 445*(7124), 168-176.

Lejmi, E., Leconte, L., Pédron-Mazoyer, S., Ropert, S., Raoul, W., Lavalette, S., . . . Plouët, J. (2008). Netrin-4 inhibits angiogenesis via binding to neogenin and recruitment of Unc5B. *Proceedings of the National Academy of Sciences, 105*(34), 12491-12496.

Leung, D., Cachianes, G., Kuang, W., Goeddel, D., & Ferrara, N. (1989). Vascular endothelial growth factor is a secreted angiogenic mitogen. *Science, 246*(4935), 1306-1309.

Lewis, J. E., Wahl, J. K., Sass, K. M., Jensen, P. J., Johnson, K. R., & Wheelock, M. J. (1997). Cross-talk between adherens junctions and desmosomes depends on plakoglobin. *Journal of Cell Biology, 136*(4), 919-934.

Lin, C.-Y., Huang, Z., Wen, W., Wu, A., Wang, C., & Niu, L. (2015). Enhancing Protein Expression in HEK-293 Cells by Lowering Culture Temperature. *PLOS ONE, 10*(4), e0123562.

Liu, H., Lu, T., Kremers, G.-J., Seynhaeve, A. L. B., & ten Hagen, T. L. M. (2020). A microcarrier-based spheroid 3D invasion assay to monitor dynamic cell movement in extracellular matrix. *Biological Procedures Online, 22*(1), 3.

Lu, X., Le Noble, F., Yuan, L., Jiang, Q., De Lafarge, B., Sugiyama, D., . . . Eichmann, A.

(2004). The netrin receptor UNC5B mediates guidance events controlling morphogenesis of the vascular system. *Nature, 432*, 179-186.

Lugo-Hernandez, E., Squire, A., Hagemann, N., Brenzel, A., Sardari, M., Schlechter, J., . . . Hermann, D. M. (2017). 3D visualization and quantification of microvessels in the whole ischemic mouse brain using solvent-based clearing and light sheet microscopy. *Journal of Cerebral Blood Flow & Metabolism, 37*(10), 3355-3367.

Maciag, T., Cerundolo, J., Ilsley, S., Kelley, P. R., & Forand, R. (1979). An endothelial cell growth factor from bovine hypothalamus: identification and partial characterization. *Proceedings of the National Academy of Sciences of the United States of America, 76*, 5674-5678.

Maeda, S., Nakagawa, S., Suga, M., Yamashita, E., Oshima, A., Fujiyoshi, Y., & Tsukihara, T. (2009). Structure of the connexin 26 gap junction channel at 3.5 Å resolution. *Nature, 458*(7238), 597-602.

Majmundar, A. J., Wong, W. J., & Simon, M. C. (2010). Hypoxia-Inducible Factors and the Response to Hypoxic Stress. *Molecular Cell, 40*, 294-309.

McCrea, P. D., Gu, D., & Balda, M. S. (2009). Junctional Music that the Nucleus Hears: Cell–Cell Contact Signaling and the Modulation of Gene Activity. *Cold Spring Harbor Perspectives in Biology, 1*(4).

Mellacheruvu, D., Wright, Z., Couzens, A. L., Lambert, J.-P., St-Denis, N. A., Li, T., . . . Nesvizhskii, A. I. (2013). The CRAPome: a contaminant repository for affinity purification–mass spectrometry data. *Nature Methods, 10*(8), 730-736.

Mendonsa, A. M., Na, T.-Y., & Gumbiner, B. M. (2018). E-cadherin in contact inhibition and cancer. *Oncogene, 37*(35), 4769-4780.

Meng, J.-J., Bornslaeger, E. A., Green, K. J., Steinert, P. M., & Ip, W. (1997). Two-hybrid Analysis Reveals Fundamental Differences in Direct Interactions between Desmoplakin and Cell Type-specific Intermediate Filaments. *Journal of Biological Chemistry, 272*(34), 21495-21503.

Messersmith, E. K., Leonardo, E. D., Shatz, C. J., Tessier-Lavigne, M., Goodman, C. S., & Kolodkin, A. L. (1995). Sernaphorin III can function as a selective chemorepellent to pattern sensory projections in the spinal cord. *Neuron, 14*(5), 949-959.

Miquerol, L., Langille, B. L., & Nagy, A. (1995). Embryonic development is disrupted by modest increases in vascular endothelial growth factor gene expression. *Development, 127*, 3941-3946.

Miyahara, M., Nakanishi, H., Takahashi, K., Satoh-Horikawa, K., Tachibana, K., & Takai, Y. (2000). Interaction of Nectin with Afadin Is Necessary for Its Clustering at Cell-Cell Contact Sites but Not for Its *cis* Dimerization or *trans* Interaction. *Journal of Biological Chemistry*, *275*(1), 613-618.

Modak, D., & Sotomayor, M. (2018). An Adhesive Interface for the Non-Clustered δ1 Protocadherin-1 Involved in Respiratory Diseases. *bioArXiv*, 498196.

Modak, D., & Sotomayor, M. (2019). Identification of an adhesive interface for the non-clustered δ1 protocadherin-1 involved in respiratory diseases. *Communications Biology, 2*(1), 354.

Mohammed, F., Trieber, C., Overduin, M., & Chidgey, M. (2020). Molecular mechanism of intermediate filament recognition by plakin proteins. *Biochimica et Biophysica Acta (BBA) - Molecular Cell Research, 1867*(11), 118801.

Molbay, M., Kolabas, Z. I., Todorov, M. I., Ohn, T.-L., & Ertürk, A. (2021). A guidebook for DISCO tissue clearing. *Molecular Systems Biology, 17*(3), e9807.

Morigi, M., Zoja, C., Figliuzzi, M., Foppolo, M., Micheletti, G., Bontempelli, M., . . . Remuzzi,

A. (1995). Fluid shear stress modulates surface expression of adhesion molecules by endothelial cells. *Blood, 85*(7), 1696-1703.

Morishita, H., Umitsu, M., Murata, Y., Shibata, N., Udaka, K., Higuchi, Y., . . . Ikegami, T. (2006). Structure of the cadherin-related neuronal receptor/protocadherin-α first extracellular cadherin domain reveals diversity across cadherin families. *Journal of Biological Chemistry, 281*, 33650-33663.

Morita, H., Nandadasa, S., Yamamoto, T. S., Terasaka-Iioka, C., Wylie, C., & Ueno, N. (2010). Nectin-2 and N-cadherin interact through extracellular domains and induce apical accumulation of F-actin in apical constriction of Xenopus neural tube morphogenesis. *Development, 137*(8), 1315-1325.

Mortensen, L. J., Kreiner-Møller, E., Hakonarson, H., Bønnelykke, K., & Bisgaard, H. (2014). The PCDH1 gene and asthma in early childhood. *European Respiratory Journal, 43*, 792-800.

Mountoufaris, G., Chen, W. V., Hirabayashi, Y., O'Keeffe, S., Chevee, M., Nwakeze, C. L., . . . Maniatis, T. (2017). Multicluster Pcdh diversity is required for mouse olfactory neural circuit assembly. *Science, 356*(6336), 411-414.

Myers, J. B., Haddad, B. G., O'Neill, S. E., Chorev, D. S., Yoshioka, C. C., Robinson, C. V., . . . Reichow, S. L. (2018). Structure of native lens connexin 46/50 intercellular channels by cryo-EM. *Nature, 564*(7736), 372-377.

Nagel, T., Resnick, N., Atkinson, W. J., Dewey, C. F., Jr., & Gimbrone, M. A., Jr. (1994). Shear stress selectively upregulates intercellular adhesion molecule-1 expression in cultured human vascular endothelial cells. *The Journal of Clinical Investigation, 94*(2), 885-891.

Navarro, P., Ruco, L., & Dejana, E. (1998). Differential Localization of VE- and N-Cadherins in Human Endothelial Cells: VE-Cadherin Competes with N-Cadherin for Junctional Localization. *Journal of Cell Biology, 140*(6), 1475-1484.

Nawijn, M. C., Brouwer, U., den Boef, L., Hesse, L., & Koppelman, G. H. (2018). *Pcdh1 Loss Leads to a SMAD3-Dependent Increase in HDM-Induced Airway Hyperresponsiveness in Mice.* Paper presented at the A28. ADVANCES IN COPD AND ASTHMA, San Diego Convention Center.

Nawroth, R., Poell, G., Ranft, A., Kloep, S., Samulowitz, U., Fachinger, G., . . . Vestweber, D. (2002). VE-PTP and VE-cadherin ectodomains interact to facilitate regulation of phosphorylation and cell contacts. *The EMBO Journal, 21*(18), 4885-4895.

Nielsen, M. S., Nygaard Axelsen, L., Sorgen, P. L., Verma, V., Delmar, M., & Holstein-Rathlou, N.-H. (2012). Gap Junctions. In *Comprehensive Physiology* (Vol. 2, pp. 1981-2035).

Nievers, M. G., Schaapveld, R. Q. J., & Sonnenberg, A. (1999). Biology and function of hemidesmosomes. *Matrix Biology, 18*(1), 5-17.

Nollet, F., Kools, P., & Van Roy, F. (2000). Phylogenetic analysis of the cadherin superfamily allows identification of six major subfamilies besides several solitary members. *Journal of Molecular Biology, 299*, 551-572.

Nowak-Sliwinska, P., Alitalo, K., Allen, E., Anisimov, A., Aplin, A. C., Auerbach, R., . . . Griffioen, A. W. (2018). Consensus guidelines for the use and interpretation of angiogenesis assays. *Angiogenesis, 21*(3), 425-532.

Nucera, S., Biziato, D., & de Palma, M. (2011). The interplay between macrophages and angiogenesis in development, tissue injury and regeneration. *International Journal of Developmental Biology, 55*, 495-503.

Nusrat, A., Parkos, C. A., Verkade, P., Foley, C. S., Liang, T. W., Innis-Whitehouse, W., . . . Madara, J. L. (2000). Tight junctions are membrane microdomains. *Journal of Cell*

Science, 113(10), 1771-1781.

Okamoto, T., Kawamoto, E., Takagi, Y., Akita, N., Hayashi, T., Park, E. J., . . . Shimaoka, M. (2017). Gap junction-mediated regulation of endothelial cellular stiffness. *Scientific Reports, 7*(1), 6134.

Osawa, M., Masuda, M., Kusano, K.-i., & Fujiwara, K. (2002). Evidence for a role of platelet endothelial cell adhesion molecule-1 in endothelial cell mechanosignal transduction : is it a mechanoresponsive molecule? *Journal of Cell Biology, 158*(4), 773-785.

Özkan, E., Carrillo, Robert A., Eastman, Catharine L., Weiszmann, R., Waghray, D., Johnson, Karl G., . . . Garcia, K. C. (2013). An Extracellular Interactome of Immunoglobulin and LRR Proteins Reveals Receptor-Ligand Networks. *Cell, 154*(1), 228-239.

Pan, Q., Chanthery, Y., Liang, W.-C., Stawicki, S., Mak, J., Rathore, N., . . . Watts, R. J. (2007). Blocking Neuropilin-1 Function Has an Additive Effect with Anti-VEGF to Inhibit Tumor Growth. *Cancer Cell, 11*(1), 53-67.

Pancho, A., Aerts, T., Mitsogiannis, M. D., & Seuntjens, E. (2020). Protocadherins at the Crossroad of Signaling Pathways. *Frontiers in Molecular Neuroscience, 13*(117).

Park, K. W., Crouse, D., Lee, M., Karnik, S. K., Sorensen, L. K., Murphy, K. J., . . . Li, D. Y. (2004). The axonal attractant Netrin-1 is an angiogenic factor. *Proceedings of the National Academy of Sciences of the United States of America, 101*(46), 16210-16215.

Payne, S., De Val, S., & Neal, A. (2018). Endothelial-Specific Cre Mouse Models. *Arteriosclerosis, Thrombosis, and Vascular Biology, 38*(11), 2550-2561.

Penuela, S., Bhalla, R., Gong, X.-Q., Cowan, K. N., Celetti, S. J., Cowan, B. J., . . . Laird, D. W. (2007). Pannexin 1 and pannexin 3 are glycoproteins that exhibit many distinct characteristics from the connexin family of gap junction proteins. *Journal of Cell Science, 120*(21), 3772-3783.

Perret, E., Benoliel, A.-M., Nassoy, P., Pierres, A., Delmas, V., Thiery, J.-P., . . . Feracci, H. (2002). Fast dissociation kinetics between individual E-cadherin fragments revealed by flow chamber analysis. *The EMBO Journal, 21*(11), 2537-2546.

Pfenniger, A., Wong, C., Sutter, E., Cuhlmann, S., Dunoyer-Geindre, S., Mach, F., . . . Kwak, B. R. (2012). Shear stress modulates the expression of the atheroprotective protein Cx37 in endothelial cells. *Journal of Molecular and Cellular Cardiology, 53*(2), 299-309.

Phng, L.-K., Potente, M., Leslie, J. D., Babbage, J., Nyqvist, D., Lobov, I., . . . Gerhardt, H. (2009). Nrarp Coordinates Endothelial Notch and Wnt Signaling to Control Vessel Density in Angiogenesis. *Developmental Cell, 16*(1), 70-82.

Plopper, G., Sharp, D., & Sikorski, E. (2013). *Lewin's CELLS*: Jones & Bartlett Publishers.

Potente, M., & Carmeliet, P. (2017). The Link Between Angiogenesis and Endothelial Metabolism. *Annual Review of Physiology, 79*, 43-66.

Privratsky, J. R., & Newman, P. J. (2014). PECAM-1: regulator of endothelial junctional integrity. *Cell and Tissue Research, 355*(3), 607-619.

Pusztaszeri, M. P., Seelentag, W., & Bosman, F. T. (2006). Immunohistochemical Expression of Endothelial Markers CD31, CD34, von Willebrand Factor, and Fli-1 in Normal Human Tissues. *Journal of Histochemistry & Cytochemistry, 54*(4), 385-395.

Qin, S., Yu, L., Gao, Y., Zhou, R., & Zhang, C. (2007). Characterization of the receptors for axon guidance factor netrin-4 and identification of the binding domains. *Molecular and Cellular Neuroscience, 34*(2), 243-250.

Raftrey, B., Williams, I., Rios Coronado, P. E., Chang, A. H., Zhao, M., Roth, R., . . . Red-Horse, K. (2020). Dach1 extends artery networks and protects against cardiac injury. *bioRxiv*, 2020.2008.2007.242164.

Rajasekharan, S., & Kennedy, T. E. (2009). The netrin protein family. *Genome Biology, 10*(9), 239.

Rampazzo, A., Nava, A., Malacrida, S., Beffagna, G., Bauce, B., Rossi, V., . . . Danieli, G. A. (2002). Mutation in Human Desmoplakin Domain Binding to Plakoglobin Causes a Dominant Form of Arrhythmogenic Right Ventricular Cardiomyopathy. *The American Journal of Human Genetics, 71*(5), 1200-1206.

Redies, C., Heyder, J., Kohoutek, T., Staes, K., & Van Roy, F. (2008). Expression of protocadherin-1 (Pcdh1) during mouse development. *Developmental Dynamics, 237*, 2496-2505.

Reiss, K., Maretzky, T., Haas, I. G., Schulte, M., Ludwig, A., Frank, M., & Saftig, P. (2006). Regulated ADAM10-dependent Ectodomain Shedding of γ-Protocadherin C3 Modulates Cell-Cell Adhesion. *Journal of Biological Chemistry, 281*(31), 21735-21744.

Renier, N., Wu, Z., Simon, David J., Yang, J., Ariel, P., & Tessier-Lavigne, M. (2014). iDISCO: A Simple, Rapid Method to Immunolabel Large Tissue Samples for Volume Imaging. *Cell, 159*(4), 896-910.

Reynolds, A. R., Hart, I. R., Watson, A. R., Welti, J. C., Silva, R. G., Robinson, S. D., . . . Hodivala-Dilke, K. M. (2009). Stimulation of tumor growth and angiogenesis by low concentrations of RGD-mimetic integrin inhibitors. *Nature Medicine, 15*, 392-400.

Rimm, D. L., Koslov, E. R., Kebriaei, P., Cianci, C. D., & Morrow, J. S. (1995). Alpha 1(E)-catenin is an actin-binding and -bundling protein mediating the attachment of F-actin to the membrane adhesion complex. *Proceedings of the National Academy of Sciences, 92*(19), 8813-8817.

Ritchie, M. E., Phipson, B., Wu, D., Hu, Y., Law, C. W., Shi, W., & Smyth, G. K. (2015). limma powers differential expression analyses for RNA-sequencing and microarray studies. *Nucleic Acids Research, 43*(7), e47-e47.

Roura, S., Miravet, S., Piedra, J., de Herreros, A. G. a., & Duñach, M. (1999). Regulation of E-cadherin/Catenin Association by Tyrosine Phosphorylation. *Journal of Biological Chemistry, 274*(51), 36734-36740.

Rual, J.-F., Venkatesan, K., Hao, T., Hirozane-Kishikawa, T., Dricot, A., Li, N., . . . Vidal, M. (2005). Towards a proteome-scale map of the human protein–protein interaction network. *Nature, 437*(7062), 1173-1178.

Rubinstein, R., Thu, Chan A., Goodman, Kerry M., Wolcott, Holly N., Bahna, F., Mannepalli, S., . . . Honig, B. (2015). Molecular Logic of Neuronal Self-Recognition through Protocadherin Domain Interactions. *Cell, 163*(3), 629-642.

Rudini, N., Felici, A., Giampietro, C., Lampugnani, M., Corada, M., Swirsding, K., . . . Dejana, E. (2008). VE-cadherin is a critical endothelial regulator of TGF-β signalling. *The EMBO Journal, 27*(7), 993-1004.

Ruhrberg, C., Gerhardt, H., Golding, M., Watson, R., Ioannidou, S., Fujisawa, H., . . . Shima, D. T. (2002). Spatially restricted patterning cues provided by heparin-binding VEGF-A control blood vessel branching morphogenesis. *Genes and Development, 16*, 2684-2698.

Ruter, D. L., Liu, Z., Ngo, K. M., X, S., Marvin, A., Buglak, D. B., . . . Bautch, V. L. (2021). SMAD6 transduces endothelial cell flow responses required for blood vessel homeostasis. *Angiogenesis*.

Rutledge, N. S., & Muller, W. A. (2020). Understanding Molecules that Mediate Leukocyte Extravasation. *Current Pathobiology Reports, 8*(2), 25-35.

Sadler, T. W. (2012). *Langman's Medical Embryology* (12 ed.): Lippincott Williams & Wilkins.

Sambrook, J., & Russell, D. W. (2006). SDS-Polyacrylamide Gel Electrophoresis of Proteins.

Cold Spring Harbor Protocols, *2006*(4), pdb.prot4540.

Sano, K., Tanihara, H., Heimark, R. L., Obata, S., Davidson, M., St John, T., . . . Suzuki, S. (1993). Protocadherins: a large family of cadherin-related molecules in central nervous system. *The EMBO Journal, 12*(6), 2249-2256.

Savolainen, S. M., Foley, J. F., & Elmore, S. A. (2009). Histology Atlas of the Developing Mouse Heart with Emphasis on E11.5 to E18.5. *Toxicologic Pathology, 37*(4), 395-414.

Scarpa, E., Szabó, A., Bibonne, A., Theveneau, E., Parsons, M., & Mayor, R. (2015). Cadherin Switch during EMT in Neural Crest Cells Leads to Contact Inhibition of Locomotion via Repolarization of Forces. *Developmental Cell, 34*(4), 421-434.

Schindelin, J., Arganda-Carreras, I., Frise, E., Kaynig, V., Longair, M., Pietzsch, T., . . . Cardona, A. (2012). Fiji: an open-source platform for biological-image analysis. *Nature Methods, 9*(7), 676-682.

Schmelz, M., Moll, R., Kuhn, C., & Franke, W. W. (1994). *Complexus adhaerentes*, a new group of desmoplakin-containing junctions in endothelial cells: II. Different types of lymphatic vessels. *Differentiation, 57*(2), 97-117.

Schmucker, D., Clemens, J. C., Shu, H., Worby, C. A., Xiao, J., Muda, M., . . . Zipursky, S. L. (2000). Drosophila Dscam Is an Axon Guidance Receptor Exhibiting Extraordinary Molecular Diversity. *Cell, 101*(6), 671-684.

Schneider, C. A., Rasband, W. S., & Eliceiri, K. W. (2012). NIH Image to ImageJ: 25 years of image analysis. *Nature Methods, 9*(7), 671-675.

Schoonderwoerd, M. J. A., Goumans, M.-J. T. H., & Hawinkels, L. J. A. C. (2020). Endoglin: Beyond the Endothelium. *Biomolecules, 10*(2).

Schreiner, D., & Weiner, J. A. (2010). Combinatorial homophilic interaction between γ-protocadherin multimers greatly expands the molecular diversity of cell adhesion. *Proceedings of the National Academy of Sciences, 107*(33), 14893-14898.

Semizarov, D., Frost, L., Sarthy, A., Kroeger, P., Halbert, D. N., & Fesik, S. W. (2003). Specificity of short interfering RNA determined through gene expression signatures. *Proceedings of the National Academy of Sciences, 100*(11), 6347-6352.

Serafini, T., Colamarino, S. A., Leonardo, E. D., Wang, H., Beddington, R., Skarnes, W. C., & Tessier-Lavigne, M. (1996). Netrin-1 Is Required for Commissural Axon Guidance in the Developing Vertebrate Nervous System. *Cell, 87*(6), 1001-1014.

Serini, G., Valdembri, D., Zanivan, S., Morterra, G., Burkhardt, C., Caccavari, F., . . . Bussolino, F. (2003). Class 3 semaphorins control vascular morphogenesis by inhibiting integrin function. *Nature, 424*(6947), 391-397.

Shalaby, F., Janet, R., Yamaguchi, T. P., Gertsenstein, M., Wu, X. F., Breitman, M. L., & Schuh, A. C. (1995). Failure of blood-island formation and vasculogenesis in Flk-1-deficient mice. *Nature, 376*, 62-66.

Shan, W. S., Tanaka, H., Phillips, G. R., Arndt, K., Yoshida, M., Colman, D. R., & Shapiro, L. (2000). Functional cis-heterodimers of N- and R-cadherins. *Journal of Cell Biology, 148*, 579-590.

Sikora, M., Ermel, U. H., Seybold, A., Kunz, M., Calloni, G., Reitz, J., . . . Frangakis, A. S. (2020). Desmosome architecture derived from molecular dynamics simulations and cryo-electron tomography. *Proceedings of the National Academy of Sciences, 117*(44), 27132-27140.

Simms, V., Bicknell, R., & Heath, V. L. (2017). Development of an ImageJ-based method for analysing the developing zebrafish vasculature. *Vascular Cell, 9*(1).

Solowiej, A., Biswas, P., Graesser, D., & Madri, J. A. (2003). Lack of Platelet Endothelial Cell Adhesion Molecule-1 Attenuates Foreign Body Inflammation because of Decreased

Angiogenesis. *The American Journal of Pathology, 162*(3), 953-962.

Sondell, M., Sundler, F., & Kanje, M. (2000). Vascular endothelial growth factor is a neurotrophic factor which stimulates axonal outgrowth through the flk-1 receptor. *European Journal of Neuroscience, 12*(12), 4243-4254.

Stahl, A., Connor, K. M., Sapieha, P., Chen, J., Dennison, R. J., Krah, N. M., . . . Smith, L. E. H. (2010). The Mouse Retina as an Angiogenesis Model. *Investigative Ophthalmology & Visual Science, 51*(6), 2813-2826.

Stappenbeck, T. S., Bornslaeger, E. A., Corcoran, C. M., Luu, H. H., Virata, M., & Green, K. J. (1993). Functional analysis of desmoplakin domains: specification of the interaction with keratin versus vimentin intermediate filament networks. *The Journal of cell biology, 123*(3), 691-705.

Staton, C. A., Reed, M. W. R., & Brown, N. J. (2009). A critical analysis of current in vitro and in vivo angiogenesis assays. *International Journal of Experimental Pathology, 90*(3), 195-221.

Stern, B., Olsen, L. C., Tröße, C., Ravneberg, H., & Pryme, I. F. (2007). Improving mammalian cell factories: The selection of signal peptide has a major impact on recombinant protein synthesis and secretion in mammalian cells. *Trends Cell Mol Biol, 2*, 1-17.

Stevenson, B. R., Siliciano, J. D., Mooseker, M. S., & Goodenough, D. A. (1986). Identification of ZO-1: a high molecular weight polypeptide associated with the tight junction (zonula occludens) in a variety of epithelia. *Journal of Cell Biology, 103*(3), 755-766.

Stillwell, E. E., Zhou, J., & Joshi, H. C. (2004). Human Ninein is a Centrosomal Autoantigen Recognized by CREST Patient Sera and Plays a Regulatory Role in Microtubule Nucleation. *Cell Cycle, 3*(7), 921-928.

Stokes, D. L. (2007). Desmosomes from a structural perspective. *Current Opinion in Cell Biology, 19*(5), 565-571.

Suchting, S., Heal, P., Tahtis, K., Stewart, L. M., & Bicknell, R. (2005). Soluble Robo4 receptor inhibits in vivo angiogenesis and endothelial cell migration. *FASEB J., 19*(1), 121-123.

Sumigray, K. D., Chen, H., & Lechler, T. (2011). Lis1 is essential for cortical microtubule organization and desmosome stability in the epidermis. *Journal of Cell Biology, 194*(4), 631-642.

Suri, C., Jones, P. F., Patan, S., Bartunkova, S., Maisonpierre, P. C., Davis, S., . . . Yancopoulos, G. D. (1996). Requisite role of angiopoietin-1, a ligand for the TIE2 receptor, during embryonic angiogenesis. *Cell, 87*, 1171-1180.

Suzuki, H., Nishizawa, T., Tani, K., Yamazaki, Y., Tamura, A., Ishitani, R., . . . Fujiyoshi, Y. (2014). Crystal Structure of a Claudin Provides Insight into the Architecture of Tight Junctions. *Science, 344*(6181), 304-307.

Tachibana, Y., Yamashita, K., & Kobata, A. (1982). Substrate Specificity of Mammalian Endo-β-N-Acetylglucosaminidase: Study with the Enzyme of Rat Liver. *Arch Biochem Biophys, 214*, 199-210.

Takahashi, K., Nakanishi, H., Miyahara, M., Mandai, K., Satoh, K., Satoh, A., . . . Takai, Y. (1999). Nectin/PRR: An Immunoglobulin-like Cell Adhesion Molecule Recruited to Cadherin-based Adherens Junctions through Interaction with Afadin, a PDZ Domain–containing Protein. *Journal of Cell Biology, 145*(3), 539-549.

Takeichi, M. (1977). Functional correlation between cell adhesive properties and some cell surface proteins. *The Journal of cell biology, 75*, 464-474.

Tammela, T., Zarkada, G., Wallgard, E., Murtomäki, A., Suchting, S., Wirzenius, M., . . . Alitalo, K. (2008). Blocking VEGFR-3 suppresses angiogenic sprouting and vascular network formation. *Nature, 454*, 656-660.

Theiler, K. (1989). *The House Mouse. Atlas of Embryonic Development* (S. S. B. M. N. York Ed.).

Theocharis, A. D., Skandalis, S. S., Gialeli, C., & Karamanos, N. K. (2016). Extracellular matrix structure. *Advanced Drug Delivery Reviews, 97*, 4-27.

Thu, Chan A., Chen, Weisheng V., Rubinstein, R., Chevee, M., Wolcott, Holly N., Felsovalyi, Klara O., . . . Maniatis, T. (2014). Single-Cell Identity Generated by Combinatorial Homophilic Interactions between α, β, and γ Protocadherins. *Cell, 158*(5), 1045-1059.

Todorov, M. I., Paetzold, J. C., Schoppe, O., Tetteh, G., Shit, S., Efremov, V., . . . Ertürk, A. (2020). Machine learning analysis of whole mouse brain vasculature. *Nature Methods, 17*(4), 442-449.

Topper, J. N., & Gimbrone Jr, M. A. (1999). Blood flow and vascular gene expression: fluid shear stress as a modulator of endothelial phenotype. *Molecular Medicine Today, 5*(1), 40-46.

Torres-Vázquez, J., Gitler, A. D., Fraser, S. D., Berk, J. D., Van, N. P., Fishman, M. C., . . . Weinstein, B. M. (2004). Semaphorin-Plexin Signaling Guides Patterning of the Developing Vasculature. *Developmental Cell, 7*(1), 117-123.

Tselepis, C., Chidgey, M., North, A., & Garrod, D. (1998). Desmosomal adhesion inhibits invasive behavior. *Proceedings of the National Academy of Sciences, 95*(14), 8064.

Tsukita, S., Furuse, M., & Itoh, M. (2001). Multifunctional strands in tight junctions. *Nature Reviews Molecular Cell Biology, 2*(4), 285-293.

Valiron, O., Chevrier, V., Usson, Y., Breviario, F., Job, D., & Dejana, E. (1996). Desmoplakin expression and organization at human umbilical vein endothelial cell-to-cell junctions. *Journal of Cell Science, 109*(8), 2141-2149.

Van Itallie, C. M., & Anderson, J. M. (2014). Architecture of tight junctions and principles of molecular composition. *Seminars in Cell & Developmental Biology, 36*, 157-165.

Van Itallie, C. M., Aponte, A., Tietgens, A. J., Gucek, M., Fredriksson, K., & Anderson, J. M. (2013). The N and C Termini of ZO-1 Are Surrounded by Distinct Proteins and Functional Protein Networks. *Journal of Biological Chemistry, 288*(19), 13775-13788.

Vanhalst, K., Kools, P., Staes, K., Van Roy, F., & Redies, C. (2005). δ-Protocadherins: A gene family expressed differentially in the mouse brain. *Cellular and Molecular Life Sciences, 62*, 1247-1259.

Vasilatos, S. N., Katz, T. A., Oesterreich, S., Wan, Y., Davidson, N. E., & Huang, Y. (2013). Crosstalk between lysine-specific demethylase 1 (LSD1) and histone deacetylases mediates antineoplastic efficacy of HDAC inhibitors in human breast cancer cells. *Carcinogenesis, 34*(6), 1196-1207.

Vasioukhin, V., Bowers, E., Bauer, C., Degenstein, L., & Fuchs, E. (2001). Desmoplakin is essential in epidermal sheet formation. *Nature Cell Biology, 3*(12), 1076-1085.

Vestweber, D. (2008). VE-Cadherin. *Arteriosclerosis, Thrombosis, and Vascular Biology, 28*(2), 223-232.

Vieira, J. M., Schwarz, Q., & Ruhrberg, C. (2007). Selective requirements for NRP1 ligands during neurovascular patterning. *Development, 134*(10), 1833-1843.

Vincent, A., Omura, N., Hong, S.-M., Jaffe, A., Eshleman, J. R., & Goggins, M. (2011). Genome-wide analysis of promoter methylation associated with gene expression profiles of pancreatic adenocarcinomas. *Clinical Cancer Research, 17*, 4341-4354.

Wälchli, T., Wacker, A., Frei, K., Regli, L., Schwab, Martin E., Hoerstrup, Simon P., . . . Engelhardt, B. (2015). Wiring the Vascular Network with Neural Cues: A CNS Perspective. *Neuron, 87*(2), 271-296.

Wallez, Y., & Huber, P. (2008). Endothelial adherens and tight junctions in vascular homeostasis, inflammation and angiogenesis. *Biochimica et Biophysica Acta (BBA) - Biomembranes, 1778*(3), 794-809.

Wang, H. U., & Anderson, D. J. (1997). Eph Family Transmembrane Ligands Can Mediate Repulsive Guidance of Trunk Neural Crest Migration and Motor Axon Outgrowth. *Neuron, 18*(3), 383-396.

Wang, H. U., Chen, Z.-F., & Anderson, D. J. (1998). Molecular Distinction and Angiogenic Interaction between Embryonic Arteries and Veins Revealed by ephrin-B2 and Its Receptor Eph-B4. *Cell, 93*(5), 741-753.

Weng, J., Xiao, J., Mi, Y., Fang, X., Sun, Y., Li, S., . . . Wen, Y. (2018). PCDHGA9 acts as a tumor suppressor to induce tumor cell apoptosis and autophagy and inhibit the EMT process in human gastric cancer. *Cell Death & Disease*, *9*(2), 27.

Whittock, N. V., Wan, H., Eady, R. A. J., Morley, S. M., Garzon, M. C., Kristal, L., . . . McGrath, J. A. (2002). Compound Heterozygosity for Non-Sense and Mis-Sense Mutations in Desmoplakin Underlies Skin Fragility/Woolly Hair Syndrome. *Journal of Investigative Dermatology, 118*(2), 232-238.

Williams, S. E., Mann, F., Erskine, L., Sakurai, T., Wei, S., Rossi, D. J., . . . Henkemeyer, M. (2003). Ephrin-B2 and EphB1 Mediate Retinal Axon Divergence at the Optic Chiasm. *Neuron, 39*(6), 919-935.

Wilson, B. D., Ii, M., Won Park, K., Suli, A., Sorensen, L. K., Larrieu-Lahargue, F., . . . Li, D. Y. (2006). Netrins Promote Developmental and Therapeutic Angiogenesis. *Science, 313*, 640-644.

Wilson, B. D., & Soh, H. T. (2020). Re-Evaluating the Conventional Wisdom about Binding Assays. *Trends in Biochemical Sciences, 45*(8), 639-649.

Witcher, L. L., Collins, R., Puttagunta, S., Mechanic, S. E., Munson, M., Gumbiner, B., & Cowin, P. (1996). Desmosomal Cadherin Binding Domains of Plakoglobin. *Journal of Biological Chemistry, 271*(18), 10904-10909.

Wolverton, T., & Lalande, M. (2001). Identification and Characterization of Three Members of a Novel Subclass of Protocadherins. *Genomics, 76*(1), 66-72.

Wong, C. W., Christen, T., Roth, I., Chadjichristos, C. E., Derouette, J.-P., Foglia, B. F., . . . Kwak, B. R. (2006). Connexin37 protects against atherosclerosis by regulating monocyte adhesion. *Nature Medicine, 12*(8), 950-954.

Wong, D., & Dorovini-Zis, K. (1992). Upregulation of intercellular adhesion molecule-1 (ICAM-1) expression in primary cultures of human brain microvessel endothelial cells by cytokines and lipopolysaccharide. *Journal of Neuroimmunology, 39*(1), 11-21.

Woolard, J., Wang, W.-y., Bevan, H. S., Qiu, Y., Morbidelli, L., Pritchard-jones, R. O., . . . Bates, D. O. (2004). VEGF165b, an Inhibitory Vascular Endothelial Growth Factor Splice Variant: Mechanism of Action, In vivo Effect On Angiogenesis and Endogenous Protein Expression. *Cancer Research, 64*, 7822-7835.

Wu, K., Yang, Y., Wang, C., Davoli, M. A., D'Amico, M., Li, A., . . . Pestell, R. G. (2003). DACH1 Inhibits Transforming Growth Factor-β Signaling through Binding Smad4*. *Journal of Biological Chemistry, 278*(51), 51673-51684.

Wu, Q., & Maniatis, T. (1999). A striking organization of a large family of human neural cadherin-like cell adhesion genes. *Cell, 97*, 779-790.

Wylie, L. A., Mouillesseaux, K. P., Chong, D. C., & Bautch, V. L. (2018). Developmental SMAD6 loss leads to blood vessel hemorrhage and disrupted endothelial cell junctions. *Developmental Biology, 442*(2), 199-209.

Yamada, S., Pokutta, S., Drees, F., Weis, W. I., & Nelson, W. J. (2005). Deconstructing the cadherin-catenin-actin complex. *Cell, 123*, 889-901.

Yano, T., Matsui, T., Tamura, A., Uji, M., & Tsukita, S. (2013). The association of microtubules with tight junctions is promoted by cingulin phosphorylation by AMPK. *Journal of Cell Biology, 203*(4), 605-614.

Yeh, H.-I., Rothery, S., Dupont, E., Coppen, S. R., & Severs, N. J. (1998). Individual Gap Junction Plaques Contain Multiple Connexins in Arterial Endothelium. *Circulation Research, 83*(12), 1248-1263.

Yoder, M. D., & Gumbiner, B. M. (2011). Axial protocadherin (AXPC) regulates cell fate during notochordal morphogenesis. *Developmental Dynamics, 240*(11), 2495-2504.

Yonemura, S., Wada, Y., Watanabe, T., Nagafuchi, A., & Shibata, M. (2010). α-Catenin as a tension transducer that induces adherens junction development. *Nature Cell Biology, 12*(6), 533-542.

Yoshida, C., & Takeichi, M. (1982). Teratocarcinoma cell adhesion: Identification of a cell-surface protein involved in calcium-dependent cell aggregation. *Cell, 28,* 217-224.

Yoshida, K., Watanabe, M., Kato, H., Dutta, A., & Sugano, S. (1999). BH-protocadherin-c, a member of the cadherin superfamily, interacts with protein phosphatase 1 alpha through its intracellular domain. *FEBS Letters, 460*(1), 93-98.

Zheng, X., Ma, N., Wang, X., Hu, J., Ma, X., Wang, J., & Cao, B. (2020). Exosomes derived from 5-fluorouracil-resistant colon cancer cells are enriched in GDF15 and can promote angiogenesis. *Journal of Cancer, 11*(24), 7116-7126.

Zhou, X., Stuart, A., Dettin, L. E., Rodriguez, G., Hoel, B., & Gallicano, G. I. (2004). Desmoplakin is required for microvascular tube formation in culture. *Journal of Cell Science, 117*(15), 3129-3140.

Zihni, C., Mills, C., Matter, K., & Balda, M. S. (2016). Tight junctions: from simple barriers to multifunctional molecular gates. *Nature Reviews Molecular Cell Biology, 17*(9), 564-580.

Zovein, A. C., Luque, A., Turlo, K. A., Hofmann, J. J., Yee, K. M., Becker, M. S., . . . Iruela-Arispe, M. L. (2010). β1 Integrin Establishes Endothelial Cell Polarity and Arteriolar Lumen Formation via a Par3-Dependent Mechanism. *Developmental Cell, 18,* 39-51.